UGA
Université
Grenoble Alpes

THÈSE

Pour obtenir le grade de

DOCTEUR DE L'UNIVERSITE GRENOBLE ALPES

Spécialité : **Sciences de la Terre et de l'Univers et de l'Environnement**

Arrêté ministériel : 25 mai 2016

Présentée par

Ugo NANNI

Thèse dirigée par **Christian VINCENT**, Ingénieur de recherche, CNRS, Université Grenoble Alpes
et codirigée par **Florent GIMBERT**, Chargé de recherche, CNRS, Université Grenoble Alpes

préparée au sein de l'**Institut des Géosciences de l'Environnement**
dans **l'École Doctorale Terre, Univers, Environnement**

Etude sismologique de la dynamique du réseau hydrologique sous-glaciaire d'un glacier alpin.

Resolving subglacial hydrology network dynamics through seismic observations on an Alpine glacier.

Thèse soutenue publiquement le **03 décembre 2020**
devant le jury composé de :

Mme. Gwenn FLOWERS
Professeur, Simon Fraser University, Vancouver, Rapportrice
M. Jérôme VERGNE
Physicien adjoint, Université de Strasbourg, EOST, Rapporteur
Mme Anne OBERMANN
Chercheur sénior, SED, ETH Zürich, Examinatrice
M. Mauro WERDER
Chercheur, VAW, ETH Zürich, Examinateur
Mme Maurine MONTAGNAT RENTIER
Directrice de recherche, CNRS, CNRM MétéoFrance, Grenoble, Présidente
M. Christian VINCENT
Ingénieur de recherche, CNRS, IGE, Grenoble, Directeur de thèse
M. Florent GIMBERT
Chargé de recherche, CNRS, IGE, Grenoble, Directeur de thèse
M. Philippe ROUX
Chercheur, CNRS, ISTerre, Grenoble, Invité

And at the instant he knew, he ceased to know.
— Jack London.

Résumé

La façon dont l'eau s'écoule sous les glaciers joue un rôle majeur dans le couplage mécanique glace-roche, qui définit fortement les vitesses d'écoulement des glaciers. Aujourd'hui, notre compréhension de la physique du réseau d'hydrologie sous-glaciaire est limitée et incertaine en raison de la rareté des mesures de terrain, qui ne représentent que partiellement l'hétérogénéité de l'environnement sous-glaciaire. L'objectif de mon travail de doctorat est d'utiliser la sismologie passive pour surmonter les difficultés observationnelles et ainsi quantifier l'évolution des conditions de pression et de la configuration du réseau d'hydrologie sous glaciare. De récents travaux montrent que l'écoulement turbulent d'eaux sous-glaciaire génère du bruit sismique dont l'étude donne accès aux propriétés hydrodynamique associées (Bartholomaus *et al.*, 2015a; Gimbert *et al.*, 2016). Ces analyses ont été menées sur une courte période, de sorte qu'il n'est pas certains qu'elles soient appropriées à l'étude de l'hydrologie sous-glaciaire sur les échelles de temps saisonnières et diurnes, qui sont les plus représentative de l'influence sur la dynamique glaciaire. De plus, ces études ne prennent pas en compte les changements dans la configuration complexe de tels réseaux hydrologique et jusqu'alors il n'existe pratiquement aucune étude ayant localisé des sources de bruit sismique spatialement éparses et temporellement variables. Dans ce travail de doctorat, j'aborde ces défis sismologiques afin de résoudre la dynamique de l'hydrologie sous-glaciaire.

Nous avons acquis sur le glacier d'Argentière (Alpes) un jeu de données continu sur 2 ans permettant d'évaluer la variation de puissance sismique induite par les flux d'eau sous-glaciaire et de la comparer à des mesures in-situ de la vitesse de glissement basale et du débit d'eau sous-glaciaire. Je montre que l'étude approfondie de puissance sismique à [3-7] Hz donne accès aux propriétés l'hydrodynamique des flux d'eau sous-glaciaires sur des échelles de temps allant de la saison à l'heure et sur une large gamme de débits d'eau (de 0.25 à 10 m^3.sec^{-1}). En combinant ces observations avec un cadre physique adéquat, j'inverse les gradients de pression et rayons hydrauliques associés et identifie une dynamique saisonnière des chenaux sous-glaciaire caractérisée par deux régimes. À faible débit, les chenaux se comportent à l'équilibre et s'adaptent aux variations de débit principalement par des changements de rayon hydraulique. À fort débit et une forte variabilité diurne en apport d'eau, les chenaux se comportent hors équilibre et subissent de fortes variations du gradient de pression hydraulique qui permettent de maintenir de fortes pression d'eau dans les cavités et favoriser des vitesses de glissement élevées en été.

Nous avons ensuite mené une expérience d'un mois avec un réseau sismique dense, complétée par des mesures d'épaisseur et de vitesse de surface du glacier. Sur cette base j'ai développé une nouvelle méthodologie pour relever le défi, jusqu'alors non résolu, de localiser des sources de bruit sismique spatialement éparses et temporellement variables. Ce faisant, j'ai obtenu une carte du système de drainage sous-glaciaire ainsi que son évolution au jour le jour. Grâce ces cartes j'ai observé quand et où ce système est distribué à travers des cavités connectées qui favorisent l'écoulement rapide du glacier ou alors localisé à travers des chenaux qui limitent l'écoulement rapide du glacier. Parallèlement à cette étude, je montre que l'on peut utiliser l'amplitude d'événements sismique haute fréquence pour étudier les structures glaciaires telles les crevasses, les variations d'épaisseur ou l'anisotropie cristalline et ce de manière complémentaire à ce qui est traditionnellement fait avec l'analyse de phase sismique.

Le premier résultat de ce travail transdisciplinaire est que l'on peut analyser des mesures sismiques passive pour quantifier l'évolution temporelle des conditions de pression et de géométrie des chenaux sous-glaciaires sur une saison de fonte complète. Le second est qu'un réseau dense de mesure sismiques peut être utiliser pour résoudre la configuration spatiale du système de drainage sous-glaciaire et la transition d'un écoulement d'eau sous-glaciaire distribué à un écoulement localisé. Ces avancées ouvrent à l'étude de tel processus sous-glaciaire sur d'autre sites et en particulier sur les calottes polaires Groenlandaise et Antarctique mais aussi à l'étude des écoulements au sein d'autres systèmes géophysiques tels les volcans, les karts ou les glissements de terrain.

Summary

The way in which water flows in the subglacial environment exerts a major control on ice-bed mechanical coupling, which strongly defines glacier sliding speeds. Today our understanding on the physics of the subglacial hydrology network is limited because of the scarcity of field measurements that yield a partial representation of the heterogeneous subglacial environment. The aim of my PhD work is to use passive seismology to help overcome common observational difficulties and quantify the evolution of the subglacial hydrology network pressure conditions and its configuration. Recent works show that subglacial turbulent water flow generates seismic noise that can be related to the associated hydrodynamics properties (Bartholomaus *et al.*, 2015a; Gimbert *et al.*, 2016). These analyses were conducted over a limited period of time making it unclear whether such approach is appropriate to investigate seasonal and diurnal timescales, I.e. when subglacial water flow influences the most glacier dynamics. In addition, previous studies did not consider spatial changes in the heterogeneous drainage system, and until now, almost no study has located seismic noise sources spatially scattered and temporally varying. In this PhD work I address those seismological-challenges in order to resolve the subglacial hydrology dynamics in time and space.

We acquired a 2-year long continuous dataset of subglacial-water-flow-induced seismic power as well as in-situ measured glacier basal sliding speed and subglacial water discharge from the Glacier d'Argentière (French Alps). I show that a careful investigation of the seismic power within [3-7] Hz can characterize the subglacial water flow hydrodynamics from seasonal to hourly timescales and across a wide range of water discharge (from 0.25 to 10 $m^3.sec^{-1}$). Combining such observations with adequate physical frameworks, I then inverted the associated hydraulic pressure gradient and hydraulic radii. I observed that the seasonal dynamics of subglacial channels is characterized by two distinct regimes. At low discharge, channels behave at equilibrium and accommodate variations in discharge mainly through changes in hydraulic radius. At a high discharge rate and with pronounced diurnal water-supply variability, channels behave out of equilibrium and undergo strong changes in the hydraulic pressure gradient, which may help sustain high water pressure in cavities and favor high glacier sliding speed over the summer.
We then conducted a one-month long dense seismic-array experiment supplemented by glacier ice-thickness and surface velocity measurements. Using this unique dataset, I developed a novel methodology to overcome the challenge of locating seismic noise sources spatially scattered and temporally varying. Doing so, I successfully retrieve the first two-dimensional map of the subglacial drainage system as well as its day-to-day evolution. Using this map, I characterize when and where the subglacial drainage system is distributed through connected cavities, which favour rapid glacier flow versus localized through a channelized system that prevents rapid glacier flow. In addition, I also use high frequency seismic ground motion amplitude to study glacier features such as crevasses, thickness or ice anisotropy in a complementary way to what is traditionally done with seismic phase analysis.

The first outcome of this cross-boundary PhD work is that one can analyse passive seismic measurements to retrieve the temporal evolution of subglacial channels pressure and geometry conditions over a complete melt-season. The second is that dense seismic array measurements can be used to resolve the subglacial drainage system spatial configuration and observe the switch from distributed to localized subglacial water flow. Such advances open the way for studying similar subglacial process on different sites and in particular in Greenland and Antarctica. This also concerns numerous sub-surface environment that host similar process such as volcanoes, karst, and landslides.

Keywords: Subglacial hydrology, passive seismology, seismic noise location, dense seismic array.
Mots clés: Hydrologie sous-glaciare, sismologie passive, localisation de bruit sismique,.

Remerciements

Trois années passées à écouter les glaciers.

Chercher jour après jour, semaine après semaine. Chercher leurs secrets, chercher à les comprendre et me chercher à leurs côtés en plongeant dans les entrailles glacées à y perdre pied. Il m'est peut-être plus facile, après l'écoulement de ce temps, de vous décrire celui des eaux sous glaciaires que de dresser un bilan. J'ai vu s'alterner de longues périodes d'ablations mettant à nue les surfaces fracturées et celles des premières neiges qui m'ont façonnées. J'ai entendu les craquements profonds qui font vibrer la surface et ouvrent l'intérieur aux éléments. J'ai connu les ponts qui se dérobent et se reforment chaque fois différemment. Mon ascension progressive dans la recherche a pris à contre-courant les lourdes masses glacées qui, elles, continuent leurs descentes. A leur image, j'ai avancé parfois par à-coup, parfois par inertie. Mais toujours un peu plus loin, un peu plus haut, encore un peu. J'ai remonté les pentes vers les hauteurs acérées et accueillantes, convoitées et enivrantes. Vers l'aventure. J'ai pu glisser, mais j'ai appris que relâcher la pression diminue le glissement, alors j'ai écouté les glaciers. J'ai écouté pendant trois années, trois années de recherche à vos côtés. Et je vous en remercie.

Vous, les intermittents parisiens pour votre intermittence bien présente et vitale. Pour nos débuts d'années rêveurs et tous ces bouts de pellicules qui forment nos prises passées et scénarisent nos demains. Merci Yoann pour tes gestes, Antonin pour me donner envie, Clovis pour tes sons, Noëllie pour ces petits détails et Romain pour ces images qui m'accompagnent. Vous êtes ces fontes printanières qui donnent vie au mouvement.

Vous, les compagnons quotidiens pour enchanter mes recherches. Pour ces midi à Eve, ces café interminables et ces sourires de tous les jours. Merci Nathan for the discussion and your hat, Romain pour tes vitesses et tes bouclettes, Samuel pour nos interludes annuels, Albane pour ta boucanerie, Sarah pour l'éclat des repas un peu tardifs, Foteini pour ce tiramisu et cette moussaka à venir, Marco pour ton côté italien, Juan Pedro pour ta fougue et tes milliers de soldats, Maria pour tes rires et ton énergie, Jérémie pour ces cafés, ces couleurs et ta curiosité, Adrien pour ton enthousiasme et tes envies inspirantes, Antoine pour me faire sourire et Benoit pour ta disponibilité et toutes ces fois sur le terrain. Vous avez été ces premières neiges, cette poudreuse qui enchante toujours autant.

Vous, les amis Grenoblois pour m'avoir tant fait découvrir. Merci Alban pour ces premiers pas en rocher et nos jeux salvateurs, Julien pour ces discours auxquels il me tarde de donner voix et nos cafés à chercher nos voies, David pour nos retrouvailles prometteuses, Jonathan for playing chess and your support, Marion et Lucas pour vos festivals, vos bois, vos histoires et nos futures et Hans pour nos samedis et ton épistémologie. Vous avez été la corde de mes traversées.

Vous, les accompagnateurs pour m'avoir tant appris. Merci Manu pour ton partage et ton inspiration, Nicolas pour ta confiance, Frédéric pour mes débuts et la suite, Dirk pour ces années à patiemment partager, Lucas pour ton esprit critique et créateur, Olivier pour m'avoir mis l'eau à la bouche, Albanne pour ta précision, Mondher pour ta patience, Guilhem pour cette ouverture, Vincent pour ta détermination, Léonard et Aurélien pour

comprendre tous ce bruit, Andy pour me montrer que c'est possible, Victor pour la beauté inspirante de tes approches, Fanny pour ta sagesse saccadée, Jean-Manu pour ton ouverture, Patrick pour m'inspirer et Adrien pour me faire questionner mes idées.

Vous qui m'avez appris comment observer et bidouiller. Merci Luc pour tous ces moments à l'atelier, ces trous percés et ces courbes déformées, Bruno pour ta grande présence et toutes ces batteries transportées, Delphine pour ton partage, Olivier pour oser t'occuper des sismomètres, Benoit pour les soudures et les questions, Luc pour ces galeries qu'il me reste à voir, Nikos for all the feedbacks and the help on our sismometers, Nico et Greg pour votre présence, Amélie et Mélissa pour vos arrangements. Vous avez été les artisans de ce cheminement sous-glaciaire.

Vous, les artistes en tout genre qui avez équilibré ma science. Merci la Meute pour ces mois si intenses, les filles pour notre projet qui brillera par son absence, Peb et les 11 petites mains pour m'avoir transformé en personnage de bande dessinée, Priscilla pour ta curiosité, EdZ pour ces dimanches au soleil à penser nos futur planches, Eric pour avoir joint montagnes et sciences et Lucie pour m'avoir poussé à donner voix à mes mots. Vous avez été ce lever de soleil qui me pousse à continuer.

Vous, les petites mains qui depuis tant d'années façonnez ce bonhomme de neige devenu glaciologue. Merci Papa, Maman, Clelia et Amelia pour être là, mais aussi Adrien et Jenni pour m'avoir ouvert à d'autres horizons, Régis pour ces sorties en vélo, les Lemaire pour votre passion pour la montagne et les Lecarrié, Paolo et Giovanni pour ces étés italiens. Vous êtes ces grains de neiges qui année après année forment les glaciers.

Vous, les inclassables. Merci, Samson pour ta folie et mon envie d'un jour bosser avec toi, Kristel pour avoir été là au tout début de mon choix, Ben pour m'inspirer à ton insu et m'avoir pris la main pour aller sur les glaciers, Susy pour ce dernier printemps si long et si court mais qui dure toujours, Victor pour ces débarquements à Grenoble, ces retours dans le Sud, être là, être toi et me donner envie de continuer, Simon pour cette année d'écoute et pour les prochaines, Fabien pour notre complexité, tes réflexions, tes visions, nos discussions au coin du feu, pour me donner envie de découvrir, Erwan pour nos documentaires à venir et Jordi pour ma naissance au Gravel et les strade bianche qui nous attendent. Vous êtes ces cristaux trouvés dans les moraines que je glisse dans ma poche.

Vous, les guides de ce cheminement. Merci Christian pour ta sagesse glaciaire et non glaciale, pour m'avoir permis de parfois prendre du recul, pour me donner cette vision complexe et indispensable. Merci Philippe pour m'avoir parfois bousculé, pour avoir pris le temps, pour avoir écouté et partagé. Merci Florent pour ton enseignement, ta patience, ton écoute, ton inspiration, ta rigueur, pour m'avoir fait confiance tout en m'accompagnement dans mon devenir de jeune chercheur. Vous avez balisé mon itinéraire, entre vos connaissances et mon apprentissage, vous m'avez accompagné dans ces aventures sous-glaciaire qui me permettent aujourd'hui de continuer à explorer.

A toi, Gwladys, ma princesse des neiges éternelle, qui m'a fait découvrir la magie des mondes polaires et des aventures partagées.

IV Spatial investigation of subglacial water flow — 97

Part I

Introduction

One of my first encounters with the wonders of the Cryosphere. © *Gwladys*.

1

Introduction

La connaissance progresse en intégrant en elle l'incertitude, non en l'exorcisant.
— Edgar Morin

1.1 General overview

Throughout their journey from falling snow to the ocean, glaciers are influenced by numerous processes that control their dynamics and mass. Yet, glaciers are not only physical objects with limited interactions with their environments, but rather natural wonders that actively take part in the evolution of the surface of the Earth through shaping landscapes and topography, acting as natural water reservoirs, tying climate to human societies, human societies to climate and hosting our dreams of discovery. Understanding the movement of glaciers is, for me, taking part in understanding the complexity of our world. Understanding glaciers is understanding our surrounding environment. Understanding glaciers is part of the long quest of humanity in facing and accepting the unknown.

Under the current climate change, the future of glaciers and ice caps is yet uncertain for the coming century because of uncertainties in climate predictions, but also because of the complex glacial and subglacial process and their interactions with the ocean. In these regards, a better understanding of the movements of glaciers is necessary to predict their fate and future in the decades to come. During my PhD I have focused on observing the subglacial environment, and especially subglacial water flow, in order to understand the response of glaciers to changes in surface melt and to contribute to the wider picture of understanding the movement of glaciers. I think that this process of understanding has to go hand to hand with an increasing cooperation and coordination among people and authorities of all kind (scientists, economists, politicians).

The work of Edgar Morin on the complexity has guided me over the past 10 years and the link between glaciology and seismology that I made during my PhD is also based on its approach of linking knowledge (see Moustard and Leduc (2020) for an overview of Edgar Morin's work).

In the high altitudes snow accumulates year to year.

The snow layer get denser and denser with time and slowly expulse air and humidity.
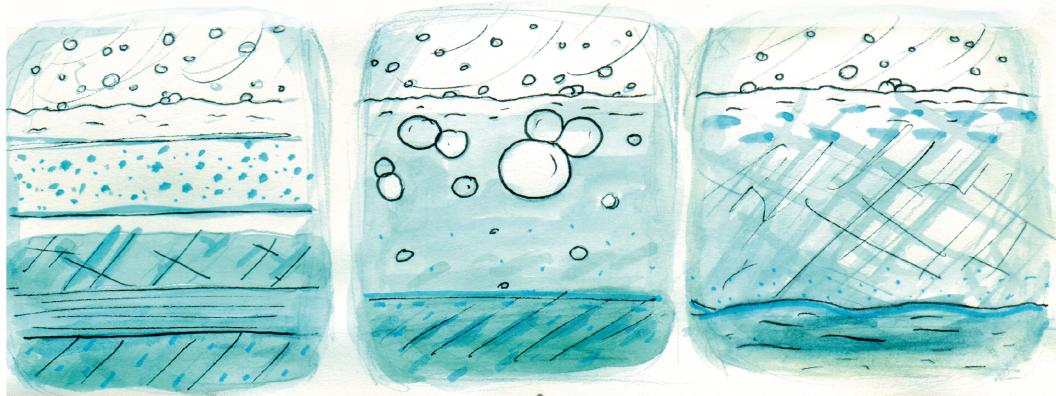
The compacted snow (firn) slowly transforms to ice, that starts to flow towards the lower altitude.

Figure 1.1: On the birth of a glacier flow falling snow. © *EdZ*[1].

On the nature of glaciers

In high altitudes and/or high latitudes, where summer temperatures barely reach the melting point, snow accumulates from year to year. Under its own weight, the snow slowly compacts to form firn that throughout time expulses most of its air, densifies and becomes ice. Over long time scales (weeks to years) ice behaves as a viscous fluid. The glacier slowly and continuously deforms under the stress applied by its own weight (Glen, 1952). In doing so ice flows and starts its journey as a glacier in its way towards lower altitudes. A glacier not only flows through creep, but also through sliding of ice over the bed (where the ice is at or above its melting point) and potential deformation of the bed itself (Weertman, 1957; Boulton and Hindmarsh, 1987). Basal sliding is often facilitated by basal temperature being at the melting point such that flowing water and/or water content within the bed reduce the bed apparent roughness (Lliboutry, 1968).

As a glacier flows, it gains mass through snowfall and loses it through ice melt and other processes such as ice blocks avalanching or icebergs production (calving) (Cuffey and Paterson, 2010). If mass losses exceed gains, a glacier has a negative mass balance and it will slowly, but surely, shrink over time. As a glacier flows down, air temperature tends to increase and surface melt becomes more and more important. This causes snow and ice to melt and results in the presence of liquid water at the surface of the glacier. Melt water is then drained following a river-like hydrology system before being conveyed into supra-glacial lakes and washed through crevasses and moulins (Hubbard and Nienow, 1997; Irvine-Fynn *et al.*, 2006; Davison *et al.*, 2019). Water entering the glacier may then be stored, transported and eventually routed to the bed. As it reaches the ice-bed interface, meltwater actively takes part in the movement

[1]Edith Tinon, EdZ, is a drawer with whom I collaborated during my PhD. See more in Part VI, from page 191.
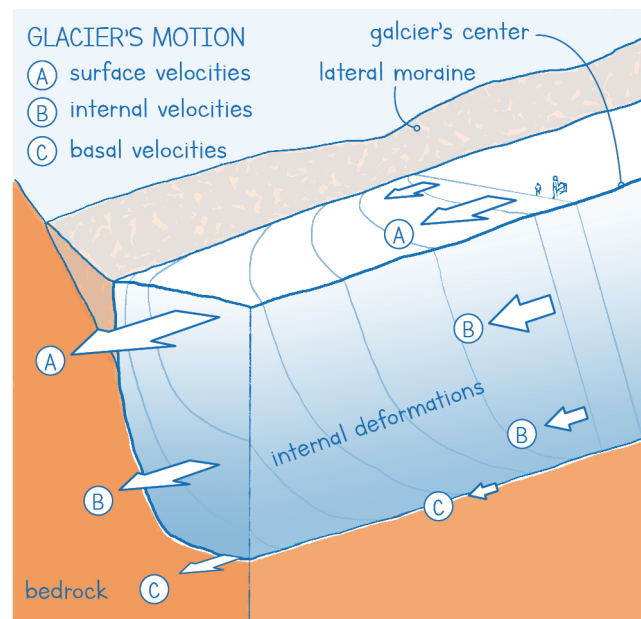
Figure 1.2: On the flow of glacier. © *Marine Jambeau*[2].

of glaciers by modulating the coupling between the glacier and its bed and may favor the slip of glaciers through pressurization (Kamb and LaChapelle, 1964; Lliboutry, 1968). The influence of water on basal motion depends on the pressure that water exerts against the cryostatic pressure of the ice. The higher the pressure the faster the sliding. It is generally thought that if water flows in an inefficient subglacial drainage system (traditionally named cavity-system) water pressure rises and thus favors fast glacier slip, while if routed through an efficient drainage system (traditionally named channel-system) water pressure tends to be low and thus favors low glacier slip (Röthlisberger, 1972; Schoof, 2010). As water reaches the glacier terminus it then exits the subglacial drainage system and joins the ocean for marine-terminating glaciers or feeds rivers in mountainous regions. For land-terminating temperate glaciers, subglacial hydrology controls the ice flow variability over short time scales (days to season), while marine-terminating glaciers are also greatly influenced by ocean circulation, sea ice, and calving of the front (Hubbard *et al.*, 1995; Moon *et al.*, 2014, 2015).

---

[2]Marine Jambeau has collaborated with our team during the past two years, joined us on the field and in the lab to tell our work through her drawings.

On the interaction of glaciers with their environment

Most of the information used in this section is from the Special Report on Ocean and the Cryosphere (SROCC) from the Intergovernmental Panel on Climate Change (https://www.ipcc.ch/srocc/).

The effect of glaciers in shaping the Earth's surface

Around 10% of the Earth's land area is covered by glaciers and ice sheets. Glaciers are long-term geomorphological agents that link tectonic, erosion and climate over millennials. During the Quaternary period (the past 2.6 million years), glaciers and icecaps have shaped our landscapes by eroding their underlying bedrock. The two main processes of erosion are abrasion and quarrying, both of which happen at the glacier bed and strongly depend on sliding speed (Alley *et al.*, 2019). Through these processes, glaciers erode on average at a rate of 1 mm per year, which does not seem that important but corresponds to a 1 km vertical erosion over one million years (Egholm *et al.*, 2009). Such erosion rates are the most important in nature, and they cause mass transport large enough to influence the stress applied on the Earth's crust and therefore influence tectonics over geological times periods (Braun, 2003; Herman *et al.*, 2010). Yet these erosion processes are poorly understood, which limits our knowledge on a wide spectrum of topics from the climate influence on tectonics over geological timescales to the effect of changes in glacier dynamics in the Artic on biogeochemical fluxes and Artic wildlife. The understanding of glacier erosion relies on a good understanding on the basal slip of glaciers and on how sediments are transported and evacuated through the subglacial drainage system.

On the response of glaciers to climate change

Over the last decades, global warming has led to widespread mass loss from ice sheet and glaciers. Between 2006 and 2015 they have lost around 700 billion of tonnes per year, with an approximate equal contribution between the Greenland Ice sheet, the Antarctic Ice Sheet and the rest of the glaciers outside those areas. This mass loss corresponds to an increase in sea level rise of about 1.7 mm per year, that is equivalent to the sea-level-rise caused by thermal expansion of the ocean (c. 1.4 mm per year) (Frederikse *et al.*, 2020). As more than 700 million people live within the first meter above sea level, sea-level-rise will, and does already, cause extreme changes in human societies across the planet. In the future, the contribution of Antarctica due to ice flow acceleration has the potential to lead to several meters' sea-level-rise within few centuries, but uncertainties arise from inadequate model representation of ice sheet processes, especially those occurring at the base of glaciers (Ritz *et al.*, 2015). Predictions for the Greenland Ice Sheet suggest a mass reduction up to 36% in 2100, corresponding to a cumulative sea-level-rise of up to 2 meters. For mountains glaciers, the future is quite clear with projected loss of more than 80% by 2100. The shrinking of glaciers in response to climate change not only affects sea-level-rise, but also has numerous impacts on water resources, infrastructure, food security as well as health and well-being. Recent studies also highlight the ecological consequences of glacier retreat (Anderson and Radić, 2020).

On the importance of glaciers for human societies

Glaciers constitute unique water reservoirs for more than 1.2 billion people, especially in Central Asia, the Andes and the northern part of North America. They are natural water reservoirs that accumulate water during winter and rain seasons and deliver it during summer and dry seasons. In Europe, especially in France, Norway and Switzerland, glaciers are also used for hydroelectric production that helps limit fossil-fuel and nuclear-based electricity production. Because of this close relation between glaciers and societies, numerous cities and villages are located near glaciated environments. This infrastructure and the people living there are often subject to natural hazards such as sudden outburst flows, mudflows and landslides that can cause extensive damages and human casualties. At the time when I write this manuscript, 500 000 cubic meters of ice, hanging at the flank of the Mt Blanc mountain range, threaten the valley of Courmayeur (Italy). This represents a football pitch covered in ice 80 m thick. Changes in glaciers cause increasing disasters, particularly because glaciers shrinking favors dammed-lakes and hillslope destabilization (Scherler *et al.*, 2011). Enabling climate resilience depends on ambitious changes in our way of life through emissions reductions, but also on our capacity to monitor, forecast and explain to the laypeople the future of glaciers and ice caps.
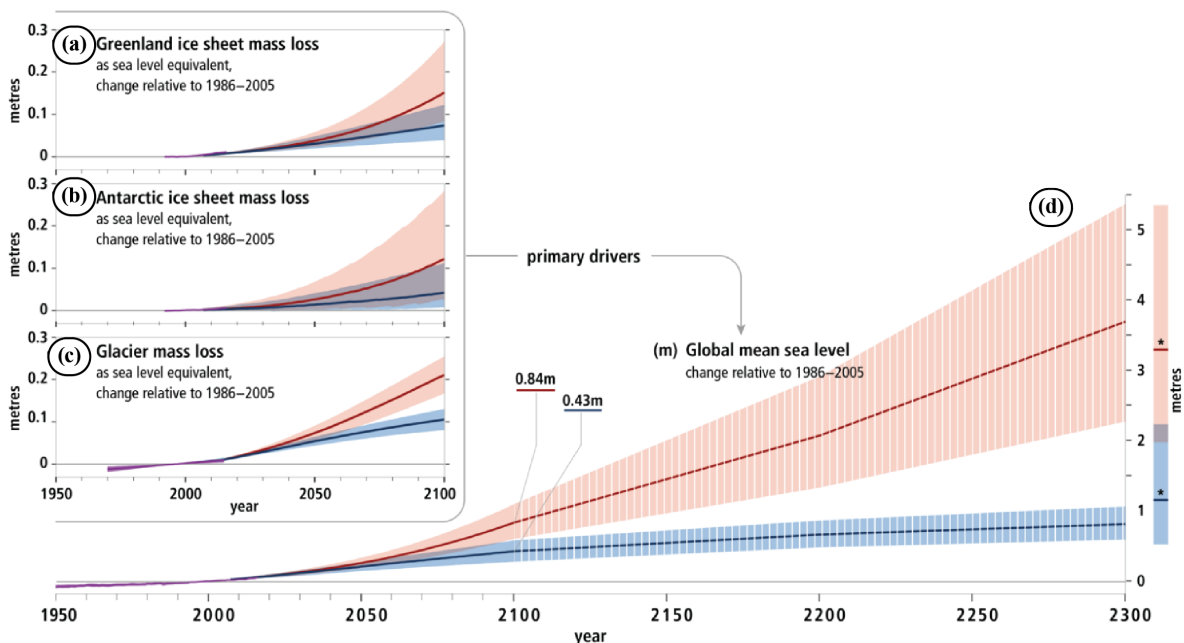
Figure 1.3: Modified after SROCC. Observed and modeled global sea level rise under low (RCP2.6, blue) and high (RCP8.5, red) greenhouse gas emissions scenarios with the contribution of (a) Greenland and (b) Antarctic ice sheet mass loss and (c) Glacier mass loss.

From a more socio-cultural aspect, glaciers and ice caps have been part of our imagination for millennia, with sacred glaciers in high mountain Asia, central Andes, or recreational use in the European Alps. Tourism and recreation have been negatively

impacted in many mountain regions, but also negatively impacted many mountain regions because of increasing infrastructure and frequentation. Last, but not least, glaciers and ice caps are part of the last Terra Incognita, the last frontiers of our societies. And sometimes Science does not need more than a little touch of curiosity to be started.

1.2 Subglacial water flow influence on glacier sliding
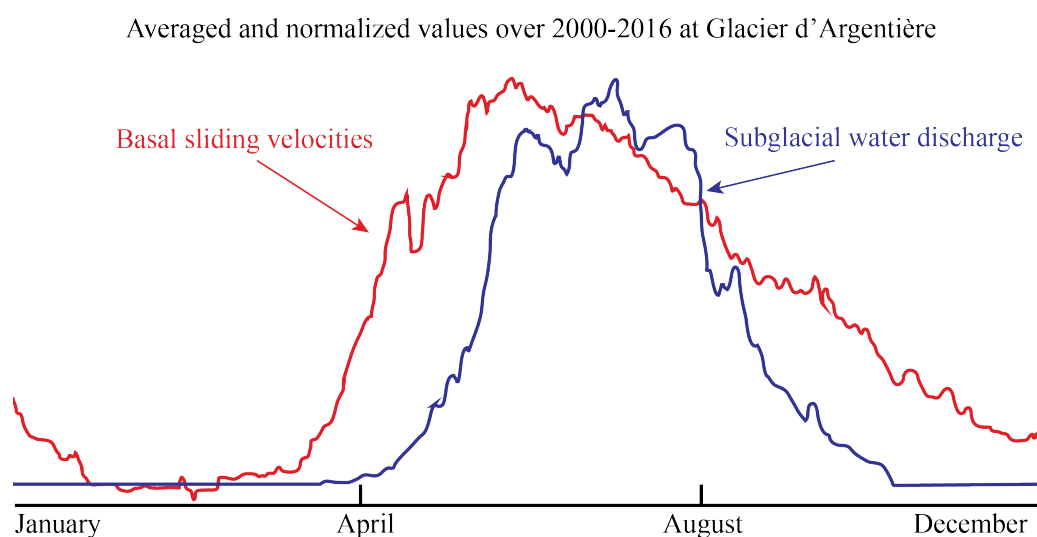
Figure 1.4: Water discharge (blue) and basal sliding velocities (red) measured at Glacier d'Argentière (French Alps) and averaged over the 2000-2016 period. Both values are scaled on a yearly basis. See Vincent and Moreau (2016) for absolute values.

Background

Today key questions remain unanswered in the process of understanding the movement of glaciers. Among which, one of the most important concerns the routing of water below glaciers. I present here an overview on basal sliding and how it is modulated by subglacial water flow.

Over hard-bed temperate glaciers and in the absence of ice-bed detachment (e.g. cavitation), sliding is thought to be controlled by a combination of regelation and creep flow around bedrock bumps that are typically around 10 to 100 mm in size (Weertman, 1957). Regelation occurs for ice assumed to be at the melting point and is driven by melting of the ice upstream of bumps and refreezing downstream where pressure is higher. Creep flow is caused by viscous deformation of the ice driven by stress differential between upstream and downstream of bumps. Those two mechanisms imply that ice rests on a thin film of water that separates ice and rock, such that there is no frictional resistance operating directly the ice-bed interface. Basal sliding is also modulated by water flowing at the base of the glacier. Pressurized water can favors the
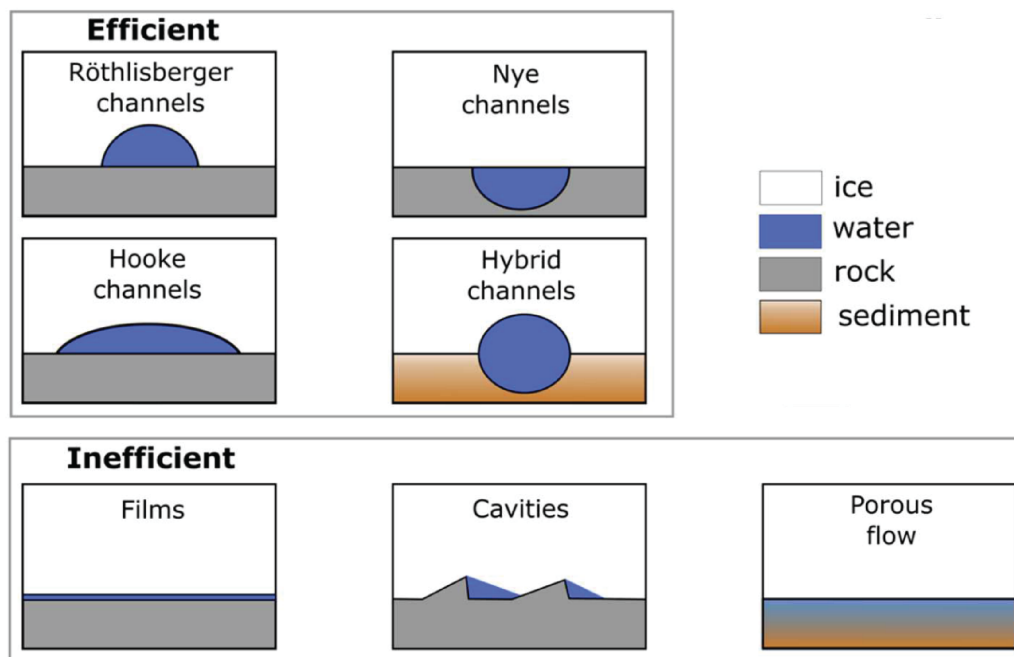
Figure 1.5: Modified after Davison *et al.* (2019). Conceptual efficient and inefficient subglacial drainage systems. Channels and cavities are depicted as filled with water, but they may not be if they are not in steady-state. Ice flow is into the page, except for inefficient cavities, where ice flow is left-to-right.

formation of cavities downstreams bumps (Lliboutry, 1968). As water pressure rises, cavities grow, reducing the apparent rugosity of the bed and sliding becomes faster. What complicates the modulation of sliding by water is that water pressure does not simply depend on water supply but rather on the way water is routed throughout the subglacial drainage system and the capacity of the drainage system itself (Röthlisberger, 1972). Over soft-bed glaciers, the sliding problem is similar but with an added contribution of bed deformation (Boulton and Hindmarsh, 1987). This deformation can be represented similarly to the sliding of ice over a hard-bed, but with different substrate properties (De Fleurian *et al.*, 2014). Subglacial water flow also occurs over and within such beds and also exerts a complex influence on the resulting sliding.

Subglacial water flow: theory and research gaps

Traditionally the subglacial drainage system is thought to be composed of two main sub-systems (Fig. 1.5). This nomenclature is based on the efficiency of these sub-systems to route water flow and on their propensities to increase or decrease water pressure and influence basal sliding.

The system that efficiently routs water is referred to as the channelized-system, as it is made of subglacial channels. Subglacial channels can be of R-type (named after Hans Röthlisberger, one of the first to describe their mechanisms in Röthlisberger (1972)), when melted into the ice by turbulent dissipation of heat (Fig. 1.6), or of
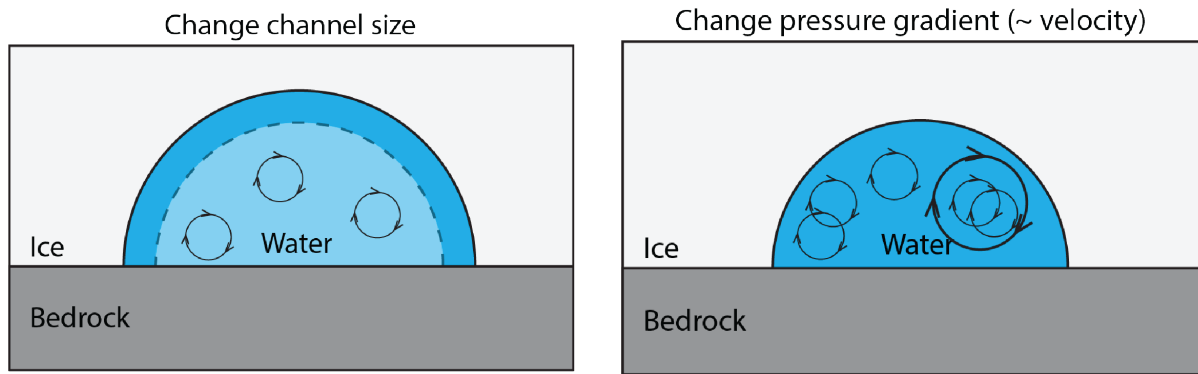
Figure 1.6: Schematic illustration of the mechanisms that control the opening and closing of R-type subglacial channels.

N-type (named after John Nye, one of the first to describe their mechanisms in Nye (1965)) when dug into basal sediments by the flowing water. Both types close by ice creep (Fig. 1.6). In steady-state, a subglacial channel tends to have low water pressure. This has huge implication for subglacial water pressure, as those channels act as low pressure potential and force drainage of the rest of water at the glacier bed. This is why channel development is often inferred to lower or keep constant glacier sliding and subsequent glacier flow. This question is of central interest in glaciology (Tedstone *et al.*, 2013, 2015). For instance, as surface melt is expected to increase, it is also expected to reach higher altitude in the Greenland ice sheet, and therefore increase meltwater supply to the bed (Zwally *et al.*, 2002). Such supply could lead to a decrease or an increase in basal sliding and resulting ice discharge to the ocean, depending on how water is routed at the glacier bed. There is now a quasi-general consensus that efficient drainage systems will develop in response to higher melt supply, promoting ice flow deceleration and therefore regulating future mass loss (Davison *et al.*, 2019). However, this is still questioned as there are yet very few direct observations of subglacial channels to test this hypothesis. Those channels are discrete in space and often missed when drilling boreholes through hundreds of meters of ice. Ground penetrating radar or active seismic imagery is often conducted with wavelengths too large to capture meters-scaled structures and when using shorter wavelengths (i.e. higher frequencies) the signal often does not reach the base of the glacier because of attenuation and scattering (Church *et al.*, 2019). There have been direct investigations through glacial speleology (Gulley *et al.*, 2009), but as they are often conducted in winter it is difficult to assess, for instance, channel opening rates, water flow velocities or water pressure inside those conduits. Dye tracing experiments (i.e. injecting dye at the surface of the glaciers and measuring the time it takes to transit to the terminus) yield indirect and averaged information that, while important, is still incomplete (Irvine-Fynn *et al.*, 2006).

The system that inefficiently routes water is referred to as the cavity-system, as it is mainly composed of small, often water-filled, cavities that open on the lee side of bedrock bumps. Those cavities open because of the sliding of glacier on the bed and close due to ice creep (Lliboutry, 1968). For soft-bed glaciers, the inefficient drainage system also includes unconsolidated layers of low permeability. This concept of cavi-
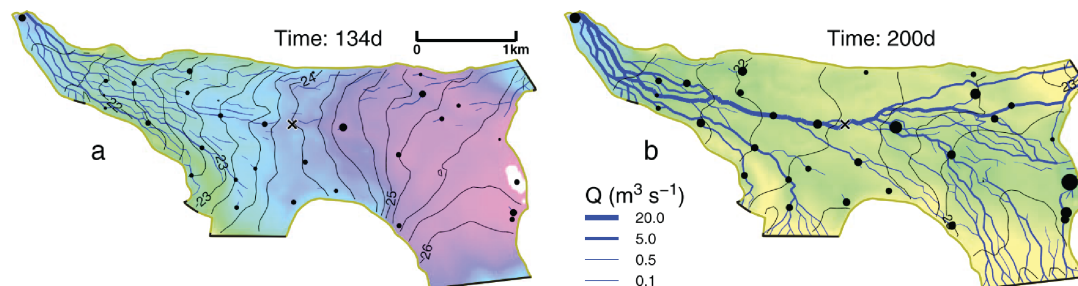
Figure 1.7: From Werder *et al.* (2013) Simulation 2007 melt season for Gornergletscher. Snapshot of the trunk on (a) 14 May and on (b) 19 July at the time of peak input, showing contours of hydraulic potential ϕ (MPa), effective pressure N, the channel discharge Q, moulin input (dots), and inflow boundaries (black lines).

ties has been proposed almost 50 years ago, but it is not clear what are the characteristics of cavities in the *real-world*. For instance, the size of the bumps that control the cavity location might range from millimetres to meters, and it is not sure which size really controls basal motion. As this system is very distributed and highly heterogeneous, point-scale observations do not have a good spatial-representation. The recent study of Rada and Schoof (2018), shows that even with more than 700 boreholes drilled over a 10 year-period on a small Yukon glacier, it is challenging to extract unique behavior of the cavity-system and even more difficult to capture the physics that controls their evolution. Their study rendered the cavity-system even more complicated than before. They highlighted the potential that the cavity-system can be divided in two sub-system depending on the linkage's state between cavities. This separation was previously proposed based on indirect observations (Murray and Clarke, 1995), especially in Greenland (Andrews *et al.*, 2014), and seems to be of great importance to the effect of subglacial water flow on glacier movements (Hoffman *et al.*, 2016). While connected cavities form a linked-cavity system that favors increase in water pressure for increasing water supply, disconnected cavities rather act as a buffer for basal sliding variations and favor high sliding in winter due to water storage. It is yet unclear how this description might hold for different types of glaciers, but this could play an important role in basal motion. There have been attempts to describe both cavity and channel systems with a unique physical framework (Schoof, 2010; Colgan *et al.*, 2012), with two different physical frameworks (Hewitt, 2013; Werder *et al.*, 2013) or with parametrized approaches that picture those system as layers with different permeability (De Fleurian *et al.*, 2014; de Fleurian *et al.*, 2016; Hoffman *et al.*, 2016). Whether one model or the other is more suitable for small-glaciers, regional or ice-sheet wide application remains unclear even if extensive model inter-comparisons have been conducted (Flowers, 2015; Fleurian *et al.*, 2018).

The challenge of observing the subglacial hydrology network

It is difficult to map the subglacial drainage system and retrieve its properties under the cover of hundreds to thousands of meters of ice. Such an observational limitation is a major obstacle in the way of further constraining the physical processes operating at the glacier bed. There are extensive observations from satellite imagery that show

that ice flow velocity varies with water supply, but those are mostly indirect (e.g. surface velocity variations) and provide motivation for studying the physical processes that control subglacial water flow, and therefore predict/model its dynamics. Recent work devoted large efforts to describe the physical processes acting within the subglacial drainage system and its influence on ice-flow. However, there are still a very few studies that made robust and spatially distributed observations of the subglacial drainage system components (Chandler *et al.*, 2013; Andrews *et al.*, 2014; Rada and Schoof, 2018). Those studies do not provide observations with the temporal and/or spatial resolution required to observe the location of subglacial channels (i.e. the efficient drainage system) and/or the true extent of the cavity-system (responsible of high water pressure). These observational limitations are mainly caused by the fact that (i) glaciers and ice sheets are often remote and inaccessible, (ii) the subglacial environment is even more inaccessible, and (iii) the subglacial drainage system is so heterogeneous that point-scale measurements (e.g. drilling, boreholes) often yield information that are hardly representative on a larger scale. Without appropriate observations of the geometry and evolution of the subglacial drainage system it is difficult to assess why and where subglacial water influences glacier dynamics by favoring or preventing fast basal sliding.

One of the objectives of my PhD work is to develop observational approaches based on passive seismology that will allows us to investigate the temporal evolution of subglacial hydraulic properties (e.g. pressure conditions and conduit's size) and the spatial configuration of the subglacial drainage system.

1.3   Seismology: a tool to remotely observe glaciers

When not mentioned information is from the book of Stein and Wysession "An Introduction to Seismology" (2003).

On the nature of the seismic signal

A source generates a seismic wave that propagates through a medium before being recorded at a receiver. The record of the ground motion at this receiver is called a seismogram and contains information about source and medium properties. For instance, the wave properties (e.g. velocity, directionality, amplitude . . .) provide information on the nature and location of the source (e.g. earthquake, bomb, rock fall, car traffic . . .). Those properties can also give access to the medium properties (e.g. density, mechanical properties, water content, layering . . .) as wave velocity is influenced by the medium of propagation. Changes in amplitude and shape of the waveforms are also affected by medium heterogeneity (e.g. scattering, attenuation, amplification . . .). Before presenting how seismology has helped unravel the secrets of Earth's interior, sub-surface, surface and beyond, I briefly introduce the notion of amplitude and phase components of the seismic signal. Those two components can be used in different and complementary ways to investigate source/medium properties, and a clear picture of their particularities is needed before moving onto the investigation of Earth's surface.
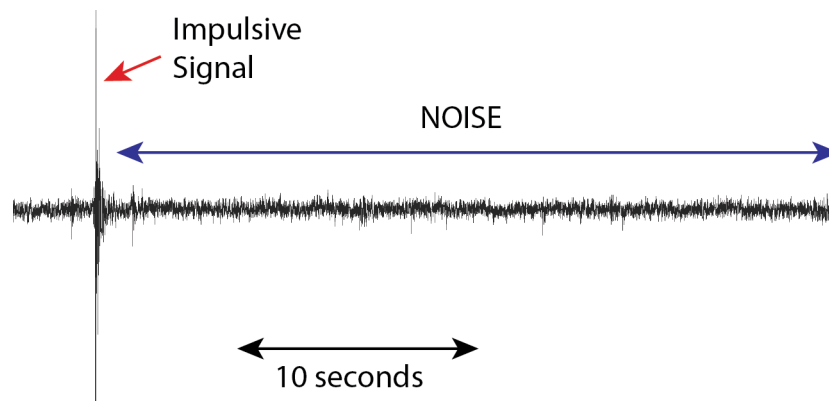
Figure 1.8: On the difference between impulsive events and seismic noise.

The propagation of a wave along a direction x can be described as a function of time t and distance by any function of the form $f(x \pm vt)$. For an harmonic wave, the constituent of seismic waves, a particularly useful form to describe the ground motion u is $u(x,t) = Ae^{i\phi(x,t)}$ with A the amplitude component and ϕ the phase component. Both components contain different information. The phase contains the temporal information of seismic signal and phase differences analysis is the most-used approach to estimate travel time, wave velocity, source location and changes in those parameters through time. Changes in phase from one sensor to the other or over time are often linked to changes in medium properties (e.g. changes in water content, temperature) that influence wave velocities or changes in source location. The amplitude specifies the velocity of a ground particle during its displacement from its rests position. The amplitude contains the information of seismic signal energy, and amplitude is often used to investigated sources magnitude, or amplification/attenuation properties of the medium of propagation. In the case of multiple superimposing wavefield, the amplitudes often sum up constructively, which is not the case for the phase that is destructive and often yields an incoherent wavefield. The differences between those two components of the seismic signal are of great importance for seismic monitoring, source location and seismic imagery.

On the general use of seismology

With a seismometer one can investigate any kind of sources and medium properties at depth and range. The main limitation to that is the trade-off between source depth and frequency range. The higher the frequency (f), the smaller the wavelength ($\lambda = 1/f$). Small wavelengths can be used to study very fine structures, but they are also more sensitive to scattering and attenuation effects and therefore do not penetrate as far as large wavelengths/lower frequencies. The primary use of seismology is the study of the Earth's interior with relatively low frequencies (< 0.1 Hz). It has been used to shed light on the Earth's structure (e.g. crust, mantle, chemical compositions), to locate mineral or oil deposits. Seismology has especially showcased itself in the study of earthquakes. Most of the information about the nature of earthquakes such as the controlling mechanisms, the slip motion, epicenter localization or resulting damages has been determined from seismograms analysis. Such observations are among the most

important data to understand plate tectonics, which is the primary process shaping our planet.

Another, more recent, use of seismology is the study of subsurface environments with relatively high frequencies (> 1Hz). This concerns the study of waves generated by processes at or near the Earth's surface (e.g. biosphere, atmosphere, hydrosphere, cryosphere . . .) and the perturbation of those waves by environmental parameters (e.g. temperature, hydrology, human activity . . .). Contrary to Earth's interior sources, environmental sources often present noisy signals because of the complexity of the subsurface environment (e.g. layering, unconsolidated sediments, water content) rather than clear impulsive events (as generated from high-energy earthquakes). There is a generally accepted distinction between impulsive events that are a short-lived impulse in ground motion with a clear starting time (e.g. earthquake-induced signal) and seismic noise that is a continuous ground motion record with no clear starting time (Fig. 1.10). While impulsive events can be easily identified and used for source properties location/analysis, seismic noise was traditionally discarded or used for imaging the medium rather than for investigation source properties (Campillo and Paul, 2003; Larose *et al.*, 2008). Because of those complex seismic signals, environmental seismology has motivated numerous methodological developments that are based on seismic noise analysis or the use of very large array of seismometers to investigate spatial variability in wave propagation and/or source location [3]. The monitoring of geomorphic processes with seismology has arisen thanks to recent progress in both hardware technology (e.g. high frequency sensitivity, temporary stations) and methodology (e.g. use of ambient noise rather than only impulsive events). This has opened a wide range of possibilities such as monitoring and investigating physical properties of mass movements (landslides, rocks falls; Levy *et al.* (2015); Walder (2017)), water flow (groundwater, open water, oceanic currents; Burtin *et al.* (2008, 2010); Schmandt *et al.* (2013); Gimbert *et al.* (2014); Gimbert and Tsai (2015)), erosion (sediment transports, abrasion) Burtin *et al.* (2008, 2010); Tsai *et al.* (2012); Bakker *et al.* (2020)), human activity (traffic noises, Diaz *et al.* (2017)), natural hazards (volcanoes, tornadoes; Aki and Richards (2002); Kumagai *et al.* (2009)) or cryosphere-related processes (avalanches, ice quakes, fractures, permafrost thawing; see Sect. 1.3). Environmental seismology has now become a relevant approach to investigate any kind of process acting at the Earth's surface that is otherwise very difficult to observe with traditional methods.

On the use of seismology to investigate subglacial water flow

Cryosphere-related seismic signals

Glaciers produce a wide range of seismic sources whose signals occupy high frequency ranges (> 1Hz) (Podolskiy and Walter, 2016; Aster and Winberry, 2017). Glacier seismologists have used those sources to infer glacier processes and properties and as in the other field of seismology, the investigated seismic signals can be composed by

---

[3]You can find further details on the problem of locating distributed sources of seismic noise to the dedicated section in Chapter. 7.1, page 102.

impulsive events or seismic noise. I focus here on seismic sources properties analysis. Traditional approaches are events-based and focus on mechanisms related to the movement of glaciers such as crevasses opening (Neave and Savage, 1970), basal shear (Helmstetter *et al.*, 2015b) or iceberg calving. The investigation of crevasses seismicity significantly contributed to the understanding of surface strain rates and how they change, which is of great importance for ice streams or tidally modulated glaciers (Winberry *et al.*, 2009, 2013, 2014). Evidence, from field observations or laboratory experiments, of basal seismic events has suggested that basal motion is not only controlled by viscous deformation but also of by sudden stick-slip events (Sergienko *et al.*, 2009; Helmstetter *et al.*, 2015b; Lipovsky and Dunham, 2016; Lipovsky *et al.*, 2019). This might implies to re-consider traditional description sof basal slip and evaluate the importance of brittle deformation in glacier dynamics. So far, a few studies have addressed this question, and it seems that basal events through stick-slip motion do not accommodate much of the basal slip (Lipovsky *et al.*, 2019; Minchew and Joughin, 2020). But we are only at the beginning of this research (Gajek *et al.*, 2019), and as I am writing this manuscript, a team led by Fabian Walter (ETH Zurich) is drilling into an Alpine glacier to reach sticky-spots responsible of stick-slip and further investigate what controls sudden basal motion. Another type of impulsive events is iceberg calving (Köhler *et al.*, 2012b; Kohler *et al.*, 2019), which contributes to glacier and ice sheet frontal retreat that is responsible of the majority of mass loss over Greenland and Antarctica (Ritz *et al.*, 2015). Detection and modeling of such events have increased in the past decade for both low (Ekström *et al.*, 2003; Tsai *et al.*, 2008) and high (Bartholomaus *et al.*, 2008) frequency seismic analyzes. This has led to a better understanding of the physics that should be taken into account to predict future changes in Greenland and Antarctic mass losses.

Contrary to event-based studies that have started almost 50 years ago (Neave and Savage, 1970), noise-based studies of glaciers are relatively recent (Bartholomaus *et al.*, 2015a). The main glacial source of seismic noise is water flow. The origin of this seismic noise is, similarly to rivers, turbulent water flow (Gimbert *et al.*, 2016). The use of seismology to investigate subglacial water flow dynamics is therefore at the boundary between seismological investigation of rivers, that of glacial processes and that of seismic noise analysis.
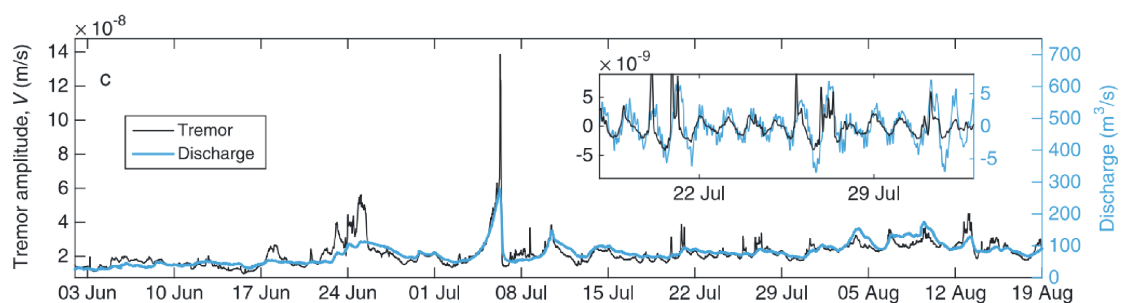
Figure 1.9: From Bartholomaus *et al.* (2015a) Tremor amplitude and water discharge into Mendenhall Lake in which terminates Mendenhall glacier. Tremor is calculated within [1.5-10] Hz.

Water-flow induced seismic noise

Turbulent water flow generates frictional forces that act on the near boundaries of the associated conduit (e.g. river or subglacial channel), and cause seismic waves (Gimbert *et al.*, 2016). The ground motion associated with those waves does not show clear arrivals times or identifiable waveforms, because of the superimposing wavefield from multiple sources. This is why they are referred to as seismic noise. A river or a subglacial channel is therefore a source of seismic noise distributed in space (where water flow is turbulent) and variable in time.
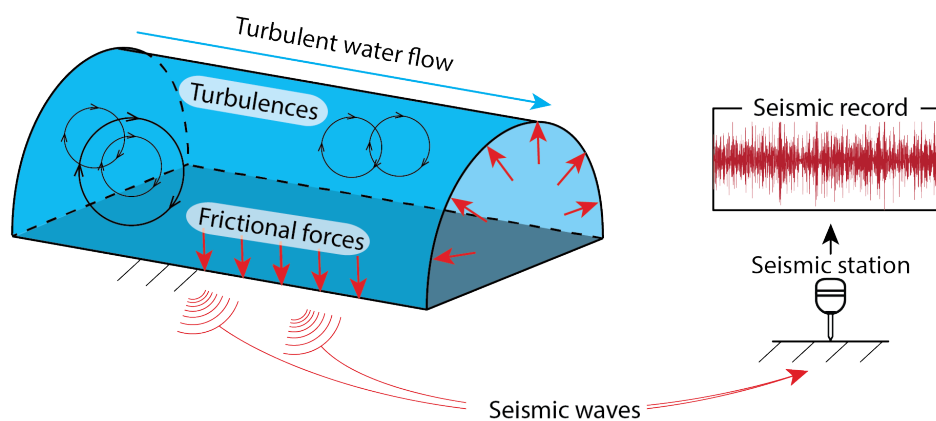
Figure 1.10: On the generation of seismic noise from turbulent water flow.

Starting from the late 2000's numerous seismological studies focused on fluvial processes such as sediment transport or water discharge-ground motion relation (Burtin *et al.*, 2008, 2010; Schmandt *et al.*, 2013). In terrestrial rivers, the two main process of seismic noise generation are indeed bed-load transport and turbulent water flow Tsai *et al.* (2012); Gimbert *et al.* (2014). It was only in 2014 that the study of Gimbert *et al.* (2014) successfully separated the contribution of those two components through developing a model that predicts the raw amplitude and specific spectral signature of water-flow-induced noise. The model is based on a physical description of the effect of forces generated by turbulent water flow on the river boundaries and how this results in seismic waves that propagate and are recorded at a given location. The main outcome of this study, is that one can use the amplitude of the ground-motion to invert for relative changes in hydraulic properties of the water flow. Those are the hydraulic pressure gradient and the hydraulic radius. Following this study, Gimbert *et al.* (2016) adapted this framework to the case of subglacial water flow as channels, unlike rivers, have the capability to be full and therefore pressurized. This led to a physical framework relating hydraulic parameters that are key for subglacial hydrology, i.e. the hydraulic radius and the hydraulic pressure gradient. However, this study focused on describing this new physical framework and investigated only a short-period of time (2 months) with limited temporal resolution.

You can find further details on the physics of water-flow induced seismic noise in the dedicated section in Chapter. 4, page 51.

One of the objectives of my PhD work is to evaluate the Gimbert *et al.* (2016) physical frameworks over timescales relevant for studying subglacial hydrology (e.g. season to hour) and to develop methodological approaches that will allows us to better understand the seismic signature of subglacial water flow in time but also to locate the associated sources of seismic noise in space.

1.4   Further readings

For going further on basal sliding I cannot not propose *The Physics of Glaciers* by Cuffey and Paterson (2010), which has been my bible since I have started studying glaciers.

For going further on the complexity of subglacial hydrology I recommend:

• *The Influence of Hydrology on the Dynamics of Land-Terminating Sectors of the Greenland Ice Sheet* by Davison *et al.* (2019) that proposes a thorough review on how subglacial hydrology controls the dynamics of land-terminating glaciers in Greenland.

• *Modelling water flow under glaciers and ice sheet* by Flowers (2015) that describes how to make a subglacial hydrology model.

• *SHMIP The subglacial hydrology model intercomparison Project* by Fleurian *et al.* (2018) that compares most of the existing subglacial hydrology models.

• *Alpine subglacial hydrology* by Hubbard and Nienow (1997) that, even if more than 20-years old, highlights key effects of subglacial hydrology on Alpine glaciers and what observations can yield.

For going further on the nature of the seismic signal and its use to investigate the earth structure I recommend *An Introduction to Seismology* by Stein and Wysession (2009). I also recommend:

• *Cryoseismology* by Podolskiy and Walter (2016) for a review of cryogenic seismic sources and the rise of cryoseismology.

• *A physical model for seismic noise generation by turbulent flow in rivers* by Gimbert *et al.* (2014) that describes how turbulent water flow generates seismic noise.

• *Array seismology: methods and applications* by Rost and Thomas (2002) that, even, if almost 20-years old, still proposes a good overview on the methods and challenges of locating seismic sources.

Chapter 2

Research questions and outline

Despite numerous improvements, and mainly because of limited observations, the physical properties of subglacial water flow and its spatial configuration remain poorly known. From this lack of knowledge arise key thematic questions that are at the center of the research I have conducted during my PhD:

Thematic question n°1: How do subglacial hydraulic properties (e.g. pressure conditions and conduit size) evolve over the melt-season and down to sub-diurnal timescales?

Thematic question n°2: What is the spatial configuration of the subglacial drainage system and how does it evolve through time?

In this work I also address key challenges with the use of passive seismology to retrieve noise source properties at high frequency. This approach was yet questioned when I started my PhD as it was associated to methodological issues that I address here:

Methodological question n°1: How well can we identify the seismic signature of subglacial water flow from other sources?

Methodological question n°2: How, and at which resolution, can we locate sources of seismic noise that are distributed in space and varying in time?

Methodological question n°3: To which extent can ground motion amplitudes be used for studying glacier features such as crevasses, thickness or ice anisotropy?

In this cross-boundary PhD work I first describe the field-measurements I conducted (**Part II**, p. 35), followed by the analysis of subglacial hydraulic properties and associated challenges (**Part III**, p. 51), then by the spatial investigation of subglacial water flow and associated geophysics experiments (**Part IV**, p. 101) and finally by the benefits of seismic amplitude analysis on characterizing glacier properties (**Part V**, p. 167). Outlook for future research is given in each chapter and the main outcomes are presented in **Part VI** (from page 191). Additional work is shown in **Chapter** 13.

Part II

Instrumentation

Last verification before leaving our seismic station for its 9-month overwintering.
© *Nathan Maier*.

Chapter 3

Seismic instrumentation

Passive and long term seismic monitoring on mountain glaciers was yet poorly done at our laboratory when I started my PhD. In addition, most previous cryo-seismic studies focus on short time periods, with seismic stations often installed in the vicinity of the glacier (Podolskiy and Walter, 2016). Obtaining year-long time series of seismic measurements in glacier environments is difficult because of harsh surface conditions. On mountain glaciers, and especially in glacier d'Argentière, summer ablation can melt by up to 6 m of ice and in winter, snow accumulation can reach up to 5 m (Vincent *et al.*, 2009). In order to monitor long time series of subglacial-water-flow induced seismic signals and other glacier process such as stick-slip and crevasses opening I therefore had to figure out a proper monitoring strategy.

During my PhD I actively took part in designing, installing and maintaining two different seismological networks. The first is shown in Fig. 5.2 (page. 62) and consists of a set of single stations installed over the glacier from spring 2016 that we used and continue to use to monitor subglacial-water-flow, stick-slip, crevasse opening and other seismogenic glacier processes. The second is shown in Fig. 8.1 (page. 113) and consists of the installation of 98-sensors on the lower part of the glacier d'Argentière for one month during spring 2018.

3.1   Learning-by-doing

During those three years I did not only install the stations on the glacier but also prepared all components of it, building adapted casing, electrical wiring, selecting appropriate materials (see Figs. 3.3 and 3.4). This has been for me the opportunity to build new skills and learn how to conduct geophysical surveys in remote environments, from the research questions to the field, through wiring and welding. I have learned a lot on how to prepare field missions, on how to setup an appropriate logistic, to deal with the trade-off between the price of our instruments and their reliability or to deal with human aspects during fieldwork. Learning by doing is at bit like learning to fly, you need a few crashes before succeeding (Floyd, 1987). I have shared this knowledge with a first year PhD student that took care of most of the seismic installations when I could

not go to the field. Sharing those field experiences was, and still is, for me an important aspect of my PhD and I tried to involve most of the PhD students of our laboratory when going out on the field. I also took part in several geophysical investigations on the glacier d'Argentière (ground penetrating radar survey, inclinometer installation, 250 m borehole drilling with hot water, GNSS surveys).

3.2 Multiple years-long seismic surveys
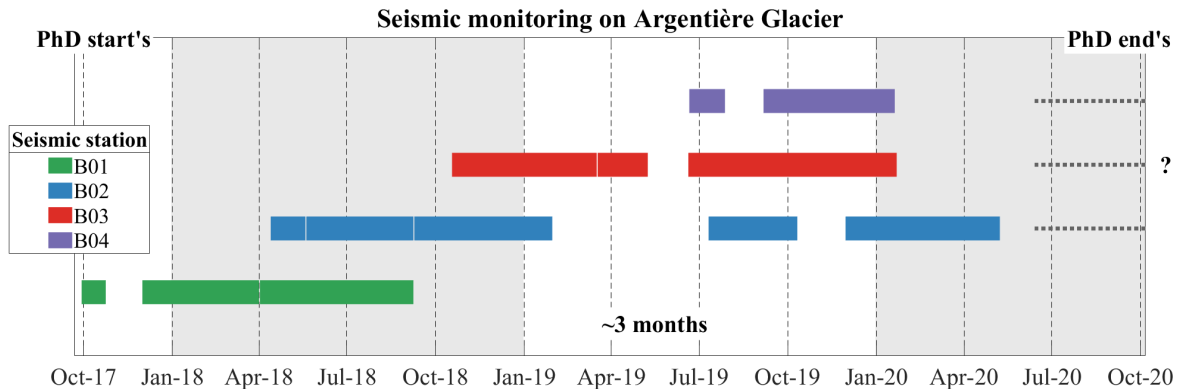
Figure 3.1: Temporal coverage of the four stations installed on Glacier d'Argentière during my PhD. Stations B02, B03 and B04 are still operational. Data gap are often due to software problem or flooded instruments. See details on Table 3.1.

One of the greatest challenge I had to face during my fieldwork was to maintain operational seismic stations over winters and melt-seasons. We made the choice at the very beginning of my PhD to use cheap seismic stations that were successfully used in Alaska few years before by Timothy Bartholomaus and Florent Gimbert (https://geobit-instruments.com/, see detail in Sect. 5.3, from page. 63). Those instruments were up to four times cheaper than the commonly used seismic stations (c. 3000 euros/sensor + digitizer) and choosing those instruments allowed us to be more flexible on the number of instruments that we could install on the glacier. One of the drawback of those instruments is that they consume up to 3 times more than the other seismic stations, which corresponds to a 65A-12V 24kg battery monthly consumption. Our collaborators at ETH Zurich, Fabian Walter and Dominik Graff, also installed three seismic stations on glacier d'Argentière that we used in our Nanni *et al.* (2020) study and chose solar panels for power source. The problem with solar panels is that they get covered by snow in winter, and this requires going back to field a few times during winter with the risk to miss stick-slip events during winter (Allstadt and Malone, 2014) or to miss the beginning of the melt season. For my PhD, I made the choice to use only batteries for powering our stations. Doing so I was sure of the time over which the stations are functioning. But batteries come with a weight problem, and often require helicopter rides to carry them on the glacier. We tried once to get the batteries on ski with sledges, but we found that this was not the most efficient way to do it. So most of the time we carried the batteries to the glacier by helicopter. To avoid multiple rotations throughout the year, we had to buy several batteries (up to 30 at once, i.e. more than 700 kg of material), and after two years I came out with a strategy based on 9 batteries that cover the end of autumn to early summer, and 3 batteries for the summer, which only

requires 3 field missions per year (see pictures in Fig. 3.2).

During the first year of my PhD I did on average one field mission per month to maintain the seismic stations, and up to twice a month in summer, plus a couple of days per month of instrumental developing/fixing at the laboratory. This resulted in a successful temporal coverage of more than 95% over a two year period. This is one of the longest, almost, uninterrupted time series of seismic measurements conducted on a mountain glacier. During the last year of my PhD, I spent less time in the field, partly because the installations were more reliable, partly because I could not go so often due to a knee injury. During this time, I trained other people to maintain the seismic stations, but several problems occurred and resulted in more than 35% data loss over a year and a half. The two main sources of problems, now that the power was fixed, were the tightness of our setup and the liability of our seismic digitizers (Fig. 3.2). Even though I worked in collaboration with field engineers at our laboratory and the instrument designers in Greece, I did not succeed to fully prevent water from coming into our digitizer and instruments. In alpine glaciers, the snowpack gets water-saturated at the beginning of the spring, and as our boxes are under the snow, liquid water often finds its ways to our instruments. The digitizer I used were not design to last for more than one or two melt-season and I often discovered them full of water. As we chose cheap instruments, the integrated software was not always correctly working and part of our data got corrupted and lost.

As I am now leaving Grenoble, we have 3 stations still working on the glacier, and I would like to change the old digitizer with more resistant ones (for instance with the widely used GeoCuber from GFZ). This will allow the seismic measurements to continue. Those measurements are indeed quite unique and I am sharing them through active collaboration with Agnès Helmstetter (U. Grenoble) that studies stick-slip events triggered by snow loading and with Josefine Umlauft (U. Leipzig) and Paul Johnson (U. Los Alamos) that apply machine learning to investigate glacier process form seismic measurements. Today we have 3 permanent stations, located along the glacier flow line at 2400 m, 2500 m and 2700 m of altitude. Those stations are of great importance for the SAUSSURE project (see Part III, from page. 51) and I plan to include the lower station, whose sensor is drilled into 70m of ice, in a long-term perspective of seismic monitoring of glacier. This would be the first of its kind. The other stations are drilled at c. 5 to 10 m into the ice in order to be easily removable after one or two years if we wish to investigate other areas or glaciers. Including a station in a long-term perspective would require being sure to have a person taking care of it and enough money for the repairs and field missions. As the station is installed in the glacier where the French Observatory for glacier (GLACIOCLIM) conducts numerous measurements I could think of a potential collaboration. Such permanent installation could also be taken over by the French network of seismic stations (RESIF), which would imply for them to maintain a station in high altitude and on a glacier.
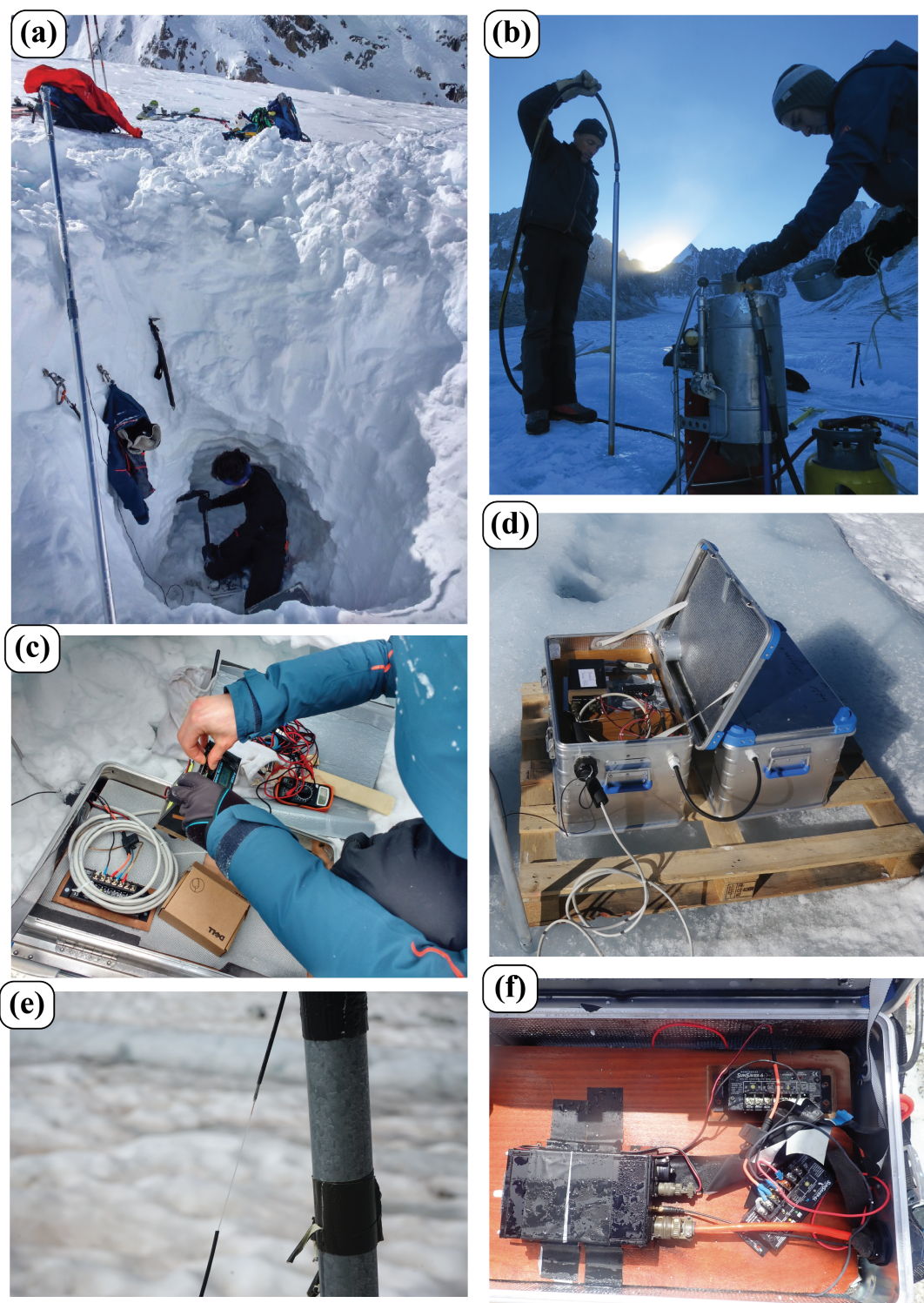
Figure 3.2: Some pictures from the field. (a) During my first winter I went several times to check the instruments, download the data and change the batteries. We often had to dig several meters of snow. (b) In fall 2018 we installed a third borehole sensor at the top of the ablation zone. We used a portable hot-water driller, and Oliver Laarman went with me to teach me how to use it. (c) Wiring cable when the temperature reaches -20C was not always easy, but this taught me to be quick an efficient and to practice before going to the field. (d) The more the batteries, the larger the installation. At that time we still add small boxes that could be transported directly with us in the helicopter without the need of a net. The year after we changed this with a larger box that can host up to 10 batteries and has the advantage to limit the forces applied on the cables between the different boxes and limit the potential water entries. (e) When melt is stronger than planned and we do not go to the field at the right time our GPS antenna can tear up. (f) Top view of the digitizer and the inside of the box. We can see the humidity that comes in through the sensor cable (orange).

3.3   Dense spatial seismic survey

Whereas the long-term installation required several people but was mainly my respon-
sibility, the dense seismic array installation was part of a wider effort in the framework
of the RESOLVE-project (see Part IV, from page. 101). This project aims at combin-
ing multi-physics sensors to refine quantitative interpretation of the processes acting
within a glacier. A central aspect of this project was the installation of 98-seismic
stations at the surface of the glacier during 35 days at the beginning of the 2018 melt-
season. As I started my PhD fall 2017, I had the opportunity to closely collaborate with
the RESOLVE team to prepare this installation. I attended a dozen of meetings and met
a wide range of people, from engineers to data managers and filmmakers. I actively
took part in designing the field installation of seismic sensors, associated GNSS sta-
tions and radar survey. I then led together with Philippe Roux the maintenance of the
seismic stations by going up every 10 days to re-install the seismic stations. Prior to
the dense array installation, I also took part in the ground-penetrating-radar campaign
to test different instruments and frequencies and then to map the bed of the glacier in
our study area. To complement the seismic array, together with Florent Gimbert and
Luc Piard, we installed a borehole sensor at c. 80m depth and a water pressure sensor
on the side of the glacier at c. 100m. We successfully drilled with a hot-water drilling
device developed by Luc Piard, and then installed the two sensors. The seismic sen-
sor was successfully coupled with the ice after two weeks, and this required few days
of testing and pulling up the sensor to ensure a proper coupling. This sensor is still
operational and will be as long as the cable holds. The pressure sensor ended up in
an englacial cavity and we could not use it for proper investigation of the basal water
pressure; we also could not get it up and we lost the instrument.

This field experiment was at the time the first dense seismic array survey conducted on
a glacier and the experience I gained taking part of it has strengthen my capability to
conduct fieldwork. At the beginning of my PhD, I was supposed to use the long-term
seismic observations to constrains subglacial hydrology/ice flow numerical models,
but I ended up spending most of the second part of my PhD working in the unique
data set obtained with this dense array experiment. Further technical details on the
instruments used for the spatial analysis can be found in Chapter 8, page. 109.

3.4   Where to find the data ?

The data from the long-term seismic survey can be found with the associated meta-
data on */bettik/ugonanni/DATA_ARG_BACKUP*. Anyone from a labeled university
can create an account to access the data via *https : //perseus.univ−grenoble−alpes.fr/*.

Part of the data are also distributed via Zenodo linked to my profil and the SAUSSURE
and RESOLVE projects.

Table 3.1: Information on the dataset collected at the four seismic stations installed during my PhD. Further technical details on the instruments used for the long-term analysis can be found in our paper Nanni *et al.* (2020) that I present in Chapter 5, page. 55.

ARG B01 S/N L17090

Start	End	Gain set	Position	SPS (Hz)	Notes
277-00h00-2017	302-23h50-2017	3	no POS file	1000	no INI/POS
340-11h20-2017	059-11h50-2018	3	45°57.8154′N 006°58.4302′E	1000	
059-12h20-2018	096-10h00-2018	3	45°57.8163′N 006°58.4306′E	1000	
097-00h00-2018	145-16h00-2018	3	45°57.8217′N 006°58.4264′E	1000	
145-16h40-2018	157-07h50-2018	3	45°57.8164′N 006°58.4233′E	1000	
157-09h20-2018	173-07h00_2018	3	no POS file	1000	no INI/POS
173-07h00_2018	193-12h40_2018	3	no GPS	1000	no GPS (shift of 537.53472 days from 01/01/2017)
193-12h50_2018	256-23h50_2018	3	45°57.8225′N 006°58.4135′E	1000	

| Start	End	Sensor	Sensitivity	Pass band	Gain	Digitizer
277-00h00-2017	302-23h50-2017	Geobit C100-MK2	1500 Vs/m	10s-98 Hz	10 Vpp	Geobit SRi32L
340-11h20-2017	059-11h50-2018	Geobit C100-MK2	1500 Vs/m	10s-98 Hz	10 Vpp	Geobit SRi32L
059-12h20-2018	096-10h00-2018	Geobit C100-MK2	1500 Vs/m	10s-98 Hz	10 Vpp	Geobit SRi32L
097-00h00-2018	145-16h00-2018	Geobit C100-MK2	1500 Vs/m	10s-98 Hz	10 Vpp	Geobit SRi32L
145-16h40-2018	157-07h50-2018	Geobit C100-MK2	1500 Vs/m	10s-98 Hz	10 Vpp	Geobit SRi32L
157-09h20-2018	173-07h00_2018	Geobit C100-MK2	1500 Vs/m	10s-98 Hz	10 Vpp	Geobit SRi32L
173-07h00_2018	193-12h40_2018	Geobit C100-MK2	1500 Vs/m	10s-98 Hz	10 Vpp	Geobit SRi32L
193-12h50_2018	256-23h50_2018	Geobit C100-MK2	1500 Vs/m	10s-98 Hz	10 Vpp	Geobit SRi32L

ARG B02

Start	End	Gain set	Position	SPS (Hz)	Notes
108-12h32-2018	114-13h10-2018	1	45°57.8009′N 006°58.4634′E	1000	Bad coupling @ 86 m depth
114-14h10-2018	131-07h20-2018	3	no GPS	1000	Bad coupling @ 86 m depth
131-08h30-2018	144-23h50-2018	3	45°57.8001′N 006°58.4599′E	1000	Bad coupling @ 86 m depth
145–2018	157–2018	3	45°57.8006′N 006°58.4558′E	1000	no data
157-08h20-2018	173-08h20-2018	3	45°57.8065′N 006°58.4580′E	1000	Good coupling @ 70 m depth
173-14h40-2018	193-09h50-2018	3	45°57.8007′N 006°58.4485′E	1000	changed digitizer to B01
193-12h40-2018	256-23h50-2018	2	45°57.8030′N 006°58.4438′E	1000	
257-08h08-2018	276-12h40-2018-	3	45°57.8072′N 006°58.4490′E	1000	
276-13h00-2018	296-06h20-2018	2	45°57.8078′N 006°58.4470E	1000	sampling problem (245 Hz)
296-11h33-2018	345-09h40-2018	3	45°57.8087′N 006°58.4389E	1000	
345-09h54-2018	35-22h30-2019	3	45°57.8127′N 006°58.4352E	1000	no data 035-081 2019
197-06h20-2019	289-19h10-2019	3	45°57.8241′N 006°58.4191E	100	
339-13h42-2019	031-12h40-2020	3	45°57.8297N 006°58.4103E	100	
031-12h47-2019	134-07h24-2020	3	dead GPS	100	flooded on 134

Start	End	Sensor	Sensitivity	Pass band	Gain	Digitizer
108-12h32-2018	114-13h10-2018	Geobit S 400 C	3000 Vs/m	1-240 Hz	0,625 Vpp	Geobit SRi32S
114-14h10-2018	131-07h20-2018	Geobit S 400 C	3000 Vs/m	1-240 Hz	0,625 Vpp	Geobit SRi32S
131-08h30-2018	144-23h50-2018	Geobit S 400 C	3000 Vs/m	1-240 Hz	0,625 Vpp	Geobit SRi32S
145–2018	157–2018	Geobit S 400 C	3000 Vs/m	1-240 Hz	0,625 Vpp	Geobit SRi32S
157-08h20-2018	173-08h20-2018	Geobit S 400 C	3000 Vs/m	1-240 Hz	0,625 Vpp	Geobit SRi32S
173-14h40-2018	193-09h50-2018	Geobit S 400 C	3000 Vs/m	1-240 Hz	10 Vpp	Geobit SRi32L
193-12h40-2018	256-23h50-2018	Geobit S 400 C	3000 Vs/m	1-240 Hz	0,625 Vpp	Geobit SRi32S
257-08h08-2018	276-12h40-2018-	Geobit S 400 C	3000 Vs/m	1-240 Hz	0,625 Vpp	Geobit SRi32S
276-13h00-2018	296-06h20-2018	Geobit S 400 C	3000 Vs/m	1-240 Hz	0,625 Vpp	Geobit SRi32S
296-11h33-2018	345-09h40-2018	Geobit S 400 C	3000 Vs/m	1-240 Hz	0,625 Vpp	Geobit SRi32S
345-09h54-2018	35-22h30-2019	Geobit S 400 C	3000 Vs/m	1-240 Hz	0,625 Vpp	Geobit SRi32S
197-06h20-2019	289-19h10-2019	Geobit S 400 C	3000 Vs/m	1-240 Hz	0,625 Vpp	Geobit SRi32S
339-13h42-2019	031-12h40-2020	Geobit S 400 C	3000 Vs/m	1-240 Hz	0,625 Vpp	Geobit SRi32S
031-12h47-2019	134-07h24-2020	Geobit S 400 C	3000 Vs/m	1-240 Hz	0,625 Vpp	Geobit SRi32S

ARG B03

Start	End	Gain set	Position	SPS (Hz)	Notes
296-14h40-2018	081-14h40-2019	3	45°56.6170′N 006°59.9795′E	1000	
082-18h10-2019	134-23h50-2019	3	45°56.6193′N 006°59.9747′E	100	
176-08h10-2019	254-06h10-2019	3	45°56.6212′N 006°59.9658′E	100	
254-09h36-2019	027-23h50-2020	3	45°56.6209′N 006°59.9551′E	100	card full on 27 (10/30 Go)

Start	End	Sensor	Sensitivity	Pass band	Gain	Digitizer
296-14h40-2018	081-14h40-2019	Geobit C100-MK2	1500 Vs/m	10s-98 Hz	10 Vpp	Geobit SRi32L
082-18h10-2019	134-23h50-2019	Geobit C100-MK2	1500 Vs/m	10s-98 Hz	10 Vpp	Geobit SRi32L
176-08h10-2019	254-06h10-2019	Geobit C100-MK2	1500 Vs/m	10s-98 Hz	10 Vpp	Geobit SRi32L
254-09h36-2019	027-23h50-2020	Geobit C100-MK2	1500 Vs/m	10s-98 Hz	10 Vpp	Geobit SRi32L

ARG B04

Start	End	Gain set	Position	SPS (Hz)	Notes
177-08h10-2019	214-00h10-2019	3	45°57.3279′N 006°59.0967′E	100	data gap 214-254
254-11h39-2019	025-23h50-2020	3	45°57.3366′N 006°59.0893′E	100	card full on 27 (10/30 Go)

Start	End	Sensor	Sensitivity	Pass band	Gain	Digitizer
177-08h10-2019	214-00h10-2019	Geobit C100-MK3	1500 Vs/m	10s-98 Hz	10 Vpp	Geobit SRi32L
254-11h39-2019	025-23h50-2020	Geobit C100-MK3	1500 Vs/m	10s-98 Hz	10 Vpp	Geobit SRi32L

DE-INSTALLATION

Digitizer

GPS (fragile !)

Seismometer

BOX 1

BOX 2

batteries
connection
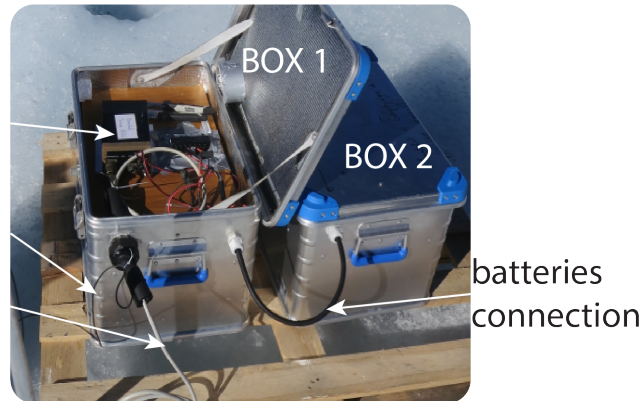
BOX 1
1) Unplug power from the
switch and remove fuses
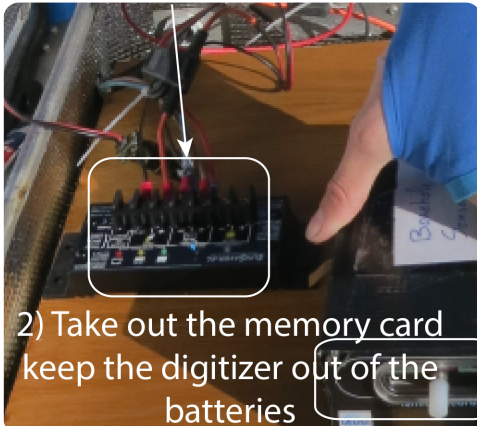
2) Take out the memory card
keep the digitizer out of the
batteries

BOX 2
1) Unplug fuse   2) Disconnect cables
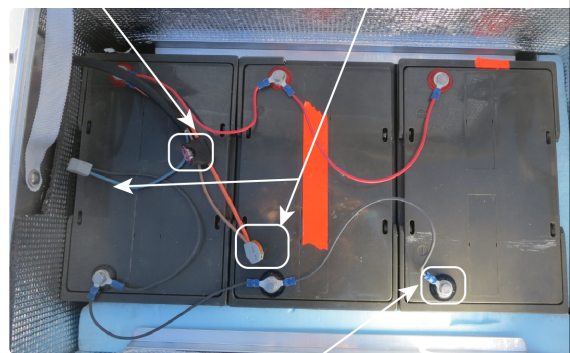
3) Disconnect batteries and put
tape on the terminals

REINSTALLATION
- 1) Put the 3 new batteries in BOX 1
- 2) connect the 3 batteries in parallel (red
cables for +, black for -)
- 3) connect the batteries to the switch with
the fused cable (positive)
- 4) connect the digitizer energy cables to the
switch but DO NOT PLUG the digitizer yet
- 5) put the wood layer between batteries and
digitizer
- 6) plug GPS and SENSOR cables
- 7) insert the memory car
- 8) plug the power to the digitizer
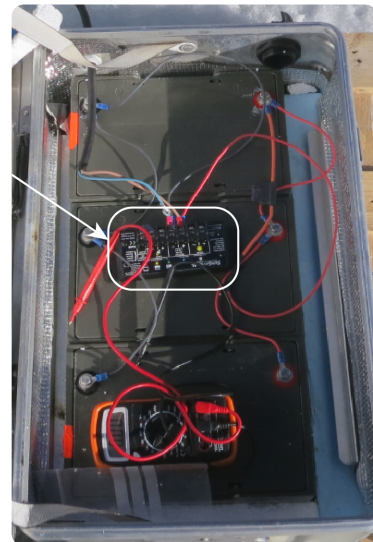
Figure 3.3: Manual for maintaining the seismic stations that I have developed to lead other people to the field.
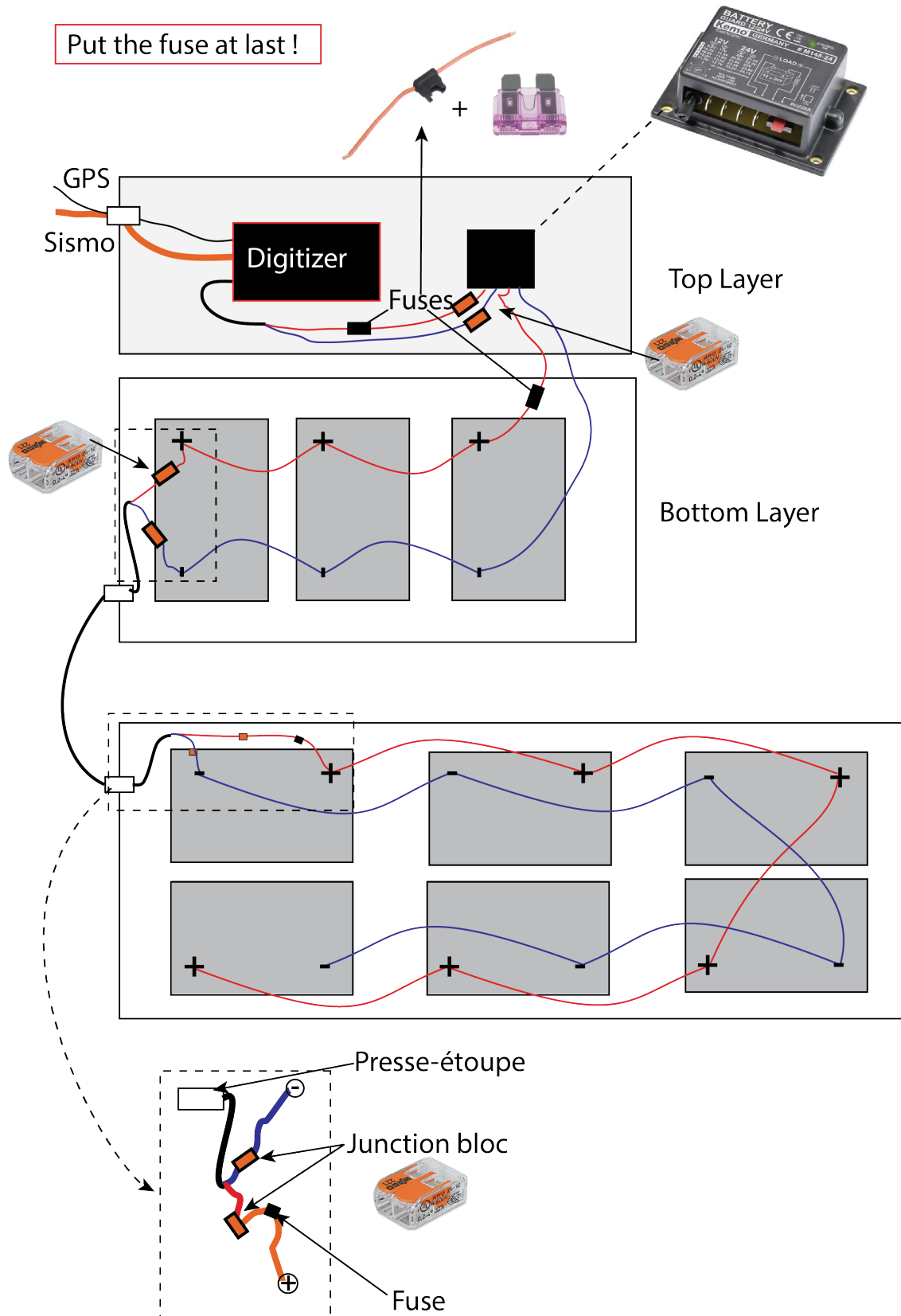
Figure 3.4: Schematic of the seismic installation I have designed to be autonomous for 9 months, from winter to melt-season.

Part III

Temporal investigation of subglacial water flow
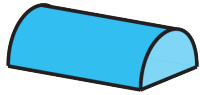
Thematic question n°1:

How do subglacial hydraulic properties evolve over the melt-season and down to sub-diurnal timescales?

Methodological question n°1:

How well can we individuate the seismic signature of subglacial water flow from other sources?

Our first (and only) attempt to carry batteries on sledges. © *Simon Escalle*.

Chapter 4

Preface

During the first part of my PhD I focused on analyzing temporal variations in subglacial-water-flow-induced seismic noise to retrieve the evolution of subglacial hydraulic properties over two timescales that are relevant to evaluate the dynamical response of glacier to meltwater input, i.e. day and season. To do so I have conducted continuous measurements of seismic power at the surface of the glacier d'Argentière and compared these against measurements of pro glacial water discharge and in-situ measured glacier basal sliding speeds over a two-year long time period (Sects. 5.5 and 5.5). I used those observations together with the physical framework proposed by Gimbert *et al.* (2014, 2016) to retrieve the temporal evolution of the hydraulic pressure gradient and hydraulic radii in the subglacial drainage system. Prior to my work this framework had been only tested against one dataset and over a limited two-month period, and it was yet unsure if subglacial-water-flow-induced seismic noise could be used to investigate the physics of subglacial water flow over seasonal and hourly timescales, and especially at the beginning of the melt-season when the water supply is particularly low. Before presenting the investigation I have conducted below I introduce in more details the physics thought to be involved in water-flow induced seismic noise.

4.1   On the physics of water-flow induced seismic noise

From river flow ...

It is evident to anyone who has walked nearby a river, a torrent or a waterfall that flowing water generates audible noise. However, the extent to which river flows also generate seismic noise (ground motion vibrations) and if so, which process (breaking waves, bubbles, turbulence or sediment transport) mainly causes such noise is a recent and active field of research. Only a few studies have been using the seismic power recorded at 1-100 Hz frequencies to study the dynamics and properties of hydrological systems. One of the first is Burtin *et al.* (2008) that observed strong spatial and temporal variations in seismic energy produced at high frequencies (>1Hz) that well correlate with meteorological and hydrological data along the nearby Trisuli river, which is

a major-trans Himalayan river. They observed both seasonal changes and 24-h cyclicity in the seismic noise level concomitantly to seasonal and daily fluctuation of the precipitation and river discharge. They suggested that the dominant source of seismic noise was the bedload transport, but at that time the contribution of other sources was yet unclear. A few years later Schmandt *et al.* (2013) inferred, from a controlled flood experiment in the Grand Canyon, that the fluid traction on rough riverbeds also drives the seismic power at lower frequency (~ 1 Hz) than the bedload transport ($\sim 15 - 45$ Hz). They also suggested that waves at the fluid-air interface could also contribute to seismic power. It was then the studies of Tsai *et al.* (2012) and Gimbert *et al.* (2014) that proposed a quantitative physical description of the processes at the origin of the seismic signal recorded near streams and rivers. They highlight that within the 1-100 Hz the two dominant processes are frictional forces exerted by turbulent water flow and bedload transport that causes particle collisions. Other sources such as hydrodynamic sounds from implosion of air bubbles and/or fluctuating internal stresses are thought to have limited importance within the 1-100 Hz frequency range and for typical flow configurations (potentially excluding waterfalls) but rather influence the sonic frequency ranges.

In Tsai *et al.* (2012) the authors describe the seismic noise induced by the transport of sediment in rivers. Their model describes the seismic waves (of Rayleigh-type) generated by impact events from saltating particles on the river bed. They show that the seismic power within 1-30 Hz is strongly influenced by the sediment flux and grain size distribution, therefore making seismic analysis suitable to remotely estimate sediment transport characteristics.
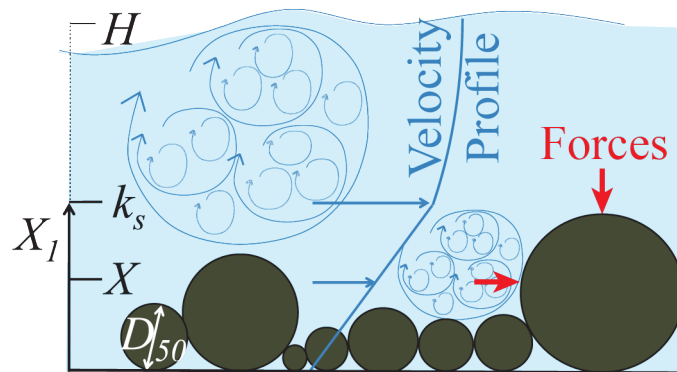
Figure 4.1: Schematic for the generation of frictional forces byt the interaction of turbulent water flow with coarse sediment at the boundaries. The turbulence depends on the bed roughness (k_s), the water depth (H), the grain size distribution (D_{50}) and size (X) and the resulting velocity profile. Forces from turbulence act on 3D on the grains. (Modified from Gimbert *et al.* (2014))

In Gimbert *et al.* (2014) the authors proposed a physical description of the seismic noise generated by frictional forces exerted at the bed due to turbulent water flow interacting with coarse sediment at the boundaries. They therefore complemented Tsai

et al. (2012) and proposed the first physical description on the river-flow processes generating seismic noise within 1-100 Hz. Their model is based on the principle that the main hydrodynamic seismic sources are caused by the interaction between turbulent water and grain-scale boundary roughness (Fig. 4.1). They assume that the seismic waves are generated by fluctuations of the force applied on riverbed grains. Those force are caused by turbulent eddies whose size distributions depend on the bed roughness and follow the Kolmogorov distribution (Kolmogorov, 1941) and have energies that depend on flow characteristics such as flow depth, bed slope and bed roughness. Finally, they converted those forces in terms of ground motion amplitude through convolution with a Green function for wave generation and propagation and therefore proposed a forward description between river properties (e.g. water flow velocity, river geometry, bed roughness . . .) and their seismic spectral signature. While their description is likely to be accurate within about an order of magnitude (~ 10 dB), the lack of other means to observe the involved physics in such setups is such that these observations remain ones that are still to be used for absolute analyzes. For relative analyzes (e.g. temporal changes) they expect good accuracy in model predictions when changes in ground properties and river geometry are limited in time.

Our understanding on how to relate the seismic power measured at a seismic station near a river (including subglacial channel) to its hydraulic parameters and/or bedload transport is thus very recent. There have been, to date, a limited number of studies that inverted hydraulic properties or bedload transport from seismic analysis and the applicability of these models at various timescales (e.g. seasonal to hourly), water flow types or water discharge ranges still has to be explored (e.g. Roth *et al.*, 2016; Bakker *et al.*, 2020; Polvi *et al.*, 2020).

... to subglacial water flow

One of the key outcomes of Gimbert *et al.* (2014)'s study is that the hydrodynamic sources dominate the seismic power within $\sim 5\text{-}15$ Hz (for most of the water flow configuration) while bedload transport rather dominates at higher frequencies ($\sim 15-45$ Hz). One can thus isolate the hydrodynamic sources to specifically investigate key hydraulic parameters, such as flow depth or flow velocities for rivers. Such an approach was therefore an opportunity for studying the physics of water flow that is otherwise very difficult to investigate. This leads us to subglacial water flow with the study of Gimbert *et al.* (2016) that adapted the Gimbert *et al.* (2014) framework to the particularity of subglacial water flow that has the capability to be full and therefore pressurized.

In the study I present in the following chapter I isolate the hydrodynamic sources generated by subglacial water flow and use the Gimbert *et al.* (2016) framework to investigate the hydraulic pressure gradient and hydraulic radii of the subglacial drainage system. My study not only addresses questions that are important to better understand glacier dynamics and subglacial hydrology but also contributes to development of physic-based approach to use seismic power analysis in geomorphology. What I

find really interesting in this study is its capacity to show that connections between different disciplines (seismology and subglacial hydrology) can help to solve long-time issues with very simple concepts (*listening to the water we cannot see*), which is not only applicable for glaciers but also for a lot of environmental systems that have flowing fluids difficult to measure (e.g. volcanoes, karst, subsurface water flow).

4.2   The SAUSSURE project

This study was conducted in close link with the SAUSSURE project (Sliding of glAciers and sUbglacial water preSSURE, https://saussure.osug.fr/), whose PI is Christian Vincent. The objective of this project is to evaluate, improve and validate friction laws that describe the sliding of glaciers in a natural scale configuration. To address these aspects, this project combines the use of advanced field measurement methodology, the development of friction laws that include relevant physical processes not yet accounted for and a modelling framework that couples ice flow and basal hydrology over the entire Argentière Glacier. Within the SAUSSURE project I am in charge, together with A. Helmstetter and F. Gimbert, of designing the seismic survey composed of 3 permanent stations installed at different altitudes on the Argentière Glacier and 9 temporary seismic stations installed over the winter (see Part II, from page 35).

Logo of the SAUSSURE project. © Marine Jambeau.

I presented this work at the Alpine Glaciology Meeting 2018 (Chamonix), at the European Seismological Commission 2018 (Malta) and at the European Geoscience Union meeting 2019 (Vienna). It is now published in Nanni *et al.* (2020).

For further details on Gimbert *et al.* (2016)'s physical framework see Sect. 5.2 on page 58.

Quantification of seasonal and diurnal dynamics of subglacial channels using seismic observations on an Alpine Glacier.

[1] University Grenoble Alpes, CNRS, IRD, IGE, Grenoble, France
[2] Laboratory of Hydraulics, Hydrology and Glaciology, ETH Zurich, Zurich, Switzerland
[3] Edytem, CNRS, Université de Savoie, Chambéry, France

Abstract

Water flowing below glaciers exerts a major control on glacier basal sliding. However, our knowledge of the physics of subglacial hydrology and its link with sliding is limited because of lacking observations. Here we use a two-year long dataset made of on-ice measured seismic and in-situ measured glacier basal sliding speed on Glacier d'Argentière (French Alps) to investigate the physics of subglacial channels and its potential link with glacier basal sliding. Using dedicated theory and concomitant measurements of water discharge, we quantify temporal changes in channels hydraulic radius and hydraulic pressure gradient. At seasonal timescales we find that hydraulic radius and hydraulic pressure gradient respectively exhibit two- and six-fold increase from spring to summer, followed by comparable decrease towards autumn. At low discharge during the early and late melt season channels respond to changes in discharge mainly through changes in hydraulic radius, a regime that is consistent with predictions of channels behaving at equilibrium. In contrast, at high discharge and high

short-term water-supply variability (summertime), channels undergo strong changes in hydraulic pressure gradient, a behavior that is consistent with channels behaving out-of-equilibrium. This out-of-equilibrium regime is further supported by observations at the diurnal scale, which support that channels pressurize in the morning and depressurize in the afternoon. During summer we also observe high and sustained basal sliding speed, which supports that the widespread inefficient drainage system (cavities) is likely pressurized concomitantly with the channel-system. We propose that pressurized channels help sustain high pressure in cavities (and therefore high glacier sliding speed) through an efficient hydraulic connection between the two systems. The present findings provide an essential basis for testing the physics represented in subglacial hydrology and glacier sliding models.

5.1   Introduction

Subglacial water flow exerts a major control on glacier and ice sheet dynamics and their response to variations in water supply (e.g. Iken *et al.*, 1997; Zwally *et al.*, 2002; Bartholomaus *et al.*, 2011; Chandler *et al.*, 2013; Hewitt, 2013; Brondex *et al.*, 2017; Joughin *et al.*, 2018). Water flowing at the base of glaciers modulates glacier basal sliding by lubricating the ice-bed interface. The higher the water pressure the weaker the basal friction, resulting in faster glacier sliding (Iken and Bindschadler, 1986; Schoof, 2010; Gagliardini *et al.*, 2007). Water pressure does not simply depend on the total water input but also on the way the water is conveyed through the subglacial drainage system (Lliboutry, 1968), a system that has, yet, yielded limited observations (Flowers, 2015).

The subglacial drainage system of hard-bedded glaciers is considered to be two-fold. First, cavities form on the downstream lee of bedrock bumps and are thought to enhance basal sliding through reducing the apparent bed roughness (Lliboutry, 1968). These cavities constitute a widespread inefficient drainage system associated with high basal water pressure, slow water flow (of the order of 10^{-2} m.s^{-1}, see e.g. Richards *et al.* (1996)) and limited hydraulic conductivity. Second, subglacial channels form into the ice from conduit melt by flowing water heat dissipation, and close through ice creep (Röthlisberger, 1972; Nye, 1965). These channels constitute a localized efficient drainage system associated with lower basal water pressure, faster water flow and higher hydraulic conductivity compared to within cavities. A drainage system for which a steady water input is routed through channels tends to slow basal sliding compared to if water is predominantly routed through cavities (e.g. Fountain, 1994; Schoof, 2010). Most of the current subglacial drainage models (Schoof, 2010; Hewitt, 2013; Werder *et al.*, 2013; Gagliardini and Werder, 2018) are based on this two-fold representation. These models succeed in capturing the two-way channel-cavity coupling but still strongly rely on the choice of model parameters (e.g. cavities and channels hydraulic conductivity, channels opening and closing rates, see Fleurian *et al.*, 2018). Observational constraints on these parameters (e.g. water pressure, channel properties) and on the channel-cavity-sliding link are however very limited because of the limited observations of the drainage system and concomitant measurements of basal sliding speed (Flowers, 2015; Fleurian *et al.*, 2018).

Direct observations of the drainage system on temperate glaciers have been relying on the analysis of water discharge measured near glacier outlet (Collins, 1979; Hooke, 1984; Tranter *et al.*, 1996; Anderson *et al.*, 2003; Chandler *et al.*, 2013), of dye tracing experiments (Willis, 1995; Nienow *et al.*, 1996), of recently exposed subglacial environments (Vivian and Bocquet, 1973; Walder and Fowler, 1994), of local water pressure boreholes measurements (Andrews *et al.*, 2014; Hoffman *et al.*, 2016; Rada and Schoof, 2018) or of radar measurements (Church *et al.*, 2019). These methods are mostly point-scale and often focus on the cavity-system due to the very narrow extent of the channel-system (Rada and Schoof, 2018). As a consequence, quantitative information on channels' long term temporal dynamics is limited, such that channels' properties (e.g. size, water flow velocity) and dynamics (e.g. opening and closure rate) remain poorly constrained.

Interactions between channels and cavities are often inferred from evaluating glacier flow-velocity variations in response to meltwater supply variability. High and sustained water supply over monthly timescales (e.g. during the peak melt season) has been linked to glacier deceleration (Bartholomew *et al.*, 2010; Sole *et al.*, 2013; Tedstone *et al.*, 2013, 2015). This behavior is related to the fact that channels-development increases the drainage system capacity and is, therefore, expected to reduce the average basal water pressure (Fountain, 1994). On the contrary, during short term water supply increase (e.g. at the early melt season or at diurnal scales), glacier velocity changes have been observed to occur concomitantly with water supply changes (Palmer *et al.*, 2011; Sole *et al.*, 2013; Vincent and Moreau, 2016). This behavior is mostly related to the pressurization of the cavity-system, causing average basal water pressure rise and subsequent basal sliding speed increase (e.g. Nienow *et al.*, 2005; Schoof, 2010; Rada and Schoof, 2018). During periods of well-developed channelized system (e.g. in summer), this behavior has also been observed because of a channelized system drainage capacity being overwhelmed by the water input changes (Bartholomaus *et al.*, 2008; Andrews *et al.*, 2014) causing pressurized channel flow. These studies have been capable to underline the overall differences between cavity and channel control on subglacial water pressure over different timescales. However, the lack of dedicated channels observations independent of those on cavities and concomitant with glacier sliding speed measurements renders difficult a more quantitative characterization of the physics of subglacial hydrology and its link with sliding.

Here we use on-ice seismology to explore the evolution of subglacial channels over two complete melt seasons. Over the last decade an increasing number of studies have shown the high potential of analyzing high-frequency (>1 Hz) ambient seismic noise to investigate turbulent water flow and sediment transport in terrestrial rivers and streams (e.g. Burtin *et al.*, 2008, 2010; Tsai *et al.*, 2012; Schmandt *et al.*, 2013; Gimbert *et al.*, 2014). The recent work of Gimbert *et al.* (2016) based on observations of Bartholomaus *et al.* (2015a) suggests that passive seismology may help filling the observational gap on the physics of subglacial channels. Gimbert *et al.* (2016) adapted to subglacial channels a physical framework that describes how turbulent water flow generates seismic waves and that was initially developed for rivers by Gimbert *et al.* (2014). Contrary to rivers, subglacial channels have the capability to be full and thus to undergo pressurized situations. By applying this modified framework to the Mendenhall

glacier (Alaska) over a two-month long summer period, the authors demonstrate that one can use concomitant seismic noise and water discharge measurements to continuously and separately quantify relative changes in channel hydraulic pressure gradient and channel hydraulic radius. They inferred that channels mainly evolve through changes in hydraulic radius over long time scales (multi-weekly), whereas changes in hydraulic pressure gradient are often short-lived (sub-daily to weekly). The use of such an approach to investigate channel physics on relevant glaciological timescales (e.g. diurnal and seasonal) yet remains to be conducted, and the resulting channels properties remain to be compared to other independent observations, such as basal sliding speed. This is the objective of our study.

We conduct a unique and almost uninterrupted two-years passive seismic survey on Glacier d'Argentière (French Alps), together with continuous measurements of subglacial water discharge, glacier basal sliding speed and local subglacial water pressure. First, we characterize the subglacial channel-flow-induced seismic power signature and use the model of Gimbert *et al.* (2016) to derive timeseries of hydraulic pressure gradient and hydraulic radius. We then compare these channel properties to the other independent measurements of glacier sliding speed and basal water pressure. We also compare our seismically-derived observations with the theory for subglacial channels physics proposed by Röthlisberger (1972) to assess the implications of these analysis for channels physics. Finally, we investigate the equilibrium state of subglacial channels to discuss the channel-cavity interactions and their potential link with basal sliding throughout the melt season. Doing so will also allow us to discuss the applicability of such an approach to improve our general knowledge on subglacial hydrology mechanisms of mountain glaciers and ice sheets.

5.2 Rational

Here we provide a brief background on the theoretical framework of Gimbert *et al.* (2016), which relates seismic noise and water discharge to subglacial channel-flow properties, and that of Röthlisberger (1972), which predicts subglacial channel hydraulic pressure gradient and hydraulic radius scaling as a function of water discharge under certain assumptions. Refer to table 5.1 in Appendix 5.8 for a summary of all variables, physical quantities, and mathematical functions defined in the following sections.

Theory of subglacial channel-flow-induced seismic noise

Turbulent water flow in a river or a subglacial channel generates frictional forces F acting on the near boundaries (e.g. river bed or conduit wall), which in turn cause seismic waves with given amplitude and spectral signature (Gimbert *et al.*, 2014). By propagating through a medium (e.g. rock, gravel or ice), seismic waves cause ground motion at any location x away from the source location x_0 (Fig. 5.1). The relationship between the force timeseries $F(t, x_0)$ applied at x_0 in a channel and the ground velocity timeseries $U(t, x)$ measured at x can be described from Aki and Richards (2002)
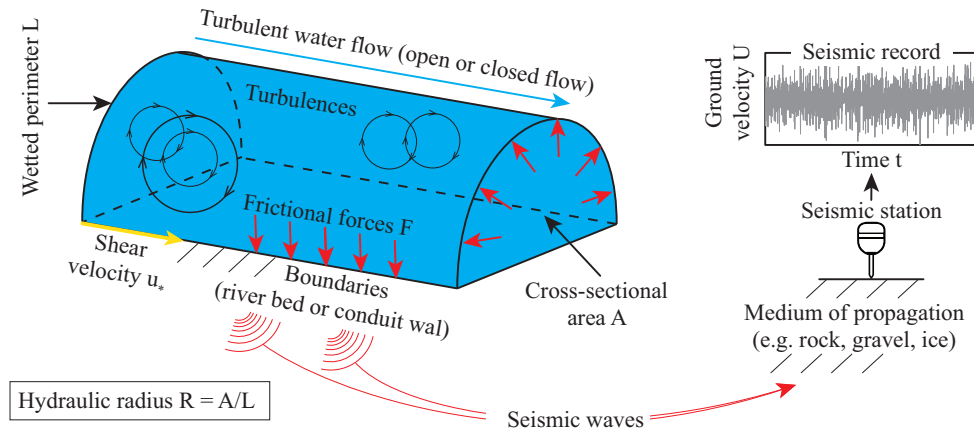
Figure 5.1: Schematic representation of subglacial channel-flow-induced seismic noise. Representation of an idealized conduit of hydraulic radius R with a wall shear velocity u_* (see Eq.(5.3)). Turbulent flow generates frictional forces F causing seismic waves and resulting in a ground velocity U that is recorded at a distant seismic station (see Eq.(5.1)).

as

$$U(t,x) = F(t,x_0) \otimes \frac{dG(t,x;x_0)}{dt}, \tag{5.1}$$

where $G(t)$ is the displacement Green's function that converts the force applied at x_0 into ground displacement at x and the notation $\otimes$ stands for the convolution operator. The seismic power P of such signal is defined over a time period T as

$$P(f,x) = \frac{U(f,x)^2}{T}. \tag{5.2}$$

where $U(f) = \mathcal{F}(U(t))$ is the Fourier transform of the ground velocity timeseries and f is the frequency. We note P_w the seismic power induced by turbulent water flow. Based on a description of the force $F(f)$ as a function of flow parameters, Gimbert $et\ al.$ (2014) demonstrated that P_w scales as

$$P_w(f) \propto \zeta(\frac{H}{k_s})W u_*^{14/3} \tag{5.3}$$

where u_* is river wall shear velocity, W is river width and ζ is a function that accounts for turbulence intensity changes with changes in the apparent roughness that depends on H the flow depth and k_s the wall roughness size (Fig. 5.1).

To relate P_w to subglacial channels properties, Gimbert $et\ al.$ (2016) expressed the shear velocity as $u_* = \sqrt{gRS}$ where g is gravitational acceleration, R the hydraulic radius and S the hydraulic pressure gradient. The hydraulic radius R is defined as the ratio of the cross-sectional area of the channel flow to its wet perimeter (Fig. 5.1). This parameter scales with flow depth for open channel-flow. The hydraulic pressure gradient S is a

function of both the water pressure rate of change in the flow direction and the bed slope. For free surface flow S equals channel slope. In a case of constant channel slope and channel geometry, increasing S means closed and pressurizing channel-flow.

Gimbert *et al.* (2016) then expressed water discharge Q as a function of water flow velocity V_w using the Manning-Strickler relation $V_w = \frac{R^{2/3}S^{1/2}}{n'}$ with n' is the Manning's coefficient (Strickler, 1981). To study P_w for a subglacial channel flow configuration, Gimbert *et al.* (2016) considered that the source-to-station distance is constant, such that changes in P_w are not caused by changes in source (channel) position. Gimbert *et al.* (2016) then assumed a constant number N of channels and thus neglected the dependency of P_w on N. Here we include the dependency of P_w on N by considering that all channels have equal hydraulic radius and hydraulic pressure gradient (i.e. are of similar size and position compared to the seismic station) such that

$$P_w \propto N\beta R^{14/3}S^{7/3} \tag{5.4}$$

$$Q \propto N\beta R^{8/3}S^{1/2}, \tag{5.5}$$

where β is a function of conduit shape and fullness that may be neglected (see supporting materials of Gimbert *et al.* (2016) for details). Combining Eqs.(5.4) and (5.5) and neglecting changes in β leads to the two following formulations for P_w,

$$P_w \propto R^{-82/9}Q^{14/3}N^{-11/3} \tag{5.6}$$

$$P_w \propto S^{41/24}Q^{5/4}N^{-1/4}. \tag{5.7}$$

From Eqs.(5.6) and (5.7) two end-member cases can be evaluated. If changes in discharge occur at constant channel geometry (i.e. constant R and N) from Eq.(5.6) we have

$$P_w \propto Q^{14/3}, \tag{5.8}$$

In contrast, if changes in discharge occur at constant hydraulic pressure gradient and channel number (regardless of whether the conduit is full or not) from Eq.(5.7) we have

$$P_w \propto Q^{5/4}. \tag{5.9}$$

Beyond these end-member scenarii, one can use measurements of P_w and Q to invert for relative changes in R and S using Eqs.(5.6) and (5.7) as:

$$S = S_{ref}\left(\frac{P_w}{P_{w,ref}}\right)^{24/41}\left(\frac{Q}{Q_{ref}}\right)^{-30/41}\left(\frac{N}{N_{ref}}\right)^{6/41}, \tag{5.10}$$

$$R = R_{ref}\left(\frac{P_w}{P_{w,ref}}\right)^{-9/82}\left(\frac{Q}{Q_{ref}}\right)^{21/41}\left(\frac{N}{N_{ref}}\right)^{-33/82}, \tag{5.11}$$

where the subset *ref* stands for a reference state, which has to be defined over the same time period for both Q and P_w, but not necessarily for R and S. Details on the derivation from Eqs.(5.6) and (5.7) to Eqs.(5.10) and (5.11) can be found in Gimbert *et al.* (2016). In the following we consider N as constant to invert for R and S, and later we support that our inversions are not significantly biased by potential changes in N (Sect. 5.6).

R-channels theory

To date, state-of-the art subglacial drainage models use the theories of Röthlisberger (1972) to describe subglacial channel dynamics (see Fleurian *et al.* (2018) for model inter-comparisons). Channels described in these theories are assumed to be of semi-circular shape and to form into the ice through melt by heat dissipation from the flowing water and close through ice creep. A channel evolves at steady state with water discharge Q if melt and creep rates change instantaneously with changes in Q. A steady-state channel is at equilibrium with Q if melt (opening) rate equals creep (closure) rate, in which case Röthlisberger (1972) predicts

$$R \propto Q^{9/22} \tag{5.12}$$

$$S \propto Q^{-2/11}. \tag{5.13}$$

For a steady-state channel not at equilibrium with Q and that responds solely through changes in pressure gradient S (i.e. R is constant) Röthlisberger (1972)' equations show that:

$$S \propto Q^2. \tag{5.14}$$

Further details on the derivation of these equations from Röthlisberger (1972) can be found in Supplementary Sect. S2. Later we compare our inversions of changes in R and S (using seismic observations) with changes in R and S as predicted by the theory of Röthlisberger (1972) for steady-state channels at equilibrium or not at equilibrium with water discharge.

5.3   Field setup

Site and glaciological context

Glacier d'Argentière is a temperate glacier located in the Mont Blanc mountain range (French Alps, see Fig. 5.2). The glacier is c. 10 km long and covers an area of c. 12.8 km^2. It extends from an altitude of c. 1700 m above sea level (asl) up to c. 3600 m asl in the accumulation zone. Its cumulative mass balance has been continuously decreasing from -6 m water equivalent (w.e) in 1975 to -34 m w.e presently compared to in the beginning of the twentieth century (Vincent and Moreau, 2016). This site is ideal to study subglacial channels properties since it presents a typical U-shaped narrow valley (Hantz and Lliboutry, 1983) and hard bed conditions (Vivian and Bocquet, 1973), two conditions that favor a well-developed R-channel subglacial network (Röthlisberger,
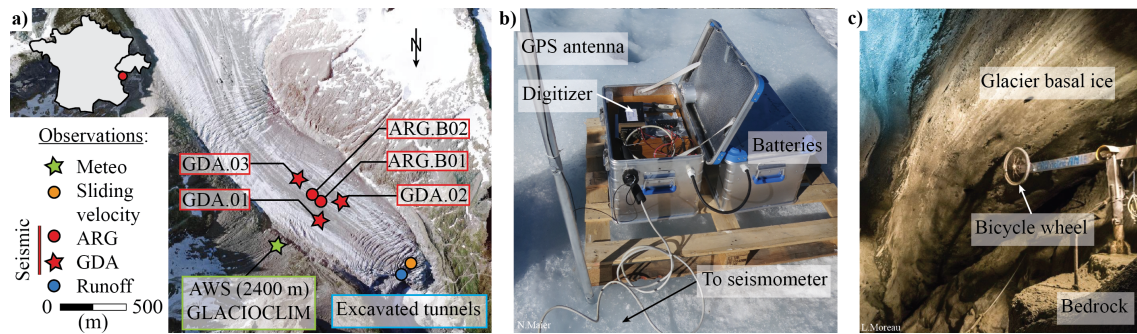
Figure 5.2: Monitoring setup of Glacier d'Argentière. (a) Aerial view of Glacier d'Argentière field site (France) and location of the instruments used in this study. The aerial photography was taken in 2015. The seismic network is composed of the GDA (red circles) and ARG (red stars) borehole stations and is located according to positions in summer 2018. Station ARG.B02 is installed c. 70 m deep in the ice whereas the four other stations are installed c. 5 m deep. The GLACIOCLIM (https://glacioclim.osug.fr/) automatic weather station (green star, AWS) provides air temperature and precipitation. Basal sliding speed (orange circle) and water discharge (blue circle) are measured thanks to direct access to the glacier base from excavated tunnels. Basal water pressure is measured at a similar location as that of basal sliding speed measurements. (b) Picture of the seismic instrumental setup used in this study. (c) Picture of the subglacial observatory with the bicycle wheel used to measure basal sliding speed. [Photo credits: (a) IGN France, https://www.geoportail.gouv.fr/, (b) N. Maier, (c) L. Moreau].

1972).

In the present study we analyze the data recorded from spring 2017 to autumn 2018 with seismometers located between 2350 and 2400 m asl (Fig. 5.2). This location corresponds to the cross-section No. 4 monitored by the French glacier-monitoring program GLACIOCLIM (https://glacioclim.osug.fr/). There the glacier is up to c. 280 m thick (Hantz and Lliboutry, 1983, updated from a radar campaign conducted in 2018). Subglacial water discharge is monitored 600 m downstream of the seismometers at 2173 m asl near the glacier ice fall in subglacial excavated tunnels maintained by the hydroelectric power company Emosson S.A. Subglacial water is almost entirely evacuated through one major snout, as supported by direct observations of very limited water flowing elsewhere. Thus discharge measured at this location is well representative of discharge subglacially routed under the seismometers location. Discharge measurements are conducted from mid-spring to early autumn with an accuracy of 0.01 m^{3}s^{-1} every 15 min by means of a Endress Hauser sensor measuring the water level in a conduit of known geometry. The minimum measurable value for water discharge is limited by the measurement accuracy and the maximum one is of 10 m^{3}s^{-1} due to the capacity of the collector. Because sediments accumulate in the collector, flushes are recorded when the latter is emptied, causing glitches in the discharge record. We remove these glitches removing Q values that present $\frac{d(Q)}{dt}$ higher than 0.2 m^3 per 15 min. Within the same tunnel network, a subglacial observatory is used to measure basal sliding speed out of a bicycle wheel placed in contact with the basal ice (Vivian and Bocquet, 1973). Since August 2017 basal sliding speed is measured at a time resolution of 5 s over a 0.07 mm' space segmentation. In the close vicinity a pressure sensor, of gauged type, is used to measure subglacial water pressure with 10 min time resolution and an accuracy of 400 Pa. The sensor is installed in a borehole drilled

from the excavated tunnels up to the glacier bottom (see Vivian and Bocquet (1973) for details). Air temperature and precipitation measurements are obtained at a 0.5 h time step through an automatic weather station maintained by the French glacier-monitoring program GLACIOCLIM and located on the moraine next to the glacier at 2400 m asl. Precipitation is measured with an OTT Pluvio weighing rain gauge with a 400 cm^2 collecting area. When air temperature is below zero, only precipitation occurrences are accurate, but not absolute values because of snow clogging.

Seismic instrumentation

We use five seismic stations installed in the lower part of the glacier (Fig. 5.2). The instruments belong to two seismic networks, denoted as GDA (3 stations) and ARG (2 stations). Stations GDA.01, GDA.02 and GDA.03 were deployed in Spring 2017 with c. 200 m inter-station distances. These stations have digitizers of the type Nanometrics Taurus, set to 16 Vpp sensitivity and a 500 Hz sampling rate, and borehole type sensors (model Lennartz 3D/BH), with an Eigen frequency of 1 Hz. Station ARG.B01 was installed in October 2017 at the center of the GDA network at about 100 m from each GDA stations. The digitizer used for that station is a Geobit-SRi32L set to a 10 Vpp sensitivity and a 1000 Hz sampling rate. The sensor is of borehole type (model Geobit-C100) with an Eigen frequency of 0.1 Hz. Station ARG.B02 was installed in April 2018 about 50 m upglacier from station ARG.B01. The digitizer used for that station is a Geobit-SRi32 set to a 0.625 Vpp sensitivity and a 1000 Hz sampling rate. The sensor is of borehole type (model Geobit-S400), with an Eigen frequency of 1 Hz. All stations were installed c. 5 m deep below the ice surface, except ARG.B02 which was placed c. 70 m deep. A few data gaps occurred during our study due to difficulties in ensuring continuous power supply and data storage on glaciers.

5.4   Methodology

Refer to table 5.1 in Appendix 5.8 for a summary of all variables, physical quantities, and mathematical functions defined in the following sections.

Calculation of seismic power at a 'virtual' station

The raw seismic record at each station is first corrected from the sensor and digitizer responses. Then, the frequency-dependent seismic noise power P is computed using the vertical component of ground motion (see Eq.(5.2)). P is calculated with the Welch's method over time windows of duration dt with 50 % overlap (Welch, 1967). The longer dt, the more likely highly energetic impulsive events occur and overwhelm the background noise within that time window (Bartholomaus *et al.*, 2015a). To maximize sensitivity to the continuous, low amplitude, subglacial channel-flow-induced seismic noise and minimize that of short-lived but high energy impulsive events, we use a short time window of $dt = 2$ s to calculate P, and average it over time windows of
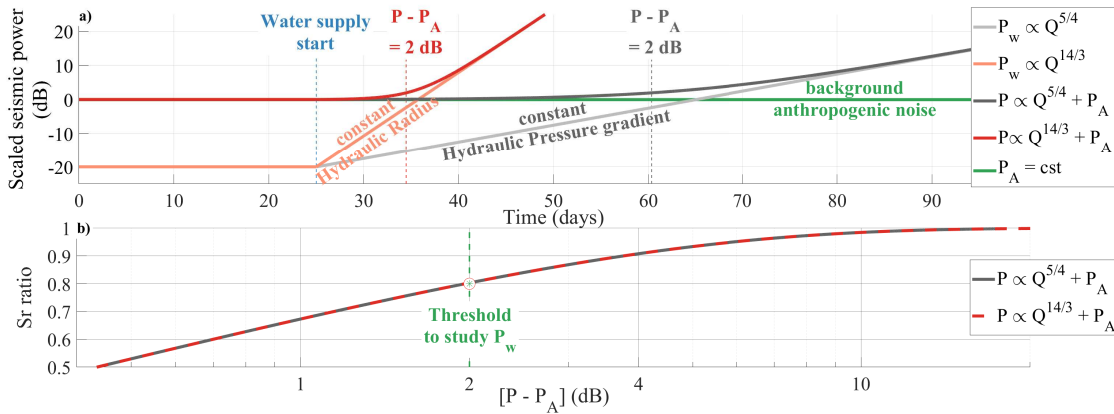
Figure 5.3: Synthetic predictions of scaling bias due to anthropogenic noise superimposing to subglacial channel-flow-induced seismic noise. (a) Synthetic anthropogenic seismic power (green line, P_A), synthetic subglacial channel-flow-induced seismic power $P_w = Q^n$ with Q the synthetic water discharge for $n = \frac{5}{4}$ (grey line) and $n = \frac{14}{3}$ (orange line) and synthetic seismic power $P = P_A + P_w$ for $n = \frac{5}{4}$ (black line) and $n = \frac{14}{3}$ (red line). (b) Evolution of Sr (see Sect. 5.4) ratio with respect to $P-P_A$ for $n = \frac{5}{4}$ (grey line) and $n = \frac{14}{3}$ (red line). Note that the two curves overlap.

15 min in the decimal logarithmic space. We express P in decibel (dB, decimal logarithmic), which allows properly evaluating its variations over several orders of magnitude.

We reconstruct a two-year long timeseries by merging records from the five available stations into one unique record at a 'virtual' station. To minimize site and instrumental effects on seismic power we shift the average power at each station to a reference one taken at ARG.B01. The seismic signal at our 'virtual' station is composed of the GDA seismic signals between May 2017 end December 2017, and of the ARG seismic signals between December 2017 and December 2018 (see Fig. S1).

Evaluating bias due to anthropogenic noise

Later in section 5.5 we show that when water discharge Q is low (in the early and late melt season) seismic power from anthropogenic noise (P_A) is comparable to the subglacial channel-flow-induced seismic power (P_w). Here we evaluate how much P_A adding to P_w can bias the evaluation of scaling predictions of Gimbert *et al.* (2016). We calculate a synthetic seismic power P as $P = P_A + P_w$ and a synthetic P_w from a synthetic Q as $P_w = Q^n$ with n being equal to $\frac{5}{4}$ or $\frac{14}{3}$ as expected from theory (see Eqs.(5.8) and (5.9)). We quantify the relative contributions of P_w and P_A to P through the parameter Sr, which we define as $Sr = log\left[\left(\frac{Q}{P}\right)^n\right]$. When Sr tends to 1, subglacial channel-flow-induced seismic power dominates the synthetic seismic power and when Sr tends to 0 anthropogenic noise power does.

In Fig. 5.3(a) we show the temporal evolution of synthetic P with a constant value for P_A and with a P_w that responds to a synthetic evolving water supply Q. The value of P is normalized by P_A, resulting in $P = 0$ dB in winter. For $P_w \propto Q^{14/3}$ (Fig. 5.3(a),

red and orange lines), P_w dominates the contribution to P within c. 10 days from the onset of water supply. For $P_w \propto Q^{5/4}$ (Fig. 5.3(a), black and green lines) P contains both P_w and P_A contributions during a period that is three times longer than for $P_w \propto Q^{14/3}$. The evolution of Sr with respect to P-P_A (Fig. 5.3(b)) is the same for both the constant hydraulic pressure gradient (red line) and constant hydraulic radius (grey line) scenarii. For P-$P_A > 2$ dB, Sr is higher than 0.8, meaning that subglacial channel-flow-induced seismic power contributes by more than 80% to the synthetic seismic power. Later in Sect. 5.5 we measure P_A during winter and use the condition P-$P_A > 2$ dB to define the periods where evaluate P_w directly from the measurement of P and investigate the subglacial hydraulic properties.

Definition of metrics to evaluate sub-diurnal dynamics

Since the P_w versus Q relationship is not unique and may vary with time (see Sect. 5.2), we expect that the diurnal timeseries of P_w versus Q may exhibit different patterns throughout the melt season; and that these patterns reveal changes in the subglacial hydraulic properties. To systematically quantify the diurnal variability of P_w, Q, R and S throughout the melt season we define three metrics that we calculate on an hydrological daily basis (defined as the period between two minimum Q within a 24 h time window). To focus on the diurnal variability only, we bandpass filter our timeseries within a [6-36] h range (see Appendix Fig. 5.11 for details). Our first metric quantifies the diurnal variability of a given variable X during a given day and corresponds to the coefficient of variation C_v defined as:

$$C_v = \frac{(X_{day})_{max} - (X_{day})_{min}}{\overline{X_{day}}} \tag{5.15}$$

with $(X_{day})_{max}$ and $(X_{day})_{min}$ the maximum and minimum value of X_{day}, respectively, and $\overline{X_{day}}$ its average. Our second metric ϕ quantifies daily hysteresis between P_w and Q by evaluating the difference between P_w when Q is rising, e.g. in the morning, and P_w when Q is falling, e.g. in the afternoon. Following the approach of Roth et $al.$ (2016) we define ϕ as:

$$\phi = \frac{\overline{(P_{w,day})_{rising}} - \overline{(P_{w,day})_{falling}}}{\overline{(P_{w,day})_{falling}}}. \tag{5.16}$$

The larger ϕ, the more seismic energy is recorded during the rising discharge period with respect to the falling one. Hysteresis can occur either because of an asymmetry between $(P_{w,day})_{rising}$ and $(P_{w,day})_{falling}$ or because of a time lag between P_w and Q. To avoid ambiguity between these two hysteresis sources our third metric corresponds to the daily time lag δt between the time $t((P_{w,day})_{max})$ when P_w is maximum and the time $t((Q_{day})_{max})$ when Q is maximum and is defined as:

$$\delta t = t((Q_{day})_{max}) - t((P_{w,day})_{max}). \tag{5.17}$$

We set the condition that for δt to be calculated, $t((P_{w,day})_{max})$ has to correspond to both the time when P_w is maximum and has a null-derivative within a [-8, 8] h' time window around $t((Q_{day})_{max})$. We note that a time delay of about 0.04 h is expected
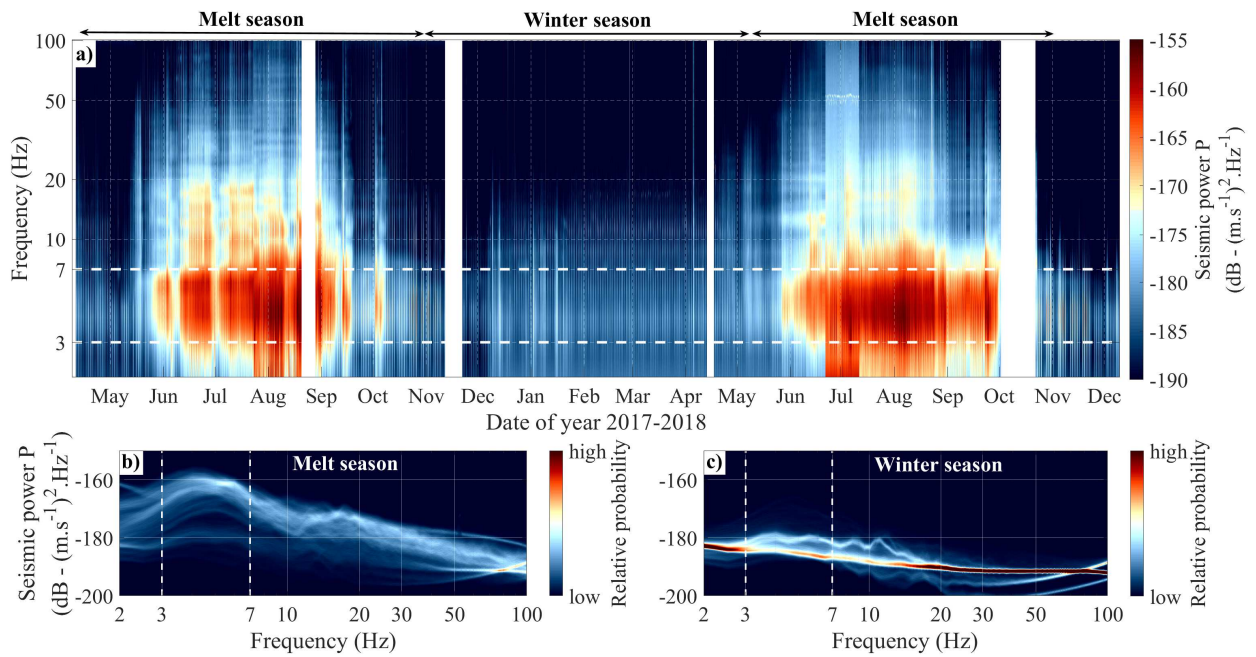
Figure 5.4: (a) Spectrogram of the observed seismic power P as a function of time (x-axis, May 2017 to December 2018) and frequency (y-axis, 1-100 Hz log-scale). Colors represent seismic power in decimal logarithmic (dB) relative to $(m.s^{-1})^2.Hz^{-1}$. White bands correspond to data gaps. (b) and (c) Spectral distribution of seismic power during the melt seasons (b) and the winter seasons (c). Colors represent occurrence probability and colorbars are identical for (b) and (c).

due to water flowing at c. $1\ m.s^{-1}$ over the c. 600 m separating our seismic stations to where Q is measured (see Fig. S2 for details). This means that any values of δt greater than $\pm\ 0.04$ h are not attributable only to water transfer time lags.

5.5   Results

Overview of observations

Seismic power P as calculated at our 'virtual' station based on records from our 5 stations (see Sect. 5.4) is shown in Fig. 5.4(a) as a function of time (May 2017 to December 2018) and frequency (2 to 100 Hz). Large seasonal changes in P are observed within the [2-10] Hz frequency range, in which P is higher by more than 2 orders of magnitude during the melt season (mid-May to September) compared to in winter. Changes in P are also observed within the [10-20] Hz frequency range with P during the melt season being about an order of magnitude larger than in winter. Significant changes of smaller amplitude are also observed at higher frequency ([20-100] Hz). Spectral distributions of P presented in Figs. 5.4(b) and (c) show widely spread P-values during the melt season (Fig. 5.4(b), variations over more than 10 dB), as opposed to being comparatively much narrower in winter (Fig. 5.4(c), variations within 1-3 dB). Seismic power within the [3-7] Hz frequency range shows the highest range of variations from winter to summer (Figs. 5.4(a) and (b)). Over the two years, the overall spectral pattern
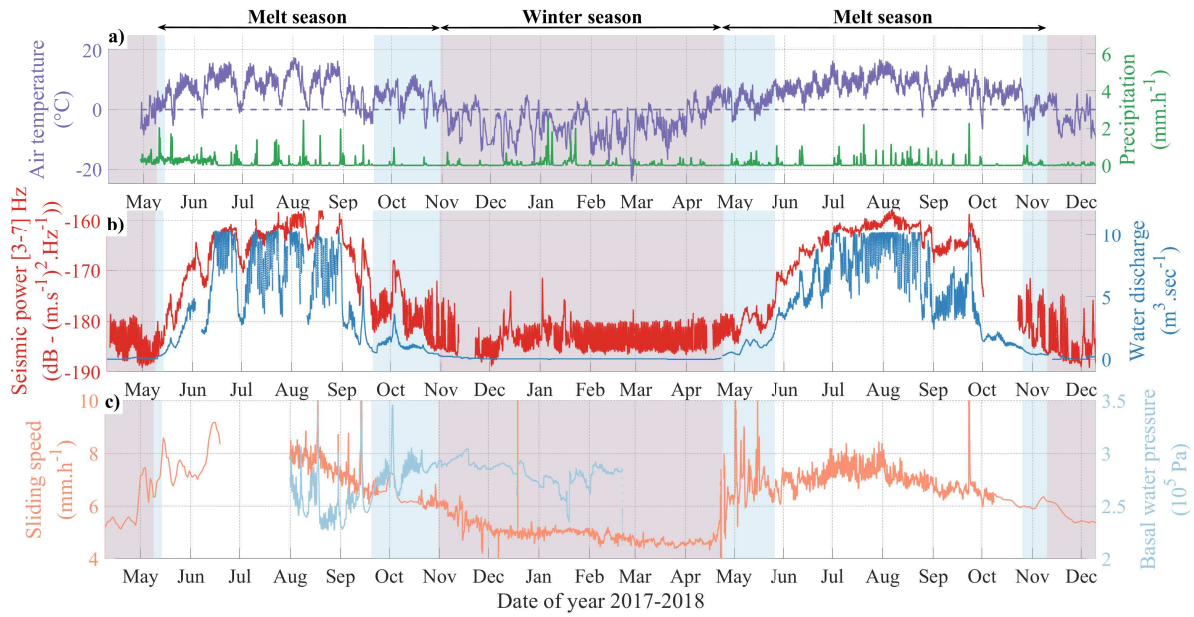
Figure 5.5: Timeseries of physical quantities measured from spring 2017 to winter 2018 at Glacier d'Argentière. All data are smoothed over a 6 h time-window. (a) Surface air temperature (purple line) and precipitation (green line) at the GLACIOCLIM AWS (Fig. 5.2). The dashed purple line shows $T = 0°C$. (b) Averaged seismic power within the [3-7] Hz frequency range at the 'virtual' seismic station (red line, $P_{[3-7]\,Hz}$, see Sect. 5.5 for details) and subglacial water discharge Q (blue line). (c) Basal sliding speed (orange line) and subglacial water pressure (light blue line) measured at Glacier d'Argentière subglacial observatory (Fig. 5.2). Note that temporal resolution in the sliding speed is lower in [May-July] 2017 and from October 2018 because of instrumental issues. Red shaded areas represent the winter season; blue shaded areas represent the periods when diurnal changes in anthropogenic noise are too pronounced to study P_w on a diurnal basis.

remains similar, although intra-seasonal variations of P during the 2017 melt season are more pronounced compared to the 2018 melt season.

The observed meteorological and hydrological conditions at Glacier d'Argentière together with the measured basal sliding speed and the seismic power $P_{[3-7]\,Hz}$ as averaged within the [3-7] Hz frequency range are shown as a function of time (May 2017 to December 2018) in Fig. 5.5. Water discharge Q shows a strong seasonal signal with discharge lower than 0.1 m^3.s^{-1} in winter and up to values higher than 10 m^3.s^{-1} in summer. These changes are consistent with air temperature values, and occur concomitantly with the evolution of $P_{[3-7]\,Hz}$ (Fig. 5.5(b)). Further details on the comparison between $P_{[3-7]\,Hz}$ and Q are presented in Sect. 5.5. Over the first months of the melt season (early May to mid-June 2017 and late April to mid-June 2018) Q increases by about 2 orders of magnitude from 0.1 to 10 m^3.s^{-1}. At the same time, the amplitude of the diurnal variations in Q increases up to 3 m^3.s^{-1} over the summer. The evolution of basal sliding speed presented in Fig. 5.5(c) depicts a rapid acceleration from 5 mm.h^{-1} in May 2017 and April 2018 to 7 mm.h^{-1} over the following month. Sliding speed then stays almost constant through the summer, and slowly decreases down to a minimum of 4.5 mm.h^{-1} in February (see also comparable observations made by Vincent and Moreau (2016) over the past decade). Basal water pressure mea-

surements (Fig. 5.5(c)) show that at the seasonal timescale the basal water pressure tends to be higher in winter than in summer by c. 2.5 1e^{+4} Pa. In summer 2017 the short-term (diurnal) variability in the basal water pressure is more pronounced than in winter, as also observed for the water discharge (Fig. 5.5(b) and Fig. 5.11). During heavy rainfall (Fig. 5.5(a)) and consequent discharge (Fig. 5.5(b)), basal water pressure variations are in phase with sliding speed (Fig. 5.5(c); e.g in August 1st, August 7th, August 18th, August 30th, September 13th or October 2nd of 2017). This evolution of the measured basal water pressure rather depicts a local behavior whereas changes in the basal sliding speed (Fig. 5.5(c)) rather represent average changes in the average basal water pressure conditions over our study area and therefore better represent the global cavity-system pressure conditions.

Measurement artifacts are observed for Q with values being thresholded at 10 m^3.s^{-1}, and for P in July 2018 when unusually high seismic power values are observed over the whole frequency range, which we associate with the initially weak ice-sensor coupling of ARG.B02. Site specificity of the GDA network used in 2017 causes higher seismic power in the [8-20] Hz frequency band in 2017 than in year 2018. These artifacts appear to not significantly affect P (at least not within the [2-10] Hz frequency range), nor the concomitant temporal evolution of P and Q over the two years.

Seismic power induced by subglacial channel-flow

We consider seismic power $P_{[3-7]\,\text{Hz}}$ averaged within the [3-7] Hz frequency range (Fig. 5.5(b) (red line)) as best representative of subglacial channel-flow-induced seismic power P_w because it shows the highest variations with changes in Q (Figs. 5.4 and 5.5). A similar frequency-signature of the subglacial channel-flow-induced seismic noise as been observed by Bartholomaus *et al.* (2015a), Preiswerk and Walter (2018) and Lindner *et al.* (2020). This frequency range is also comparable to those observed for water flow in rivers (Schmandt *et al.*, 2013; Gimbert *et al.*, 2014). As Q increases from less than 0.1 m^3.s^{-1} in early May to about 10 m^3.s^{-1} end of July, P_w increases by up to 30 dB (i.e. 3 orders of magnitude). Differences in relative variations of P_w across stations are lower than 0.5 dB including during periods of high discharge (Fig. S2). This supports the accuracy and validity of our 'virtual' station reconstruction to study the subglacial channel-flow-induced seismic power (Sect. 5.4). Variations in P_w follow those of Q during the melt season and over seasonal to weekly times scales (Fig. 5.5(b)). Both the high sub-monthly variability in Q and air temperature observed in 2017 and the rapid changes in Q occurring in fall 2017 and 2018 are also observed in the temporal evolution of P_w. In winter we observe high seismic power bursts from December to mid-January occurring when Q is null but concomitantly with the beginning of heavy snowfall events. These bursts are not associated with subglacial channel-flow-induced seismic noise but likely correspond to repeating stick-slip events triggered by snow loading similar to those observed previously by Allstadt and Malone (2014). When Q is lower than 2 m^3.s^{-1} during winter, early spring and fall, we observe regular weekly and daily variations in $P_{[3-7]\,\text{Hz}}$ that superimpose to the background variations (Fig. 5.5(b)). This regular pattern corresponds to anthropogenic noise, as previously observed by Preiswerk and Walter (2018) in a similar setup.
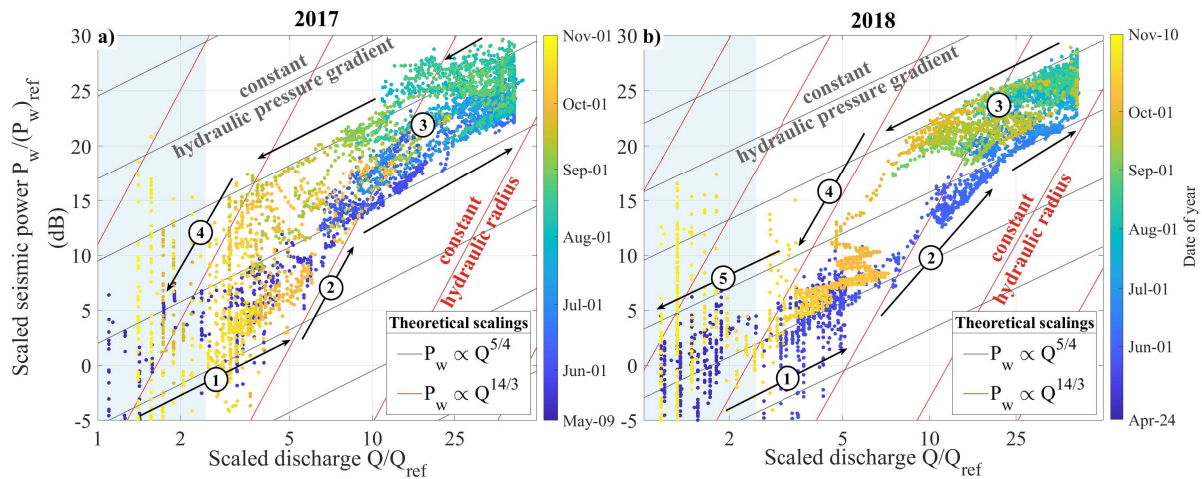
Figure 5.6: Observed (dots) and predicted (lines) changes in subglacial channel-flow-induced seismic power $\frac{P_w}{(P_w)_{ref}}$ versus changes in water discharge $\frac{Q}{Q_{ref}}$ during the melt season of years 2017 (a) and 2018 (b). Temporal signals are filtered with a 1-h lowpass filter. The color scale differs for the two years and varies with time from early April to mid-November. Lines show predictions calculated from Eqs.(5.8) and (5.9) for constant hydraulic radii and varying hydraulic pressure gradient (red lines) and for constant hydraulic pressure gradient and varying hydraulic radii (black lines). Blue shaded areas represent the period when Q is lower than 1 $m^3.s^{-1}$. Arrows show the direction of time and circled numbers refer to periods described in the main text. Reference values $(P_w)_{ref}$ and Q_{ref} are taken the first day of the 2017 melt-season (May 10th 2018).

Based on the condition proposed in Sect. 5.4 ($P-P_A > 2$ dB) we use the periods [May 14th - November 1st] 2017 and [April 21th - November 10th] 2018 to investigate the subglacial hydraulic properties (white and blue areas in Figs. 5.5 and 5.8). During these periods we subtract the mean winter diurnal pattern of P_A (defined between January 29th and April 4th 2018) from $P_{[3-7]\,Hz}$ to obtain P_w (Fig. S3). At the diurnal scale, because P_A can slightly vary from day to day depending on the anthropic activity (e.g higher anthropic activity during working days than holidays), the periods of very early and very late melt season are still strongly influenced by day-to-day changes in P_A. To study diurnal changes in P_w without being biased by anthropogenic noise we limit our analysis to the periods [May 15th - September 22st] 2017 and [May 27th - October 28th] 2018 (white areas in Figs. 5.5 and 5.8; based on direct observation shown in Fig. S3). Later in Sect. 5.5 we filter P_w with a 5-day lowpass filter (i.e. removing variability lower than 5 days) when inverting for the hydraulic properties. Doing so allows to study with confidence the early and late melt-season by reducing the influence of the diurnal variability in P_A on P_w while keeping sub-weekly variations in P_w and Q (see Fig. S4 for details).

Comparison of observations with predictions from Gimbert *et al.* (2016)

Analysis of seasonal changes

Seasonal scale observations and predictions of the subglacial channel-flow-induced seismic power P_w versus water discharge Q are shown in Fig. 5.6. We find that theoretical predictions from Gimbert *et al.* (2016) (red and black lines) are consistent with our observations (colored dots), which exhibit a general trend between that predicted at constant hydraulic pressure gradient (Fig. 5.6, see black lines calculated using Eq.(5.7)) and that predicted at constant hydraulic radius (Fig. 5.6, red lines calculated using Eq.(5.6)). As Q increases at the very onset of the melt season (in end of April), observed P_w-values follow the trend predicted under constant hydraulic pressure gradient (Fig. 5.6 ①). As Q increases more rapidly from mid-May to end of June (Fig. 5.5(b)), P_w follows a different trend of evolving hydraulic pressure gradient (Fig. 5.6 ②). The general trend from July to September is then dominated by changes in hydraulic radius (Fig. 5.6 ③). As Q decreases during the melt season termination, observed P_w values follow the trend of evolving hydraulic pressure gradient in a similar manner as during the early melt season (Fig. 5.6 ④). At the end of the melt season 2018 (Late October to November) our observations also show a trend of changing hydraulic radius although this observation is not as clear in 2017 (Fig. 5.6 ⑤). A clear counter-clockwise seasonal hysteresis of up to 10 dB power difference is observed in Fig. 5.6 between P_w and Q. This shows that for a similar water discharge, higher subglacial channel-flow-induced seismic power is generated in the late melt season compared to in the earlier melt season. The 10 m^3s^{-1} measurement threshold in Q is well observable for the two years but does not bias the observed scaling of changing hydraulic radius observed during summer.

Analysis of diurnal changes

Observations and predictions of the diurnal relationship between the subglacial channel-flow-induced seismic power P_w and water discharge Q throughout the melt season are shown in Fig. 5.7. We quantify the diurnal behaviors over the two melt seasons by calculating the hysteresis amplitude ϕ and time lag δt (see Sect. 5.4) and through comparing our observations with the theoretical predictions calculated for four selected days (panels (a) to (h) in Fig. 5.7). We selected these days based on three criteria: they represent typical variations of P_w and Q over their respective periods ($\sim \pm 5$ days around their date); they show that our observations capture diurnal variations from unique days without multi-days averaging; they give a pedagogical support for the reader to interpret values of the hysteresis amplitude ϕ and time lag δt shown in Fig. 5.7i. We focus on these two indicators as they allow to evaluate respective changes of P_w versus Q.

The seasonal evolution of the daily hysteresis amplitude ϕ presents two peaks in late-May / early-June and in late-August / early-September, which are consistently observed in both 2017 and 2018 (phases ① in Fig. 5.7(i)). The seasonal evolution of the diurnal time lag between δt of P_w to Q is similar to that of ϕ, with peak values at $\delta t > 2.5$ h in late-May / early-June and in late-August / early-September (Fig. 5.7(i)). This supports that hysteresis is mainly caused by phase difference between P_w and Q
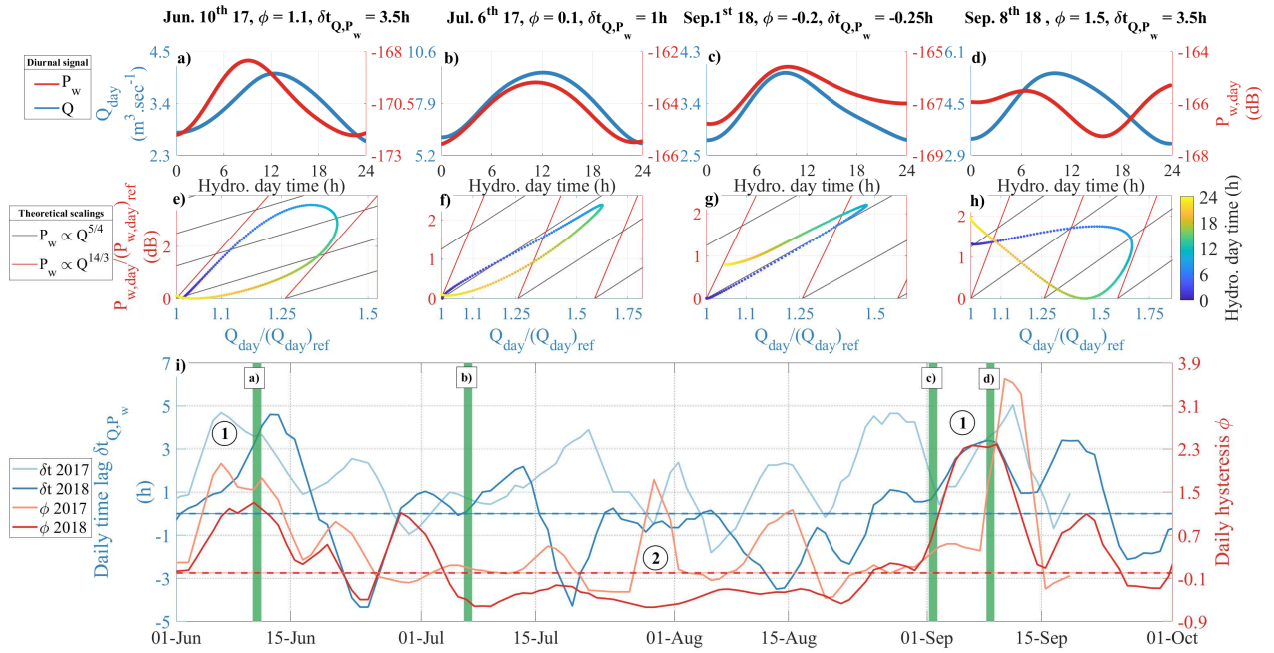
Figure 5.7: Diurnal observations of the subglacial channel-flow-induced seismic power P_w and water discharge Q and comparison with predictions from Gimbert *et al.* (2016). (a) to (d) Daily evolution of the [6-36] h bandpass filtered seismic power $P_{w,day}$(red line) and water discharge Q_{day} (blue line) for four selected hydrological days. Values of $P_{w,day}$ and Q_{day} are centered on the average respective absolute value of the corresponding day. Corresponding values of daily $\delta t_{Q,P_w}$ and ϕ are shown top of the panels. (e) to (h) Observed (colored dots) and predicted (red and black lines calculated with Eqs.(5.6) and (5.7)) P_w versus Q daily relationships. Note that y-axis bounds differs from panel to panel. Both variables are normalized by their daily minima. (i) Daily time lag $\delta t_{Q,P_w}$ between $P_{w,day}$ and Q_{day} peaks (blue lines) and daily hysteresis ϕ between $P_{w,day}$ and Q_{day} (red lines). Shaded lines are data of year 2017, plain ones of year 2018. Dashed lines show $\delta t_{Q,P_w} = 0$ (blue) and $\phi = 0$ (red). Timeseries are smoothed over 5 days. Green vertical bars show times of the four selected hydrological days with the corresponding panel number. Circled numbers refer to the two phases described in the main text.

rather than by asymmetrical changes P_w when Q rises compared to when Q falls Q (Sect. 5.4). The variability of δt over the season is much larger than the predicted 0.04 h instrumental time lag (see Sect. 5.4), such that its evolution represents real changes in the relationship between P_w and Q.

In the early and late melt season (phases ① in Fig. 5.7(i)), $P_{w,day}$ peaks, in average, more than 3 h before Q_{day} (e.g. Fig. 5.7(e)). These long time delay δt are concomitant to a pronounced asymmetrical shape in $P_{w,day}$ with a steeper rising than falling limb (e.g. Fig. 5.7(e)). This results to large clockwise hysteresis in $P_{w,day}$ versus Q_{day} as well pictured by the high hysteresis values during these periods ($\phi > 1$, phases ① in Fig. 5.7(i)). For example, on June 10th our observations follow the trend of evolving hydraulic pressure gradient in the morning and the one of changing hydraulic radius in the afternoon and at night. On September 8th our observations follow the trend of changing hydraulic radius in the early morning and the one of evolving hydraulic pressure gradient in the afternoon. On the contrary to these periods, in summer (phase ② in Fig. 5.7(i)), both ϕ and δt are low with $\phi \simeq 0$ and 2 h > δt > -2 h. At this time,

δt has a more pronounced seasonal and year-to-year variability than ϕ (Fig. 5.7(i)) with values oscillating within [2 ; -2] h and minimum values reaching $\delta t < $ -4 h. In July and August (e.g. panels (b) and (c) in Fig. 5.7), P_w peaks nearly at the same time as Q with $\delta t < 0.5$ h and with an almost symmetrical diurnal evolution (Fig. 5.7(i)). For both summer days (July 6th and September 1st), our observations mainly follow the trend of changing hydraulic radius throughout the whole day, with a non-null hysteresis that shows that hydraulic pressure gradient may also change. This two-phases seasonal evolution shows that the early and late melt season diurnal changes in Q cause a pronounced diurnal variability in the hydraulic pressure gradient and limited diurnal changes in the hydraulic radius, whereas over the summer channels show a more marked response to diurnal changes in Q through changes in hydraulic radius.

Inversions of changes in hydraulic radius and hydraulic pressure gradient

We invert for the relative changes of hydraulic radius $\frac{R}{R_{ref}}$ and hydraulic pressure gradient $\frac{S}{S_{ref}}$ using Eqs.(5.10) and (5.11) and our observations of timeseries of Q and P_w once filtered with a 5-day lowpass filter (see Fig. S4 and Sect. 5.5 for details). In the following for the sake of readability we use the notation R, S and V to refer to $\frac{R}{R_{ref}}$, $\frac{S}{S_{ref}}$ and the relative basal sliding speed $\frac{V}{V_{ref}}$. Reference values for these three variables are taken as their minimum value over the two years, which occur on May 10th 2017 for R, May 14th 2018 for S and March 28th 2018 for V.

Analysis of seasonal changes

The temporal evolution of R, S and V are presented in Fig. 5.8. We recall here that the changes in V can be considered as a good proxy for changes in water pressure in the subglacial cavity network (see Sect. 5.5 for details). We find that all three variables show a well-marked seasonal evolution, with low values during the early and late melt season and high values in summer. However, differences between R, S and V exist over the melt season. For both years, R starts increasing from the onset of the early melt season, until reaching a maximum within two months in late-June to early-July. R is then two times larger in average than in the early melt season. In contrast, during the first weeks of the melt season 2018, S rapidly decreases (Fig. 5.8 ①), concomitantly with an abrupt increase in V by a factor of 1.5 compared to winter. This shows that as the average water pressure rises in cavities and enhance sliding, channels on the contrary undergo depressurization. During the melt season 2017 we do not observe such behavior possibly because of a timeserie of P_w that starts about three weeks later than in 2018. The increase in S then occurs with a delay of about one month in 2018 and of about one week in 2017 compared to that in R, and S reaches a maximum in August (Fig. 5.8 ②). S is at that time on average five to six times larger than in the beginning of the melt season. As S increases, V and R have already past their summer maximum. Contrary to the conclusions obtained on the Mendenhall Glacier (Alaska) where S presents no significant trend over the two-month long investigated period
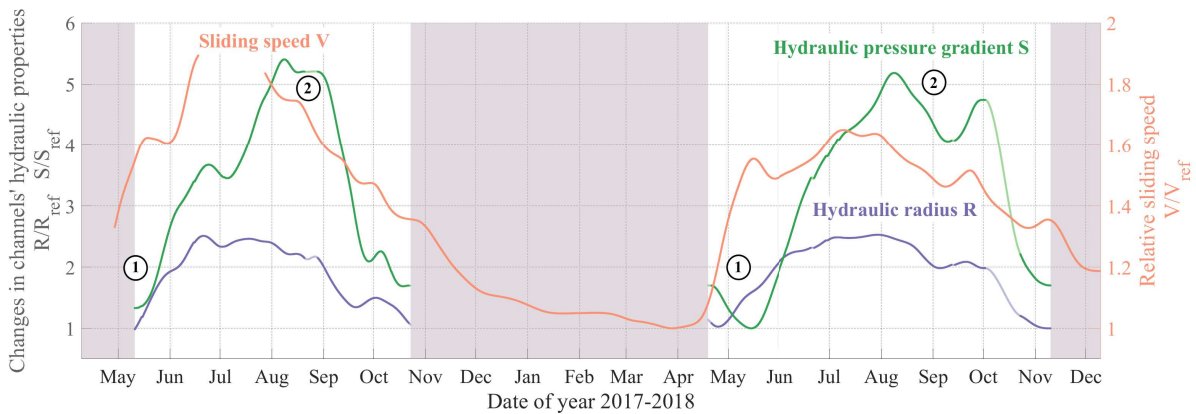
Figure 5.8: Seasonal evolution of the hydraulic radius and hydraulic pressure gradient as inferred from seismic observations as well as of glacier basal sliding speed as measured in-situ. (a) Relative hydraulic pressure gradient $\frac{S}{S_{ref}}$ (green line), relative hydraulic radius $\frac{R}{R_{ref}}$ (purple line) and relative sliding speed (orange line). Red shaded areas represent the winter season. Temporal signals of R and S are calculated using 5-day lowpass filtered timeseries of Q and P_w and are further smoothed applying a 30-day lowpass filter. Shaded lines correspond with period with no data and show interpolated values of R and S using a cubic spline interpolation. Reference values for the three variables are taken as their minimum value of the two years (i.e. May 10th 2017 for R, May 14th 2018 for S and March 28th 2018 for V). Circled numbers refer to the three phases described in the main text.

(Gimbert *et al.*, 2016), seasonal changes in water discharge at Glacier d'Argentière are inferred to cause changes in both R and S. From early to mid-September, R and S decrease concomitantly and reach their minimum in late October. The summer to winter transition is most pronounced for S, which decreases by about a factor of 4 within less than a month (September to October) while R decreases more gently.

Analysis of diurnal changes

Figure 5.9 describes how channel and cavity properties behave at the diurnal scale throughout the melt season. We quantify the diurnal behavior throughout the two melt seasons with the time lag δt between R and Q daily maxima, noted $\delta t_{Q,R}$, and between S and Q daily maxima, noted $\delta t_{Q,S}$. We also calculate the amplitude of the diurnal variations C_v for R, S and V (see Sect. 5.4 for definitions). In the same scopes as in Sect. 5.5 we illustrate in panels (a) to (d) in Fig. 5.9 the diurnal evolution of R and S for the same four selected days as in Fig. 5.7.

$C_v(R)$ and $C_v(S)$ both present seasonal variation, with maximum values being reached mid-summer. The amplitude of $C_v(S)$ is however up to three-times larger than that of $C_v(R)$ since $C_v(S)$ reaches up to 80 % in August while $C_v(R)$ only increases up to 30 % for (Fig. 5.9(f)). In contrast, the seasonal evolution of $\delta t_{Q,R}$ and $\delta t_{Q,S}$ drastically differs (Fig. 5.9(e)). On one hand, the temporal evolution of $\delta t_{Q,R}$ presents no marked changes throughout the season and generally remains within a range of ± 1 h (Fig. 5.9(e)) as highlighted by the four selected days (Figs. 5.9(a) to (c)). This shows that R and Q
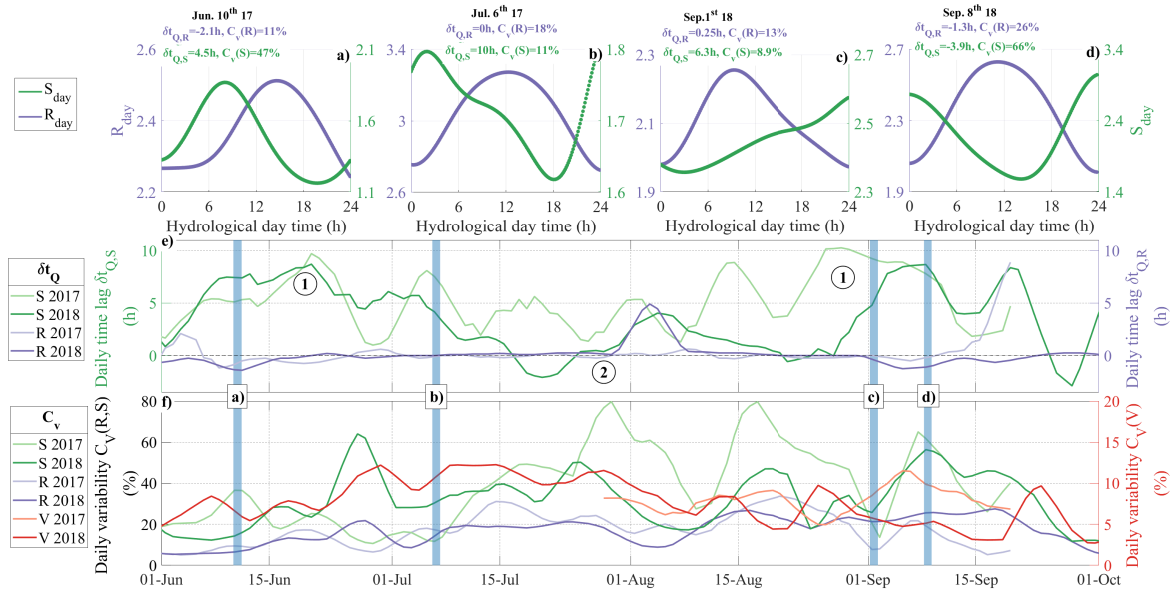
Figure 5.9: Diurnal evolution of the hydraulic radius R and hydraulic pressure gradient S and comparison to glacier dynamics. (a) to (d) Daily timeseries of R (purple line) and S (green line) for four selected hydrological days across the melt season. Timeseries are band-pass filtered within [6-36] h. Values of R_{day} and S_{day} are centered on the average respective absolute value of the corresponding day. Corresponding daily values of $\delta t_{Q,R}$, $\delta t_{Q,S}$, $C_v(R)$ and $C_v(S)$ are shown top of the panels. Note that y-axis bounds differ from panel to panel. (e) Daily time lags $\delta t_{Q,R}$ between R_{day} and Q_{day} peaks (purple lines) and $\delta t_{Q,S}$ between S_{day} and Q_{day} peaks (green lines). (f) Sub-diurnal variability C_v of R (purple lines), S (green lines) and the basal sliding speed V (red line). Timeseries are smoothed over 5 days. Blue vertical bars shows location of the four selected days with the corresponding panel. Shaded lines are data of year 2017, plain lines are data of year 2018. Circled numbers refer to the two phases described in the main text.

are consistently in phase on a diurnal basis throughout the melt season. On the other hand, the temporal evolution of $\delta t_{Q,S}$ presents average values of about 5 h with two peaks of $\delta t_{Q,S} > 8$ h in June and August (Fig. 5.9(e) ①) and a period of low values ranging within [0;5] h in mid-summer (Fig. 5.9(e) ②). These changes in S are clearly observed in the diurnal snapshots (e.g. Figs. 5.9(a) to (d)) that show a marked increase in hydraulic pressure gradient in the morning before the rise in hydraulic radius. Such a difference in diurnal dynamics between R and S shows that channels exhibit high hydraulic pressure gradients in the early morning time while their hydraulic radius grows slowly to reach its maximum at the same time as the water discharge does.

We also compare in Fig. 5.9(f) the diurnal dynamics of channel properties to the diurnal dynamics of the average water pressure conditions in cavities by comparing $C_v(R)$ and $C_v(S)$ with $C_v(V)$. Over the melt season, $C_v(V)$ exhibits a pattern that is similar to $C_v(R)$ and $C_v(S)$, with higher values observed for the three variables in summer (> 10 %) than during the early and late melt season (< 10 %). This shows that short-term variability in channels properties (i.e. R and S) correlates well with the short-term variability in average water pressure condition in cavities. From late August to mid-September 2017, we observe that $C_v(S)$ reaches up to 60 % over less than a week, followed c. a week later by a rapid rise in $C_v(V)$ (Fig. 5.9(f)).
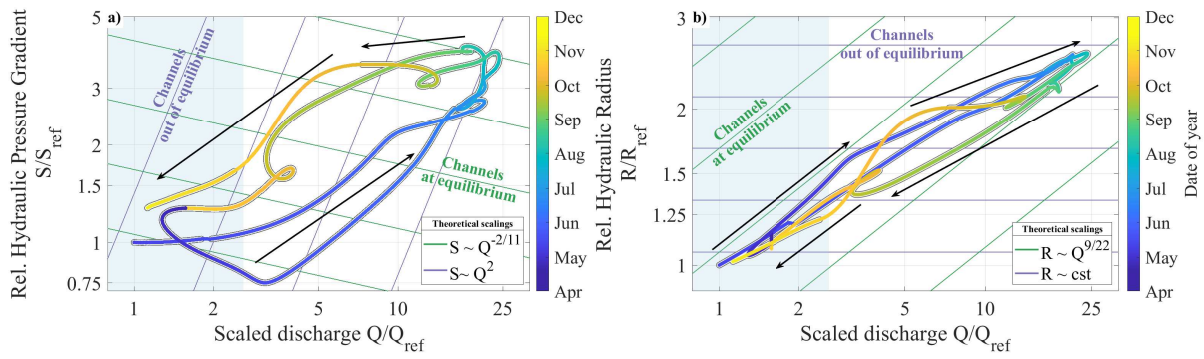
Figure 5.10: (a) Relative hydraulic pressure gradient $\frac{S}{S_{ref}}$ and (b) hydraulic radius $\frac{R}{R_{ref}}$ as inverted
from seismic observations and as shown as a function of measured relative water discharge
$\frac{Q}{Q_{ref}}$. Timeseries of R and S are calculated from 5-day lowpass filtered timeseries of Q and P_w,
and are then 30-day lowpass filtered (same as in Fig. 5.8). Timeseries of Q is 30-day lowpass
filtered. Reference values for all three variables are taken as the first day of the 2017 melt-
season (May 10th 2017). We compare our data to the predictions of Röthlisberger (1972) for
subglacial channels evolving at equilibrium with Q (green lines, $S \propto Q^{-2/11}$ and $R \propto Q^{9/22}$) and
for subglacial channels evolving through hydraulic pressure gradient changes only (blue lines,
$S \propto Q^2$ and $\frac{\delta R}{\delta Q} = 0$). Arrows show the direction of time. Blue shaded areas represent the period
when Q is lower than 1 m^3.s^{-1}. Line sections without the black edges show interpolated values
of R and S using a cubic spline interpolation as in Fig. 5.8.

Comparison of inversions with predictions from Röthlisberger (1972)

Our seismically derived S and R values are shown in Fig. 5.10 as a function of relative
changes in water discharge Q, along with scaling predictions calculated using the the-
ory of Röthlisberger (1972) assuming channels at equilibrium (melt rate equals creep
rate) with $S \propto Q^{-2/11}$ and $R \propto Q^{9/22}$ (Eqs.(5.14) and (5.12), green lines in Fig. 5.10) and
channels out-of-equilibrium that respond to changes in Q only through changes in S
with $S \propto Q^2$ and R is constant (Eq.(5.13), purple lines in Fig. 5.10). We find that R and
S generally exhibit variations with Q that lie between those expected for channels at
equilibrium and those expected for channels evolving at constant hydraulic radius. At
low discharge ($\frac{Q}{Q_{ref}} < 4$, $Q < 1$ m^3.s^{-1}) during the early and late melt season (Fig. 5.10
①) our derived changes in S and R with Q approach the theoretical prediction for
channels behaving at equilibrium. At high discharge ($\frac{Q}{Q_{ref}} > 4$, $Q > 1$ m^3.s^{-1}); mid-May
to early October, Fig. 5.10 ②) changes in S and R with changes in Q significantly de-
parts from predictions of channels at equilibrium and approaches the one of channels
evolving out-of-equilibrium through changes in S solely. The transition between the
two regimes herein observed is quite abrupt for S which switches from being a decreas-
ing to being an increasing function of Q. For R, the transition is marked by a weaker
dependency on Q as thi latter is high. During the period when $Q/Q_{ref} > 5$, best datafit
of R with Q gives $R \propto Q^{0.27} \propto Q^{6/22}$ and for the periods when $Q/Q_{ref} < 4$ it gives R
$\propto Q^{0.36} \propto Q^{8/22}$. This latter scaling is similar to the predicted scaling of $R \propto Q^{9/22}$ calcu-
lated using the theory of Röthlisberger (1972) assuming channels at equilibrium.

5.6 Discussion

Potential bias from changes in the number and position(s) of channel(s)

As stated in Sect. 5.2, the subglacial channel-flow-induced seismic power P_w depends on the number of subglacial channels N (Eqs.(5.10) and (5.11)) and on the source-to-station distance, which we both considered as constant in our analysis. Here we discuss how much potential changes in N and in channel(s) positions may bias our inversions of S and R. On one hand, given the glacier configuration in our study area (250 m thick, 500 m wide Fig. 5.2(a)), channels-to-seismic station distance is similar regardless of whether channels are located at the glacier center or on its sides. Therefore, we do not expect changes in channel spatial positions to bias our inverted values of R and S. On the other hand, we estimate how much the observed changes in P_w would require changes in N if they were to be explained only by an evolving number of channels rather than evolving S or R. From Eq.(5.10) we have that S weakly depends on N compared to on P_w and on water discharge Q. As a result, explaining the measured variations of P_w while imposing S constant would require N to change by more than 4 orders of magnitude ($5^{41/6}$), which is unrealistic. From Eq.(5.11) we have that R weakly depends on N compared to on Q. As a result, explaining P_w variations while imposing R as constant would require N to change by more than factor of 30 ($4^{-82/33}$), which is also likely unrealistic since at the onset of the melt season channels are expected to form an arterial network with few channels being kept over summer (Schoof, 2010; Werder *et al.*, 2013). Therefore, we do not expect potential changes neither in channel positions nor in N to cause significant bias in our inverted values of R and S.

Implications for inferring water discharge using seismic noise

As opposed to Gimbert *et al.* (2016) who inferred little variations in hydraulic pressure gradient over its two-month long period of survey on the Mendenhall Glacier, on Glacier d'Argentière we infer high and sustained channel pressurization over the whole summer and early fall (June-October). This has implications for the physics of subglacial channels, which we further discuss in Sect. 5.6, and also for our capacity to invert for discharge Q based on observed seismic power P. If one considers the equilibrium assumption over the melt season this yields, under Röthlisberger (1972) steady-state equilibrium assumptions, to the scaling $Q \propto P_w^{33/31}$ (see Eqs.(5.6) and (5.12)). When applied over the melt season using our observations of P_w at Glacier d'Argentière, this underestimates the measured discharge by more than 65%. As shown in Fig. 5.10, such assumption is only valid for the early and late melt season when both discharge and its variability are low. Using the approximation $Q \propto P_w^{33/31}$ may be more appropriate for periods of low melt water input and in settings with limited water input variability such as in Antarctica. If one now considers the empirical relationship $Q \propto P_w^{11/24}$ obtained from the period of channels being out of equilibrium (using Eq.(5.6) and $R \propto Q^{6/22}$, see Sect. 5.5), this leads to an uncertainty of less than 10% on the estimated water discharge over the melt season at Glacier d'Argentière. We therefore

suggest that the $Q \propto P_w^{11/24}$ relationship may be preferred for inverting discharge based on seismic observations during periods of high melt water input and in settings with strong seasonal variability in water input (e.g. Alpine and Greenland glaciers).

Implications for subglacial hydrology and ice dynamics

Understanding channels approaching equilibrium at low subglacial water discharge

During the early melt season ($\frac{Q}{Q_{ref}} < 4$, $Q < 1$ m^3.s^{-1}; Figs. 5.5 and 5.10) channels are inferred to approach an equilibrium situation for which hydraulic pressure gradient scales weakly with changes in subglacial water discharge (Fig. 5.10). This behavior supports that the channel's hydraulic capacity is sufficient to accommodate water input at this time of the year. We propose that, at those times, changes in water supply occur at a rate that is lower than that at which channels adjust their hydraulic radius. During the early melt season, low rates in water input changes are likely caused by water supply from melt being highly damped by the snow cover (Marshall *et al.*, 1994; Fleming and Clarke, 2005). During the late melt season ($\frac{Q}{Q_{ref}} < 4$; Fig. 5.10), the cause of low rates in water input is less clear. We suggest that such rates could be induced by englacial stored water being slowly released (Flowers and Clarke, 2002; Jansson *et al.*, 2003). Because of the well-developed drainage system at those times, channels could also adjust faster their hydraulic radius than during the early melt season and therefore could behave at equilibrium for higher rates in water input than during the early melt season.

Using periods when channels approach equilibrium to estimate channel(s) size and number

Using Eqs.(6) and (8) of Hooke (1984) that predict the conditions of equilibrium for steady-state channels and assuming that total discharge is equally distributed over channels of identical geometry (R-channels), we find that in our case equilibrium is predicted if the number of channels lies between 4 and 6 (using an ice thickness of 250 m, a down-glacier surface slope of 5 and a total water discharge of 1 m^3.s^{-1}; see Appendix Sect. 5.9). For a lower (resp. higher) number of channels, discharge per channel and thus channel-wall melt is higher (resp. lower) than the expected channel-wall creep, which violates the equilibrium condition. Our estimate of 4 to 6 channels is consistent with the numerical modelling results of Werder *et al.* (2013) of 4 to 5 dominant channels lying below the Gornerglestcher tongue (CH), a glacier which has a geometry similar to that of the tongue of Glacier d'Argentière (c. 500 m wide, c. 300 m maximum thickness). Further insights on the spatial evolution of the subglacial drainage system could be gained using seismic arrays to locate the source(s) of subglacial flow-induced-seismic noise (Lindner *et al.*, 2020).

We propose to estimate the absolute size of channels at the season initiation based on the channel number previously proposed. With 5 ± 1 channels and 1 m^3.s^{-1} equally distributed discharge, the average discharge per channel is of about 0.20 ± 0.05 m^3.s^{-1}

(uncertainty is obtained from that on channels number). Considering that subglacial flow-induced-seismic noise is likely sensitive to water flow speed on the order of 1 m.s^{-1} (Gimbert *et al.*, 2016) we can estimate a minimal channel cross-section area of about 0.20 ± 0.05 m^2, and a resulting channel radius of 0.35 ± 0.05 m (for semi-circular R-shaped channels). We note that absolute inversions of R and S could be done by explicitly formulating the Green function G in Eq.(5.1), and be compared to the present estimation using channels at equilibrium. However, this is beyond the scope of this study.

Understanding highly pressurized channels during the summer season

At water discharges higher than 1 m^3.s^{-1} (Fig. 5.5(b)) and relative changes in water discharge Q higher than 4 ($\frac{Q}{Q_{ref}}$ >4; Figs. 5.8 and 5.10)) the hydraulic pressure gradient S in channels remains high (Fig. 5.10). Considering that bed slope is constant, these high S-values require channels to be full and pressurized. During these periods of high discharge, as S increases with relative changes in Q (Fig. 5.10(a)) channels respond to changes in discharge in the same way as theoretically expected for cavities but not for channels by Schoof (2010). Such an behaviour is therefore opposed to the theoretical steady-state predictions of Schoof (2010) and Werder *et al.* (2013) that instead support that channels have a water pressure decreasing as they develop over the summer.

Using Hooke (1984) and our estimate of 5 channels made in Sect. 5.6, we find that in our case channel-wall melt (i.e. opening rate) is expected to dominate ice creep (i.e. closing rate) for $Q > 1$ m^3.s^{-1} (see Sect. 5.9 for details on the calculation). At steady-state this should either lead to channel growth and/or to an abrupt decrease in S down to free-flow situation (i.e. atmospheric pressure). These two scenarii are not observed during summer since R stays mainly constant (i.e. limited channel growth) and S presents high values supporting closed-flow over hourly timescales. We propose that the summer channel pressurization (high S) is due to channels responding to marked diurnal and short-term changes in water supply (as theoretically described in Schoof (2010)), and that channels behave out-of-equilibrium because changes in water input occur at a rate that is higher than that at which channels can adjust their hydraulic radius.

This interpretation is supported by our diurnal analysis on R and S evolution. In the morning, S is inferred to rise earlier than R (Fig.5.9), suggesting that channel-wall melt does not accommodate the increase of Q fast enough and causes pressurized flow. As water supply increases, channels start to respond to the water input and grow by channel-wall melt leading to a delayed hydraulic radius R increases compared to S (Fig. 5.9). At the same time the channel capacity increases with R (Röthlisberger, 1972) leading to a decrease in S before Q reaches a maximum as shown in Fig. 5.9. During the afternoon, as the water supply decreases, R slowly decreases by much less than a percent per hour (Fig. 5.9). At this rate, ice creep is capable to adjust changes in R fast enough in order to limit open channel-flow (Fig. S6). This could explain why S does not show an abrupt decreases down to the early melt season values as one would expect if open channel-flow occurs (Fig. 5.9). The hydraulic pressure gradient therefore builds

up from day-to-day over the summer. During night-time, as Q is at its minimum, the closure rate still adjusts channel size and therefore allows R to remain nearly constant through summer. This proposed scenario is consistent with both the investigated diurnal dynamics in the hydraulic properties and may explain the unexpected pressurized channels during summer. Estimation of melt and creep rates calculated from Hooke (1984) in a similar manner as in Sect. 5.6 supports the plausibility of such diurnal dynamics (see Appendix Sect. 5.9 for details). Further measurements remain to be conducted on glaciers with different geometries (e.g. flatter), different bed conditions (e.g soft bed glaciers) and different spatialization of water input (e.g. discrete water input through moulins) to evaluate the effect of such parameters on the subglacial hydrology dynamics. For instance, it is possible that our proposed channel's dynamic is limited to hard-bedded glaciers as soft-bedded glaciers have the capacity to store water and possibly damper the pronounced short term variability in water supply. In such setup, sediment erosion would complement ice wall melt and allow channels to be kept a much lower hydraulic pressure gradient than described in our study.

Channel dynamics, cavity water pressure and basal sliding

Our observations and subsequent analysis (Figs. 5.8 and 5.10) indicate that over the summer channels are pressurized and behave out-of-equilibrium. On the other hand, during summer the glacier sliding speed remain high, especially in 2018, (Fig. 5.5), which shows that the average basal water pressure (which is mainly set by pressure in cavities) is also high. These concomitantly high pressures in channels and in cavities suggest that the two systems may be well connected.

During summer, because of channel-flow pressurization, the channel-system does not operate under a significantly lower hydraulic potential than that of the cavity-system. This would therefore prevent significant water flow from cavities to channels, and leads to cavities that are kept pressurized. This sustained high water pressure at the glacier basis favors high glacier sliding speed over summer. Such channel-cavity-sliding link, has been previously suggested (Hubbard and Nienow, 1997; Andrews *et al.*, 2014; Rada and Schoof, 2018) but was not based on an independent analysis of the cavities and channels hydraulic conditions as we propose here through combining seismic and basal sliding speed measurements.

We suggest that during these periods of pronounced short-term variability in water supply, the whole drainage system becomes well-connected although with a limited drainage capacity. Thus the channel system may participate in maintaining high pressure in cavities and thus high sliding speed during periods of high water supply variability. Short-term variability in water supply may lead to pronounced glacier acceleration even during situations of a well-developed channel network. Such subglacial hydrology/ice dynamics link deserves further investigation through combination of seismic observations and subglacial hydrology/ice dynamics models (e.g. Gagliardini and Werder, 2018). Indeed a better understanding of the impact of short-lived water input on glacier dynamics is necessary as under climate warming short-term cli-

matic variability and extreme event occurrences are expected to increase (Hynčica and Huth, 2019), potentially causing greater glacier acceleration than previously thought (e.g. Tedstone *et al.*, 2015).

5.7   Conclusions

We investigate the physics of subglacial channels and its link with basal sliding beneath an Alpine glacier (Glacier d'Argentière, French Alps) through the analysis of a unique two-year long dataset made of on-ice measured subglacial water-flow-induced seismic power and in-situ measured glacier basal sliding speed. Our study shows that the theory of Gimbert *et al.* (2016) is consistent with our observations and that the analysis of the seismic power measured within the [3-7] Hz frequency range allows to study the subglacial drainage properties over a complete melt season and down to diurnal timescales.

We quantify temporal changes in channels' hydraulic radius and hydraulic pressure gradient using the theory of Gimbert *et al.* (2016) and measurements of water discharge concomitant to our seismic record. Our approach allows to isolate subglacial water-flow-induced seismic power from that of other seismic sources, and makes possible observing changes at various timescales (from seasonal to hourly) and water discharge ranges (from 0.25 to 10 $m^3.sec^{-1}$). At seasonal timescales we support, for the first time, that hydraulic radius and hydraulic pressure gradient both present at least a two-fold increase from spring to summer, followed by a comparable decrease towards autumn. Comparing our analysis to the theoretical predictions of Röthlisberger (1972) we identify that channel dynamics over the season is characterized by two distinct regimes yet unprecedentedly reported. At low discharge during the early and late melt season our analysis supports that channels respond to changes in discharge mainly through changes in hydraulic radius, and that the strong changes in hydraulic radius and weak changes in pressure gradient are similar to those predicted by theory for channels behaving at equilibrium. We propose that, at those times, changes in water input occur at a rate that is lower than that at which channels adjust their hydraulic radius. During the early melt season, these low rates in water input changes are likely caused by water supply from melt being highly damped by the snow cover. From this equilibrium channel-dynamics condition we are able to estimate the number of channels, which we find to be between 4 to 6, each channel having a radius of about 0.5 m in the early melt season that may go up to 2 m in summer. At high discharge and high short-term water-supply variability (often during summertime) we show that channels undergo strong changes in hydraulic pressure gradient, a behavior that is not expected for channels at equilibrium. Instead, those changes in hydraulic pressure gradient are well reproduced by theory under the end-member consideration of no changes in channel geometry in response to changes in water input. We propose that, at those times, channels behave out-of-equilibrium because changes in water input occur at a rate that is much higher than that at which channels adjust their hydraulic radius. This interpretation is supported by *R* and *S* behaviors at the diurnal scale, which show that channels pressurize in the early morning and depressurize in the afternoon as their hydraulic radius slowly grow concomitantly with the water sup-

ply rise. At night when water discharge decreases, ice creep then allows channels to recover their initial early morning hydraulic radius. We do not capture significant decrease of the hydraulic pressure gradient during those days, which indicates that the hydraulic pressure gradient builds up from day-to-day concomitantly to a hydraulic radius that is kept nearly constant. Channels may thus remain pressurized over the whole summer because of the short-term (diurnal, rain) variability in water supply, which forces channels to respond through a transient-dynamic state. We expect our analysis of subglacial hydrology to be applicable to glaciers of similar geometry (relatively steep U-shaped valley glaciers) and similar highly variable and distributed water supply than those of Glacier d'Argentière.

Channels behaving out-of-equilibrium during most of the melt season also has implications for the use of subglacial water-flow-induced seismic power P_w to invert for water discharge Q. The empirical relationship between Q and P_w that we derive during the period when channels are out-of-equilibrium allows estimating a water discharge from seismic noise with an error of less than 10 %, while an error of 65 % is obtained when assuming channels at equilibrium. Our presently proposed out-of-equilibrium relationship for inverting discharge could be applied in settings with strong seasonal variability in water supply (e.g. Alpine and Greenland glaciers). During summer we also observe high and sustained basal sliding, supporting that the widespread inefficient drainage system (cavities) is likely pressurized. We propose that channels being also pressurized may help sustain high pressure in cavities and thus high glacier sliding speed.

These results demonstrate that on-ice passive seismology is an efficient tool to overcome the classical observational limitations faced when investigating subglacial hydrology processes. In this respect, our results bring new constraints on channels physics, on links between channels, cavities and sliding, and on the use of passive seismology to invert for subglacial water discharge. In the future, an essential step towards strengthening our knowledge on the physics of subglacial processes would be to assess the applicability of our findings over a wider range of glacier geometries (e.g. soft bed glaciers and ice sheets) both through extended on-site seismic survey and the use of our seismically-derived observations as constraints for subglacial hydrology/ice dynamics models.

Codes and data availability

Timeseries of of physical quantities shown in Figs. 5.5 and 5.8 can be found at `https://doi.org/10.5281/zenodo.3701520`. The complete dataset will be made publicly available in the future. Ongoing work is taking place to meet the format and documentation required for the release for the complete seismic survey, which is expected to happen fully or partially by mid-2021. In the meantime, it is available on request from the corresponding author. The Python and SAC codes for seismic power calculation are given in the Supplementary Materials and additional codes can be found at `https://doi.org/10.5281/zenodo.3731508`.

5.8 Appendix

Frequency content of Q and P_w

We show in Fig. 5.11 the power spectrum of the water discharge Q (blue lines) and subglacial channel-flow-induced seismic power P_w as a function of the period. We observe for both variables a well-defined peak at one day and 12 h period. This shows that these signals present a clear diurnal and sub-diurnal variability, and supports our choice to band-pass-filter these signals within [6-36] h to study these short-term variabilities.
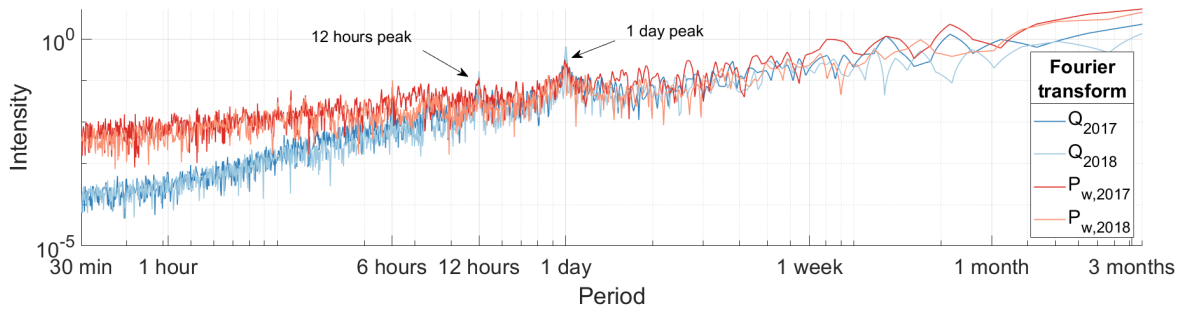

Figure 5.11: Power spectrum of the water discharge Q (blue lines) and subglacial channel-flow-induced seismic power P_w (red lines) shown a function of the period. Both axis are in logarithmic scale (1 over the frequency.)

Evaluating theoretical melt and creep rates with Hooke (1984)' equations

We used in this study the equations 6 and 8 of Hooke (1984) to evaluate the theoretical melt rate $\dot{m}$ and creep rate $\dot{r}$, as follows

$$\dot{m} = C_2 Q^{3/5} sin(\beta)^{6/5}, \tag{5.18}$$

$$\dot{r} = C_3 \frac{Q^{2/5}}{sin(\beta)^{1/5}} H^3, \tag{5.19}$$

with H the ice thickness, β the down-glacier surface slope, C_2 and C_3 constant. We use the values of Hooke (1984) for the two constants: $C_2 = 3.731e^{-5}$ m$^{-4/5}$ s$^{-2/3}$ and $C_2 = 5.71e^{-14}$ m$^{-16/5}$ s$^{-3/5}$. For the glacier geometry we use using an ice thickness of 250 m and a down-glacier surface slope of 5.

5.9 Supplementary Materials

Seismic power methodology

Temporal reconstruction

We show in Fig. 5.12 the seismic stations used to reconstruct the 'virtual station' seismic power . The overlapping period of mid-October 2017 is used to adjust, over a 10 days time window, the GDA seismic power to the ARG.B01 seismic power. The overlapping period of mid-June 2018 is used to adjust, over a 9 days time window, the ARG.B02 seismic power to the ARG.B01 seismic power.
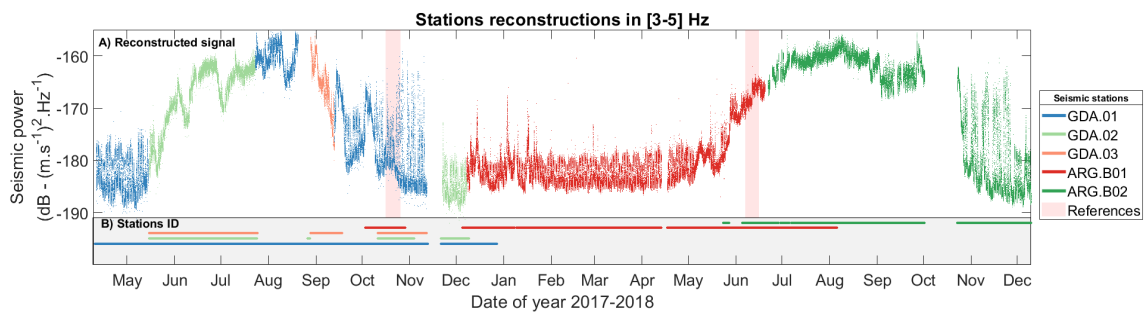

Figure 5.12: Time series of the corrected and assembled seismic power within the [3-5] Hz frequency range. We used this range to assemble the five stations seismic signals and apply the baseline shifts. Color coding refers to the corresponding stations and stations period of activity are shown in the light grey horizontal band. Light red vertical bands show the period used to constrain the baseline shift.

Evaluating instrumental bias in δt interpretation

The subglacial channel-flow-induced seismic power P_w comparison between the different stations of our seismic network (Fig. 2) is shown in Fig. 5.13. We do not observe a significant time lag (< 5 min) between P_w measured at 2 stations 200 m appart (GDA.02 and GDA.03). It is important to note that this lag time δt_{inst} does not directly correspond neither to the water transit time, nor to the water flow speed between our instruments. This effect is mainly related to the seismic waves properties when propagating within the glacier. Our analyses is important for the intra-diurnal time scale, because this means that if Q and P_w are out of phase by more than δt_{inst} = 15 min (because Q measurement is done 600 m away from the seismic station) then this delay expresses subglacial hydraulic properties.

Evaluating the potential bias from impulsive events contribution to seismic power

Over alpine glacier, impulsive events can be of diverse origins from serac falls (Roux *et al.*, 2008), crevasses opening (e.g. Neave and Savage, 1970; Lindner *et al.*, 2020), hydraulic fracturation, microseismicity linked with water discharge (Iken and Bindschadler, 1986; Preiswerk and Walter, 2018) or even basal stick-slip events as recently
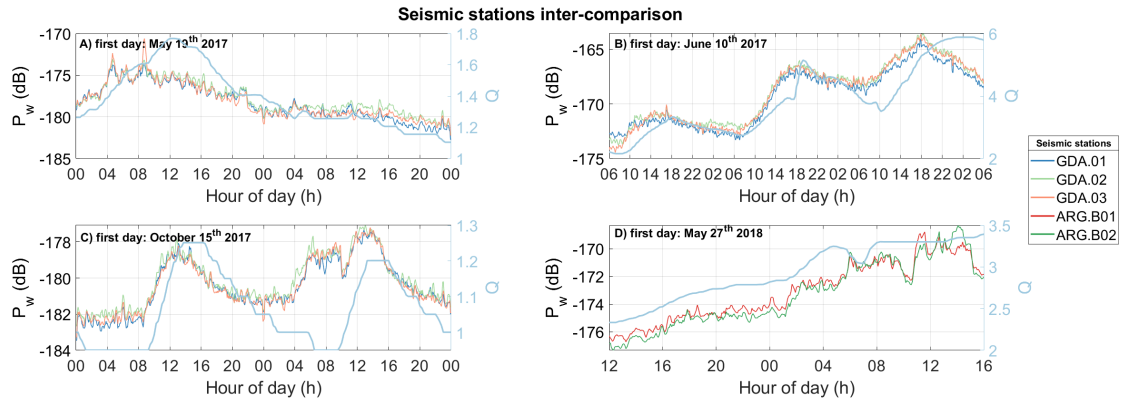
Figure 5.13: Time series of the measured seismic power within [3-7] hz at the different stations. (a) and(b) for the GDA network and (c) and (d) for the ARG network. Measurement is smoothed over 15 minutes, with one point every 15 minutes.

shown on Glacier d'Argentière by (Helmstetter *et al.*, 2015b). It is crucial to limit the influence of such impulsive events when aiming to study the subglacial channel-flow-induced seismic power. With respect to water tremor, impulsive events are characterized by short time-scale amplitude burst above the noise level by up to several order of magnitude. An important parameter for the Welch method is the time period dt over which we compute the Fourier transform FT. The seismic power P is calculated as $P = 10 \times log10\left[\left(\frac{FT}{dt}\right)^2\right]$. The longer dt, the greater number of impulsive events have the chance to occur. And the more the impulsive events within dt, the more they influence P and hidden the turbulent water flow source. The size of this window is limited by the frequencies investigated. To limit the impulsive events influence and still be able to investigate a frequency range down to 1 Hz we have chosen for our study a $dt = 2$ sec.

I show in Fig. 5.14 the influence of the chosen time window for the PWelch's analysis on the seismic power. In order to focus on background noise and limit the influence of impulsive events I tested the influence of the time windows over which I calculate the seismic power. For low frequency we observe that the seismic power in December/-January is greatly influenced by the time window, with much higher seismic power for long time window. This is because at this time numerous stick-slip events occur due to snow loading, and that these events contribute to the seismic power. The longer the time window, the more these events contribute and this support our choice of 2 sec time windows to focus on the background noise.

Evaluating the anthropogenic signature influence on sub-diurnal timescales

Because the anthropogenic noise power presents a well-marked diurnal variability that could bias the analyses of the P_w analyses, we determine, from visual inspection in Fig. 5.15, the period during which P_w dominates the seismic power as averaged within [3-7] Hz frequency range. In Fig. 5.16 we show how a 5 day-lowpass filter allows us to study the mutliday variations of the seismic power while limiting the influence of the daily variations in the anthropogenic influence. We filter P_w to increase the influence of the multiday variability with respect to the short term variability.
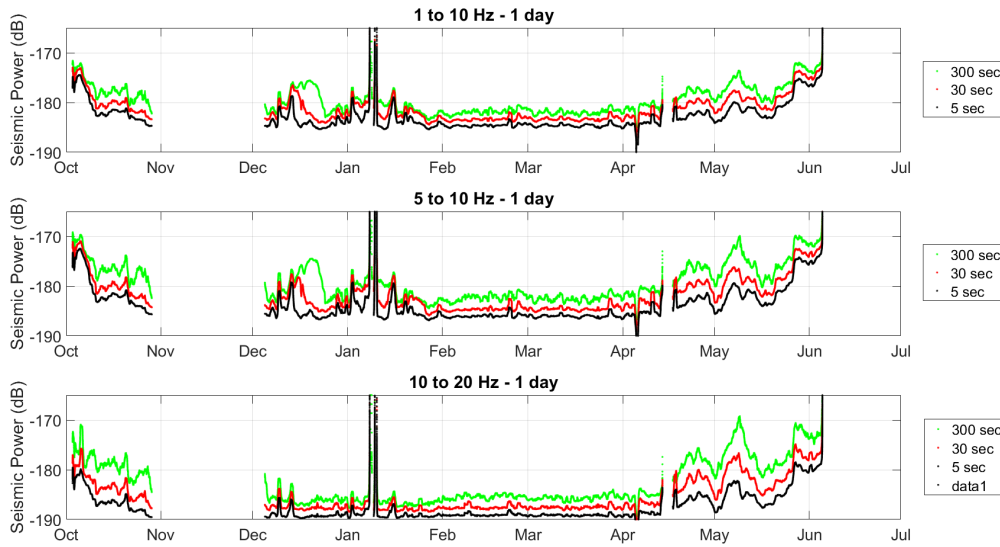
Figure 5.14: Influence of the time window used to calculate the seismic power as a function of the frequency. Seismic power is then averaged over 1 day for visual representation.

Evaluating the spatial sensitivity of the seismic record

During their journey from the source to the seismic station, seismic waves are attenuated. This behavior is related to energy dissipation within the propagation medium, here the ice, and because the higher the source to station distance, the larger the traveling distance and the thus lower the signal energy is. The attenuation of a signal with an amplitude of P_0 is defined a:

$$P_d = P_0 \frac{1}{d^n} e^{-\frac{2\pi d f}{v_c Q}}, \tag{5.20}$$

with d the distance from the source, n the geometrical exponent with $n=1$ for surface waves and $n=2$ for body waves, f the considered frequency, v_c the waves propagation velocity and Q the quality factor. The higher Q the more dissipative the medium is. Numerous values of Q have been proposed for alpine glacier ice within our frequency range, from $Q=6\pm1$ when considering only the uppermost glacier ice (first meters, Gusmeroli *et al.*, 2010) up to $Q=70$ for the 100 to 500 m layer (Kohnen, 1969). For our investigation we cover $Q = [5, 20, 60, 100]$. We seek here to quantify the area around our seismic stations that can contribute within a certain energy, here 10 dB, to the measured seismic power P. We investigate two cases with a closest source S_1 located at d_1 = 1 and $d_{1'}$ = 200 m from the sensor. The former would represent a surface source, the latter a basal one at the glacier basis. We then searched for the distance $d(S_1,S_2)$ between the closest source S_1 and a second one S_2 where $P_{S_1} - P_{S_2} = 10$ dB. This threshold value represent a relative value of 10% with respect to energy emitted from S_1 with no consideration of the absolute energy.

Figure 5.17 (a) shows that with respect to a surface source S_1 located at 1 m from the sensor, only the sources within a 10 m radius area will contribute to the [3-7] Hz signal energy by 10 dB, 10%, with respect to S_1. This area is reduced for increasing
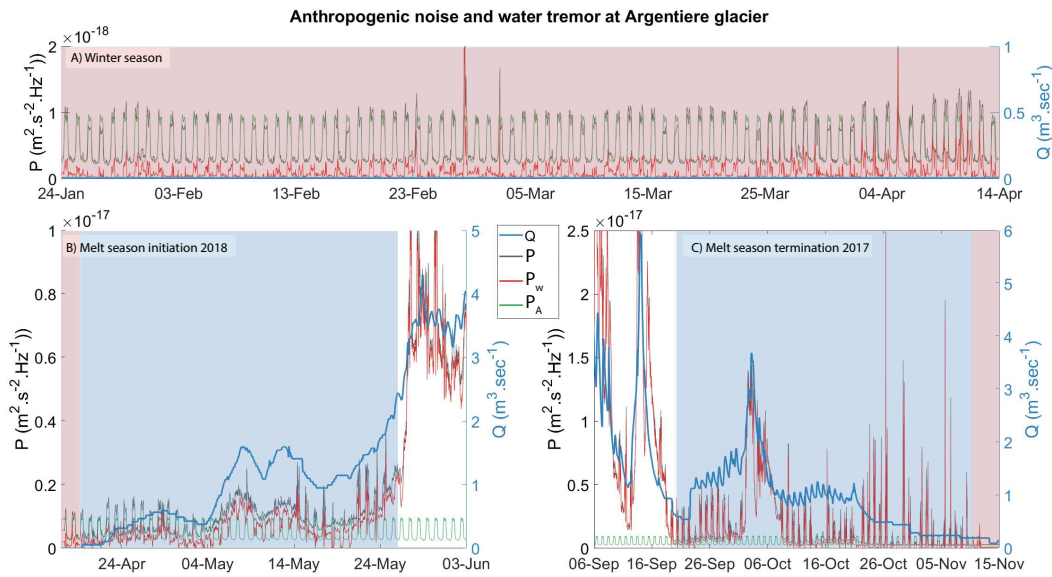
Figure 5.15: Time series of the measured seismic power (P, grey line), the daily-fitted anthropogenic noise seismic power (P_A, green line), the computed water tremor($P_w = P - P_A$, red line) and the measured water discharge (Q, blue line). The three periods (a) winter season, b) melt season initiation and c) melt season termination) presented are key to characterize the relative contributions of P_A and P_w to P. Shaded blue area represents the hydrological winter period where $Q<Q_{lim}$, light shaded blue area represents the period where the diurnal anthropogenic spectral is too pronounced to study P_w on a daily basis. x and y axis scale are not correspondant between the panels.

frequencies and quality factor. When we consider a source located at the glacier basis (Fig. 5.17 (b)), we observe that all sources within 500 to 1500 m from the sensor would contribute to the [3-7] Hz signal energy by 10%. The frequency and the quality factor effect is now dominated by the exponential decrease from equation 5.17. These results shows that if we consider water tremor signal within [3-7] Hz, a quality factor of $Q=20$, and a closest source at the glacier base then the measured signal will be dominated by sources located within a radius of 800 m from our sensor.

Theoretical channel properties

Evaluating theoretical channels dynamics with Röthlisberger (1972)' equations

In his paper, Röthlisberger (1972) proposes the two following equations for steady-state channels at equilibrium:

$$4R^2 = \left(\frac{2^{4/3}\rho_w g}{\pi^2}\right)^{3/8} k^{-3/4} Q^{3/4} \left(\frac{dp}{dx}\right)^{-3/8} \tag{5.21}$$

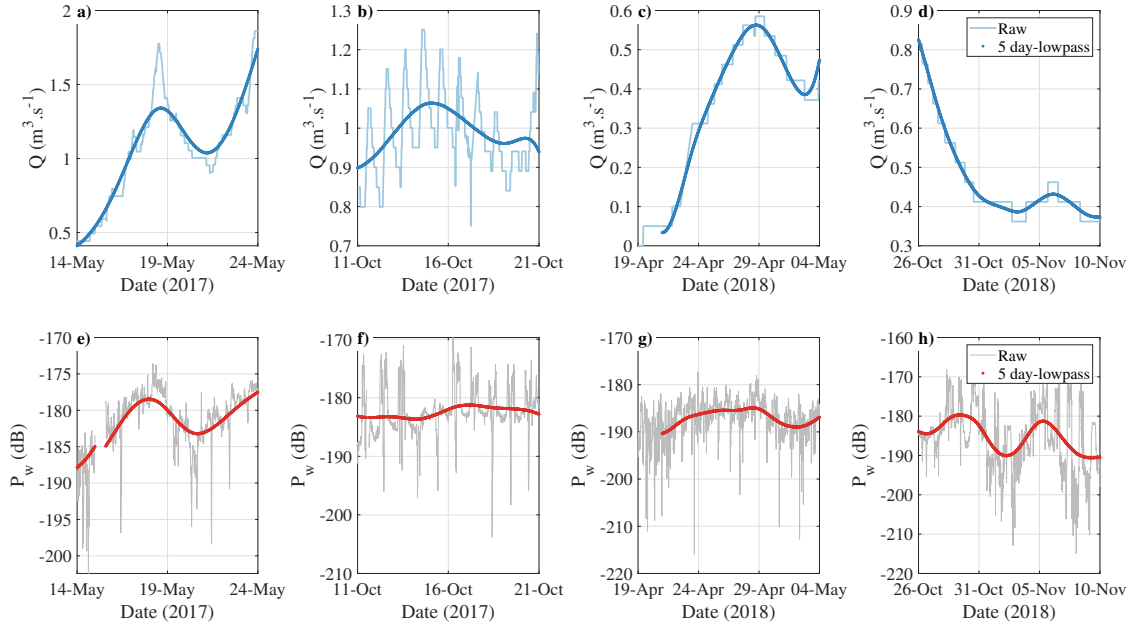$$\frac{dp}{dx} = Bk^{-6/11}(nA^{-8n/11}Q^{-2/11}(P-p)^{8n/11}), \tag{5.22}$$

Figure 5.16: (a) to (d) Time series of the measured water discharge Q at a 15 min time step (shaded blue line) and the 5 day-lowpass filtered Q (dark blue line) for the tips of both 2017 and 2018 melt seasons. (e) to (h) Time series of the subglacial induced seismic power P_w at a 15 min time step (shaded grey line) and the 5 day-lowpass filtered Q (dark red line) for the tips of both 2017 and 2018 melt seasons.

with $\frac{dp}{dx}$ the hydraulic pressure gradient S, P the cryostatic pressure, k the channel roughness, B equals to constant, A and n ice flow parameters. Taking equation 5.22 and considering constant effective pressure $(P\text{-}p)$ and flow parameters leads to

$$S \propto Q^{-2/11}.$$

Now inserting equation 5.22 in 5.21 and considering constant channel roughness, leads to

$$R^2 \propto Q^{3/4}\left(Q^{-2/11}\right)^{-3/8},$$
$$R^2 \propto Q^{66/88}Q^{6/88},$$
$$R^2 \propto Q^{9/11},$$
$$R \propto Q^{9/22}.$$

For a steady-state channel not in equilibrium with Q that responds solely through changes in S this leads to

$$S^{3/8} \propto Q^{3/4},$$
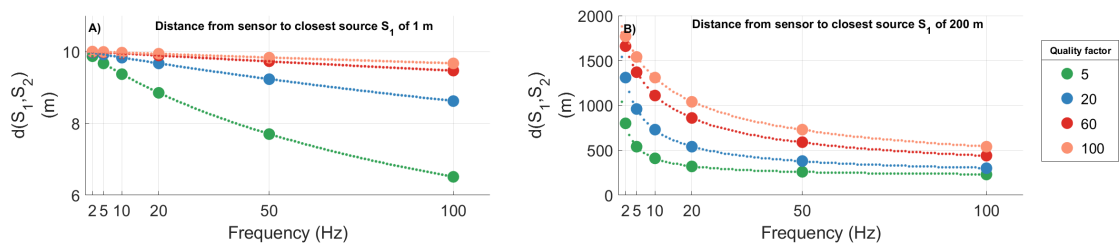$$S^{3/8} \propto Q^{6/8},$$
$$S \propto Q^2.$$

Figure 5.17: Synthetic effect of attenuation on seismic surface wave ($n=1$). The two panels show the distance $d(S_1, S_2)$ of a source S_2 to the closest source S_1 where the attenuation is such that $P(S_1)_{sensor} = (S_2)_{sensor} + 10$ dB depending on the frequency and the quality factor. This distance represents the radius of source location within which any given source will contribute for at least 10% to the recorded seismic power with respect to a source located at distance of 1 m (left panel) and 200 m (right panel) from the sensor.

Evaluating theoretical melt and creep rates with Hooke (1984)' equations

We use here equations 6 and 8 of Hooke (1984) to evaluate the theoretical melt rate $\dot{m}$ and creep rate $\dot{r}$, which are as follows

$$\dot{m} = C_2 Q^{3/5} sin(\beta)^{6/5}, \tag{5.23}$$

$$\dot{r} = C_3 \frac{Q^{2/5}}{sin(\beta)^{1/5}} H^3, \tag{5.24}$$

with H the ice thickness, β the surface slope, C_2 and C_3 constant. We use the values of Hooke (1984) for the two constants: $C_2 = 3.731e^{-5}$ m$^{-4/5}$ s$^{-2/3}$ and $C_2 = 5.71e^{-14}$ m$^{-16/5}$ s$^{-3/5}$. We show in Fig. 5.18 the theoretical channel growth rate for a R-channel at steady state. Calculations are made following Eqs.(5.24) and (5.23). The equilibrium condition, melt rate equals creep rate, is verified when the channel growth rate equals zero. This shows that for a given glacier geometry (slope an thickness), the equilibrium condition depends only on the water discharge. The more the channel number, the less the discharge per channel for a given output discharge and therefore the longer the equilibrium condition can be satisfied.

We show in Fig. 5.19 the synthetic closure rate of an open channel and compared it to the observed channel radius changes, assuming that the hydraulic radius changes equals the channel radius changes. Our comparison show that for the observed range of channel radius changes (5 to 10 %) the channel response time is of about a couple of hours. Therefore channel could creep fast enough at sub-diurnal timescale to equilibrate channel growth by melt.

We estimate melt and creep rates using equations 6 and 8 of Hooke (1984) as here above. From mid-May to early July, hydraulic radius R increases by a factor of 3 to 4. For constant number of channels, this results in summer channels radius of [1.00 - 1.25] m. Over the summer R varies by 4 to 8 % on a daily basis, which corresponds to diurnal changes of [4 - 10] cm.day^{-1} in channel radius. Such changes are on the same order of magnitude as those calculated with Hooke (1984) equations which predict a
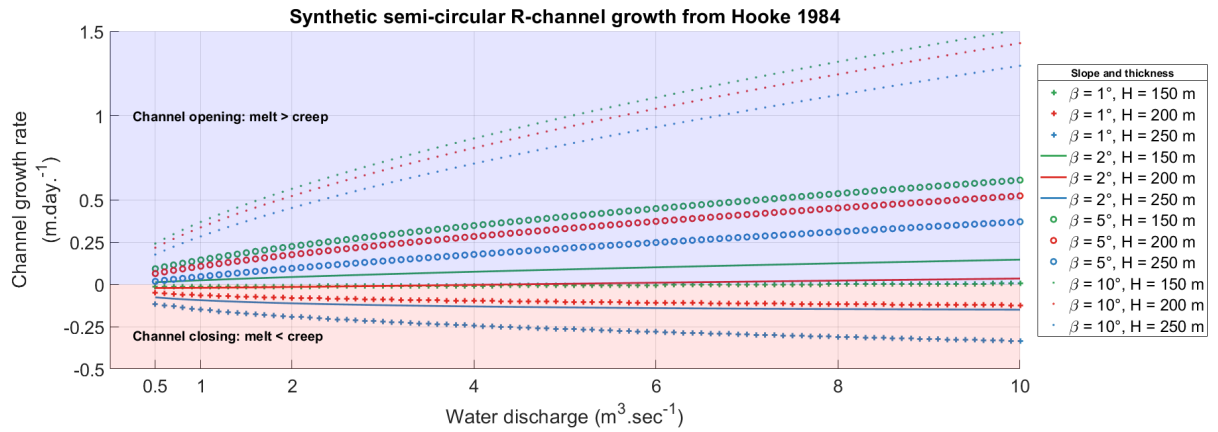
Figure 5.18: Synthetic evolution of a semi-circular shaped R-channel. Melt ($\dot{m}$) and creep ($\dot{r}$) rate are calculated from Eqs.(5.24) and (5.23) of Hooke (1984) with the constants C_2 and C_3 as in Hooke (1984), the slope and the ice thickness are shown in the legend. The curves show $\dot{m} - \dot{r}$, with the shaded blue area $\dot{m} > \dot{r}$ and the shaded red area $\dot{m} < \dot{r}$.

melt rate of about [10-25] cm.day^{-1} and creep rate of about [5-20] cm.day^{-1} for these periods ($Q \propto 5$ m^3.sec^{-1}). This shows that subglacial channels have the capability to adjust their size on a daily basis in response to water input variability. Channels can thus rapidly close during the water discharge decrease and possibly keep a closed-flow behavior over summer. This supports the plausibility of the channels' diurnal dynamic proposed previously based on our observations.

Author contribution

U.N., F.G. and C.V. designed the study. U.N. performed the seismic analysis with input from F.G. and F.W.. U.N. interpreted the results with input from F.G.. U.N. led the writing of the paper and F.G., C.V., F. W. and D. G. contributed to it. L.P and L.M were in charge of the basal sliding speed measurements. All authors participated to field installations.
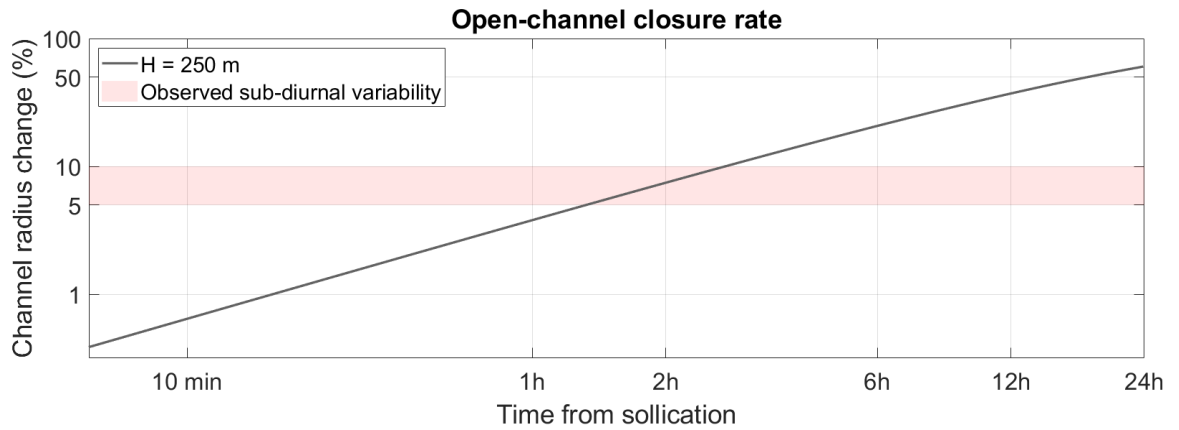
Acknowledgements

Figure 5.19: Synthetic closure rate of an open-channel computed for a channel size $R(t) = R_0 e^{(-c\sigma_i^n t)}$, with $R(t)$ the channel radius through time, R_0 the initial channel size, $c = 1e^{-24}$ Pa^{-3}.s^{-1} the ice viscosity (Cuffey and Paterson, 2010), $n = 3$ the Glen's flow constant (Cuffey and Paterson, 2010) and $\sigma = \rho_i g h_i$ with $\rho_i = 900$ kg.m^{-3} the ice density, $g = 9.81$ m.s^{-2} the acceleration due to gravity and $h = 250$ m the glacier thickness. The time is defined with $t = 0$ the moment when channel become open (free flow) and the change are expressed in % with respect to the initial size, 10% being $R(t) = R_0 \times 0.9$. Shaded red area shows the observed sub-diurnal variability in hydraulic radius at Glacier d'Argentière during summer of years 2017 and 2018.

Table 5.1: Summary of all variables, physical quantities, and mathematical functions used in the main text.

Variable/Symbol[a]	Description	Units	Reference[b]
F	Frictional force generated by turbulent water flow	N	Eq. 5.1
x_0	Seismic source location		Eq. 5.1
x	Source-to-sensor distance	m	Eq. 5.1
U	Ground velocity	m.s^{-1}	Eq. 5.1
t	Time	s	Sect. 5.2
G	Displacement Green's function		Eq. 5.1
T	Time period of the seismic signal	s	Eq. 5.2
f	Frequency of the seismic signal	Hz	Eq. 5.2
dt	Time duration of Welch's window to calculate seismic power	s	Sect. 5.4
P	Seismic power	dB[c]	Eq. 5.2, Figs. 5.4 and 5.3
$P_{[3\text{-}7]\,\text{Hz}}$	P as averaged within the [3-7] Hz frequency range	dB	Fig. 5.5
P_w	Seismic power induced by turbulent water flow	dB	Eq. 5.3, Figs. 5.3 and 5.9
P_A	Anthropogenic noise	dB	Sect. 5.4, Fig. 5.3
V_w	Water flow velocity	m.s^{-1}	Sect. 5.2
u_*	River/channel bed shear velocity	m.s^{-1}	Eq. 5.3, Fig. 5.1
W	Water conduit width	m	Eq. 5.3
H	Water flow depth	m	Eq. 5.3
k_s	Conduit wall roughness size	m	Eq. 5.3
β	Function of conduit shape and fullness		Eq. 5.4
n'	Manning's coefficient		Sect. 5.2
g	Gravitational acceleration	m.s^{-2}	Sect. 5.2
Q	Subglacial water discharge	m.s^{-3}	Eq. 5.5, Figs. 5.5 and 5.9
R	Hydraulic radius		Eq. 5.11
	Relative hydraulic radius from Sect. 5.5 on		Eq. 5.11, Figs. 5.8 and 5.9
S	Hydraulic pressure gradient		Eq. 5.10
	Relative hydraulic pressure gradient from Sect. 5.5 on		Eq. 5.10, Figs. 5.8 and 5.9
N	Number of subglacial channel(s)		Eq. 5.4
V	Glacier basal sliding speed	mm.h^{-1}	Figs. 5.5, 5.8 and 5.9
S_r	Anthropogenic noise quantificator		Sect. 5.4, Fig. 5.3
X_{day}	Any variable X bandpass filtered within [6-36] h		Eq. 5.15, Figs. 5.9 and 5.7
$(X_{day})_{max}$	Daily maximum of a given variable X	dB	Eq. 5.17
$\delta t_{Q,X}$	Time lag between $(Q_{day})_{max}$ and $(X_{day})_{max}$	h	Eq. 5.17, Figs. 5.9 and 5.7
$C_v(X)$	Coefficient of diurnal variation of a given variable X	%	Eq. 5.15, Fig. 5.9
$(P_{w,day})_{rising}$	P_w during the daily increase in Q	dB	Eq. 5.16
$(P_{w,day})_{falling}$	P_w during the daily decrease in Q	dB	Eq. 5.16
ϕ	Daily hysteresis between P_w and Q		Eq. 5.16, Fig. 5.7
X_{ref}	Reference state of a given variable X at a reference time		Eqs. 5.10 and 5.11
			Figs. 5.6, 5.7, 5.8, 5.9 and 5.10

(a) First section lists variables characterizing the propagation of seismic wave, second section lists variables characterizing the seismic power properties, third section lists variables and constants related the physical properties of river flow, fourth section lists variables characterizing the hydraulic and glaciological properties of the subglacial drainage system and fifth section lists the indicators defined to investigate subglacial water flow properties.

(b) Relevant occurrences in the main text of the variables, physical quantities, and mathematical functions.

(c) Decimal logarithmic relative to (m.s^{-1}) ^{2}.Hz^{-1}.

Outlook: storms and erosion

While investigating temporal variations in the seismic power induced by turbulent water flow at Glacier d'Argentière I came across very interesting observations that I could not present in our Nanni *et al.* (2020) paper. In this paper I indeed focused on the seasonal and diurnal variations and on inverting subglacial hydraulic properties at such timescales. I take the opportunity of this manuscript to present two other aspects that I deem of great interest.

6.1 Using storm events to investigate subglacial hydrology and glacier dynamics

While I focused on diurnal and seasonal timescale in Nanni *et al.* (2020) there is a third timescale that hosts strong variations in water supply but that is not caused by surface melting but by abrupt precipitations. Storms events can last from few hours to couple of days and cause abrupt changes in glacier velocities. Studying those events could yield to key insights on short term responses of basal sliding to changes in subglacial drainage system. In addition, those events can potentially induce very rapid changes in the stress at the glacier basis, and such changes could favor seismogenic process such as stick-slip. Passive seismology could be used in two manners, the first by looking at the properties of the sub glacial drainage system (changes in pressure and drainage efficiency) the second by looking at the seismic activity.

Starting from summer 2017 to fall 2020 we have acquired on Glacier d'Argentière a series of measurements including basal water pressure, surface velocity, sliding velocity, internal deformation, water discharge, meteorological conditions and of course seismic measurements. We will soon have more than 3 years' seismic measurements on Glacier d'Argentière, and a quick analysis show that I could isolate up to 15 storms events that trigger changes in seismic power, water discharge and glacier dynamics. I aim in a near future at putting together all the physical quantities we measured during those storms and also collaborate with Agnès Helmstetter, that investigated numerous stick-slip events in the past (Helmstetter *et al.*, 2015b). The aim would be to investigate how such rapid changes in water input influence the basal condition both in terms of stress (changes in velocities and stick-slip activities) and in terms of subglacial hydrol-
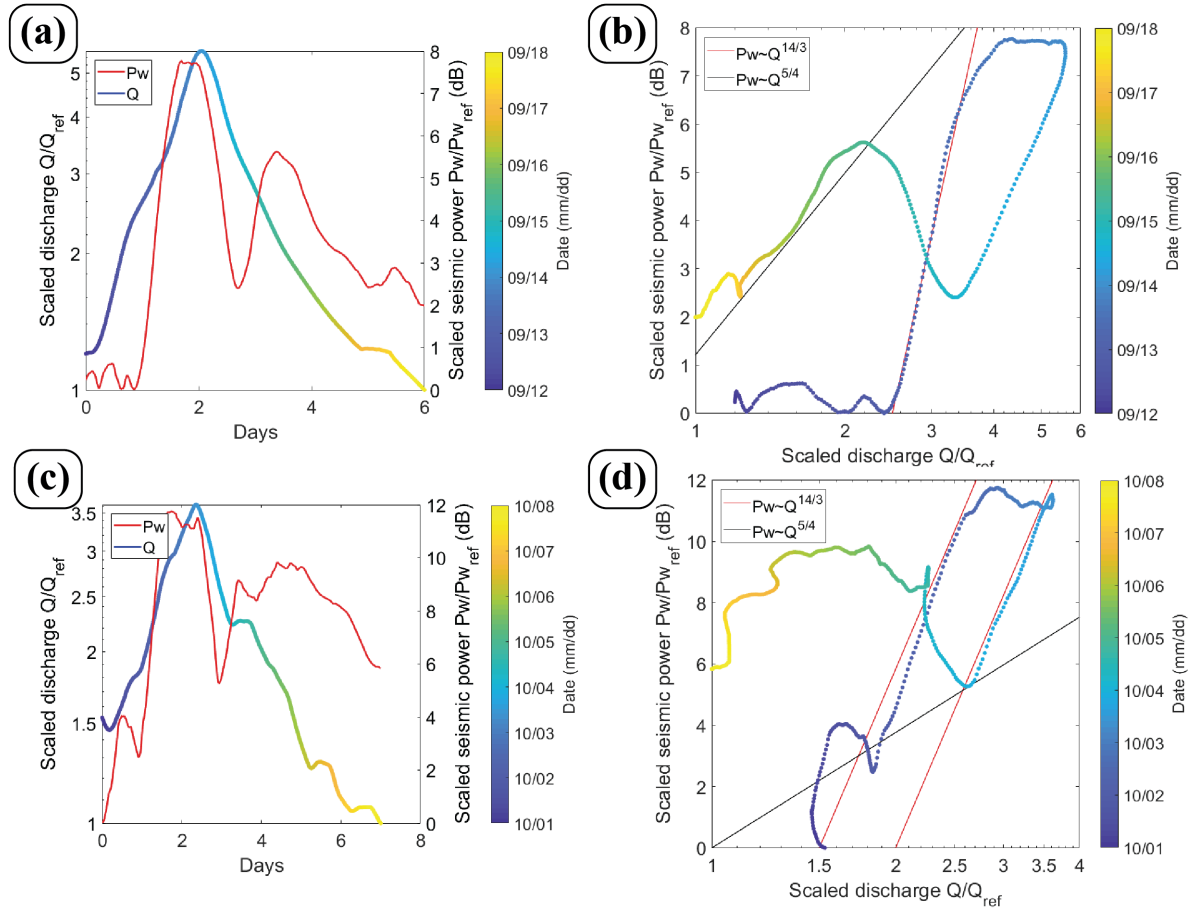
Figure 6.1: Evolution of the discharge and the seismic power during a storm event in September 2018 (a, b) and October 2018 (c, d). (a, c) Scaled discharge (colour) and seismic power (red) as a function of time. (b, d) Scaled seismic power as a function of discharge. Black lines show the predicted scaling for changes in hydraulic radius only and red line for changes in hydraulic pressure gradient. For details on the diagram representation refer to Fig. 5.6.

ogy.

To highlight the potential of studying such events I show in Fig. 6.1 the seismic power and the subglacial water discharge measured during two storms events in 2017. The diagram and temporal representation are the same as used in Nanni *et al.* (2020) and shown in Fig. 5.6. What we can observe is that for two storms the seismic power response to increasing water discharge is very similar (Fig. 6.1(a,c)). It presents two clear peaks and two different trends in the Q versus P_w diagrams. Those trends are similar to the one I previously described in Fig. 5.6 and this suggests that first subglacial channels accommodate the increasing water input by increasing the hydraulic pressure gradient and then they change their size (hydraulic radius). This shows that those events might induce a particular dynamic in the subglacial hydraulic properties, and this is particularly promising for future work to be conducted on this direction.

6.2   Monitoring subglacial sediment transport and glacier erosion rate

Before starting my PhD I worked a little on the role of glacier in shaping the Earth's surface through erosion and sediment transport. This topic has always interested me and a lot of questions remains as highlighted by the recent special issue on Annals of Glaciology that stresses that glacier erosion and the interplay between glaciers and geomorphology are still poorly know (Alley *et al.*, 2019). Two recent studies (Herman *et al.*, 2015; Koppes *et al.*, 2015) have highlighted that the relation between basal sliding velocities and erosion rate are still difficult to assess because of lacking observations and incomplete physical framework. The main question is how the erosion depends on basal sliding, is it a linear dependency, a cubic one or an even more non-linear relationship? Glacier erosion also greatly depends on how well sediments are washed away from the glacier base, that depends on the sediment transport by subglacial rivers. To address such question one needs accurate basal sliding measurements and erosion rate. Those are often very difficult to obtain. While working on Glacier d'Argentière I reflected on how our measurements could also contribute to the study of glacial erosion. I have occasionally worked on this aspect and discussed about it with Jean-Louis Mugnier (Univ. Chambéry) and his master student Arthur Schwing. I see in our dataset two opportunities.

The first opportunity is to estimate sediment transport from seismology. Studies of fluvial process and associated sediment transport have shown that sediment transport generates a seismic noise with frequency that are on similar ([10-20] Hz), but slightly higher than, to the spectral signature of water flow ([2-10] Hz) (Tsai *et al.*, 2012; Bakker *et al.*, 2020). This implies that sediment transport might be inferred from seismic analysis is the same way as we did for subglacial water flow (Nanni *et al.*, 2020). Our seismic measurements could therefore be used to estimate the subglacial sediment transport. The second opportunity is to investigate the relation between basal sliding velocities and erosion rate. There is not yet a clear consensus on how basal sliding velocities relates to erosion rate. The particularity of our setup is that where water discharge is measured there is a sediment collector that is flushed when full and those flushes are recorded in the water discharge signal. Based on the size of the sediment collector and the occurrence of the flushes through time, one could thus evaluate the amount of sediment transported within subglacial conduits. When compared to the continuous measurements of basal sliding velocities (Vincent and Moreau, 2016) or to the inversion made from seismic measurements (see previous point) such a proxy of sediment transport could be very useful.

Part IV

Spatial investigation of subglacial water flow

Methodological question n°2:

How, and at which resolution, can we locate sources of seismic noise that are distributed in space and varying in time?
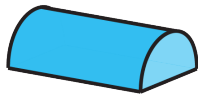
Thematic question n°2:

What is the spatial configuration of the subglacial drainage system and how does it evolve through time?

Spring meltwater before diving into the bowels of the Glacier d'Argentière . © *Benoit Urruty*.

7

Preface

During the second part of my PhD I focused on analyzing spatial characteristics in the seismic wavefield recorded at the surface of the Glacier d'Argentière to retrieve the spatial configuration of the drainage system. To do so I have contributed to the installation and one-month maintenance of a 98-sensors dense seismic array during the RESOLVE-Argentière project (Sect. 7.2) and I have developed an innovative source location methodology based on a systematic seismic analysis of the phase coherence. I used those observations to retrieve the spatial organization of subglacial water flow and its temporal evolution at the beginning of the 2018 melt-season. Prior to this work, no previous work retrieved two-dimensional maps of the subglacial water flow or any kind of similar distributed source of high-frequency (>1Hz) seismic noise. There are two main reasons for that. The first one is purely instrumental, as this requires particularly dense seismic installation to allow dense sampling of the seismic wavefield. The second one is methodological, as the current geophysical approaches are mostly used to locate individual seismic events and are poorly adapted to locate distributed and changing sources of seismic noise. Before presenting the investigation I have conducted, I introduce in more details the current challenges concerning the location of distributed sources of noise.
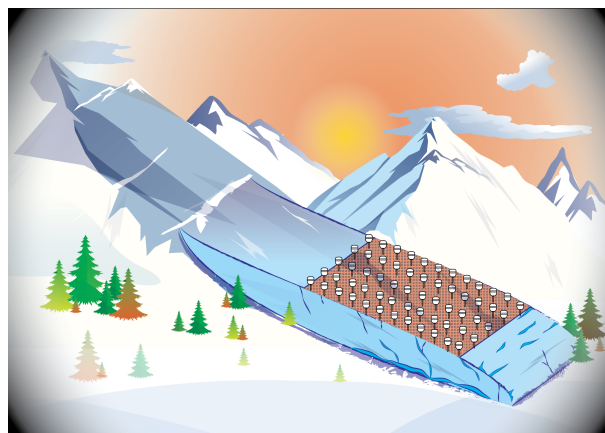
Logo of the RESOLVE-Argentière project.

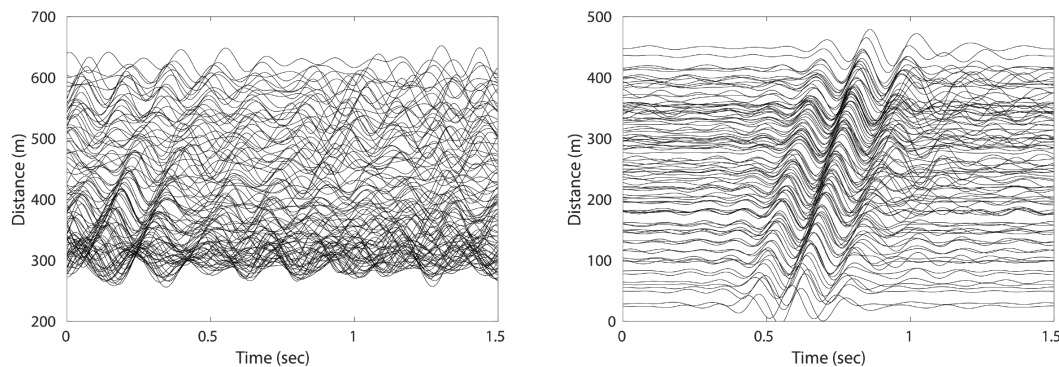## 7.1   Locating distributed sources of seismic noise

Background

Figure 7.1: Examples of waveforms recorded over the 98 sensors on the vertical components. (left) Multiple superimposing wavefield with no dominant pattern. (right) Dominant waveforms from a single event. Amplitude are normalized at each sensors and signals are filtered within [8-15] Hz.

Locating impulsive events such as the one linked to earthquakes, crevasse opening or nuclear explosions is now done routinely. The method often consists of picking the arrival times of seismic waves such as S-waves or P-waves at different stations and then estimat tinghe location of the source based on a basic triangulation problem. This requires one to know or assume the wave propagation velocities, which today are often known thanks to the large catalog of observations (Stein and Wysession, 2009) or models of the Earth structure (e.g. the Preliminary Reference Earth Model, PREM, Dziewonski and Anderson, 1981). On the other hand, locating noise events is more complicated as seismic noise does not present clear arrival times as shown in Fig. 7.1. This lack of clear arrival time renders almost impossible the use of methods developed for locating impulsive events.

Understanding and locating sources of seismic noise is not a recent issue but has been on the table for more than 100 years. As early as in 1930, the study of Banerji (1930) discussed the physical processes causing the pronounced peak in microseismicity observed for periods of $\sim$ 4-10 s on most of the seismometers of the world. Thanks to extensive seismic and meteorological observations, the author confirms the idea of that time that such tremor (i.e. seismic noise) is caused by waves formed thanks to storm events that interact with the shoreline and generate Rayleigh waves. In the mid-20th century it has then been shown that ocean waves generate seismic waves (i) by interacting with the shoreline with a characteristic spectral signature at periods of $\sim$ 8-16 s (Hasselmann, 1963) and (ii) because of wave-to-wave interaction with a characteristic spectral signature at periods of $\sim$ 4-8 s (Longuet-Higgins, 1950). To illustrate the microseism peaks I show in Fig. 7.2 the power spectral density obtained at the South Pole from Anthony *et al.* (2015). There we can clearly observe the two peaks, which show that these tremors are measured even in the most remote place on Earth. Microseisms have mainly been used to study the Earth structure using noise cross-correlation techniques from the early 2000's with Campillo and Paul (2003) but it is

only in the mid-2000's that the source locations of those microseism were successfully obtained (e.g. Stehly *et al.*, 2006; Shapiro *et al.*, 2006).
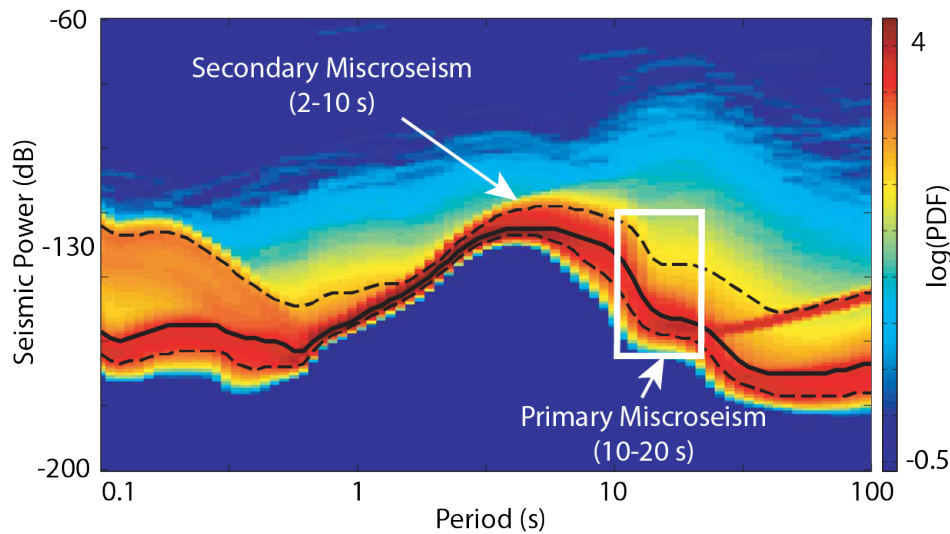

Figure 7.2: Probability density function of power spectral density (PSD) for the vertical-component of South Pole station QSPA (146 m borehole) for December 2007–December 2012. Adapted from Anthony *et al.* (2015).

In their study, Stehly *et al.* (2006) averaged several months of seismic noise measurements within the periods of interest (e.g. 2-10 s for the secondary microseism) and performed cross-correlation between one pair of stations. Cross-correlating the signals from two different stations is similar to finding the time shift between the instant when the wave was recorded at station 1 and when it was recorded at station 2. In the case of sources homogeneously distributed around the station, there is no asymmetry in the cross-correlation (left panel in Fig. 7.3), but if there is a dominant source this yields to an asymmetry as shown in the right panel of Fig. 7.3. One can use this asymmetry and variations in travel times observed in different directions to then determine the azimuth of the sources of noise by minimizing the cross-correlation residual in a way similar to the earthquake triangulation.

Using a similar approach, Shapiro *et al.* (2006) located the origin of the dominant noise source for the 26 s period microseismic peak. To do so, they used stations across the globe and determined the origin of this tremor as storms event along the coast of Africa (Fig. 7.4(d)). In this case the source was inside the seismometers array and could be regarded as a punctual source. For such sources that are persistent over hours to days, one could perform thousands of cross-correlations and stack the results to increase the source location precision. One could also average the seismic noise over long time before performing cross-correlation. When working in natural environment and investigating river or glacier process, sources of seismic noise have higher frequencies (i.e. lower spatial coherence) and are often distributed in space but also highly varying in time. In addition, seismic arrays are often not installed around the sources because of field conditions. Because of such complexity, only a limited number of studies have addressed the problem of locating distributed sources of seismic noise associated with flowing water or in glacier environments.

Evenly distributed noise sources

Nonisotropic distribution of noise sources

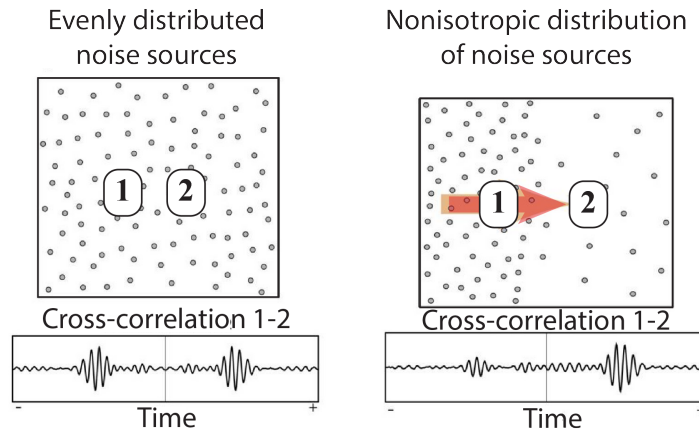Cross-correlation 1-2

Cross-correlation 1-2

Time

Time

Figure 7.3: Schematic illustration of the principle of cross-correlation and the effect of inhomogeneous distribution of noise sources. Adapted from Stehly *et al.* (2006).

Application in environmental seismology

One of the first studies that located distributed sources of noise at high frequency (> 1Hz) is the one of Burtin *et al.* (2010). They used cross-correlation of continuous seismic records at several pairs of stations installed along a river (Fig. 7.5(a)). The dominant noise was generated by the river. To locate the sources that were expected to be distributed, i.e. along the river, they investigated which stations were sensitive to the same signal by keeping only the times when the correlation indicated a coherent signal between at least two stations. They then performed waveform predictions prescribing sources on a regular grid with distributed sources and tried to obtain the same coherence as observed. Their results are shown in Fig. 7.5(a) and reveal their ability of identifying river locations where sources most contribute to the seismic signal. Their study shows that one can locate linearly distributed seismic sources using seismometers close to the sources. Because the instruments were not located close enough to each other they could not investigate the signal coherence at short spatial/temporal scale and therefore could not spatially well-resolve the sources geometry. They could thus only invert the sources back-azimuth (i.e. the source direction) but because they knew the route of the river they estimated the sources location as the intersection between their azimuth and the river. Such an approach is suitable when the water-routes are known (e.g. surface and visible sources) but would be poorly effective in the case of sub-surface sources of noise such as subglacial water flow. Another way to locate sources as been proposed by Vore *et al.* (2019) that estimated the location of subglacial water flow using an array located on a glacier (Fig. 7.5(b)). They did not use seismic coherence but conducted a frequency-dependent polarization analysis. Such an approach is suitable for analyzing seismic signals with no discernible structure and with a limited number of seismic stations. It consists of first calculating the wave polarization at different stations and then estimating the back-azimuth as shown in Fig. 7.5(b). This method has the advantage to be easily applicable to noisy signals, but if stations are too sparse and/or too far from the sources then a precise source location cannot be determined. As shown in Fig. 7.5(b) and because of a reduced number of stations that were located too far apart, they could only retrieve a general direction of the subglacial sources but not the system's geometry. A similar approach was con-
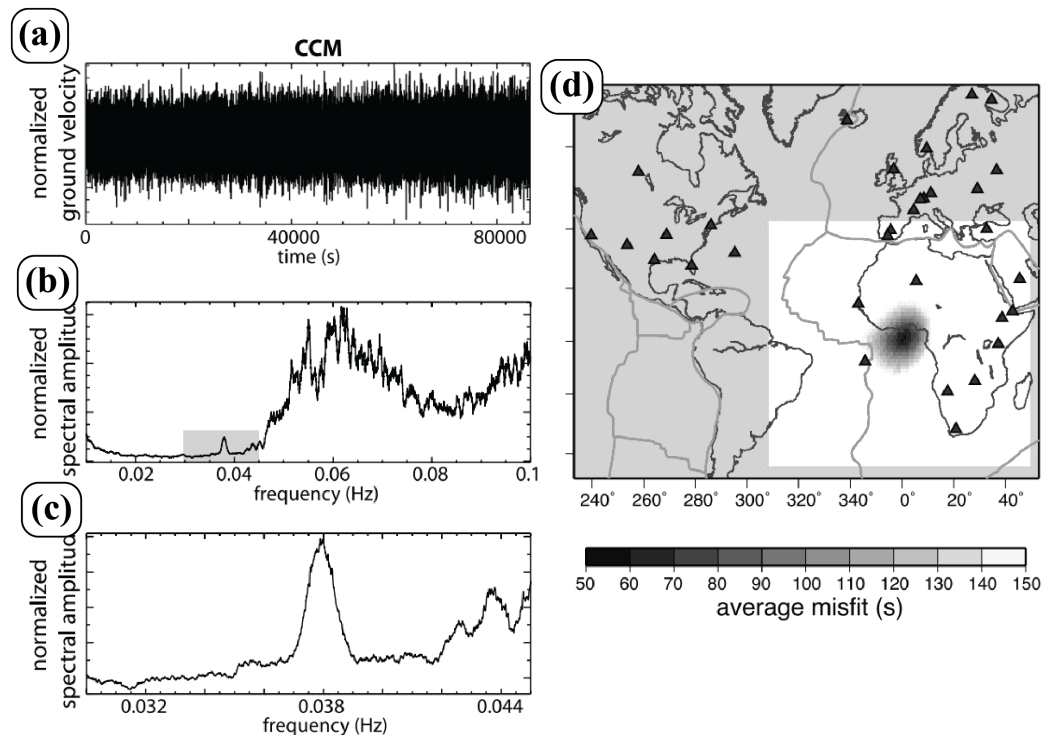
Figure 7.4: Examples of observation of the 26 sec (0.038 Hz) microseism from analysis of day-long vertical component records of seismic noise shown in Shapiro *et al.* (2006). (a) Seismograms. (b) Amplitudes of the Fourier spectra. (c) Spectra zoomed around the 26 sec peak. (d) Results of the grid-search location of the source of the 26 sec microseism seen by North American, European, and African stations using 48 cross-correlations.

ducted by Preiswerk *et al.* (2018) to study seismic burst in glaciers. But as for Vore *et al.* (2019) the seismic array was too sparse and way too far from the sources and only back-azimuth have been retrieved. Lindner *et al.* (2020) installed a series of sensors across the Plain Morte Glacier (CH) to locate water flow and glacial icequakes. They installed their sensors close to the sources and close to each other to tackle the problems previously highlighted that arise from non-dense enough seismic installations. They used a matched-field-processing approach that uses the coherence of the seismic wavefield across stations and matches a modeled wave field to the observations (see Sect. 9.3 for details). As shown in Fig. 7.5(c) they successfully located some events, but those events were mainly associated with crevasses opening or hydraulic fracturing. Such mechanisms generate impulsive events and are therefore much easier to locate as we present in Chapter 8. In addition, their seismic array was too sparse and not close enough to the sources, which limited their source location precision and often only yielded sources azimuth only. The study of Corciulo *et al.* (2012) used a similar approach to locate and hydrocarbon field. As shown in Fig. 7.5(d) they successfully located their sources in depth and range, but because of an array whose geometry was not adapted to the sources' spectral signature they could only obtain a broad punctual location and could not infer the spatial geometry of their sources.

The studies I present in the following chapters address the problem of locating distributed noise sources in order to retrieve the first two-dimensional maps of the subglacial drainage system. Those studies are in close link with the RESOLVE geophysics experiment during which we installed a dense seismic array at the surface of the Glacier d'Argentière.

7.2   Installing a dense seismic array on a glacier

The RESOLVE-Argentière project is led by Philippe Roux from the IsTerre laboratory in Grenoble and Florent Gimbert, and aims to combine multi-physics sensors to refine quantitative interpretation of the process acting within a glacier. Our team was multi-disciplinary, composed of geophysicists, physicists and engineers that are experts in wave physics, geophysical imaging, electromagnetic theory and massive data processing. I am an active member of this project and contributed to the seismic array design and installation, to link the different fields of research by providing them the glaciological context, to analyse passive seismic data including evidences for stick-slip, crevasses opening, subglacial-water-induced noise or seismic waves scattering. My involvement in this project was rendered possible thanks to my collaboration with Philippe Roux that contributed to supervise and advise me over the last two years of my PhD. Such type of seismic monitoring is particularly unique given (i) the high number of deployed sensors (98), which enables monitoring with unprecedented density and coverage in such set-up, (ii) the acquiring of supplementary data providing key complementary constraints on glacier structure and dynamics, and (iii) the targeted site and time period of the year, where and during which key glacier structural and dynamical changes occur both in space and time and may be studies specifically with our array.

Outline

In Chapter 8 I first present the overview of the RESOLVE project based on the paper I co-authored with Florent Gimbert and the RESOLVE-team. In Chapter 9 I present how I have been able to retrieve the first two-dimensional maps of the subglacial drainage system by analyzing the phase of the wavefield in an innovative manner. In link with this paper I also present unpublished results that concern the methodology I developed to locate distributed sources of noise based on ground motion amplitude variations and how this could complement other phase's based approaches.

I presented part of those works at Cargese Summer School 2019 (Corsica), at the American Geoscience Union meeting 2019 (San Francisco) and at the European Geoscience Union meetings 2019 and 2020 (Vienna).
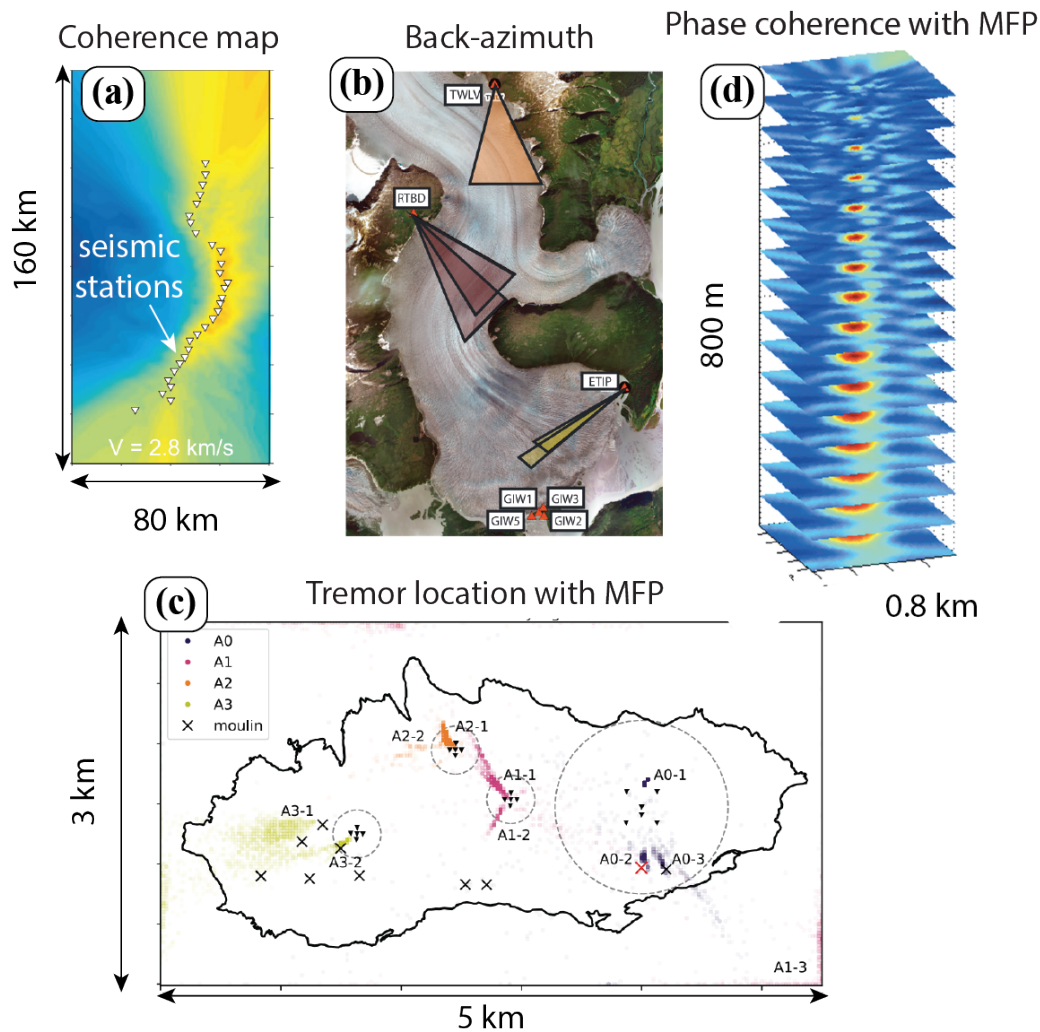
Figure 7.5: Examples of distributed noise sources location from previous studies. (a) Burtin *et al.* (2010) on water flow on the Trisuli river in the Himalayas. Best coherence maps for a frequency of 3.5 Hz from noise correlation functions. Yellow to red colors stand for areas of strong coherence (most probable source of noise) and white triangle for the seismic station which are located along the river. (b) Vore *et al.* (2019) on locating subglacial water flow in an Alaskan glacier. Map of back azimuth directions at stations on Taku Glacier that correspond to back azimuth probabilities. Each triangle represents a different polarized, Rayleigh wave glaciohydraulic tremor frequency band, with the width of a triangle representing the range of back azimuth estimates between the 25th and 75th percentiles of measurements for the day. (c) Lindner *et al.* (2020) on glacio-hydraulic tremor on Glacier de la Plaine Morte (CH). MFP locations over the frequency range 8.5-12 Hz assuming Rayleigh wave velocities (colored dots). The thick black line indicates the glacier margin, the black triangles the locations of the seismic stations, and the crosses locations of moulins. (d) Corciulo *et al.* (2012) on locating a hydrocarbon field. Three-dimensional MFP output representation. Color scale represents the amplitude of the MFP output the closer to red the more the modeled phase agrees with the observations and therefore the more accurate the source location.

The RESOLVE project: a multi-physics experiment with a temporary dense seismic array on the Glacier d'Argentière

[1] University Grenoble Alpes, CNRS, IRD, IGE, Grenoble, France
[2] University Grenoble Alpes, CNRS, IRD, UGE, ISTerre, Grenoble, France
[3] Laboratory of Hydraulics, Hydrology and Glaciology, ETH Zurich, Zurich, Switzerland
[4] Aix Marseille Univ, CNRS, Centrale Marseille, LMA, France

Short note to the reader

I decided to include this paper as a chapter in my PhD thesis as I devoted almost half of my PhD working on the RESOLVE-project and this paper describes the full experiment. For this paper I contributed significantly to writing the sections about the seismic amplitude analysis (Sects. 8.2, 8.3 and 8.4), the matched-field-processing (Sects. 8.3 and 8.4) and contributed to writing the Introduction (Sect; 8.1), Discussion (Sect; 8.4) and Summary (Sect; 8.5) through numerous discussions and group meetings. I made all of the figures presented in the paper (expect Figs. 8.6 and 8.10) based on outputs from the different expert in each field in order to ensure a consistency throughout the paper.

In this paper we first present our motivations for conducting such an experiment and we document the site and all aspects of our experiment. We then conduct preliminary analysis using multiple seismic techniques such as template matching and match field processing to illustrate the dataset and its capability to assess novel components of key glacier processes such as subglacial hydrology, stick slip motion and englacial fracturing. All data related to our experiment will be made available when the paper will be published, with all the necessary data access information being given in the Data and Resources section. We finally discuss in which ways further work using this dataset could to our view help tackle key remaining questions in the field.

This study is a good illustration of an interdisciplinary work gathering scientists with different but complementary expertise targeting fundamental problems to address remaining challenges in cryo-seismology. Given the uniqueness of such type of experiment, we envision that it will be of particular interest by both seismologists and glaciologists. The glaciology community may be interested by our unprecedented location of glacial features such as crevasses, basal stick-slip, subglacial water flow and analysis of the glacier geometry. The seismology community may be interested by our novel way to couple seismic observations and complementary observations, our systematic source location strategy or on our amplitude analysis. In a time of increasing seismological investigation of the cryosphere (Booth *et al.*, 2020; Walter *et al.*, 2020), our study highlights that community efforts can overcome numerous observational limitations that will bring key insights in the process controlling glacier dynamics.

Abstract

Recent work in the field of cryo-seismology demonstrates that high frequency (>1 Hz) waves provide key constraints on a wide range of glacier processes such as basal friction, surface crevassing or subglacial water flow. Establishing quantitative links between the seismic signal and the processes of interest however requires detailed characterization of the wavefield, which at the high frequencies of interest necessitates the deployment of large and particularly dense seismic arrays. Although dense seismic array monitoring has recently become routine in geophysics, its application to glaciated environments has yet remained limited. Here we present a dense seismic array experiment made of 98 3-component seismic stations 23 continuously recording during 35 days in early spring on the Glacier d' Argentière, French Alps. The seismic dataset is supplemented by a wide range of complementary observations obtained from ground penetrating radar, drone imagery, GNSS positioning and in-situ instrumentation of basal glacier sliding velocities and subglacial water discharge. Through applying multiple processing techniques including event detection from template matching and systematic matched-field processing, we demonstrate that the present dataset provides enhanced spatial resolution on basal stick slip and englacial fracturing sources as well as novel constraints on the heterogeneous nature of the noise field generated by subglacial water flow and on the link between crevasse properties and englacial seismic velocities. We finally outline in which ways further work using this dataset could help tackle key remaining questions in the field.

8.1   Introduction

The deployment of large and dense seismic arrays has recently become routine in various geophysical contexts thanks to new technological developments of autonomous wireless geophones and increases in computational power. Spatially dense arrays allow enhancing the characterization of high frequency (>1 Hz) body waves and surface waves propagating in the subsurface, such as for example in near-surface fault systems exhibiting hundreds to few tens of meters long structures (e.g. the Newport-Inglewood Fault, see Lin *et al.* (2013a), and the San Jacinto Fault, see Mordret *et al.* (2019)). The improved resolution provided by dense arrays helps increase the completeness of impulsive seismic event catalogs (Vandemeulebrouck *et al.*, 2013), such that the spatio-temporal dynamics of sources may be studied in greater detail and event catalogs be used to conduct subsurface imaging (Chmiel *et al.*, 2019). Dense arrays also help to detect other sources of radiation (e.g. tremor and anthropogenic sources) compared to what is possible with single stations or regional networks (Inbal *et al.*, 2016; Li *et al.*, 2018; Meng and Ben-Zion, 2018).

Dense array monitoring techniques have however little been applied to the study of glaciers, although a number of seismic investigations have demonstrated that high frequency (> 1Hz) waves can provide key constraints on glacier dynamical processes and structure characteristics (Podolskiy and Walter, 2016). Analysis of impulsive sources yields insights on basal stick-slip motion (Weaver and Malone, 1979; Allstadt and Malone, 2014; Helmstetter *et al.*, 2015b; Lipovsky and Dunham, 2016; Lipovsky *et al.*, 2019) and englacial fracturing (Neave and Savage, 1970; Roux *et al.*, 2010; Mikesell *et al.*, 2012; Podolskiy *et al.*, 2019). Continuous monitoring of englacial seismic velocities using background noise or impulsive arrivals yields insights on glacier structure such as the geometrical properties of surface or basal crevasses (Walter *et al.*, 2015; Lindner *et al.*, 2020; Zhan, 2019; Sergeant *et al.*, 2020). Analysis of continuous sources helps unravel the physics of subglacial water flow (Bartholomaus *et al.*, 2015a; Gimbert *et al.*, 2016; Lindner *et al.*, 2020; Nanni *et al.*, 2020), the geometry and location of glacial moulins (Helmstetter *et al.*, 2015a; Roeoesli *et al.*, 2016; Aso *et al.*, 2017) and the occurrence of subglacial sediment transport (Gimbert *et al.*, 2016).

The restricted use of dense array monitoring techniques in the above-mentioned applications may limit our understanding in several ways. The mechanisms responsible for stick-slip motion remain poorly identified, and the use of dense array monitoring techniques to more accurately infer where stick-slip motion occurs and whether and at which rate stick-slip asperities migrate could help better infer the involved mechanisms and the necessary conditions for stick slip to occur (Lipovsky *et al.*, 2019). The relationship between crevasse characteristics such as depth or deformation rate and the seismic signal is yet not fully established (Lindner *et al.*, 2018), and the capability to precisely locate crevasse fracturing events while concomitantly monitoring changes in englacial seismic velocities using dense arrays could enable doing so. The feasibility to infer the geometry of the subglacial drainage system as well as the dependency of

subglacial water-flow-induced noise amplitudes and thus of inversions of subglacial flow physics (Gimbert *et al.*, 2016; Lindner *et al.*, 2020; Nanni *et al.*, 2020) on sensor position remain unexplored and could be addressed using dense array seismic observations.

Properly evaluating the knowledge gain dense seismic arrays may provide in order to address the above-mentioned challenged requires (i) monitoring a glacier that gathers all processes of interest, (ii) covering scales and durations over which significant changes operate, and (iii) acquiring complementary observations to test the seismically-derived findings and replace these into a wider glaciological context. Here we present data and preliminary analysis from a 98-sensors array deployed over 35 days during early spring 2018 on an Alpine Glacier, the Glacier d'Argentière in the French Alps (Fig. 8.1). We also provide and analyze key complementary observations from ground penetrating radar (GPR), drone imagery, Differential Global Positioning System (GNSS) positioning and in-situ instrumentation of basal glacier sliding velocities and subglacial water discharge. We report that the selected glacier, the time period of investigation as well as the completeness of the present dataset allow satisfying all three above-mentioned conditions. Through applying multiple processing techniques including event detection from template matching and systematic match-field-processing, we demonstrate that the present dataset allows enhancing the spatial resolution associated with basal stick slip and near surface crevassing event locations as well as provides novel constraints on the degree of heterogeneity of the noise field caused by subglacial water flow and the link between crevasse properties and englacial seismic velocities. We finally outline in which ways further work using this dataset could help overcome classical observational limitations and yield address the above-mentioned challenges. The paper is structured as follows: we first describe the experimental configuration for all geophysical instruments in section II, we then present seismic array results in section III and finally discuss the various aspects of our findings as well as outline future studies that may be conducted with this dataset in section IV.

8.2   Experiment design

Field site

The Glacier d'Argentière is located in the Mont Blanc Massif (French Alps, 45.55' N, 6.57'E, Fig. 8.1(a) and is the second largest French glacier. It is about 10 km long, covers an area of about 12 km2, and extends from an altitude of 1700 m asl up to about 3600 m asl. The upper part of the glacier is constricted in a typical U-shaped narrow valley where ice sits on granite. The lower part of the glacier rather is characterized by a sharper incised, V-shaped valley where ice sits on metamorphic rocks (Vallis, 1969; Hantz and Lliboutry, 1983; Vincent *et al.*, 2009). The glacier generally exhibits temperate bed conditions (Vivian and Bocquet, 1973), i.e. basal ice temperature is at the pressure melting point and water flow occurs at the interface as a result of being produced by year-round basal melt and summer surface melt (Cuffey and Paterson, 2010).
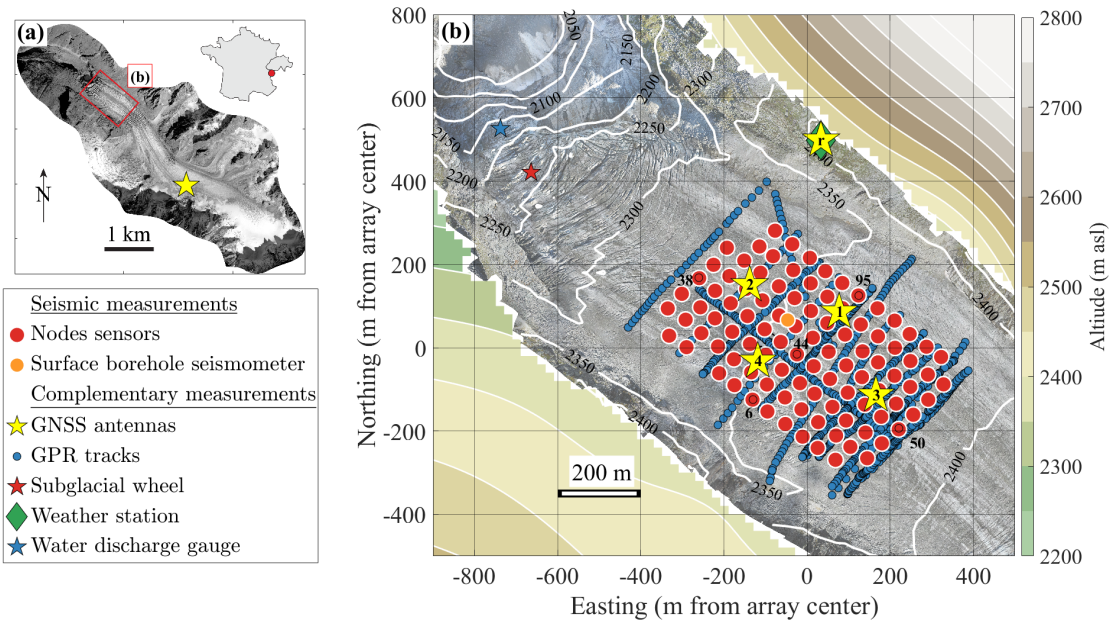
Figure 8.1: Maps of the Glacier d'Argentière and of the instruments deployed during the dense array experiment. (a) Aerial picture of the Glacier d'Argentière taken in 2003. The red rectangle indicates the area shown in Fig. 8.1(b), which we focus on in this study. The yellow star refers to a permanent GNSS station and the red dot in the inset shows the location of the glacier with respect to French borders. (b) Map showing the lower part of the Glacier d'Argentière along with the instrument's positions. White contours indicate glacier surface topography as retrieved from structure from motion, and color contours indicate topography outside of the glacier. The various symbols refer to Instruments as specified in the legend. Numbers associated with red circles indicate nodes that are used for illustrative examples in Fig. 8.4.

The monitored site is located in the lower part of the glacier (about 2 km from the glacier front) and at about 2400 m asl (Fig. 8.1(a)). In this area the surface slope is gentle (1-2%) and crevasses are restricted to an area of about 200 m from the glacier sides (Fig. 8.1(b)). The glacier flows at a year average velocity of about 60 m.yr-1 in its center, about half of which is due to sliding at the ice-bed interface and the other half to internal ice deformation (Vincent and Moreau, 2016). Internal ice deformation in the area mainly occurs through ice creep, except on the glacier sides where englacial fracturing may play a role. A strong seasonality is observed in glacier dynamics, with summer (typically May to September) velocities being equal to about 1.5 times winter velocities (Vincent and Moreau, 2016), as a result of melt water input lubricating the ice-bed interface and enhancing basal sliding (Lliboutry, 1968; Cuffey and Paterson, 2010).

The above-presented features of the Glacier d'Argentière make it an ideal case study to address our objectives of unravelling glacier structure and flow processes from seismic observations. Seismic studies over the past decade on this glacier have demonstrated the capability to use seismic observations in order to identify serac instabilities (Roux *et al.*, 2008), surface crevassing (Helmstetter *et al.*, 2015a), subglacial water flow (Nanni *et al.*, 2020) and basal stick-slip (Helmstetter *et al.*, 2015b). These processes generate a large panel of signals with broad azimuthal distributions and frequency contents that may be used for tomography.

Seismic instrumentation and geophysical investigation

Seismic instrumentation

Sensors of the dense seismic array (see red dots in Fig. 8.1(b) are Fairfield ZLand 3 components nodes set up with a sampling frequency of 500 Hz (hereafter referred to as nodes). These sensors have a cut-off frequency of 4.5Hz, a sensitivity of 76.7 $V.m^{-1}.s^{-1}$ and a typical power autonomy of about 35 days. We deployed the nodes on April 24 when the glacier was entirely covered by an about 3 m thick snow layer. We placed the sensors about 40 m apart from each other in the along-flow direction and about 50 m apart in the across-flow direction in order to enable subwavelength analysis in the 4-50 Hz frequency range of interest. We buried them into snow about 30 cm below the surface to ensure that sensors were levelled and well coupled over several days to a few weeks until snow melt uncovered it. This depth is also shallow enough to allow GNSS signal reception for time synchronization. Given that snow melt occurred at an average rate of about 2-3 cm/day during the investigated period and at this location, the 30-cm deep deployment necessitated sensors re-deployment once over the instrumented period, an operation that we conducted on May 11.

We supplemented the seismic array by one three-component borehole seismic station placed at 5 m below the ice-surface (see orange dot in Fig. 8.1(c). This Geobit-C100 sensor connected to a Geobit-SRi32L digitizer provides higher sensitivity (1500 $V.m^{-1}.s^{-1}$), higher frequency sampling (1000 Hz) and a lower cut-off frequency (0.1 Hz) compared to the nodes. This seismic station is the same as the one used for the two-year long seismic study of Nanni *et al.* (2020).

Recovery of surface and bed digital elevation models from structure from motion surveys and ground penetrating radar

We construct a digital surface elevation model based on a drone geodetic survey that we conducted on September 5, 2018 when the glacier surface was snow free and crevasses could be identified. We used a senseFly eBee+ Unmanned Aerial Vehicle and acquired a total of 720 photos using the onboard senseFly S.O.D.A. camera (20 Mpx RGB sensor with 28 mm focal lens). We generate a digital elevation model of 10-cm resolution using differential Global Positioning System (GPS) measured ground control points (see green stars in Figure 2a) and the Structure for Motion algorithm implemented in the software package Agisoft Metashape Professional version 1.5.2. A detailed description of the processing steps can be found in Kraaijenbrink *et al.* (2016); Brun *et al.* (2016).

We calculate a crevasse map (see black dots in Fig. 8.2a) based on the surface digital elevation model, which has been shown to be more reliable and precise than using optical/radar images (Foroutan *et al.*, 2019). We first apply a 2D highpass filter with a
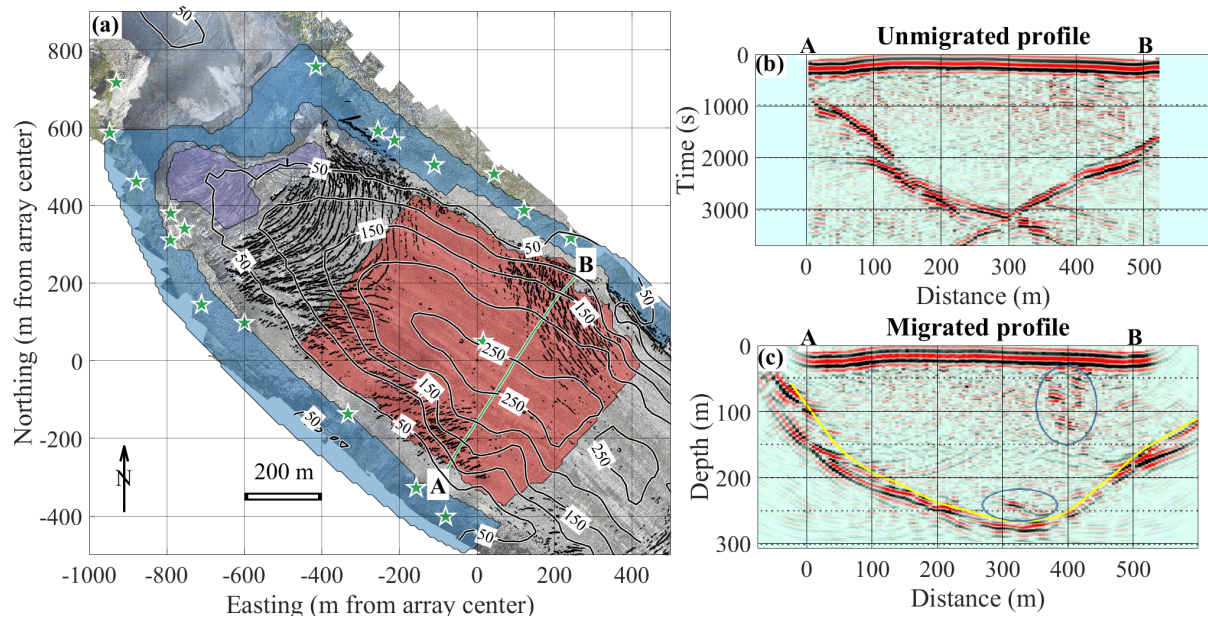
Figure 8.2: (a) Reconstructed ice thickness (black contours) and surface crevasse maps (black dots), along with the locations of various data constraints used to establish the surface and bed DEMs. Green stars correspond to the GNSS measured ground control points, while colored areas differentiate between observations used to constrain the bed DEM: the blue area is from a 2018 surface DEM, the purple area corresponds to where ice-bed coordinates are known from in-situ borehole measurements and from excavated tunnels, and the red area corresponds to where glacier depth is inferred from the GPR measurements. The green line shows the track associated with the selected GPR profile shown in (b) and (c). (b) and (c) Examples of processed (b) unmigrated and (c) migrated GPR data acquired along the AB profile shown in (a). The yellow curve corresponds to the picked interface and the blue ellipses highlight local reflectivity anomalies.

cutting frequency of 10 m, meaning that we keep all features that present variations in the DEM less than 10 m. We then define any location as being part of crevasses where elevation change is negative and larger than 50 cm, and apply a 2D median filter with a 1 by 1 m kernel in order to remove artifacts from boulders and moraines.

To establish a digital elevation model of the glacier bed we primarily use Ground Penetrating Radar (GPR) data acquired using a system of two transmitting and receiving 4.2 MHz antennas connected to a time triggered acquisition developed especially for glacial applications by the Canadian company Blue System Integration Ltd. The GPR signal processing consists of correcting for source time excitation. We use both dynamic corrections to reproduce a zero-incidence acquisition from data acquired with a 20 m offset between source and receiver (Normal Moveout correction) and static corrections to highlight elevation variations along a profile. We do so using a constant wave velocity of $0.168 \, 10^{-9} m.s^{-1}$ that is typical for ice (Garambois *et al.*, 2016). We then apply a [1-15 MHz] Butterworth band-pass filter followed by a squared time gain amplification to the signal in order to increase signal-to-noise ratio. We show an illustration of the processed GPR data in Fig. 8.2b, where the direct air-wave first arrival is followed by a large reflectivity V-shape pattern reaching $3000 \, 10^{-9}$ s around the center of the profile. This latter profile corresponds to the ice/bedrock interface, although its

apparent shape is biased by waves being reflected by the closest ice-bed interface rather than that located straight below the instrument. We correct for this bias by applying a frequency-wavenumber Stolt migration technique (Stolt, 1978) and converting time into distance using the constant wave velocity of $0.168\ 10^{-9}m.s^{-1}$. We note that prior to migration we add null traces (i.e. with null amplitudes) in places where harsh glacier surface conditions (mainly crevasses) prevented us to acquire data. As illustrated in Fig. 8.2c the migration process is effective in correcting the artefacts due to the geometrical variation of the interface along the profile, which now appears as smooth and continuous. We then pick the ice-bed reflection (see yellow line in Fig. 8.2b) over all GPR profiles, such that a three-dimensional bed DEM can be reconstructed.

We reconstruct a three-dimensional bed DEM over a larger area than that covered by GPR surveys by (i) incorporating additional constraints like glacier edge elevation as measured from drone imagery (see purple area in Fig. 8.2a) and in-situ borehole measured ice-bed interface elevations as obtained from the excavated tunnels located further down-glacier from the dense seismic array (see blue area in Fig. 8.2a) (ii) interpolating all data using a kriging method onto on a 10*10 m grid. We estimate from different first onset pickings that the recovered depth uncertainty is of about 5 m below the seismic array, while we note that it likely is considerably larger and more on the order of few tens of meter outside of the array, where observations are sparser.

In Fig. 8.2a we show the two-dimensional map of ice thickness as reconstructed based on subtracting the bed DEM from the surface DEM (using 25-m spaced contour lines). The glacier bed generally exhibits a gently dipping valley, with a maximum ice thickness of about 255 m at the center of the seismic array. Glacier thickness decreases relatively sharply on the glacier margins where surface crevasses are observed. We also observe that bed elevation significantly increases down glacier, which results in a decrease by more than 150 m in glacier thickness. Beyond these generic characteristics we identify two interesting reflectivity features in the migrated GPR images (see blue ellipses in Fig. 8.2c) that correspond to localized scattering observed near the surface and a large reflectivity pattern observed just above the deepest portion of the interface. The near surface scattering feature could be caused by deep crevasses, and the deeper feature could be caused by englacial and/or subglacial water conduits as recently proposed by Church *et al.* (2019), who made similar GPR observations in a temperate glacier and were able to verify such an interpretation from in-situ borehole observations.

Meteorological and water discharge characteristics

We use air temperature and precipitation measurements obtained at a 0.5 h time step with the automatic weather station maintained by the French glacier-monitoring program GLACIOCLIM (Les GLACIers un Observatoire du CLIMat; https://glacioclim.osug.fr/), which is located on the moraine next to the glacier at 2400 m asl (see green diamond in Fig. 8.1(b)). Precipitation is measured with an OTTPluvio weighing rain gauge. Water discharge routing subglacially is monitored at a 15 min time step in tunnels excavated
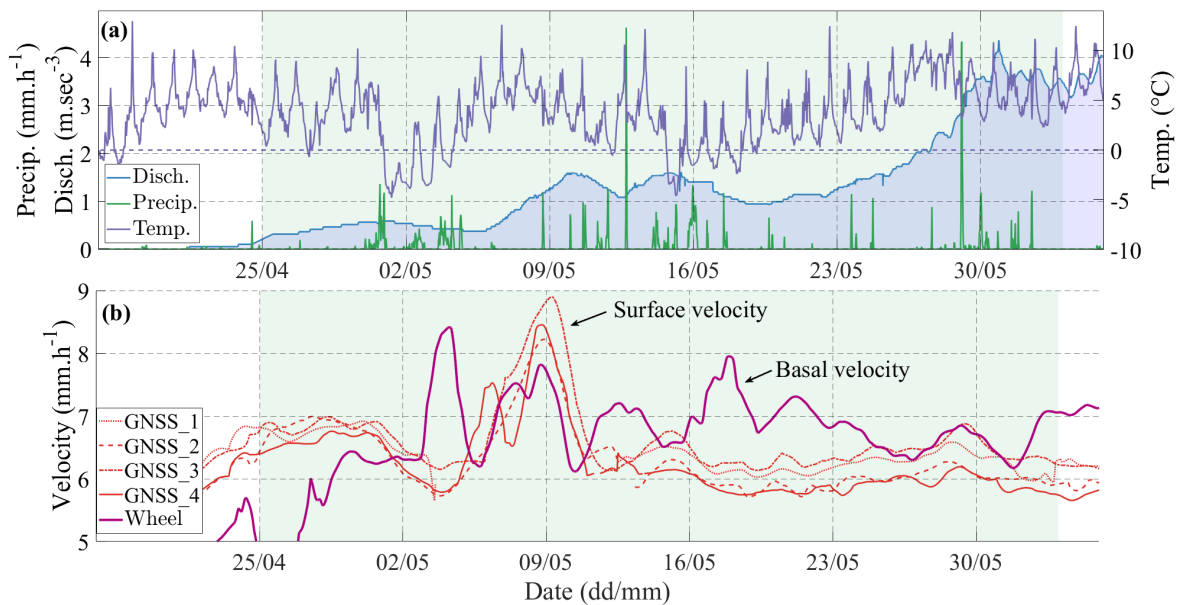
Figure 8.3: Time series of physical parameters associated with meteorology, hydrology and glacier dynamics during the dense-array experiment (from April 25th to June 6th, green area). (a) Glacier outlet water discharge (blue), surface temperature (purple) and precipitation (green). (b) Horizontal glacier flow velocities as measured at the glacier surface through GNSS monitoring (GNSS, orange lines) and at the glacier base through direct "wheel" monitoring (thick purple line). See Nanni *et al.* (2020) for the complete time series of discharge, temperature, precipitation and sliding for 2016-2018.

into bedrock by the Emossons hydraulic power company, which are located 600 m downstream of the array center (at 2173 m asl) near the glacier ice fall (see blue star in Fig. 8.1(b)).

We can see that temperature generally increases over the instrumented period, from a multi-daily average of about 0 C at the beginning of the measurement period to about 5 C at the end (Fig. 8.3a). This general increase drives the general increase in water discharge, which varies from few tenths of $m^3.s^{-1}$ to several $m^3.s^{-1}$ over the period. Episodic water precipitation events also occur during the instrumented period, but have little to no effect on subglacial discharge likely as a result of the snow cover acting as a buffer.

Glacier dynamics instrumentation and general features

We evaluate changes in glacier dynamics over the instrumented period by means of two observational methods. The first one is particularly unique to the present site, and consists of glacier basal sliding velocity measurements made continuously in the down glacier serac fall area (see red star in Fig. 8.1(b)) by means of a bicycle wheel placed directly in contact with the basal ice at the extremity of an excavated tunnel (Vivian and Bocquet, 1973; Vincent and Moreau, 2016). The wheel is coupled with a potentiometer that retrieves its rotation rate, which is then recorded digitally and converted back to a sliding velocity at a 1-s sampling time. The second type of measurements consists of

4 glacier surface and 1 reference bedrock GNSS stations (see yellow stars in Fig. 8.1b) of type Leica GR25 acquiring the GNSS signals every second, supplemented by a permanent ARGR GNSS station from the RESIF-RENAG network (http://renag.resif.fr) on the bedrock close to the glacier 3 km uphill (see yellow star in Fig. 8.1a). The GNSS antennas on the glacier are installed on 8-m long aluminum masts anchored 4-m deep in the ice and thus emerging about a meter above the snow surface at the beginning of the measurement period. The temporary station placed next to the glacier side provides a useful reference for validating kinematic GNSS processing approaches, evaluating station positions from every single set of GNSS signal recordings (i.e. every second, as opposed to static processing, which cumulates GNSS signals over a much longer time). We conduct such kinematic processing using the TRACK software ((Herring *et al.*, 2010), http://geoweb.mit.edu/gg/docs.php). Our processing chain includes the use of the on-line tool SARI (https://alvarosg.shinyapps.io/sari/) for the removal of outliers that arise from low satellite coverage in the glacier valley and to perform a de-trend and re-trend analysis to estimate and correct for offsets due to manual antenna mast shortening as snow melt progresses. We also correct for multi-path effects induced by GNSS signal reflections from the ground, although we find that those are attenuated by the combination of GPS and GLONASS signals thanks to their different sidereal periods (24 h for GPS and 8 days for GLONASS). We finally calculate position time series at a 30-s time step sufficient to capture glacier dynamics and subsequently evaluate three-dimensional velocities by the linear trends of the position components. The horizontal velocity is calculated as $v_h = \sqrt{(v_N^2 + v_E^2)}$ where v_N and v_E are the North and East components, respectively.

To facilitate comparison of basal sliding and surface velocity here we smooth both timeseries at a 36-hr timescale (Fig. 8.3b), since daily down to sub-daily fluctuations in basal sliding velocities are largely affected by unconstrained variations in the local ice roughness in contact with the wheel, as for example when an ice-carried rock debris passes over the wheel. Although basal sliding velocity is to be lower than surface velocity, here both quantities have similar absolute values because the sliding velocity is measured at a place where the glacier is much steeper and thus driving stress is much larger than at the GNSS locations. We observe an increase in basal sliding velocity from 4.5 mm/h to more than 6 mm/h at the very beginning of the monitored period. This acceleration is not seen in the GNSS observations, which could be due to the glacier seasonal acceleration occurring earlier at this location. We also observe one major glacier acceleration event in the location of the dense seismic array occurring between May 4th and 8th likely due to the large concomitant increase in water discharge (see Fig. 8.3a) causing basal water pressurization (Cuffey and Paterson, 2010).

8.3   Preliminary results

Seismic noise spectral characteristics

We investigate the spatial and temporal variability of seismic power P (in dB) across a wide range of frequencies by applying Welch's method (Welch, 1967) to calculate

power over 4 seconds-long vertical ground motion timeseries (with 50 % overlap) prior to averaging it (in the decibel space) over 15 minutes-long time windows. This strategy allows limiting the influence of impulsive events (which are studied in more details in the next sections) on the seismic power while enhancing that of the background continuous noise (see Bartholomaus *et al.* (2015a) and Nanni *et al.* (2020) for more details). In Fig. 8.4 we present 1-100 Hz spectrograms (i.e. seismic power at any given frequency and time) over the first half of the instrumented period (April 25th to May 14th) together with timeseries of 2-20 Hz frequency median seismic power at 5 different stations of the array, four of which are located on the four array sides and one of which in the array center (see node numbers in Fig. 8.1b and Figure A1 for spectrograms across all stations, over the entire frequency range and the entire experimental period). Time periods when sensors tilted as a result of snow melt causing them no longer buried are manifested by drastically reduced seismic power values across the whole frequency range (see node 6 from May 8 to May 11). Fortunately, sensor tilt only occurred at a small number of seismic stations (11 out of 98) and during a restricted time duration (less than 2 days on average, see Figure A1). We also observe that seismic power did not change significantly from prior to after sensor re-installation in May 11, which suggests that these are not significantly affected by potential changes in sensor coupling to snow. All stations generally experience similar multi-day (i.e. four days' average, see black lines) variations in seismic power that are highly correlated with multi-day discharge variations (see also Fig. 8.3a), although seismic power precedes discharge variations by several days likely as a result of it being primarily set by the hydraulic pressure gradient, which is highest during periods of rising discharge (Gimbert *et al.*, 2016; Nanni *et al.*, 2020). Although shorter term (e.g. diurnal) variations in seismic power are also similar across stations when discharge is low (from April 24 to 28 and from May 1 to May 5) and -anthropogenic noise dominates (Nanni *et al.*, 2020), the picture is different at higher discharges when seismic power is caused by subglacial water flow. During time periods such as in April 29 and from May 5 to May 14 seismic power exhibits pronounced (up to 10 dB) and broad frequency (1-100 Hz) short time scale (sub-diurnal to diurnal) variations at certain stations (e.g. node 6 (Fig. 4a), node 44 (Fig. 4c) and node 50 (Fig. 4d)) while not at others (e.g. node 38 (Fig. 4b) and 95 (Fig. 4e)). We also observe that at certain stations seismic power appears to be continuously or intermittently enhanced at distinct frequencies, as for instance node 38 that systematically presents much higher seismic power above 20 Hz and node 44 that presents particularly high power at frequencies around 20 Hz from April 27 to May 1. These discrepancies suggest that ground motion amplitude measurements are sensitive to a heterogeneous and intermittent subglacial hydrology network and/or to subglacial water flow sources exhibiting strong directivity variations.

Detecting and locating stick slip events using template matching

We perform an event-detection analysis based on a template matching technique in order to identify high-frequency (>50 Hz) basal stick-slip events. As in Helmstetter *et al.* (2015b) we conduct a two-step analysis. We first build a catalog of events by applying a short-term-average over long-term-average (STA/LTA) detection method (Allen, 1978) to the continuous high-pass filtered signal (>20 Hz) and identifying an
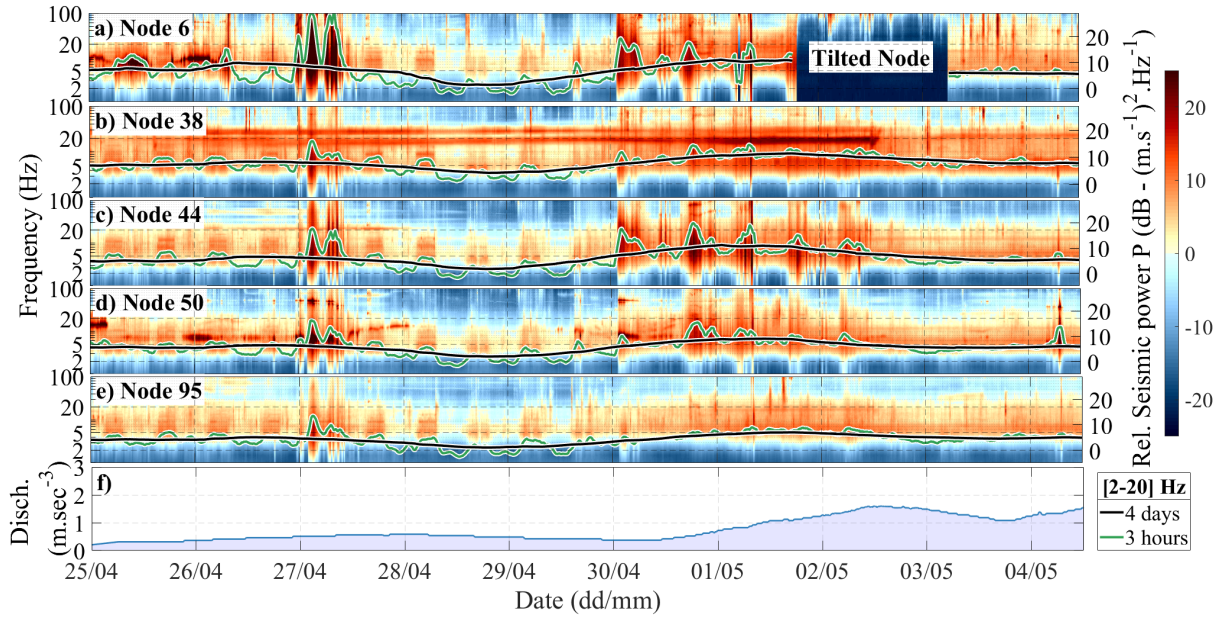
Figure 8.4: a to e) Spectrograms calculated at five selected stations (see corresponding numbers in Fig. 8.1) across the array from April 25th to May 13th, i.e. during the first half of the measurement period. Curves indicate 2-20 Hz frequency mean seismic power as smoothed over short (3 hours, green lines) and long (4 days, black lines) periods. See Figure A1 for all spectrograms and all stations over the whole period. (f) Glacier outlet water discharge as shown in Fig. 3.

event when the STA/LTA ratio exceeds a factor of 2. We then select all events with short duration (<0.2 s) and high average frequency (>50 Hz) and define groups of events referred to as clusters when their correlation with each other exceeds 0.8. For each cluster, we compute the average waveform to define the *template* signal associated with this cluster. We visually check that events present distinct P and S wave arrivals and use a polarization analysis to ensure that they are not associated with surface waves (Fig. 8.5a). We then use the template matching filter method (Gibbons and Ringdal, 2006) in order to detect smaller amplitude events that are not picked but belong to the identified clusters. This analysis is conducted using the borehole station, which has a higher sensor sensitivity and sampling rate compared to the nodes. We identify 31 active clusters during the dense array experiment period. Interestingly, these clusters constitute a large part of the 46 clusters identified on a much longer period (from December 2017 to June 2018, using the borehole sensor which ran almost continuously, see Fig. 8.6). Although the amplitude of these signals varies quite strongly through time (Fig. 8.6a), waveform characteristics strikingly remain similar (Fig. 8.6b). All 46 identified clusters exhibit similar characteristics to that shown in Fig. 8.6, and their activity does not appear to be temporally correlated with each other, nor with external drivers related to meteorology, hydrological or glacier dynamics.

We retrieve the position of the 31 identified clusters by first manually picking on each node the P and S arrival times associated with the event in each cluster that is associated with the largest correlation with the template event (see orange crosses in Fig. 8.5a), and then invert for the location of each event and the associated P and S waves velocities, assuming velocities are homogeneous and identical for all events. We
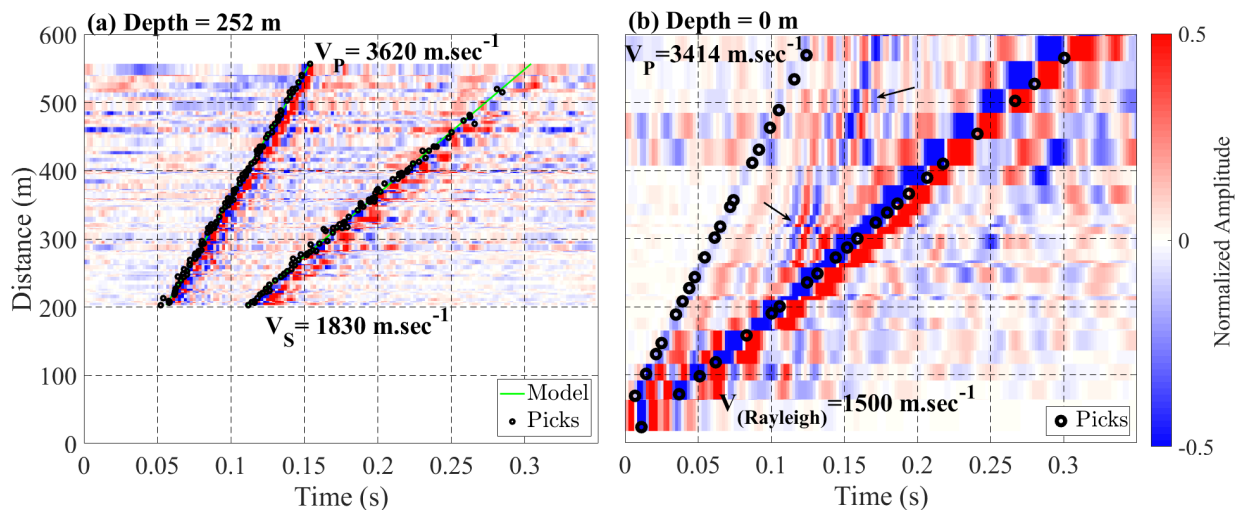
Figure 8.5: Broad band seismograms of (a) a basal event as identified from pattern matching and (b) a surface event as identified from match-field-processing MFP and associated manual picking of arrival times. Black circles correspond to picked P, S and Rayleigh arrival times and green lines on (a) correspond to predicted arrival times using P-wave velocity $V_P = 3620$ m.sec^{-1} and S-wave velocity $V_S = 1830$ m.sec^{-1}. In addition to the direct and surface waves, a hyperbola event is visible at large offsets for panel (b, see black arrows). The zero time corresponds to the event time. Events location is shown in Fig. 8.8.

do not consider refracted waves because the first arrival is the direct wave for most sensors and most events. Moreover, even when the refracted wave is faster, it is usually less impulsive and has a smaller amplitude than the direct wave. We look for P and S wave velocities using a grid search analysis with a step of 10 m.s-1 and the Nonlinloc software (Lomax *et al.*, 2000) to locate clusters. We assume a standard error of arrival times of $21e^{(-3)}$ s for P waves, $4\ 1e^{(-3)}$s for S waves and of $3.51e^{(-3)}$ s for calculated travel times, which is obtained for VP=3620 m.s^{-1} and VS=1830 m.s^{-1}. We can see in Fig. 8.5a that the picked arrival times (black circles) are in good agreement with the computed travel times (green lines). The root-mean-square error for this event is 2.4 ms, about one sample (2 ms).

We show the locations of basal icequakes versus depth in an average transverse section in Fig. 8.7a and on a two-dimensional map in Fig. 8.8. They are mainly located in the lower part of the array and in the central part of the glacier or in North-East side, while there is no event observed in the South-West side. Icequake depths range between 80 m and 285 m, and are in good agreement with the bedrock topography estimated from the radar profiles. Uncertainty on absolute source depth is on the order of 10 m (see errorbars in Fig. 8.7b), and the estimated seismic wave velocities of V_P=3620 m.s^{-1} and V_S=1830 m.s^{-1} (Fig. 8.7b) are in good agreement with velocities measured on other alpine glaciers (Podolskiy and Walter, 2016). V_S is much better constrained by the data than V_P (Fig. 8.7b), however the good match between icequake depth and bedrock topography suggests that our inferred seismic wave velocities correspond to reasonable estimates.
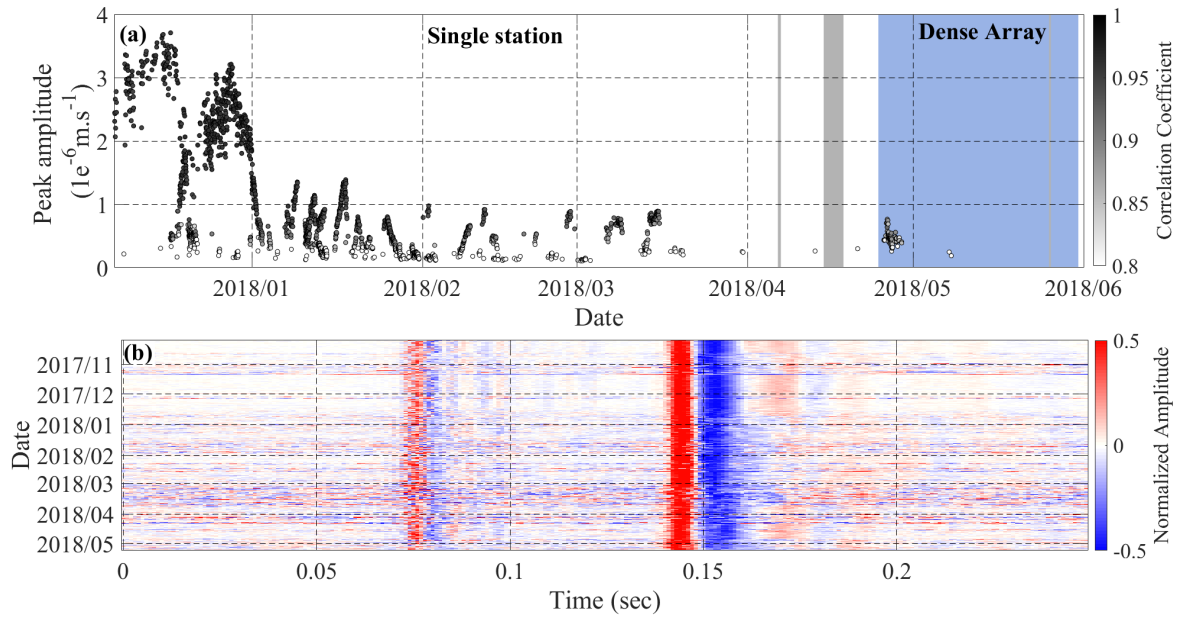
Figure 8.6: a) Time series of peak amplitude for one cluster of repeating basal events. Shading indicates correlation with template signal. Grey areas indicate gaps in the data, the blue area highlights the time period spanned by our dense-array experiment. b) Waveforms of all events of the cluster normalized by peak amplitude (using the North component of the borehole station). Each horizontal line represents one event. The zero time corresponds to the event time.

Location of events using Systematic match-field-processing

Contrary to in the previous section where a priori constraints on waveform characteristics and wave velocity are used to target basal stick-slip events, here we aim to test the capability of locating a wide range of seismic events generated by naturally occurring sources (either impulsive or continuous) with no a priori knowledge on waveform characteristics and minimal a priori knowledge on medium properties. The rationale is that the limited a-priori knowledge for source identification is balanced by the high spatial and temporal resolution provided by the array processing technique, which may enable the emergence of characteristic patterns that may be used for source identification.

We conduct Matched-Field Processing (MFP), which consists of recursively matching a synthetic field of phase delays between sensors with that obtained from observations using the Fourier transform of time-windowed data (Vandemeulebrouck et al., 2013; Chmiel et al., 2019). We obtain the synthetic field from a source model with a frequency-domain Green's function that depends on 4 parameters, which are the source spatial coordinates x, y and z and the medium phase speed c. The MFP outputs range from 0 to 1. The closer to 1, the more the modelled phased matches to observations, and therefore the more likely the source model properties represent the true source properties. Here we use a spatially homogeneous velocity field within the glacier, which has the advantage of a fast-analytical computation but also results in more ambiguity between z and c. Contrary to classical beamforming techniques in which a planar wave front is often assumed, our MFP approach considers spherical
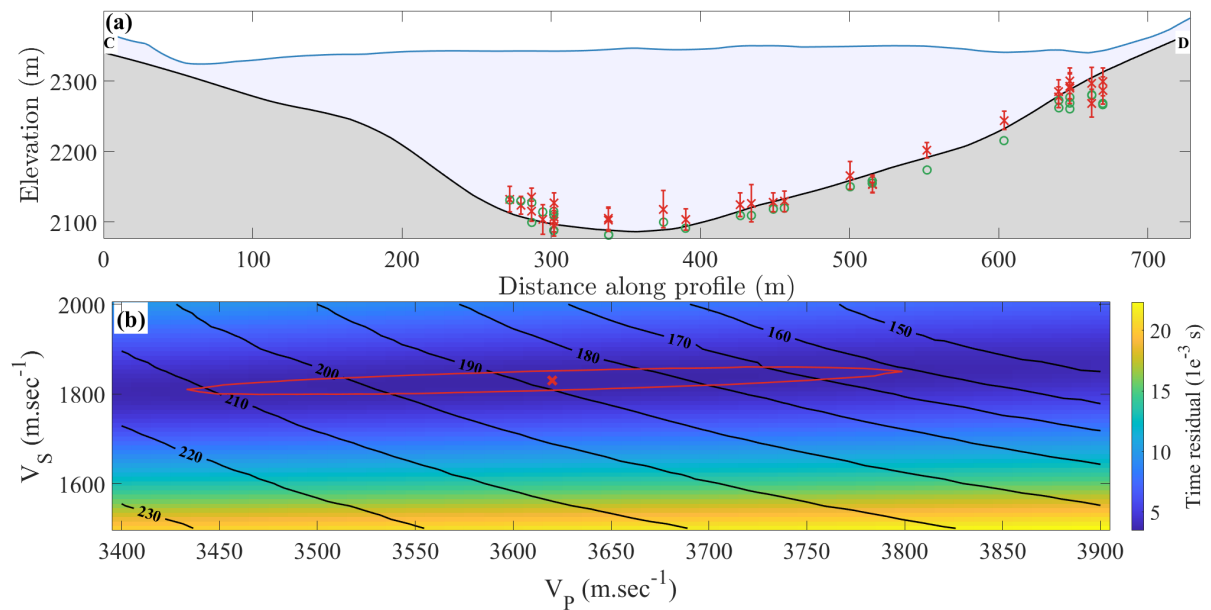
Figure 8.7: (a) Two-dimensional representation of stick-slip event locations (red crosses lines). The glacier cross-section corresponds to that along the CD profile shown in Fig. 8.8. Depth error bars show the 95% confidence interval. Red crosses indicate the bedrock depth at the location of each icequake, green circle indicate the projected depth along CD profile. (b) Average time residuals (background image) and average icequake depth (black contours) as a function of the seismic wave velocities Vp and Vs used to locate basal icequakes. The cross indicates the velocities V_P=3620 m.sec^{-1} and V_S=1830 m.sec^{-1} that minimize the average time residuals. The red line limits the range of V_P and V_S with an average residual smaller than 105% of the minimum value.

waves and allows locating sources closer to and within the array. To build a large catalog of events, we apply MFP over short time windows of 1-s with 0.5-s overlap, across 16 frequency bands of 4 Hz width equally spaced from 5 to 20 Hz and over the entire period. Calculating source locations over such a large number of windows requires minimizing computational cost. We do so by using a minimization algorithm that relies on the downhill simplex search method (Nelder-Mead optimization) instead of using a multi-dimensional grid search approach. As the exploration of the solution space is characterized by a certain level of randomness, we maximize the likelihood that our minimization technique finds a global minima and thus the dominant source over the considered time window through (i) starting the optimized algorithm from a set of 29 points located at a depth of 250 m inside and near the array (see black crosses in Fig. 8.9d) with a starting velocity c=1800 m.s^{-1} and (ii) taking the highest MFP output out of the 29 inversions found after convergence.

In Fig. 8.9b,c we present two examples of events located inside and outside the array and associated with a high MFP output of 0.92. The half-size of the focal spot in the MFP output field gives a measure of the location uncertainty (Rost and Thomas, 2002), which is about 10 m for events located inside the array and can increase up to 40 m when for events up to 100 m away from the array edges. Gathering all sources over one continuous day of record, we find that the associated MFP outputs distribution exhibit a heavy tail towards high values (see red area in Fig. 8.9a for an example at 13
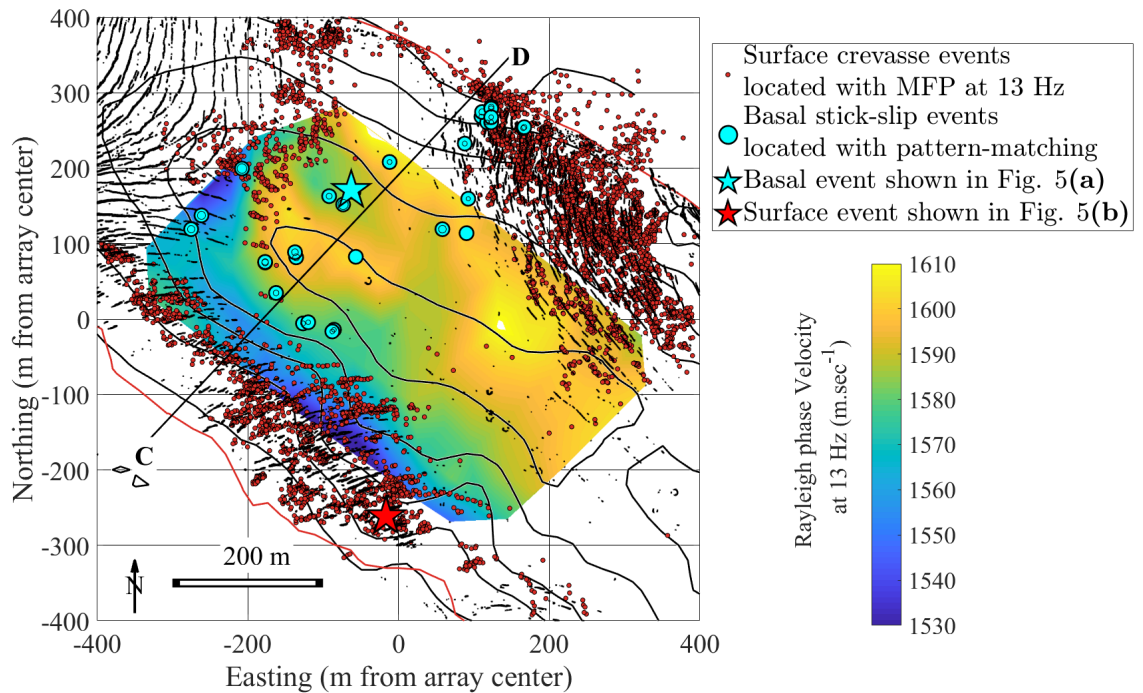
Figure 8.8: Map showing the positions of basal icequake clusters (filled circles) from classical source-location inversion and events located with match-field-processing (MFP) at 13 Hz during the whole period with an MFP output higher than 0.8 (red circles). Those events correspond mostly to surface events associated to crevasses and occasionally to rockfalls on the glacier sides. The colors of basal icequake circles (gray colorbar) indicate the distance above bed at which the events are localized. The blue-to-yellow colormap depicts phase velocities from Rayleigh-wave travel-time tomography at 13 Hz. The C-D profile refers to the profile in Fig. 7 and the green and gray stars refer, respectively, to the events shown in Fig. 5(a) and 5(b). Black points show crevasses, contour lines show ice thickness (m) and the red line shows the glacier extent as in Fig. 2.

Hz). Such a heavy tail is not obtained for a random field, in which case MFP outputs exhibit a distribution shifted towards almost one order of magnitude lower values. This suggests that most identified sources correspond to real and detectable seismic events. Well resolved seismic events with MFP outputs higher than 0.8 are located near the surface and nicely delineate crevasse geometries, such that they likely correspond to englacial fracturing (see red dots in Fig. 8.8). A restricted number of these events are however located outside of the glacier and likely correspond to rock falls. Typical waveforms associated with englacial fracturing events exhibit clear P and surface waves arrivals (Fig. 8.5b), as well as hyperbola arrivals that likely correspond to reflected waves at the glacier/bedrock interface (see black arrows in Fig. 8.5b).

Using catalogs of events for structure inversion

Dense-array techniques for seismic imaging often involve interferometry analysis on continuous seismic noise. Such techniques however require an equipartitioned wavefield inherited directly from homogenously distributed noise sources and/or indirectly from sufficiently strong scattering (Lobkis and Weaver, 2001; Fichtner and Tsai, 2019).
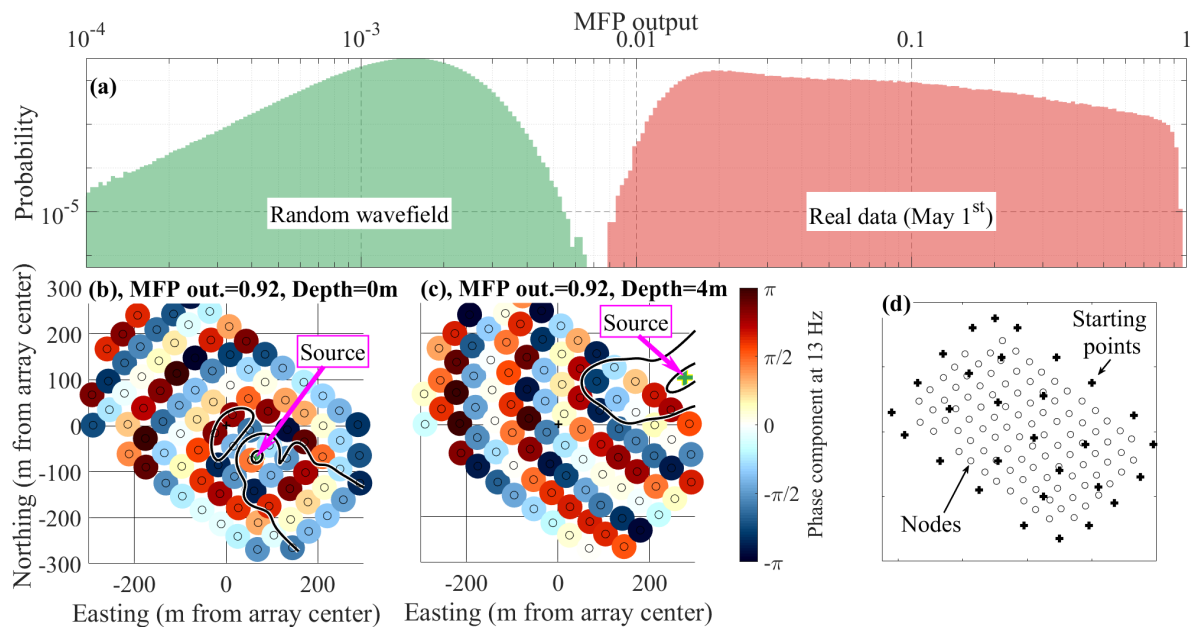
Figure 8.9: (a) Distribution of the MFP output values at 13 Hz as obtained when applying MFP on one day (May 1st) of real data (red) and on a numerically-generated random wavefield (green). The bottom panels (b) and (c) show the phase fields observed over a 1-s time window at 13 Hz for two selected events. Location obtained from MFP using our minimization process is shown by the pink arrow/green cross, while the contour line shows 0.1 and 0.8 MFP outputs iso-contours calculated by applying grid search over the glacier surface. Panel (d) shows the locations of the 29 starting points (black crosses) used for the MFP with respect to the nodes (black circles) location.

These conditions strongly limit the applicability of such techniques on glaciers where sources are often localized and waves in ice being weakly scattered (Sergeant *et al.*, 2020). An alternative way is to use localized and short-lived sources with known positions (Walter *et al.*, 2015) as those previously identified using our systematic MFP technique, which are numerous and quite evenly distributed in space (Fig. 8.8).

We consider the catalog of sources associated with MFP outputs larger than 0.6, located near the surface (z<10m) and close to the array (within a radius of 400 m from the array center). With these criteria our catalog includes about 106 sources gathered over the 35 days of continuous recordings. In order to further demonstrate that our MFP output inversions yield reliable velocities (i.e. the ambiguity between z and c is limited for these sources), we use the velocities as outputted from our MFP algorithm to establish the observed dispersion curve, as opposed to conducting a classical f-k analysis (Capon, 1969). We infer surface wave phase velocity at each frequency between 3.5 Hz and 25 Hz by fitting a Gaussian function to the probability density distributions of velocities in each frequency bin, and taking the center of the Gaussian function as the most representative velocity in that frequency bin (see Fig. 8.10a (inset) for an example at 13 Hz). We note that the presently constructed dispersion curve is similar to the one that would be obtained using a classical f-k analysis (not shown). We find that surface wave velocity increases gently from 1560 m.s^{-1} to 1630 m.s^{-1} as frequency decreases from 25 Hz down to 7 Hz, and then increases sharply up to 2300 m.s^{-1} as frequency decreases down to 3.5 Hz. These dispersion curve char-

acteristics can be reproduced with a three-layer one-dimensional elastic model (using the Geopsy package, (Wathelet *et al.*, 2020)) that incorporates a gentle velocity increase (from 1670 to 1720 m.s^{-1} for Vs) at 40 m depth and a drastic velocity increase (from 1720 to 2800 m.s^{-1} for Vs) located between 200 and 220 m depth (Fig. 10b). These values were obtained by trial and error tests in order to mimic both the high-frequency slight changes observed in the experimental dispersion curve and the large variation at low frequencies. The slightly slower velocities and density within the first 40-m deep layer may be due to surface crevasses, and are consistent with surface events being associated with smaller P wave velocities than those associated with stick-slip events at the ice/bedrock interface (Fig. 8.5). The 200- to 220-m deep drastic discontinuity reflects the ice/bedrock interface, consistent with of the radar-derived average glacier thickness beneath the seismic network (Fig. 8.2a).

We go one step further and perform two-dimensional surface wave inversions from eikonal wave tomography (Lin *et al.*, 2013b; Mordret *et al.*). We first extract c. 200,000 Rayleigh wave travel times using the best (associated with MFP outputs larger than 0.9) seismic events and then perform a simple linear inversion for the slowness (starting from a homogeneous initial model with a phase velocity of 1580 m/s, see Fig. 8.10a) assuming straight rays as propagation paths and an a-priori error covariance matrix that decreases exponentially with distances over 10 m. The weight of the spatial smoothing is chosen at the maximum curvature of the standard trade-off analysis (L-curve) based on the misfit value (Hansen and O'Leary, 1993), and the inversion produces a residual variance reduction of c.98% relative to the arrival times for the homogeneous model. In Fig. 8.8 we show the Rayleigh wave phase velocity maps obtained as a result of the travel-time inversion on a regular horizontal grid with steps of 5 m and using 13-Hz Rayleigh waves, which have largest sensitivity between 20 and 60 m depth (Fig. 8.10c) according to kernel sensitivity computations performed on the three layer elastic model (Fig. 8.10b) using the code of (Herrmann, 2013). We observe that locations with higher crevasses density are generally associated with lower phase velocities, as observed in the left and bottom sides of the array. This observation is however not systematic, since high velocities are also observed in the top right and top side of the array where crevasses are also present. This could be explained by crevasses being shallower or by crevasses having a different azimuthal orientation at these locations. This latter potential source of bias could be investigated by explicitly accounting for anisotropy in the tomography inversion scheme (Mordret *et al.*).

8.4   Discussion

Interpreting spatial and temporal variations ground motion amplitudes

Although our seismic array observations generally exhibit spatially homogeneous multi-day changes in seismic power, there exists specific times when changes in seismic power are spatially heterogeneous. A surprising observation is that these heterogeneous changes are observed down to the lowest frequencies (3 to 10 Hz) associated with
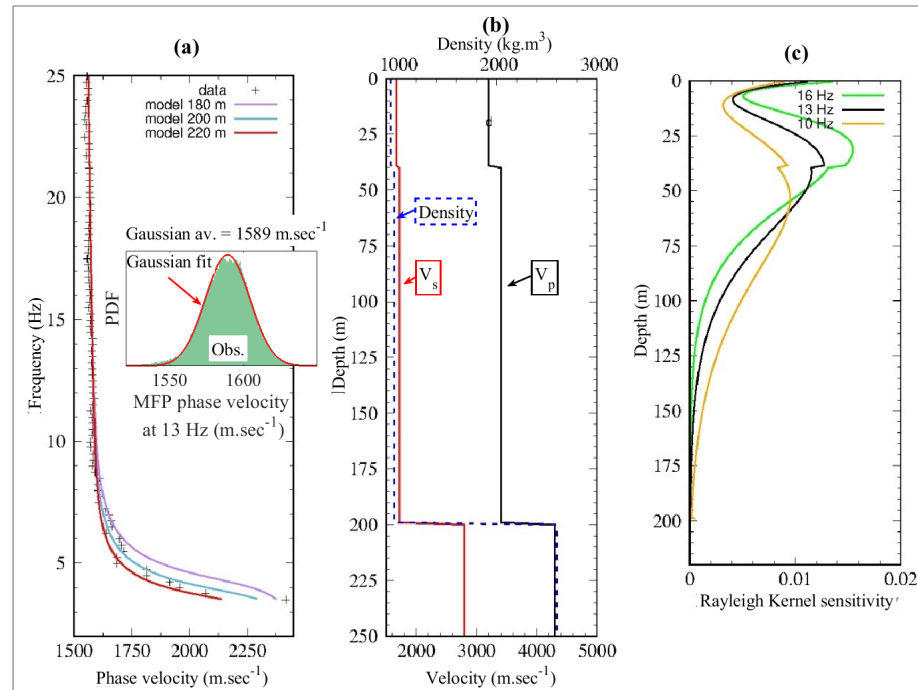
Figure 8.10: Inversion of a 1D structure using an average surface wave dispersion curve. (a) Comparison between the observationally-derived dispersion curve (black crosses) and synthetic Rayleigh wave dispersion curve computed using the elastic model displayed in (b) for glacier thicknesses of 180 m (purple), 200 m (blue) and 220 m (red). Inset show phase velocity distribution obtained from match-field-processing at 13Hz (green) with associated Gaussian fit (red) and central value. (b) Synthetic model used to predict the observed dispersion curve. (c) Sensitivity kernels of Rayleigh waves as a function of depth for three frequencies: 16 Hz (green), 13 Hz (black) and 10 Hz (orange).

wavelengths larger than the inter-station spacing, such that the observed spatial heterogeneity cannot solely be caused by inelastic attenuation. This suggests that ground motion amplitude measurements may be sensitive to a heterogeneous and intermittent subglacial hydrology network and/or to subglacial water flow sources exhibiting strong directivity variations.

It remains to be investigated as to (i) which process among near-field effects, site effects or source properties variability control the spatial variability in the signal amplitude and (ii) how to extract the source signature in order to investigate its properties.

Progress towards understanding the origin of amplitude spatial variability in the seismic signal could be made in various ways. Punctual sources identified from the MFP analysis could be used to investigate seismic wave attenuation/amplification/scattering and quantify the effect of site response in the overall observed variability in seismic power. Site response could then be related to site attributes (e.g. crevasses, thickness, snow layer) in order to further understand the effect of glacier geometrical features on the seismic amplitude wavefield. Full waveform modeling combined with wave polarity analysis could also be conducted in order to further understand how wave focusing in the near field domain could lead to such heterogeneous amplitude fields. In order to investigate subglacial hydrology properties (e.g. water pathways, pressure/flow ve-

locity conditions) one could then retrieve the subglacial hydrological properties from inverting the surface amplitude field. Investigating spatial changes in the seismic amplitudes over our array may give access to the yet poorly captured geometry of the subglacial drainage system.

Towards a better understanding of the physics of stick slip events

The application of template matching to our dense seismic array observations confirms that stick-slip events operate at the ice-bed interface, as previously suggested by Helmstetter *et al.* (2015b) based on single station observations. The additional observation that events are all located in the downglacier part of the array and thus not homogeneously distributed provides further observational support that specific bed conditions (e.g. water pressure, bed shear stress, bed roughness, bed topography, carried sediments) are necessary for these events to occur (Zoet *et al.*, 2013; Lipovsky *et al.*, 2019).

Further insights into the physics controlling the spatio-temporal dynamics of these events could be gained with this dense array through preforming relative event location within each cluster, instead of simply inferring a cluster location as presently done. This could be done from cross-correlations between events at each station and relocating events using double-differences methods. Such an analysis could allow studying the differences in sources characteristics within each cluster with more details and identifying whether or not stick-slip asperities migrate, and if they do in which directions and at which rates relative to glacier dynamics.

Using systematic source location to retrieve sources and structural properties

Systematic MFP analysis with adequate parametrization opens a route to continuous, automatic, and statistics-based monitoring and imaging of glaciers. A wide diversity of seismic sources may be identified and studied separately with this technique by scanning through the different ranges of MFP outputs. High MFP output observations may be used to study the spatio-temporal dynamics of crevasse propagation with unprecedented details. Such observations may allow better understanding the underlying mechanisms associated with crack growth and propagation, in particular the potential role of fluids in modifying the stress field. Lower MFP outputs may be used to investigate spatially distributed sources generating coherent signals only over a restricted number of array stations. These distributed sources may include a wide range of tremor sources (e.g. water flow) or various features acting as scatterers. MFP outputs may also offer unique opportunities for seismic imaging based on identifying specific events generating waves of particular interest for structural analysis, such as bed-refracted waves as shown in Fig. 8.5 (see black arrows).

8.5   Summary

We present a dense seismic array experiment made of 98 3-component seismic stations
continuously recording during 35 days in early spring on the Glacier d'Argentière,
French Alps. The seismic dataset is supplemented by a wide range of complementary
observations obtained from ground penetrating radar, drone imagery, GNSS position-
ing and in-situ instrumentation of basal glacier sliding velocities and subglacial water
flow discharge. We show that a wide range of glacier sources and structure charac-
teristics can be extracted with high definition through conducting multiple seismic
processing techniques including event detection from template matching and system-
atic match field processing. Future studies focusing more specifically on each aspect
of the herein presented observations may enable novel quantitative insights on spatio-
temporal changes in glacier dynamics and structure.

Acknowledgements

8.6   Supplementary materials: spectrograms of all nodes

I include here the 98 spectrograms acquired during the RESOLVE project both because
this is part of the RESOLVE study but also because in the following two chapters I
investigate what cause the spatial and temporal variations in seismic amplitude.
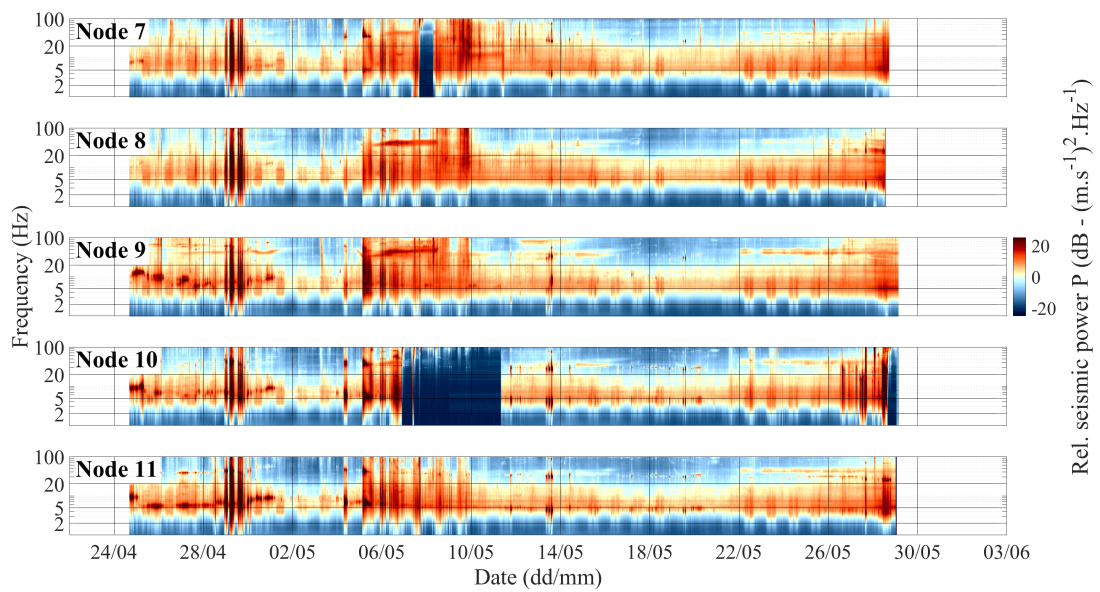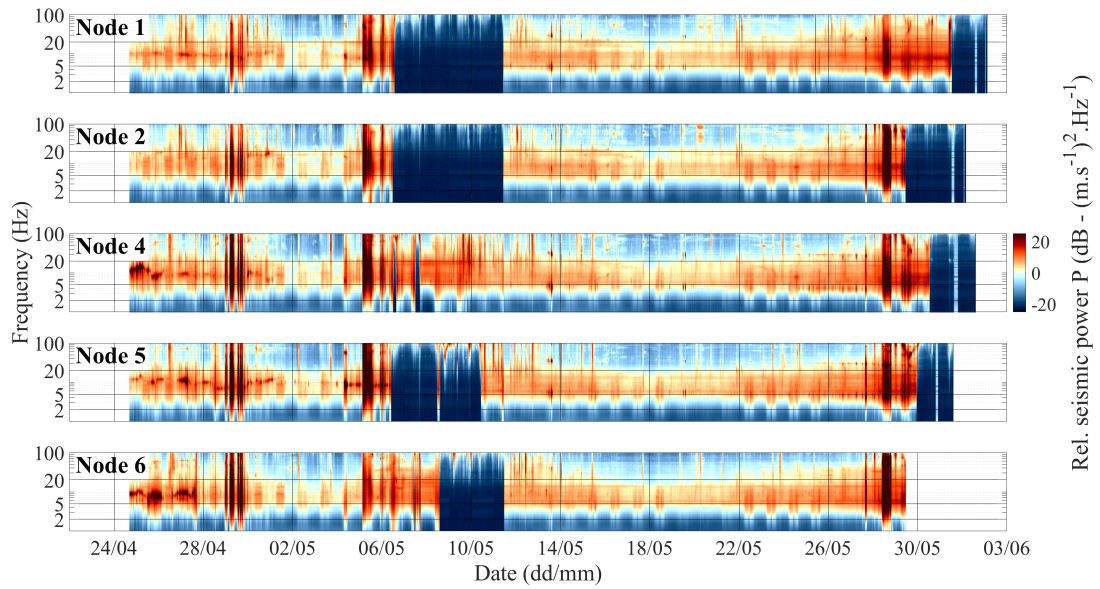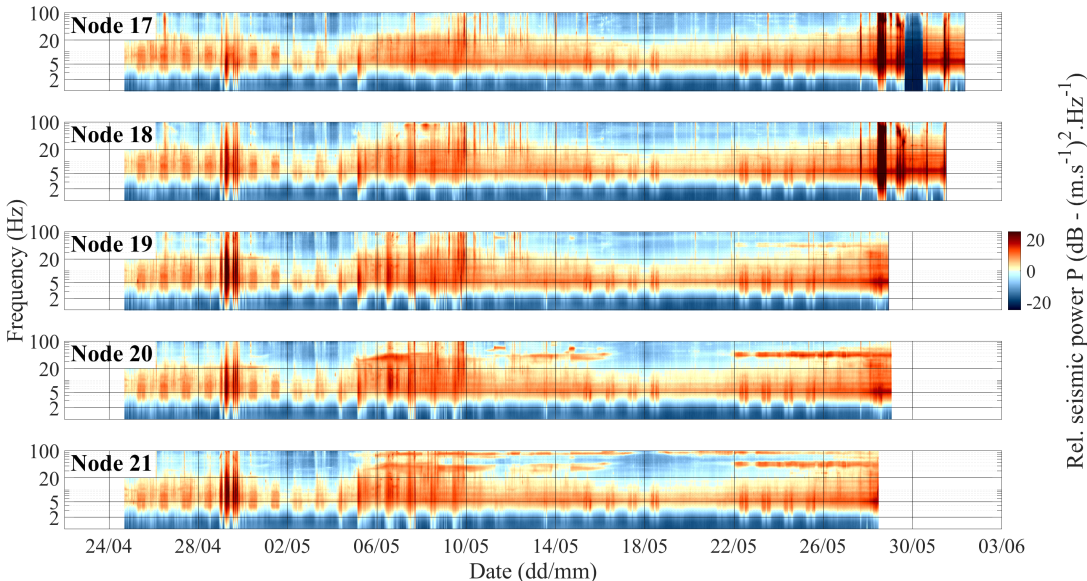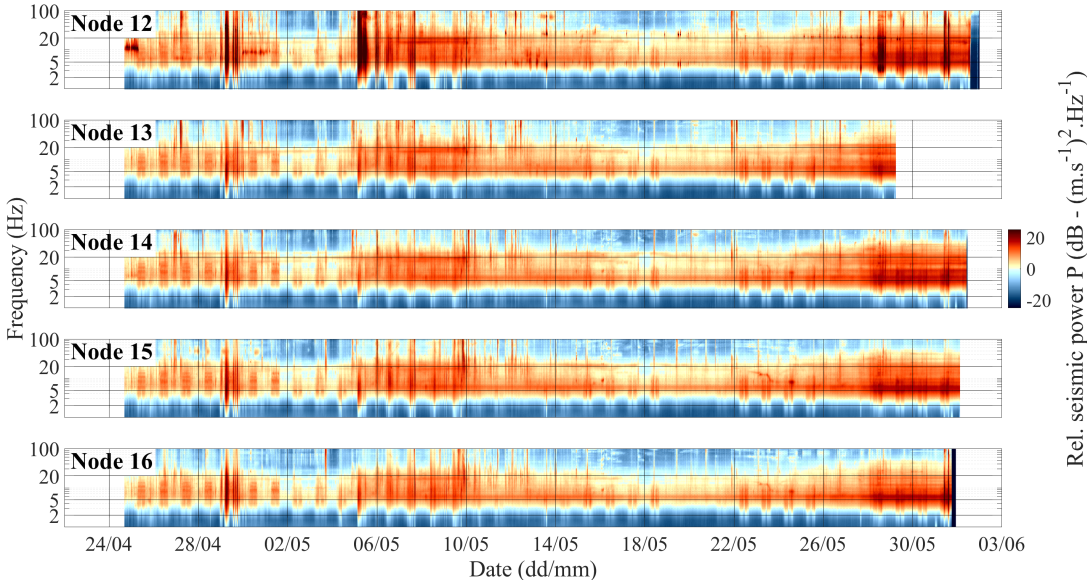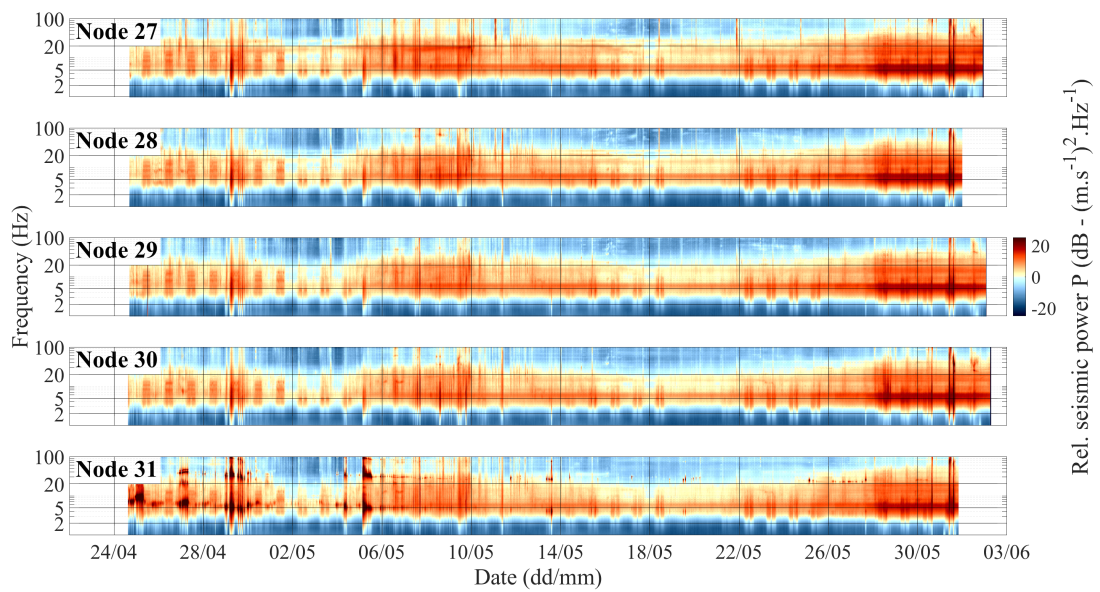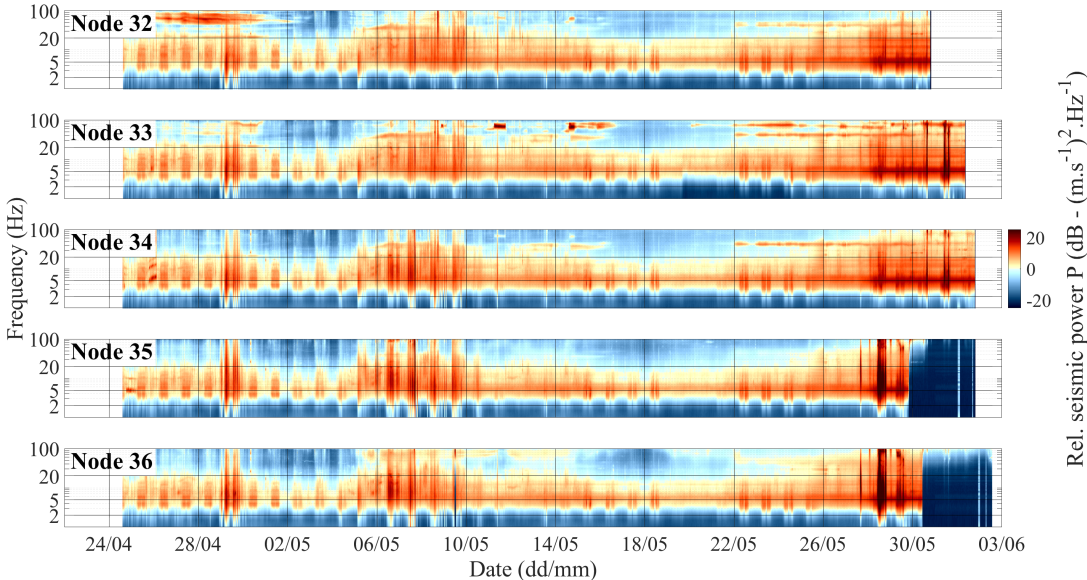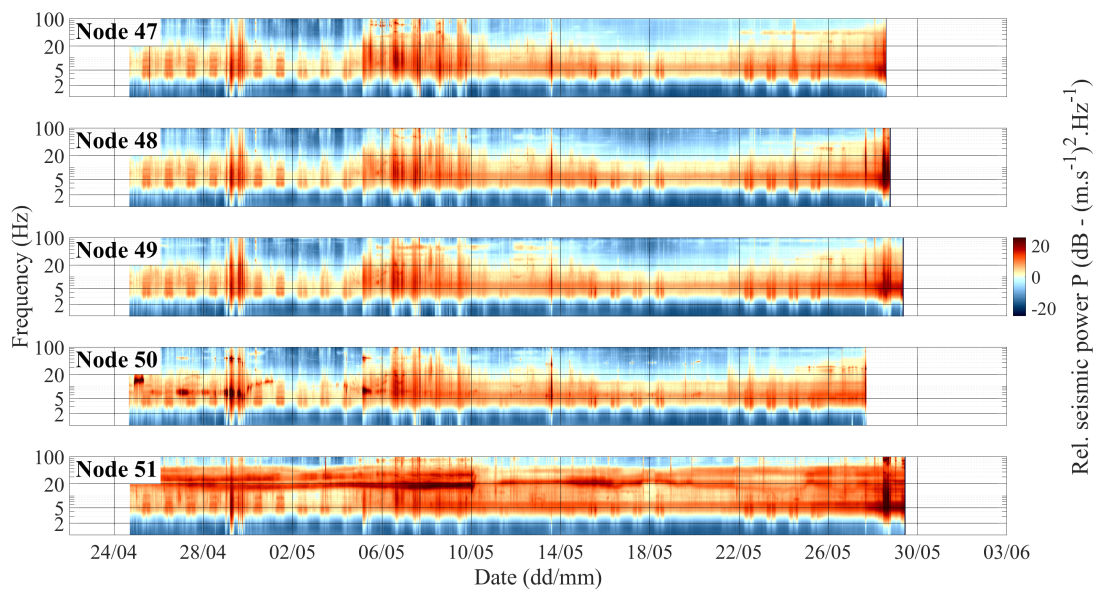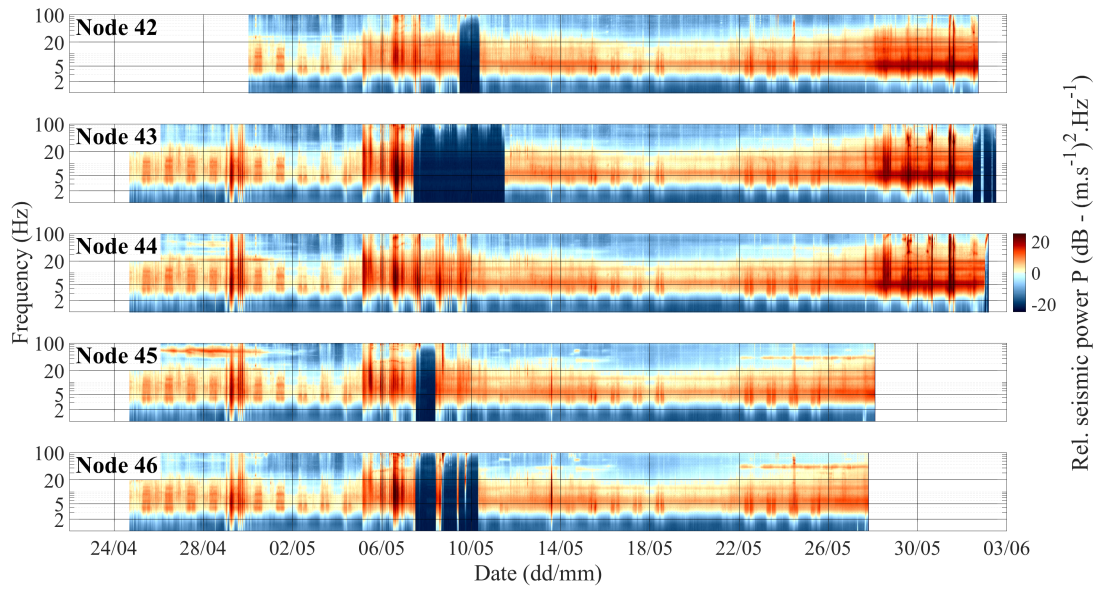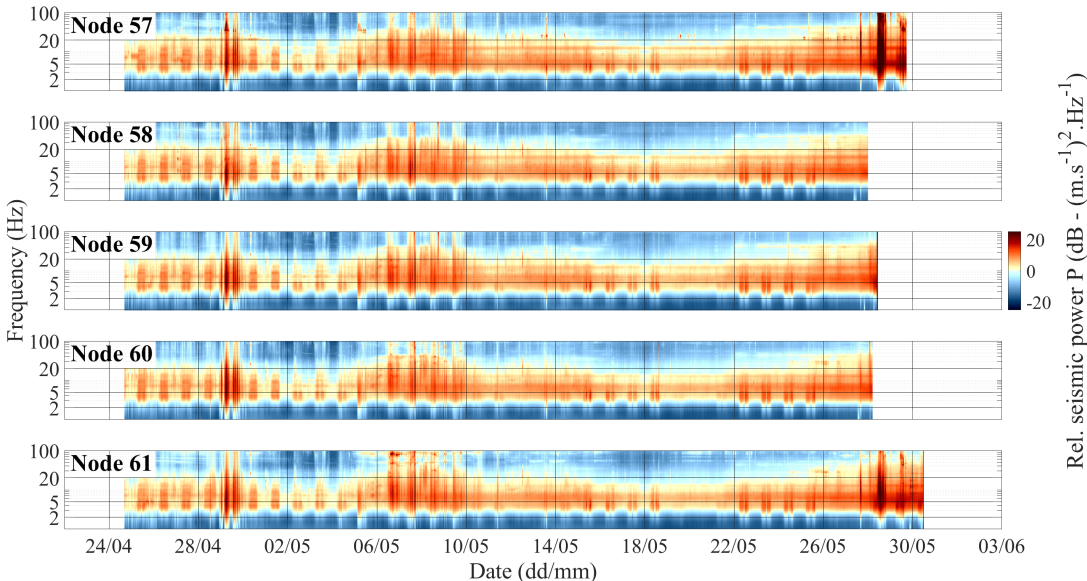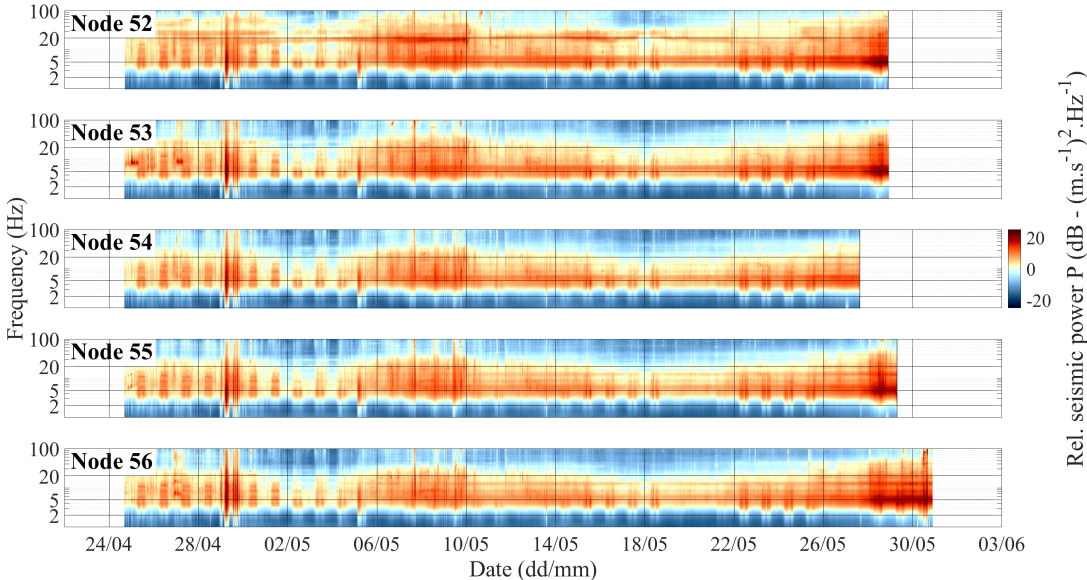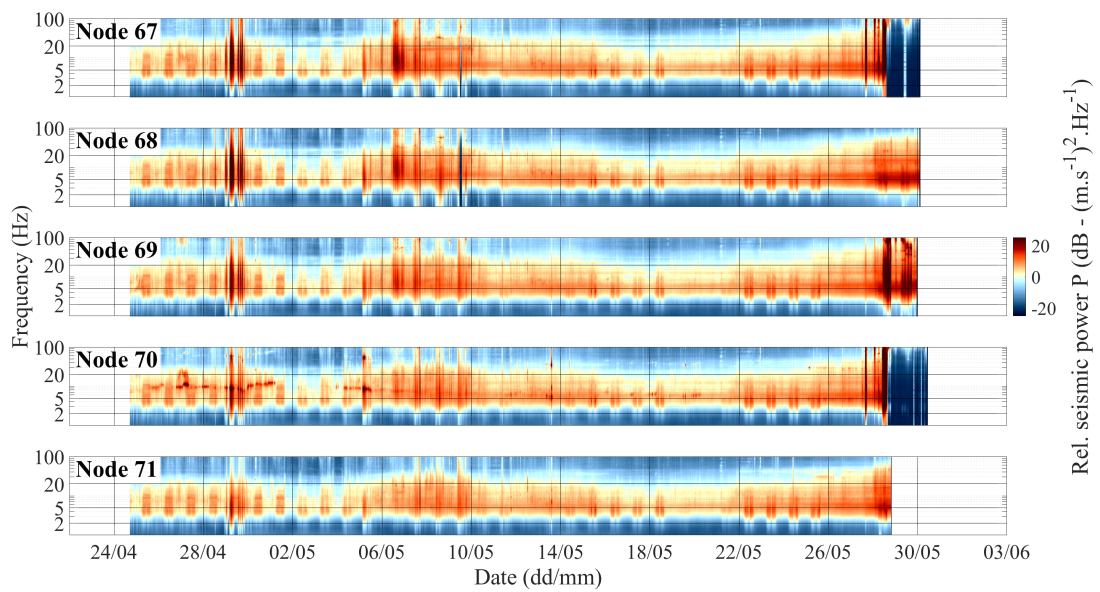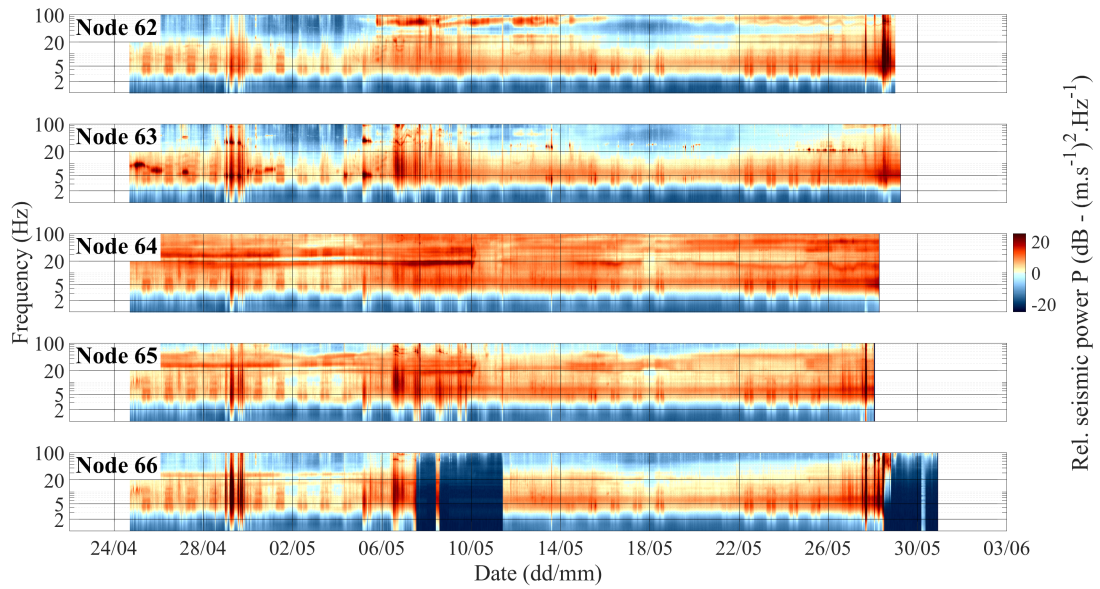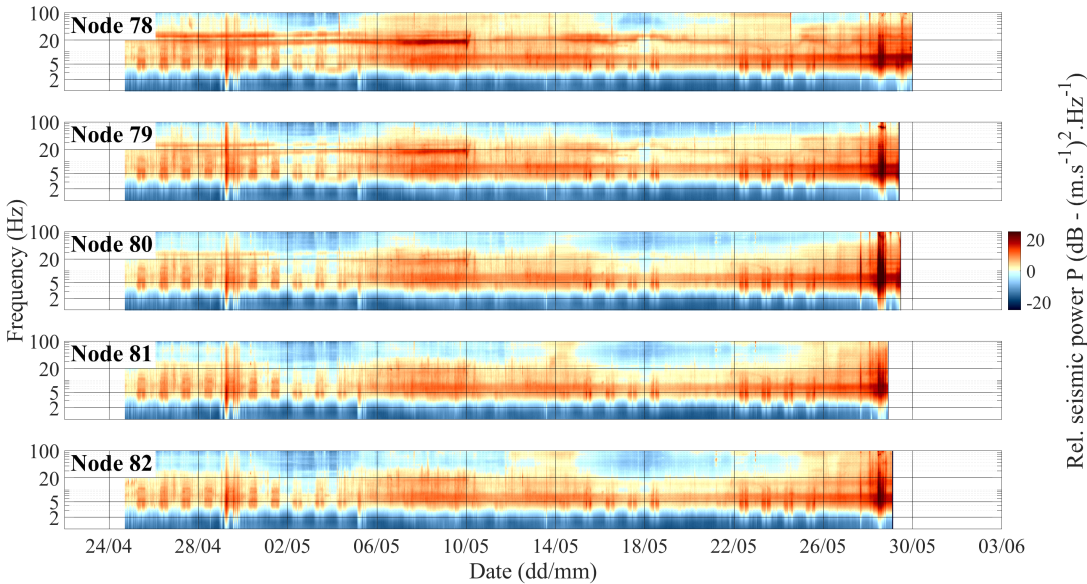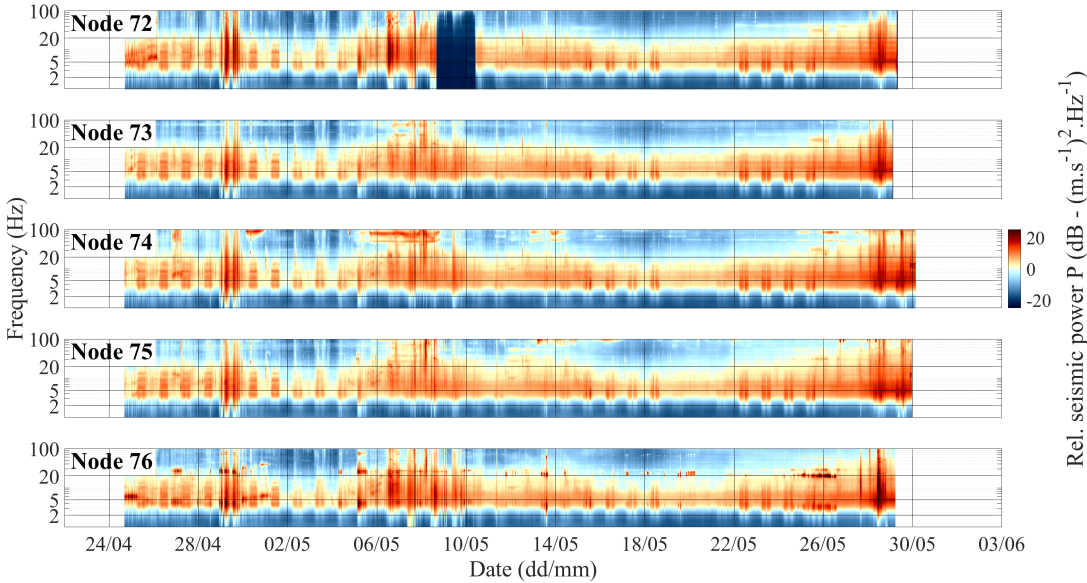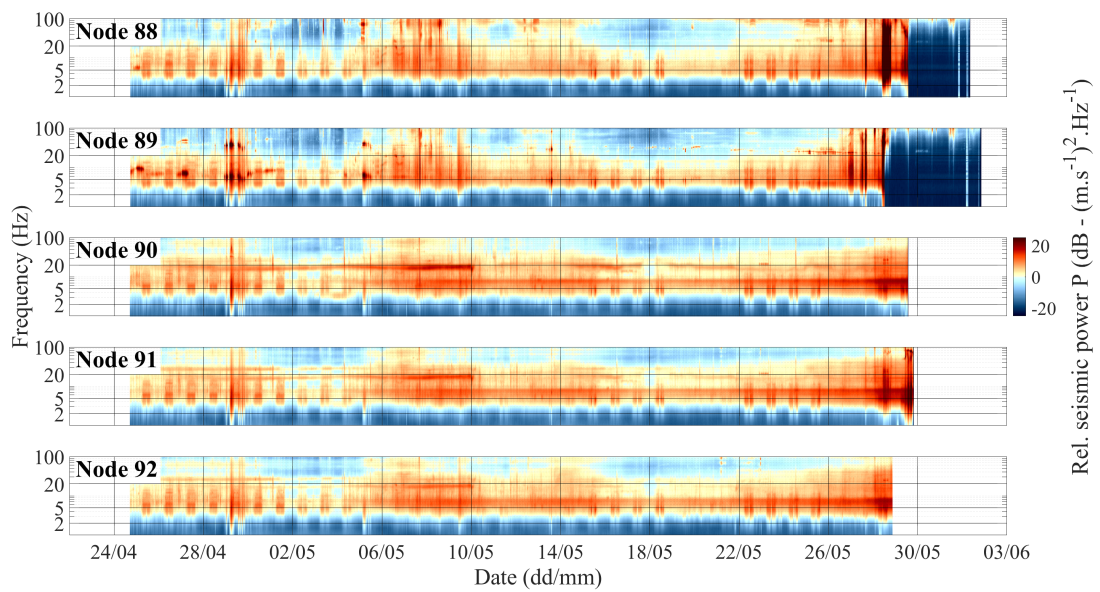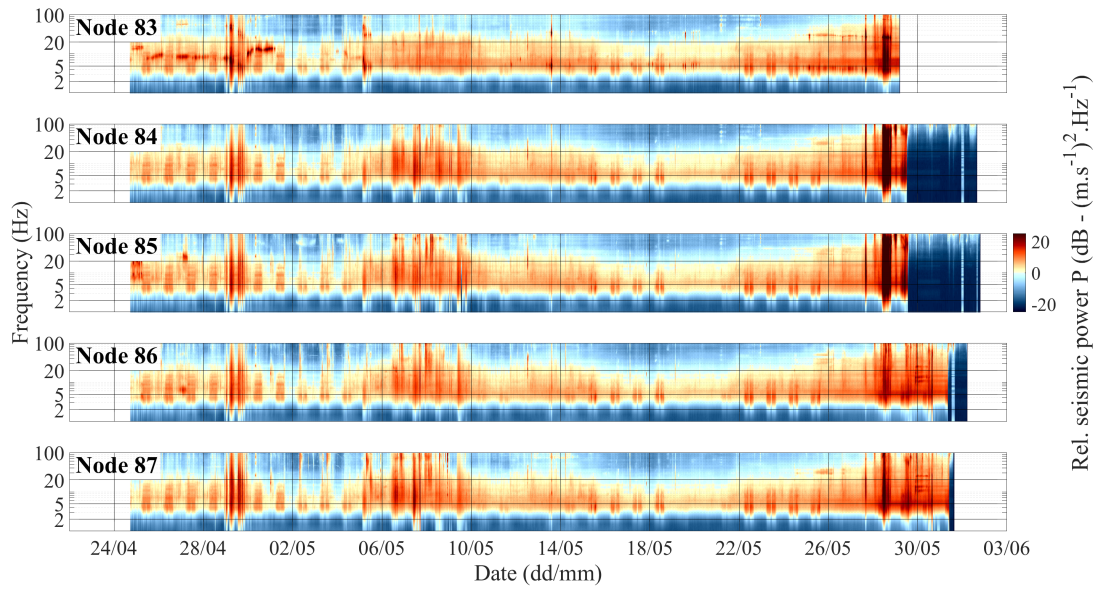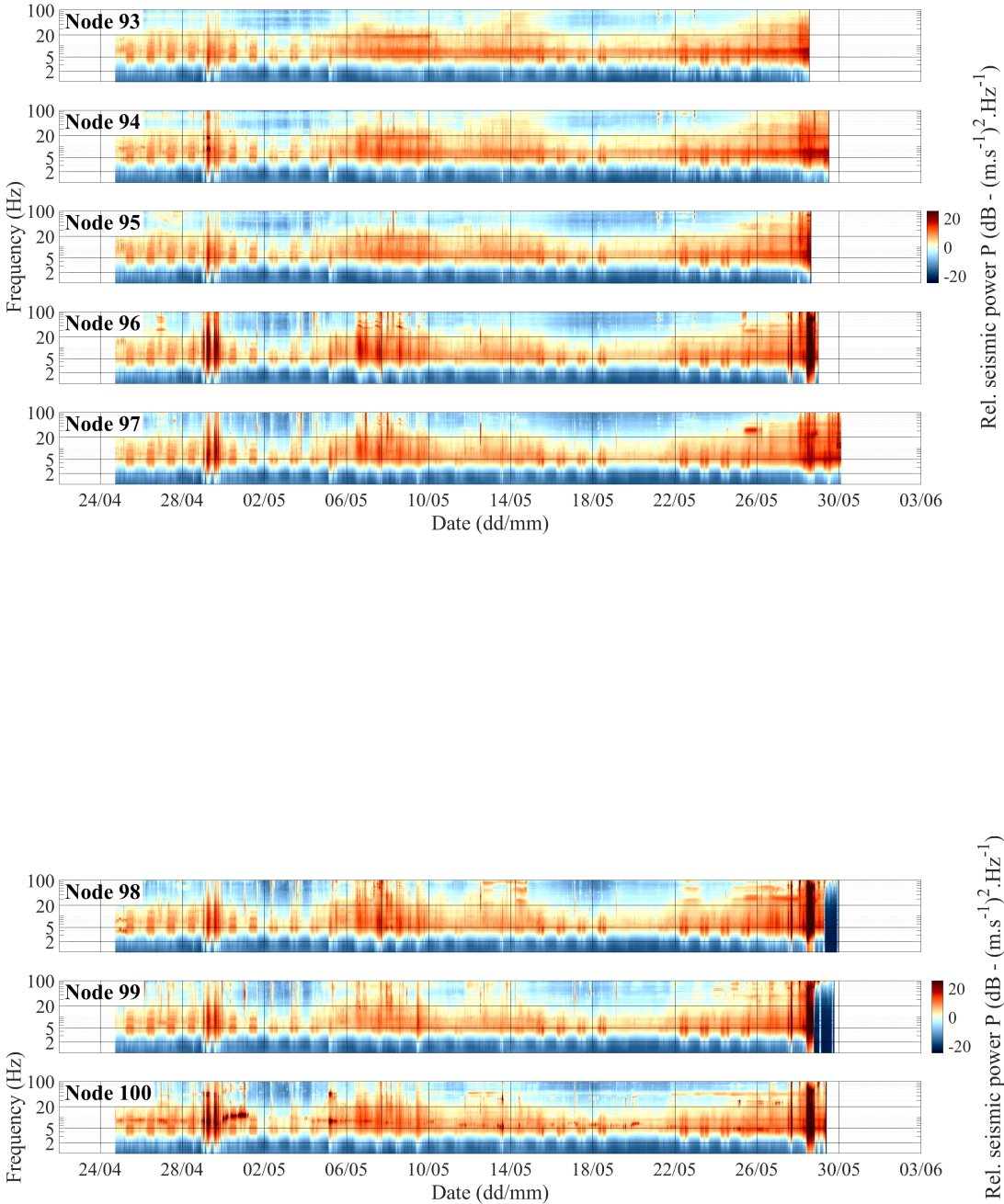
Chapter	**9**

Resolving the 2D temporal evolution of subglacial drainage with dense seismic array observations

This chapter is centred on a paper that was submitted to Nature Geosciences on October 9th 2020 : **Ugo Nanni**, *Florent Gimbert, Philippe Roux, Albanne Lecointre : Resolving the 2D temporal evolution of subglacial water flow with dense seismic array observations.*

Short note to the reader

Here I use the unique dataset obtained during the RESOLVE-project to derive the first two-dimensional maps of the subglacial drainage system. I decided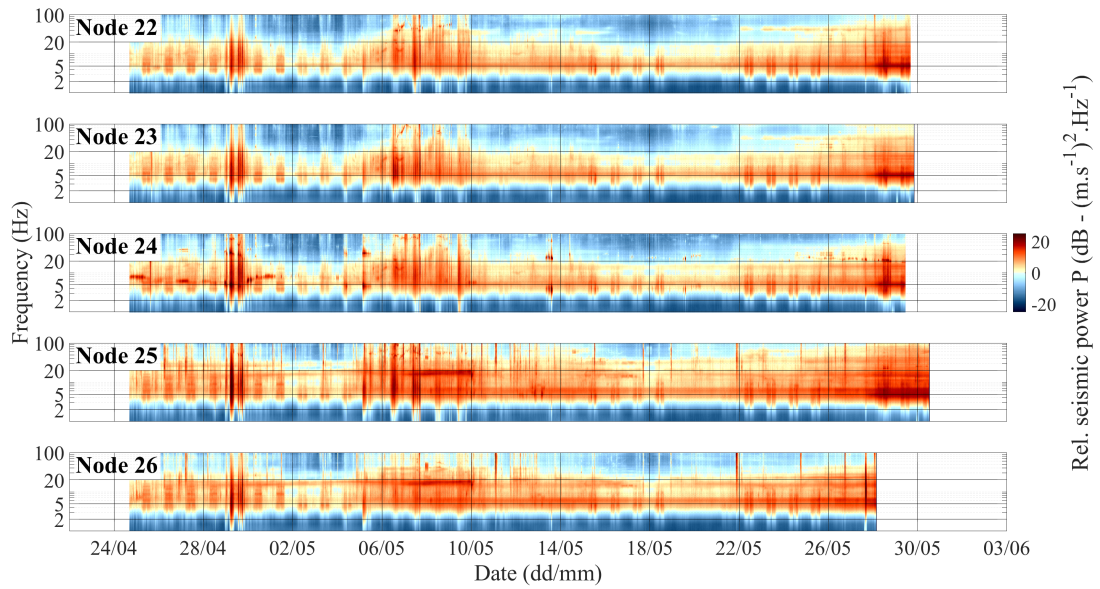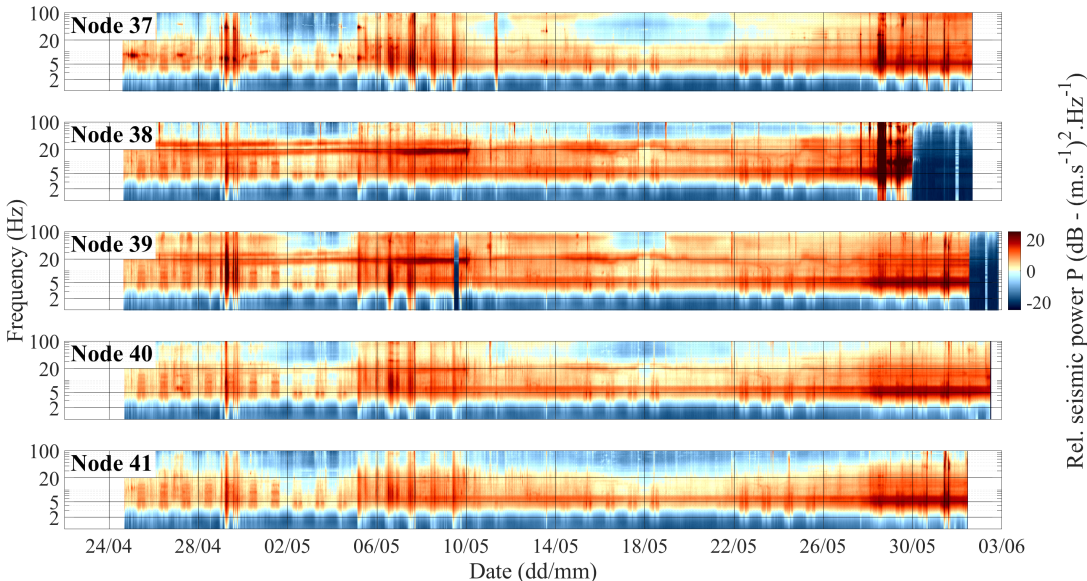 to submit this paper to Nature Geosciences as this study answer (i) a key issue for subglacial hydrology dynamics, which is retrieving the spatial configuration of the subglacial drainage system and (ii) a key issue in seismology, which is locating source of seismic noise spread in space and varying in time. Our investigation strategy will also benefit to other communities that study, for instance, volcanoes (Soubestre *et al.*, 2019), aquifers (Larose *et al.*, 2015), rivers (Bakker *et al.*, 2020), earthquakes initiation (Gradon *et al.*, 2019), as we introduce an innovative approach to locate distributed sources of seismic noise acting at the same time.

Abstract

Water routed at the ice-bed interface exerts a major control on glacier basal motion, which strongly sets the contribution of glaciers and ice sheets to sea level rise. However, our understanding of when and where subglacial water flow enhances or limits glacier flow is limited due to the paucity of direct observations on subglacial drainage characteristics. Here we demonstrate that dense seismic array monitoring combined

with an innovative systematic source location technique allows us, for the first time, to retrieve a two-dimensional map of the subglacial drainage system as well as its day-to-day temporal evolution. We are able to observe when and where the subglacial drainage system is distributed through a connected cavity system favoring fast glacier flow versus localized through a channelized system preventing fast glacier flow. Applying a similar seismic monitoring strategy in other glacier settings including Ice Sheets may help diagnose their susceptibility to increased meltwater input due to climate warming.

9.1 Introduction

Meltwater produced at the surface of glaciers is routed to its bed through crevasses and moulins and moves towards its terminus through the subglacial drainage system (Shreve, 1972). There, water pressure controls ice-bed mechanical coupling, which sets glacier sliding speeds and therefore exerts a major control on the stability of glacier and ice sheets (Zoet *et al.*, 2013; King *et al.*, 2020) and their contribution to sea-level rise (Iken *et al.*, 1997; Bartholomew *et al.*, 2010). Subglacial water pressure exhibits a complex dependency on the way water is routed at the base, which strongly depends on the subglacial hydraulic connectivity. Where subglacial channels are present the drainage system is efficient with high hydraulic connectivity and tends to reduce subglacial water pressure and promote low glacier sliding speed (Schoof, 2010; Tedstone *et al.*, 2015). At the contrary, where cavities are present, the drainage system is often inefficient with low hydraulic connectivity and tends to enhance subglacial water pressure and promote high glacier sliding speed (see Methods). The studies of Andrews *et al.* (2014); Hoffman *et al.* (2016) proposed that, in Greenland, cavities could be isolated or connected to, and drained by, the efficient drainage system. The presence of weakly connected cavities with very low permeability (Hoffman *et al.*, 2016) might regulate basal traction of large portions of the bed and be responsible to low winter velocities in Greenland or long term changes in basal traction (Maier *et al.*, 2019). Recent borehole observations (Rada and Schoof, 2018) in Alaska support the existence of such system even on alpine type glaciers and suggest that the degree of hydraulic connectivity across cavities play an important role on basal sliding velocities as it controls the spatial persistency of high water pressure areas. However, because of very limited observations of the drainage system, it remains uncertain when and where isolated cavities, connected cavities and/or channels operate and therefore under which conditions (e.g. water supply, glacier geometry) meltwater supply to the bed enhances or limits fast glacier flow. The majority of field measurements used to investigate subglacial water flow are in-situ measurements that often require ice-drilling (Rada and Schoof, 2018). These are thus point-scale and associated with limited temporal coverage, such that they provide a very partial representation of the heterogeneous nature of the subglacial flow network (Rada and Schoof, 2018; Davison *et al.*, 2019; Chandler *et al.*, 2013). In particular, we lack clear observations for assessing which area of the bed experiences one of the three components of the subglacial drainage system and how those systems evolve through time. This observational lack limits our understanding on the role played by subglacial hydrological conditions on promoting fast basal sliding and therefore causes large uncertainties in predicting the future of glaciers and ice sheets (Tedstone *et al.*, 2015; Dehecq *et al.*, 2019).

Recent works indicate that seismic noise generated by subglacial turbulent water flow
(Bartholomaus *et al.*, 2015a; Preiswerk *et al.*, 2018) can be used to retrieve temporal
changes in its physical properties (e.g. water pressure or drainage efficiency) (Gimbert
et al., 2016; Nanni *et al.*, 2020) and possibly locate subglacial water flow in space (Lind-
ner *et al.*, 2020; Vore *et al.*, 2019). Yet, the few studies that have tried locating water
flow were limited by sparse seismic observations (Venkatesh *et al.*, 2003; Burtin *et al.*,
2010; Vore *et al.*, 2019; Lindner *et al.*, 2020) and/or methodological approaches that did
not allow retrieving source epicentral coordinates (Burtin *et al.*, 2010; Vore *et al.*, 2019).
Locating noise-like sources indeed represents a major geophysical challenge (Rost and
Thomas, 2002) since these sources are widely and continuously distributed in time
and space, such that retrieving source locations requires dealing with an incoherent
wavefield resulting from the superposition of multiple sources acting simultaneously
(Fig. 7.5). As a consequence, phases from different sources may not sum-up coherently
and averaging the phase field prior to location, as commonly done, is not suitable for
locating short-lived distributed noise sources.

Here we demonstrate that well resolved maps of the subglacial drainage system can be
retrieved from conducting an innovative passive seismic analysis. We use a particu-
larly dense seismic array and adapt the Matched-field-processing (MFP) analysis (Rost
and Thomas, 2002) to the particularity of dealing with distributed sources. To do so
we conduct a short-term and small-scale analysis of the phase coherence with spatial
sampling at or below the seismic wavelength (ideally at a sub-wavelength scale (Rost
and Thomas, 2002)) near the targeted sources (in the near-field, i.e. within a couple of
wavelengths from the sources (Almendros *et al.*, 1999)).

9.2   Seismic monitoring and source location strategy

We use a one-month 98 three-components seismic record acquired at the surface of the
Glacier d'Argentière (French Alps, Fig. 9.1) during the onset of the melt-season. At
this location subglacial water flow strongly influences glacier dynamics (Vincent and
Moreau, 2016) and generates continuous seismic noise most pronounced in the [3-7]
Hz (Nanni *et al.*, 2020) frequency range, in which seismic wavelengths are on the order
of [200-500] m. With 40 to 50-m sensors spacing our array covers an area of 400x600
m2 and enables near-field and sub-wavelength analysis of the subglacial-water-flow-
induced seismic noise. We locate seismic sources through applying Matched-field-
processing (MFP), which consists in recursively matching predicted with observed
phase delays (see Methods). MFP has been extensively applied to locate spatially
well-separated sources such as those generated by hydrothermal activity (Legaz *et al.*,
2009), oil and gas injection (Chmiel *et al.*, 2019) (Fig. 7.5), icequakes (Sergeant *et al.*,
2020) or englacial moulins (Röösli *et al.*, 2014), but has still been poorly applied to lo-
cate distributed seismic sources as expected for subglacial water flow (Venkatesh *et al.*,
2003). We adapt this technique to the particularity of dealing with distributed sources
through conducting a systematic (every 0.5 seconds) analysis of the phase coherence
over 1-sec long time windows with no a-priori on the waveforms or on the number
of sources. We calculate an MFP output as the correlation between the observed and
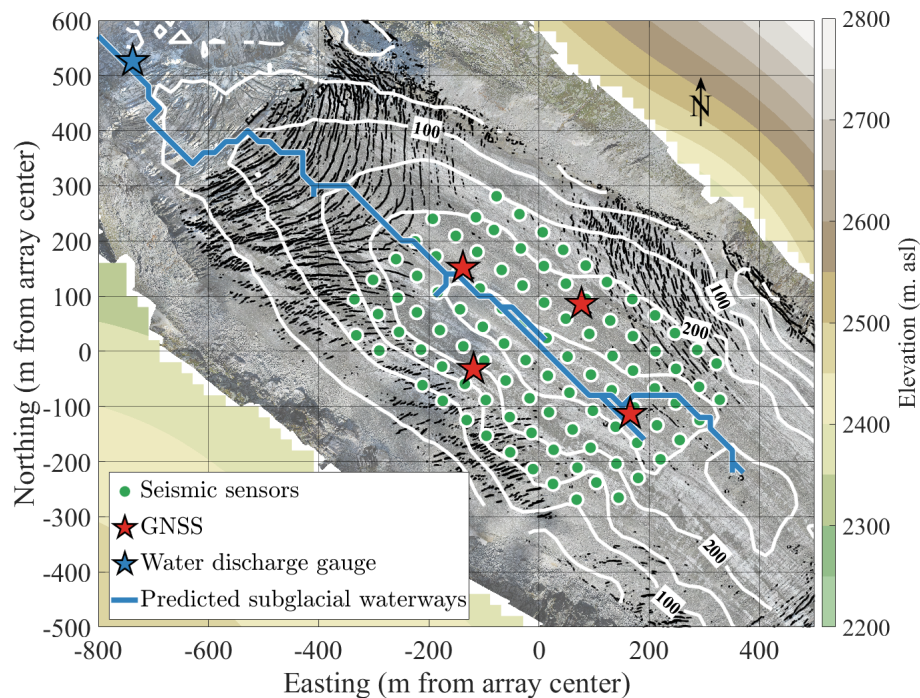
Figure 9.1: Monitoring setup of Glacier d'Argentière. Aerial view of Glacier d'Argentière field site (France, Mont Blanc mountain range) and location of the instruments used in this study. The seismic network (green dots) is composed of 98 seismic stations Fairfield Nodal Z-Land 3 components and is located according to positions at the beginning of the survey period. Surface displacement is measured thanks to four GNSS stations functioning over the study period (red stars). Subglacial water discharge (blue star) are measured thanks to direct access to the glacier base from excavated tunnels. White contour lines show 50 m-spaced ice thickness contours as obtained from combining radar measurements and surface elevations. Blue line show subglacial waterways as predicted from hydraulic potential calculation. Glacier flows towards northwest (up-left).

modelled phase delays and it ranges from 0 to 1. A clear global phase coherence yields an MFP output close to 1 and indicates a clear dominant and punctual source (e.g. crevasse opening (Sergeant *et al.*, 2020)). If several local phase coherences exist, as expected for flowing water, this indicates multiples sources spread over the area and the associated MFP output is low. In such case our innovative location scheme allows concomitantly localizing up to 29 different sources (see Methods) and thus enables revealing weak and distributed noise sources that could otherwise be hidden by the most dominant source (Sergeant *et al.*, 2020). With this systematic approach we localize more than 10^6 seismic sources per day (Fig. 9.3(a)), which allow us to evaluate statistically representative spatio-temporal source patterns.

9.3   Methods

In the original paper Methods are located on the supplementary materials.

Dense seismic array survey

From April 22nd to June 6th 2018 we installed and maintained 98 three components Fairfield Nodal Z-Land geophones over a 400 x 600 m^2, area with a station-to-station spacing of 40 m in the along-flow direction and of 50 m in the across-flow direction, and over an altitude range of [2330-2390] m (Fig. 9.1; https://resolve.osug.fr/). All stations have a 500 Hz sampling rate and a low cut off frequency of 5 Hz. Nodes were installed at a depth of 30 cm in the 4-m thick snow cover, and had to be reinstalled on May 11th due to snow melt, which occurs at a rate of 5 cm per day. The reader should refer to Chapter 8, page 109 for a detailed description of the experiment.

Complementary measurements

Concomitantly with our seismic survey, we use continuous records of subglacial water discharge, which is measured in subglacial excavated tunnels maintained by the hydroelectric power company Emosson S.A about 600 m downstream of the nodes-array-center (at 2173 m a.s.l.). We also installed 4 GNSS stations at the corners of the seismic-array to measure the surface velocity during this period that is on the order 0.1 m. d-1 at this time of the year and this area of the glacier (Vincent and Moreau, 2016). One week prior to the seismic deployment we conducted a ground penetrating radar campaign with a 5 MHz signal over our study area to improve previous estimates of the bed topography made by of Vincent *et al.* (2009). We also conducted in September 2018 an aerial survey in order to derive a digital elevation model of the glacier surface using stereo-photogrammetry. Combining these two digital elevation models, we calculated the ice thickness of our study area as shown in Figure 9.1. Ice thickness reaches up to 270 m at the center of the seismic array, with a well-marked talweg (valley-shaped bed) along the glacier flow direction and a progressive diminution of the ice thickness downglacier of our array. Air temperature and precipitation measurements are obtained at a 0.5 h time step through an automatic weather station maintained by the French glacier-monitoring program GLACIOCLIM (https://glacioclim.osug.fr/) and located on the moraine next to the glacier at 2400 m.

Hydraulic potential calculation

We calculate the hydraulic potential ϕ following (Shreve, 1972) as

$$\phi = \rho_w g z_b + K[\rho_i g(z_s - z_b)] \tag{9.1}$$

Where g is the acceleration due to gravity (9.81 m.s^{-2}), ρ_w is the density of water (1000 kg.m^{-3}), ρ_i is the density of ice (917 kg.m^{-3}), z_b and z_s are the elevation of glacier bed and surface (m) and K the ratio of water pressure/ice overburden pressure, i.e. a uniform flotation fraction. Here we use a flotation fraction of 0.5 that likely represents a case where subglacial channels have developed enough to efficiently drain the bed (Shreve, 1972). We then calculate the water flow directions based on the hydraulic potential gradients by following the path that minimize the gradient with minimum

upstream area of 150m2 for the waterway to initiate using the TopoToolBox developed by Schwanghart and Scherler (2014).

Matched field processing

For the ease of understanding I have added an extra figure (Fig. 9.2) to the original manuscript that schematizes our methodology.

Matched field processing (MFP) consists in providing a probabilistic estimate of the dominant source location (Kuperman and Turek, 1997) from evaluating the phase coherence of the seismic signal over an array of sensors. The method consists in recursively matching the phase delays of a model-based synthetic wave field ("trial source") with the phase delays observed between the sensors over the array. This consists in first computing the discrete Fourier transform of a given data vector $d(t)$ recorded by the 98 sensors over a frequency ω to obtain the complex data vector $d(\omega)$ and calculate the corresponding cross-spectral density matrix (CSDM) as

$$K(\omega) = d(\omega)d^H(\omega), \tag{9.2}$$

where H is the Hermitian transpose. The CSDM captures the relative spatial phase difference between the sensors. We then define a set of values to be explored for trial sources. In this study we set 4 degrees of freedom for the MFP processing with a depth, range and phase velocity grid (X, Y, Z, C). For each element a of this 4D grid we modelled Green's function replica vector $d(\omega, a)$ under the hypothesis of a homogenous medium as

$$d(\omega, a) = e^{(i\omega r_a)/c}, \tag{9.3}$$

where c is the medium velocity and r_a the distance between each receiver and the trial source position a. To match the observed CSDM with the replica vector we calculate the Bartlett processor as

$$B_{Bartlett(\omega,a)} = \sum |d(\omega, a^H K(\omega)d(\omega, a)|. \tag{9.4}$$

Such operation is equivalent to the cross correlation between the observed wave filed phase and the modelled one. We refer to the values of $B_Bartlett(\omega)$ as the MFP output. The MFP output, calculated at specific frequencies, ranges from 0 to 1. The closer to 1 is the MFP output, the more the modelled phase matches to observations, and therefore the more likely the trial source properties (x, y, z, c) represent the true properties. We suggest that MFP output values can also be seen as an indicator of the number of receivers over witch the signal is coherent, e.g. a value of 0.1 would indicates a source that generates a signal coherent over 10% of the array.

We perform source location by systematically applying MFP every 0.5 sec over 1-sec long signal segment of (using the vertical component). We filter the signal within the [3-7] Hz frequency range and coherently apply the MFP each 0.1 Hz within this

range. To maximize our algorithm efficiency and minimize computational costs we
use a gradient-based minimization algorithm (Nelder-Mead optimization) to converge
to the best match between the trial and the observed phase delays rather than an ex-
haustive grid-search exploration. The convergence criterion is reached when the vari-
ance of values obtained over the last 5 iterations of the optimization is smaller than
$1e^{-2}$ with a maximum of 3000 iterations. We use 29 different starting points for our
optimization. They are located 250 m below the glacier surface and they uniformly
cover an area of 800 x 800 m^2 centered on the array. We set the initial velocity to 1800
m.sec^{-1}. After convergence, we obtain 29 punctual localizations per signal segment (1
sec), which may be located all in the same place if a clear global convergence exists (i.e.
high MFP output), or at up to 29 different locations if up to 29 local minima exist (i.e.
low MFP output). We found that this approach is comparable to using sub-arrays of
variable size to perform the MFP over different areas of the glaciers. This allows us to
locate multiple sources acting at the same time, which is otherwise not possible with
classical MFP approaches. Further details on the methods and related physics can be
found in Chmiel *et al.* (2016).

Statistic of the MFP output

We narrow the MFP output selection by keeping only (1) the location yielding realistic
phase velocities ([1200-3600] m.sec^{-1}), (2) the localizations at ± 400m from the array
center and within 400 m below the glacier surface and (3) the localizations associated
with proper convergence of the minimization process (< 3000 iterations). The number
of located sources after this selection (Fig. 9.4) decreases as the MFP output increases,
with more than 5000 daily sources associated with MFP output lower than 0.05 and
less than 1 daily source associated with MFP output higher than 0.75. We show in Fig.
9.3(b, c) the distribution of the sources properties (vertical position) and in Fig. 9.3
(e, f) the spatial probability of source location over the complete study period for two
MFP outputs band ([0.07-0.16] and [0.75-0.99]). Such 2D representation is obtained
by summing the total number of sources in each 8 x 8 m^2 cell of an 800 x 800 m^2 (x, y)
grid centered on our seismic array.

It is important to note that at low MFP output (e.g. [0.07-0.16]), only a few sensors dis-
tinguish the source. This leads to a shorter aperture of the effective seismic array that
limits depth resolution. The trend of higher probability of source location at depth is
however observed here for tens of thousands of sources.

On the precisions of the source location

When compared to the crevasses field at our study location (Fig. 9.1), we observe that
our MFP analysis yields source location, with MFP output higher than 0.75, a precision
in range down to 10 m (Fig. 9.3) for an average wavelength of λ of c. 300 m at 5 Hz
(Sergeant *et al.*, 2020). While the expected Rayleigh's limit gives a maximum resolution
of $\lambda/4$ (c. 75 m at 5 Hz) in the far-field domains (Rost and Thomas, 2002), laboratory
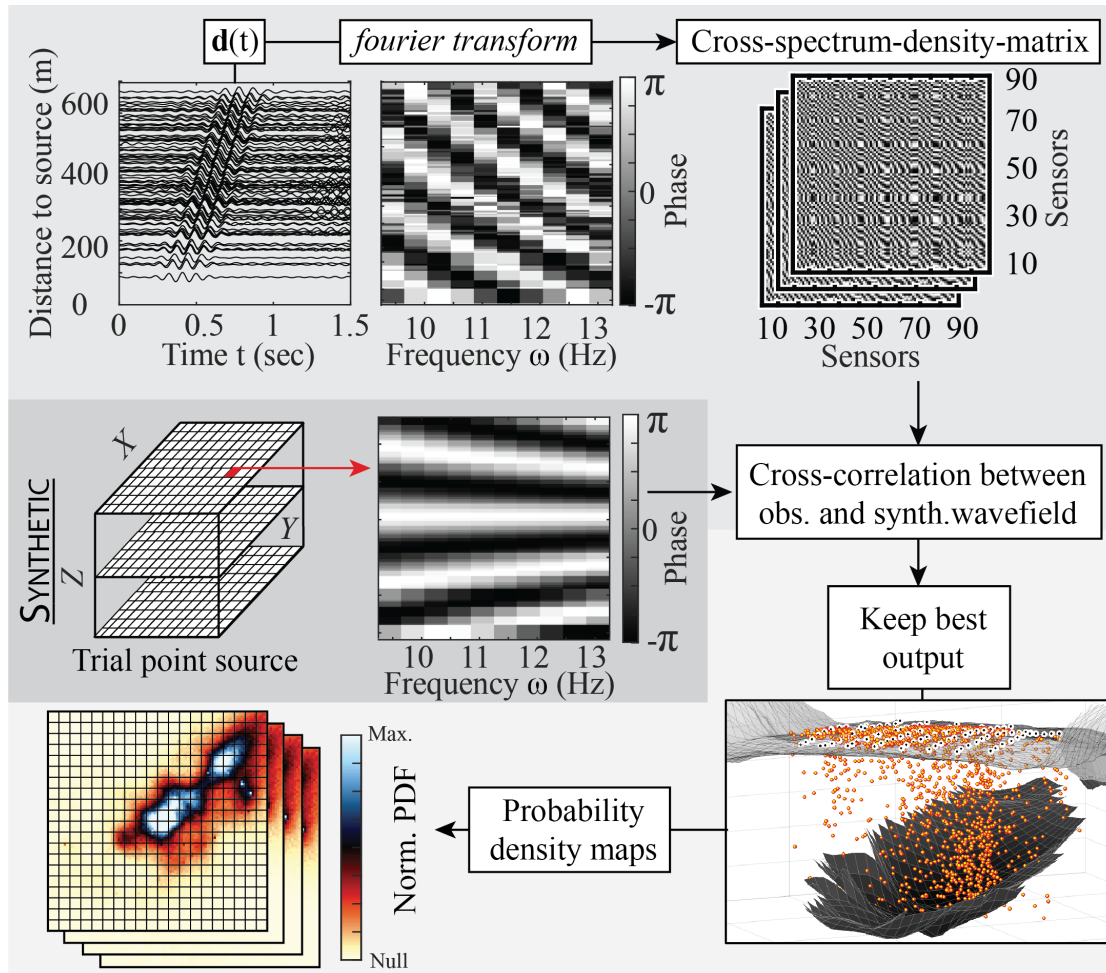
Figure 9.2: Processing strategy to derive probability density maps of sources location from dense seismic observations. (top) Processing of the seismic observations over a 1 sec time window to calculate the Cross-spectral-density-matrix (CSDM) from the Z component of the seismic signal. (middle) Computation chain of the gridded model-based synthetic wave field replica vector. (c) Source localization processing chain with an example of a gridded MFP output and of a (X, Y, Z, C) distribution obtained over a 3 hours' time period and represented against the survey area geometry. Processing chain of probability density maps computation is shown over the (X, Y) grid for a given (Z, C, MFP output) thresholds.

experiments (Pyrak-nolte *et al.*, 1999) suggest that the seismic signal bears information of spatial structures down to $\lambda/8$ (c. 32 m at 5 Hz) in the near-field of sources. Our unique instrumental setup combined with our systematic analysis of phase coherence allow us to overcome the Rayleigh's far-field limitations and obtain 2D maps of source location with resolution in range of about 10 m for high MFP outputs. For lower MFP output we expect a lower resolution due to a smaller aperture of the array sensitive to the local phase coherence. We acknowledge then fact that the width of the area shown in Fig. 9.4, may not represents the true width of the subglacial channel, that is expected to be on the order of 1 to 10 m at this location (Nanni *et al.*, 2020). The observe width of c. 50 m, is likely due to the uncertainty on the source location because of the large wavelengths investigated here.

Seismic power

The seismic power P is calculated at each sensor using the vertical component of ground motion within [3-7] Hz and the Welch's method over 4-s time windows with 50% overlap as done in Chap. 5. We use a short 4-s time window because the longer the time window, the more likely highly energetic impulsive events occur and overwhelm the turbulent-water-flow induced noise. With such short time window we therefore maximize sensitivity to the continuous, low amplitude, turbulent-water-flow induced noise and minimize that of short-lived but high energy impulsive event.

Turbulent water flow hydraulic properties

We stress that the inversions of hydraulic properties depend on the average seismic amplitude with very little dependency on the spatial variations. Therefore, our inversions are to be considered independent from the source location even if they both arise from the seismic signals.
See Chapter 5 for details.

9.4 Results

Retrieving the geometry of subglacial channels

We show in Fig. 2(d, e) the normalized spatial probability of source location obtained over the study period for high and low MFP output ranges. We observe that events associated with a good global phase coherence (MFP output > 0.8) are mainly located at the glacier surface (Fig. 2(b)) where crevasses are observed (Fig.2(e)) and are associated with phase velocities (c. 1580 m.sec^{-1}) typical of surface waves (Sergeant *et al.*, 2020), consistent with these corresponding to crevasses-induced icequakes (Fig. 1(a)). On the contrary, sources associated with local phase coherence (MFP output within [0.05-0.3]) are preferentially located at depth near the ice-bed interface (Fig. 2(d)). The associated phase velocities (Fig.2(c)) vary up to c. 3600 m.sec^{-1}, which is consistent with body waves being generated in addition to surface waves and thus with sources occurring at depth. The associated spatial pattern show two well-defined spots of high location probability elongated in the along flow direction. The first covers an area of c. 100 x 300 m^2 at maximum ice thickness, the second is located 50 m downglacier of the former and covers an area of 50 x 100 m^2. The spatial pattern exhibited by seismic sources associated with low MFP outputs (Fig. 2(d)) presents a similar geometry to that expected based on a prediction of a subglacial channel position obtained based on hydraulic potential calculations (see Methods). The width of the high probability patches is much greater than the expected width of a subglacial channel (c. 5 m) (Werder *et al.*, 2013), and we suggest that this is caused by a seismic wavelength λ of c. 300 m at 5 Hz, which limits our resolution at c. $\lambda/6$, i.e. 50 m (Rost and Thomas, 2002) (see Methods). The observed spatial pattern supports that we successfully retrieve the geometry of subglacial channels.
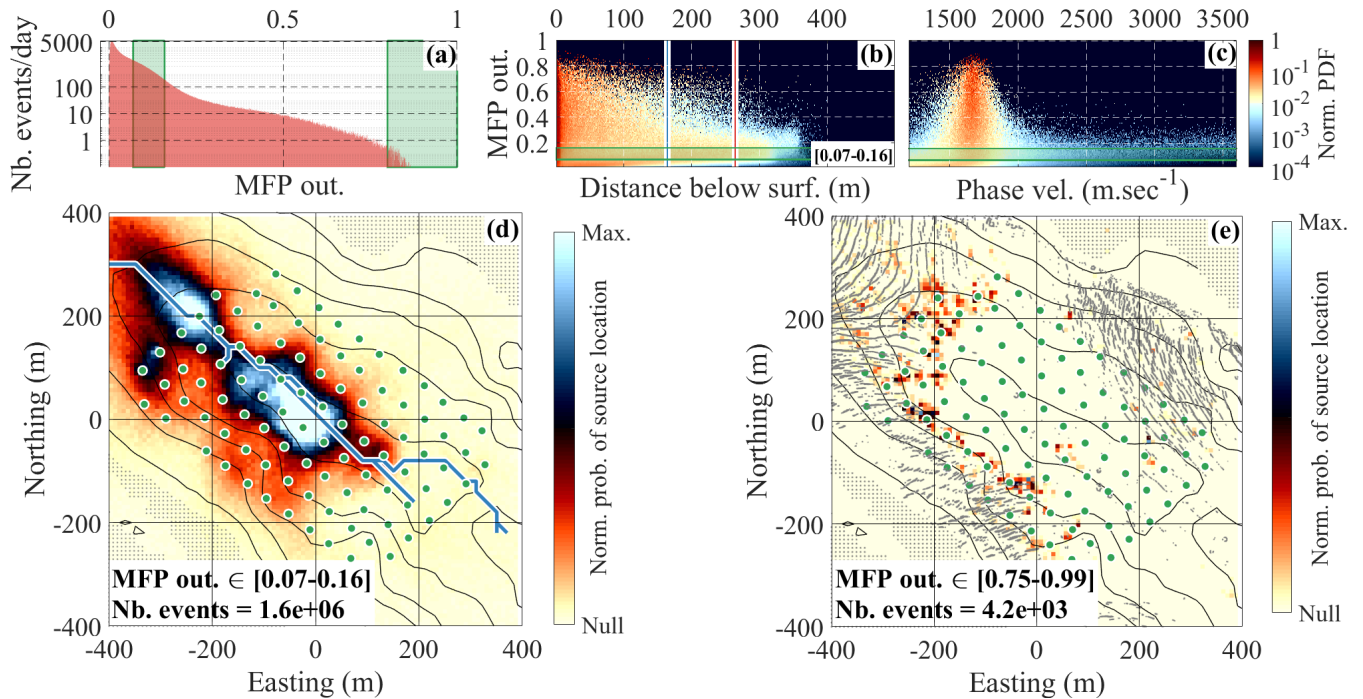
Figure 9.3: Statistics and 2D representation of the MFP output for the 5±2 Hz frequency range. (a) Distribution of the average number of events located per day after applying our selection as a function of the MFP output. Green shaded areas show the MFP output range for which we investigate the sources spatial distribution. (b) Normalized probability distribution of the MFP output as a function of source depth relative to the surface. Vertical red line shows the maximum ice thickness; green line shows the median ice thickness. (c) Normalized probability distribution of the MFP output as a function of phase velocity. Note that color scales are logarithmic and distribution are normalized per MFP output bands of 0.01. Green shaded areas show the [0.07-0.16] MFP output range. (d, e) 2D representation of the normalized probability of source location obtained with 8x8 m^2 pixels' grid on the study area for two MFP output ranges ([0.07-0.16] (d) and [0.75-0.99] (e)). Contour lines show 50-m spaced ice thickness contours as presented in Fig. 9.1. Grey shaded areas show ice-free areas. Green dots show the seismic array. Blue line in (d) shows the subglacial waterways as predicted from hydraulic potential calculation as shown in Fig. 9.1. Black dots in (e) show crevasse location as shown in Fig. 9.1.

Switch from a cavity-dominated to a channel-dominated drainage system

To further investigate the different components of the subglacial drainage system we conduct a temporal analysis through calculating source location maps averaged over 2-day, which is long enough to gather sufficient statistics while short enough to properly investigate its temporal evolution (Fig. 3). In Fig. 4 we show the 2D coefficient of determination between the spatial pattern observed on May 24-25th (Fig. 3(o)) and each of the patterns shown in Fig. 3. The closer to 1 is this coefficient, the more the drainage system is observed to be channelized (Fig. 4). We complement this analysis with the inversion of the hydraulic pressure gradient and of the hydraulic radius(Nanni *et al.*, 2020; Gimbert *et al.*, 2016) that characterize the efficiency and pressure conditions of subglacial water flow (see Methods for details). Over the study period we observe two distinct dynamics in the subglacial drainage system configuration (Fig. 3) and re-
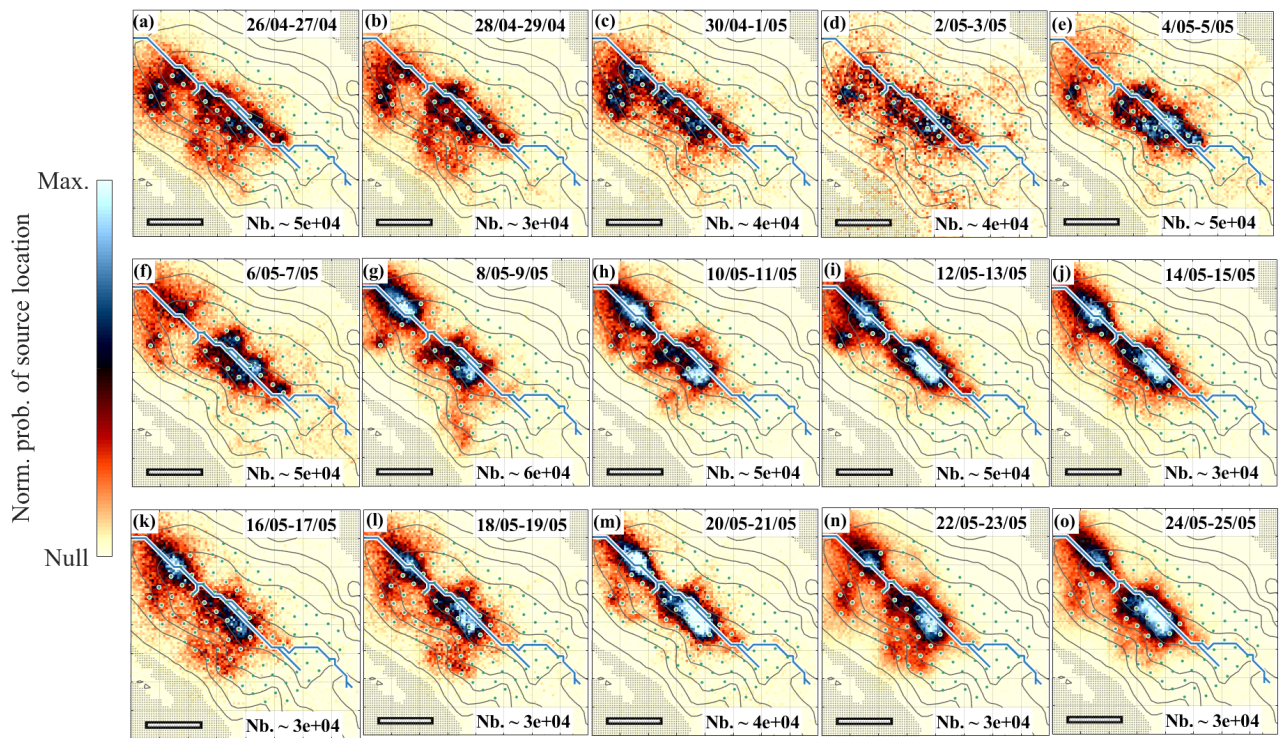
Figure 9.4: 2D maps of subglacial water flow source location obtained from MFP. Temporal evolution of the spatial pattern of source location density obtained for the 5±2 Hz frequency range and the [0.07-0.16] MFP output range. All maps are averaged over 2 days' time-windows, with the associated number of located sources shown on the lower right corner. Color scales ranges are normalized for each time window by the maximum probability. Panel (o) corresponds to the characteristic pattern used Fig. 9.5 for the coefficient of determination calculation. Contour lines show ice thickness as presented in Fig. 9.1. Grey shaded areas show ice-free areas and scale is 200 m for the white stripes. Blue lines show the subglacial waterways as predicted from hydraulic potential calculation as shown in Fig. 9.1.

lated hydraulic properties (Fig.4) that indicate a gradual transition from a distributed-inefficient to a channelized-efficient subglacial drainage system in response to increasing water supply.

In the beginning of the period (until c. May 10th) we observe that subglacial water flow is distributed rather than channelized (Fig. 3). At this time of increasing water discharge (from 0.1 m.sec^{-3} to almost 2 m.sec^{-3}, Fig. 4) we observe two clear peaks in hydraulic pressure gradient (green line, Fig. 4, May 1st to May 10th) and a constant hydraulic radius (purple line, Fig. 4). This indicates a low hydraulic efficiency (Nanni *et al.*, 2020). We also observe marked accelerations of the glacier surface velocity by up to c. 50%, which is to be caused by increasing basal sliding (Vincent and Moreau, 2016). This likely indicates subglacial water pressurization (Lliboutry, 1968). Those concomitant observations are clear evidences that we observe the distributed cavity-system with our seismic analysis. This was unexpected from previous cryoseismic-studies (Nanni *et al.*, 2020; Gimbert *et al.*, 2016; Lindner *et al.*, 2020; Bartholomaus *et al.*, 2015a), that expected turbulent (i.e. seismogenic) water flow to occur only in channels, but this is consistent with theoretical work (Kamb, 1987) and borehole field observations (Rada and Schoof, 2018) that support turbulent water flow
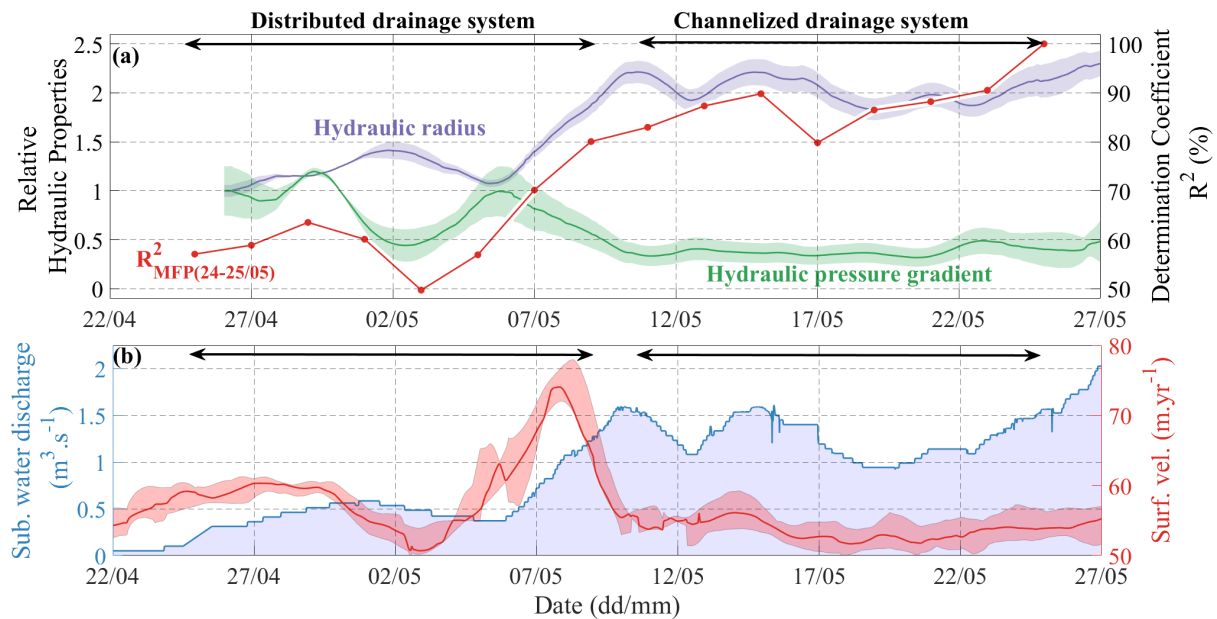
Figure 9.5: Temporal evolution of subglacial hydraulic properties, seismic observations and glacier flow. (a) Left axis shows the relative hydraulic properties as averaged over the 98 sensors. Hydraulic pressure gradient with a ± 1 MAD (median absolute deviation) shaded envelope (green) and hydraulic radius with a ± 1 MAD shaded envelope (purple). Both values are expressed as relative to April 26th. Right axis shows temporal evolution of the spatialized seismic observations using the determination coefficient R^2 of the source location pattern shown in Fig. 9.4(o) (red). (b) Subglacial water discharge Q (blue line) with shaded blue area under the Q curve added for the ease of reading. Median surface velocity over the 4 on-ice GNSS stations (red line) with the minimum/maximum shaded envelope.

within the connection between cavities. This show that we are capable to determine the area of the bed where cavities are connected, versus where they are weakly connected, and might not generate seismic noise because of reduced permeability (Hoffman *et al.*, 2016).

While progressing through time (from c. May 11th), subglacial water flow progressively localizes into a narrower zone near maximum depth where hydraulic potential calculation predicts subglacial channels location. In contrast with the first part of the period, the increase in Q does not cause glacier acceleration but rather a slight deceleration. At this time, we observe a doubling of the hydraulic radius with almost no variation in hydraulic pressure gradient. This indicates increased drainage efficiency (high hydraulic radius) that lowers basal water pressure (deceleration), which is typically expected when subglacial channels develop. Our observations are therefore direct evidences of subglacial channels that reduces basal water pressure and favors slow glacier flow. Surprisingly, we observe an absence of clear source locations in the upglacier part of our array (Fig. 3) that might be caused by less turbulent subglacial water flow compared to the downglacier area, or a reduced channelized flow. The former aspect is likely to be caused by the downglacier bed over-deepening that favors unstable and turbulent water flow (Lliboutry, 1983), whose induced noise would dominates the seismic wavefield.

9.5 Discussion

Implications for glacier hydrodynamics

We highlight here three outcomes of our study that are key to understand which area of the bed experiences one of the three components of the subglacial drainage system and how their evolution influences glacier flow. Firstly, in term of channel-system dynamics, we observe that channels are located at the minimum of the hydraulic potential gradient for an ice thickness of about 200 m and develop for water discharge as low as 2 m.sec-3. The observed morphology of subglacial channels, with along flow discontinuities in their morphology, questions the traditional vision of continuous subglacial channels (Shreve, 1972; Schoof, 2010), and further studies should investigate such particularity. This is particularly important because the spatial extent of channels control the traction at the glacier bed (Werder *et al.*, 2013). Secondly, in term of cavity-system dynamics, our maps show that cavities do not cover the whole ice-bed interface but rather limited areas where they are connected with connections that present similar hydraulic conditions to those in channels (turbulent water flow). We suggest that the areas where we observe turbulent water flow (i.e. seismic sources) represent the connected cavities whereas the absence of seismic sources rather represents the non-seismogenic water flow within the weakly connected cavity system or absence of water flow. This weakly connected system is indeed considered to have much lower permeability than the connected system, which would prevent sustained turbulent water flow. Our spatialized observations are thus key for testing our understanding on how evolves the distributed drainage extent and how it influences basal hydraulic connectivity. This is particularly important as Rada and Schoof (2018) suggests that the degree of hydraulic connectivity at the bed is a better predictor of changes in basal sliding velocities than the basal water pressure. Thirdly, we observe a gradual transition between the cavity-dominated and the channel-dominated system in both time and space. We suggest that this indicates that the two systems form a continuous drainage system rather than a system with clear physical separations between channels and cavities. We suggest that channels and cavities might be described with a unique physical framework as proposed by Schoof (2010) to which should be incorporated spatial changes in permeability to take into account the weakly connected cavities as suggested by Hoffman *et al.* (2016).

Summary and perspectives

In this study we provide well-resolved spatial observations of the channel-system geometry and of the extent of the cavity-system. Those are the most direct evidences of the subglacial drainage dynamics. We show that with an adapted seismic investigation it is possible to retrieve two-dimensional 2D maps of the subglacial drainage system from very low water discharge (~ 0.1 m^3.sec^{-1}) to peak melt-season water discharge (Nanni *et al.*, 2020). Thus we can simultaneously observe the distributed and channelized drainage systems through time and space and evaluate the hydraulic connectivity across cavities.

Our geophysical approach can be easily exported to other glaciers in remote areas, from mountain glaciers to ice caps, especially with the current easing of seismic deployments (Walter *et al.*, 2020; Booth *et al.*, 2020). This will allow the glaciological community to gather key information's on the subglacial environment properties without the need of laborious and/or expensive instrumentation such as active sources (Smith *et al.*, 2015) or deep drilling (Rada and Schoof, 2018). Our seismological approach is not only suitable for the investigation of cryosphere-related processes but also for other environmental applications such as monitoring volcanic sources (Soubestre *et al.*, 2019), tracking changes in river and associated sediment transport (Bakker *et al.*, 2020) or investigate three-dimensional structure of active fault zones (Mordret *et al.*, 2019). Those environments host processes (e.g. lava flow, tremor in fault zones) that generate distributed sources of noise similar to subglacial water flow. We show here, that investigating low spatial phase coherences with an unsupervised and systematic perspective is comparable to using sub-arrays of variable size, which allows us locating multiple seismic sources acting at the same time. For dense array installation, we recommend to use a sub-wavelength and near-field configuration when possible and avoid averaging the phase prior to evaluating phase coherence. Our methodology has a great potential to yield well-resolved spatialized observations of sub-surface environments and overcome numerous observational limitations in environmental geophysics.

Acknowledgments

Outlook: using variations in seismic amplitude to retrieve source locations

10.1 Introduction

In Chapter 9, I focused on investigating the phase component of the seismic signal to retrieve spatial information on the subglacial drainage system. Yet, the seismic signal not only contains a phase component but also an amplitude component that could be used to study source location or medium properties. Traditionally, because of the complexity of the wavefield at high-frequency, source localization techniques have not been focusing on the amplitude component as widely as it has been done on the phase. In this study I investigate how spatial variations in seismic amplitude could be used to retrieve the spatial configuration of the seismic sources associated to subglacial water flow. Before doing so, there are key aspects of the seismic properties that need to be considered.

The amplitude of the seismic signal decays as the wave travels away from the source. This is caused by the a geometrical spreading of the wave and the attenuation properties of the medium. This decay can be modeled as:

$$A(r) = A_0 * \left(\frac{v_g}{(r\pi^2 f)} \right)^{\alpha} * e^{\frac{\pi f r}{2 v_g Q}}, \tag{10.1}$$

with r the source-to-station distance, α the geometric attenuation parameter, f the frequency, v_g the group velocity and Q the quality factor of the material. The elastic part of the attenuation depends on the quality factor Q that characterizes the propensity of the medium to transmit the seismic waves, the higher Q the more transmitting the medium is. The geometric attenuation parameter α equals to 0.5 for surface waves and to 1 for body waves (Aki and Richards, 2002). However, this Eq. 10.1 description's is only valid for a far-field configuration, which is when the distance from the sources are at least at a few wavelengths. This is because of complex behaviors of the amplitude within the first wavelengths from the source that are yet poorly understood (Pyrak-nolte *et al.*, 1999). Based on this formulation of the amplitude variation with distance

one can use variations in the amplitude field to locate sources in the near-field. Over the past two decades, numerous studies have used such approach in environmental setup when phase coherence methods were ineffective.

The most common method is the Amplitude Source Location (ASL) that infers the source location by approximating the amplitude decay as a function of the hypocentral distances following Eq. 10.1. This method has been applied to locate debris flows (Kumagai *et al.*, 2009; Ogiso and Yomogida, 2015; Walter *et al.*, 2017), volcano-seismic signals and tremors (Battaglia, 2003b,a; Inza *et al.*, 2011; Kumagai *et al.*, 2013) as well as sources in glaciated environments (Jones *et al.*, 2013; Röösli *et al.*, 2014). Most of theses studies assume an isotropic waves radiation around a punctual source (Battaglia, 2003a), which might not be always true for sources that have directional mechanisms and present a directivity in the associated wavefield (e.g. as expected from crevasses). So far it is unknown if turbulent-water-flow-induced seismic sources generate an isotropic wavefield or not (Gimbert *et al.*, 2014). A drawback of these amplitude-based source localization is that it is often limited to the far-field because of the complexity of the seismic amplitude in the near-field (Walter *et al.*, 2017). This results in a loss of information and resolution as the larger the source-to-station distance, the more the seismic amplitude is attenuated and get modified by the medium it goes through. In addition, the amplitude is constructive, i.e. intensities from different sources can add to each other. This means that the further away from the source, the more sources might contribute to the measured seismic amplitude. This therefore makes it difficult to identify the contribution of different sources in the measured signal. Because of these issues, both near-field and far-field analyses of the amplitude are complicated to conduct for locating distributed sources in environmental setups.

I present here the analysis of seismic amplitude I have conducted with our dense seismic array measurements and show that such investigation does yield promising results on the spatial and temporal evolution of subglacial-water-flow-induced seismic sources.

10.2   Methods

I calculate the frequency-dependent seismic power P using the vertical component of ground motion recorded at each node. P is calculated with the Welch's method over time windows of duration of 4 secs with 50% overlap. I then average P over time windows of 15 min in the decimal logarithmic space and express P in decibel (dB). Doing so maximizes the sensitivity to the continuous, low amplitude, seismic noise and minimize that of short-lived but high energy impulsive events. P is calculated every 0.5 Hz step and then averaged with a median operator over a given frequency band (e.g. [3-7] Hz). All spectrograms can be seen in Chapter 8, Section. 8.6, page. 129. There, it is well observable that there are strong differences between each sensor, and that these differences also evolve with time.

To study the source location in both time and space I calculate seismic power anomalies at small time step. For a given time-window of length dt, I calculate the relative seismic amplitude $P_{rel}(n, dt)$ at each node n as follows:

$$P_{rel}(n, dt) = P(n, dt) - m(P(1 : N, dt)), \qquad (10.2)$$

with N the number of nodes and m the median operator. Doing so allows me to investigate the spatial variations of the seismic power at each time-window without being biased by the multi-daily trend of varying seismic power. Here I use $dt = 2$ hours in order to capture short-term variations of the seismic amplitude that might give access to the source spatialisation. $P_{rel}(n, dt)$ can then be averaged over different period of time (e.g. over the whole period to extract a median pattern). Here I focus on short-period changes in order to look at the spatial signature of sources. If I would calculate the amplitude anomalies over longer period of time, then I would be influenced by daily to weekly trend. I think that selecting short time windows is the best way to look at those spatial anomalies and possibly investigate the sources signatures.

10.3   Observations

Daily evolution

I show in Fig. 10.1 the daily evolution of the 2 hour-averaged seismic amplitude spatial anomaly in the same frequency band as that used to describe source locations (i.e. 5 ± 2 Hz). Over the first part of the observation period, the amplitude spatial pattern varies smoothly in space (with spatial variations on the order of 150 m, c. half of the investigated wavelength). This pattern is characterized by higher seismic amplitudes at the glacier center than on its flanks. Over the second part of the period, higher amplitudes are observed downglacier with respect to upglacier. Overall, higher amplitude tends to be observed in the along flow direction where ice thickness is the greatest. For specific days (April 27th, May 3rd, 4th and 5th; Fig. 3), however, I observe a strongly distinct pattern, characterized by larger amplitude changes (on the order of $\pm$ 5 dB) operating over shorter spatial scales (on the order of the inter-stations distance of 40 to 50 m). The highest amplitudes align with the along flow direction, with one to two lines located at the center and a third one on the left flank of the glacier. Occurrence of these higher amplitude is concomitant with the initial increase in water discharge (Fig. 9.5). These short scales spatial changes in amplitude are to reflect changes in sources properties/location rather than in site effects. I think that site effects would not change that fast, this is why I consider those rapid changes to be caused by sources effects. I conduct a detailed analysis of of amplitude could be influenced by site effects in Chapter 11, from page 169.

Characteristic pattern

To better investigate the spatial patterns previously highlighted I compute the median relative seismic power over our seismic array over the whole period (Pattern 1;
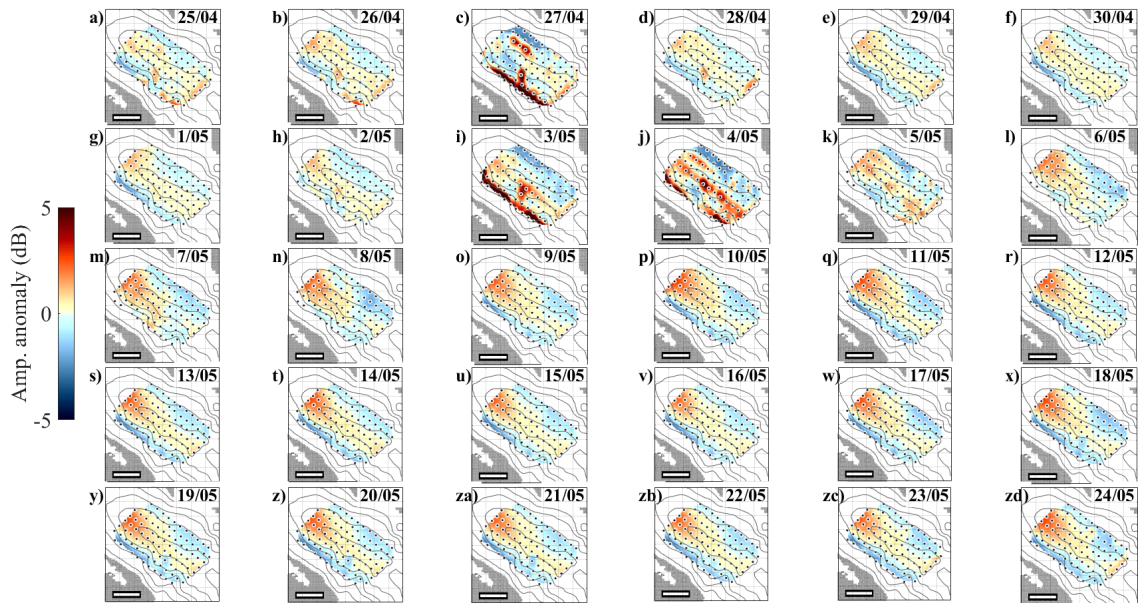
Figure 10.1: 2D maps of the seismic amplitude anomaly. Temporal evolution of the spatial pattern of the amplitude anomaly obtained for the 5 ± 2 Hz frequency range. All maps are daily average of 2 hours-amplitude anomalies. Colour scales ranges are equal for each time window and represent the amplitude anomaly in decimal logarithmic (dB) relative to $(m.s^{-1})^2.Hz^{-1}$. Contour lines show ice thickness as presented in Figure 1. Grey shaded areas show ice-free areas and scale is 200 m for the white stripes. For graphical purpose I linearly interpolated the seismic power at each sensor over a sub-meter grid that covers the seismic-array.

Fig. 10.2(a)) and over May 4th (Pattern 2; Fig. 10.2(b)). I choose this day as it corresponds to the one that shows the strongest spatial variations. For the May 4th average shown in Fig. 10.2(b) we observe strong spatial variations of the seismic power, with changes of more than 5 orders of magnitude from one nodes to the other, i.e. over less than 50 m. These short wavelengths of changes in seismic power are observed for all frequency bands (Fig. 10.3). The general pattern depicts strong lateral changes (across glacier-flow) with line of high seismic power ($> +2$ dB) along glacier flow that alternates with lines of low seismic power (< -2 dB). High seismic power is observed on the left flank of the glacier and then on the centre of the glacier along glacier flow.

What is very interesting is that, overall, the pattern seems to be consistent across frequencies. I suggest that the associated sources dominate this whole frequency range. Such large range of frequencies is consistent to what we observed for subglacial water flow in Chapter. 5. What is also very interesting and highlighted in Fig. 10.3 is that the observed geometries do not changes much with the frequency while the investigated wavelength varies from c. 300m at 5 Hz to c. 50 m at 30 Hz (for surface wave velocities of c. 1500 m.sec^{-1}). At low frequency ([3-17] Hz) we observe a trend of higher seismic power upstream than downstream with a difference of about 2 order of magnitude. For higher frequencies, this difference is less pronounced and seismic power tends to be higher downstream than upstream. In the case of sources located at the base of the glacier (c. 250 m below the array), this means that our observation depicts near-field
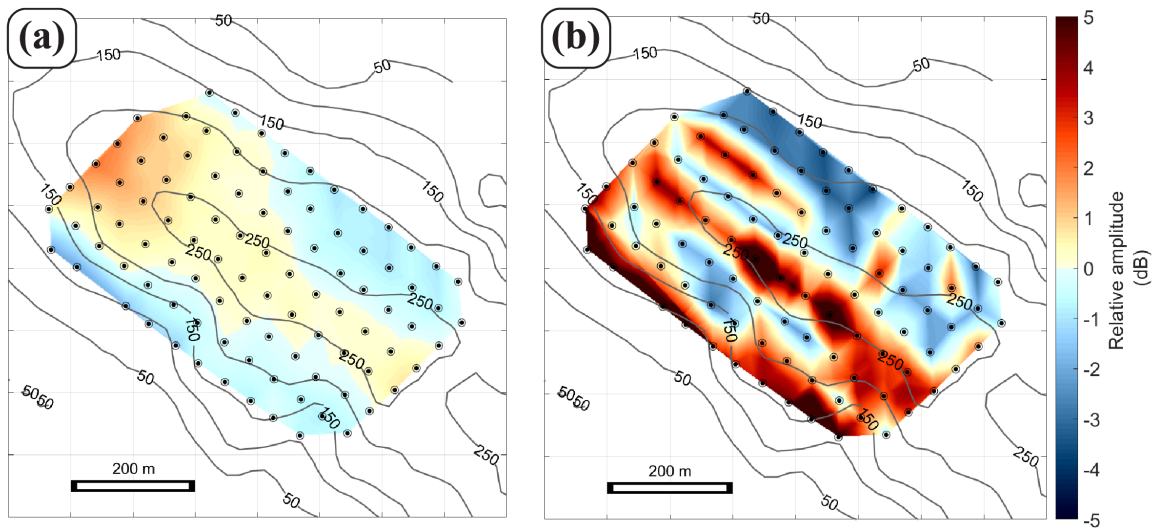
Figure 10.2: 2D maps of the seismic amplitude anomaly (a) averaged over the entire period
and (d) over May 4th for the [3-7] Hz frequency range.
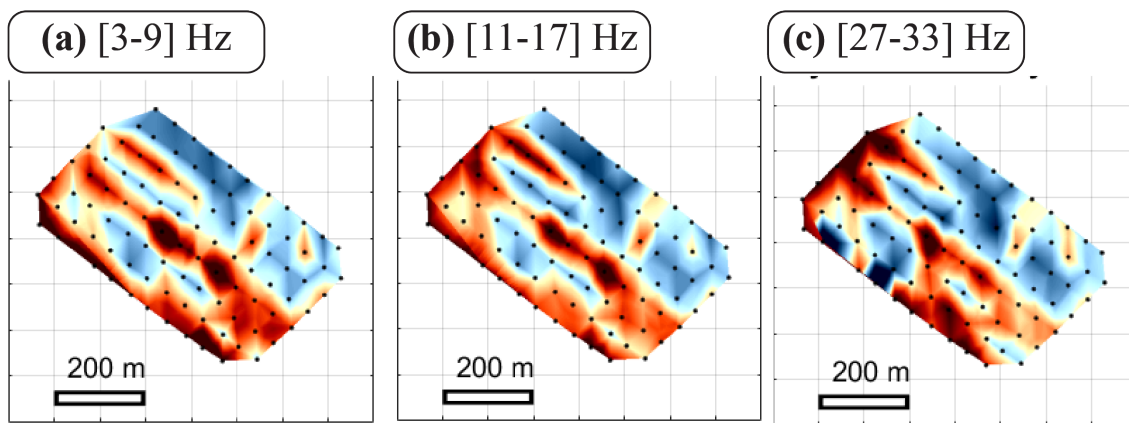
Figure 10.3: 2D maps of the seismic amplitude anomaly calculated at different frequency
ranges for the day of year 125, which corresponds to May 4th shown in Fig. 10.1.

changes in amplitude for the lower frequencies and far-field changes for the higher
frequency.

Temporal evolution of characteristic patterns

I investigate the temporal occurrence of the two characteristic spatial patterns of seis-
mic power previously described (Pattern 1; Fig. 10.2(a)) and Pattern 2; Fig. 10.2(b)). To
do so I compute the 2D cross-correlation of these patterns with the spatial relative seis-
mic power calculated every 2 h. The closer to 1 the closer the pattern at a given time is
similar to the master pattern (1 or 2). In Fig.10.4 I represent the temporal evolution of
the cross-correlation coefficient with Pattern 1 (plain lines) and with Pattern 2 (dashed)
for different frequency bands. As both patterns (1 and 2) represent median condition
of the seismic power (daily or over the whole period), none of the cross-correlation
calculated coefficient each 2 hours reaches exactly 1. This is a similar approach to that

shown in Fig. 9.5.

I observe that the occurrence of Pattern 1 varies over the study period, but the general trend is that this pattern dominates the spatial variability of the seismic power with cross-correlation values above 0.75 more than 50% of time at low frequencies and up to 80% at higher frequencies. At low frequencies ([3-13] Hz, plain thick lines) this pattern is less dominant over the first week than at high frequencies ([17-33], dashed thin lines). The temporal evolution of the cross-correlation coefficient of Pattern 1 shows two well-marked periods of low values that are consistent through all frequencies, the first in April 27th and the second from May 4th to May 8th. At these times, values go down to 0 for the lower frequency bands and down to their minimum value for higher frequency bands. These two periods are concomitant with the increase in the cross-correlation coefficient associated with Pattern 2. This pattern shows general trend over the study period of low occurrence, with two peaks that are well-marked for the low frequency bands ([3-17] Hz) and less pronounced, but still significant, for the higher frequency bands. During these two periods, while the occurrence of Pattern 1 is significantly low, the occurrence of Pattern 2 is on the contrary significantly high, with values that goes up to 0.75 for low frequency bands ([3-13] Hz).

I observe in Fig.10.4 that the high values of cross-correlation coefficient with Pattern 2 (green lines) occurs during the first rises of the subglacial water discharge (blue lines). These rises are also concomitant with an increase in the hydraulic pressure gradient (green lines). The hydraulic pressure gradient indeed only shows two majors peaks over our study period, while the hydraulic radius (purple lines) shows a gradual increase by a factor of 3 over the study period. The hydraulic radius trend presents a similar pattern as the cross-correlation coefficient with Pattern 1 (grey lines), with a gradual increase over the first week, and decreasing values concomitant to rise in hydraulic pressure gradient, followed by a marked increase by a factor of 2 at the end of the second week that leads to almost constant values over the rest of the study period. The surface velocities (red lines) present a clear peak from May 5th to May 10th that is followed by a 1 to 2 days delay in the second peak in hydraulic pressure gradient and the second period of high occurrence of Pattern 2. Those changes in pressure conditions and sliding velocities are obtained independently from the spatial variation in amplitude and their concomitant evolution suggests that our analysis is sensitive to changes in subglacial hydrology dynamics.

Synthetic amplitude variation

At this point, I think that the maps shown in Fig. 10.3 can be interpreted as the surface signature of subglacial-water-flow induced noise. However such pronounced spatial changes in amplitude raise questions on their origin(s). What is especially unexpected is that we observe at [3-7] Hz (the frequency the most sensitive to water flow) changes in amplitude of several dB that occur over c. 50 m, which corresponds to 1/6 to 1/4 of the wavelength. To investigate such abrupt changes I have conducted synthetic tests by modeling the amplitude maps obtained for sources with a geometry similar to the
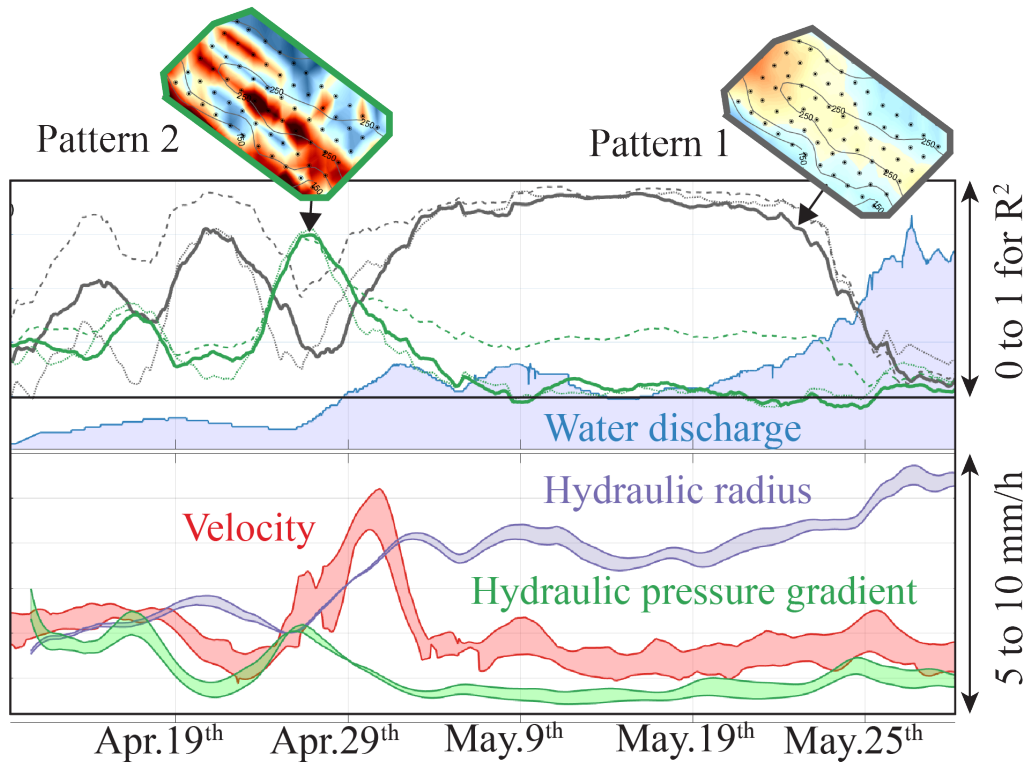
Figure 10.4: Timeseries of physical quantities measured over the RESOLVE study period and of the 2D cross-correlation scores obtained from the spatial patterns shown in Fig. 10.1 and 10.3. (a) Subglacial water discharge (blue) as measured at in the subglacial galleries. Values range from 0 to 1 $m^3.sec^{-1}$. 2D cross-correlation scores obtained from Pattern 1 (grey lines) and 2 (green lines) 2D cross-correlation with all 2h-timewindow calculated relative seismic power within 3 frequency bands. The scores and the velocities are averaged over 24h, and the sub-glacial water discharge over 2h. (b) Surface velocity range (red) as measured over the 4 GNSS stations (Fig. 8.1), with the upper and lower boundaries are the maximum and minimum measured surface velocities. Relative hydraulic radius (purple) and hydraulic pressure gradient (green) as derived from the seismic power shown in Fig. 9.5. Relative values range from 0 to 2.5.

one expected for subglacial water flow.

To do so I combined the far-field description of the amplitude decay presented in Eq. 10.1 to a formulation of the amplitude decay in the near-field proposed in Gimbert *et al.* (2014). This allows me to take into account the effect of being close to the source and in the near field at such low frequencies. For sources close to the sensors, i.e. within few wavelengths, Eq. 10.1 becomes

$$A(r) = A_0 * \left(1 + (\frac{(r\pi^2 f)}{v_g})^3\right)^{1/6} * e^{\frac{\pi f r}{2 v_g Q}}. \tag{10.3}$$

I compare the two Eqs. 10.1 and 10.3 in Fig. 10.5. We can observe that the near-field formulation yields amplitude values of one (e.g. equal to the source amplitude) within the first wavelength whereas the far-field one goes to unrealistically high values. To conduct the synthetic tests I used different values of Q and a frequency of 5 Hz. I

Geometrical spreading for plane waves
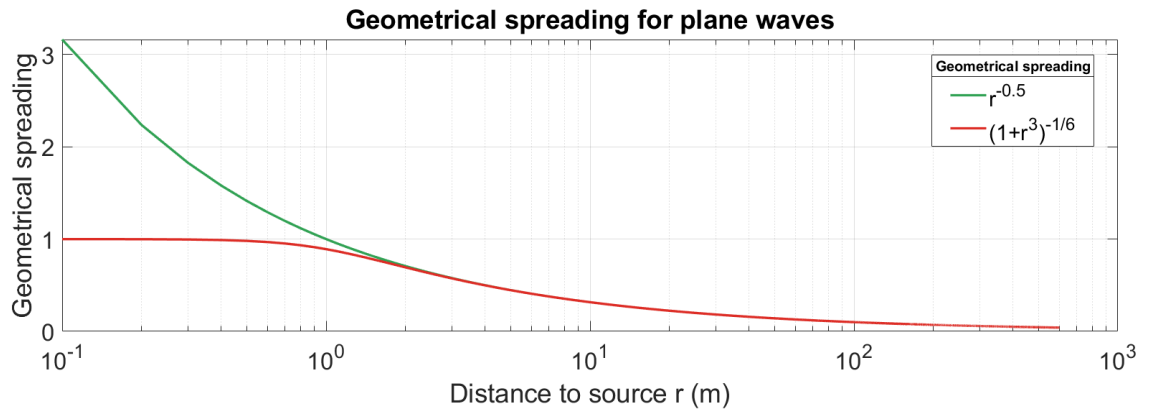
Figure 10.5: Synthetic attenuation caused by geometrical calculated in the case of a near-field hypothesis (red curve) and of a far-field hypothesis (green curve) for a surface wave. Y-axis show the normalized amplitude that attenuates as a function of distance shown in X-axis normalize by the wavelength. So x=1 at 1 wavelength from the source and y=1 when the amplitude equals the source's amplitude. Note that after c. 10 m the curves overlap.

first took those values from the literature but then conducted a systematic analysis of seismic attenuation based on the events located during the RESOLVE-project (see Chapter 11, from page 169). Here, I show the result for values of Q within [4,8,16,32], and from the study I have conducted later in Chapter 11, it appears that values between 5 and 10 are the most probable. The array that I use for the synthetic model has the same geometry as the one deployed on Glacier d'Argentière. I use sources located at the surface as subglacial water flow preferentially generates surface waves. For surface waves the source depth is unimportant as the glacier depth is on the order of the wavelength at the frequency of interest. I then used two different background noise Bg, one of 0% and one of 10% of the maximum amplitude in order to represent the best the glacier condition. I calculated the amplitude at each node n following

$$P_w(e) = 10 * log10(A(r)^2 + Bg^2) \tag{10.4}$$

What I observe is that a line of sources generates a strong amplitude anomaly with typical amplitude decay of c. 3 dB over a distance of c. 150 m when there is a background noise (bottom panels in Fig. 10.6) and of c. 5 dB in the absence of background noise. For the study of subglacial channels, this is quite promising as this show that even at low frequency (5 Hz) we can observe spatial changes over the seismic array in the amplitude field. At such frequency, the wavelengths are indeed on the order of 300 m, and we would have not expected to resolve changes in amplitude at scale smaller than a quarter of the wavelengths. Such results are very encouraging and support the use of the spatial anomaly in the seismic amplitude to investigate the spatial distribution of (sub)glacial seismic noise sources.
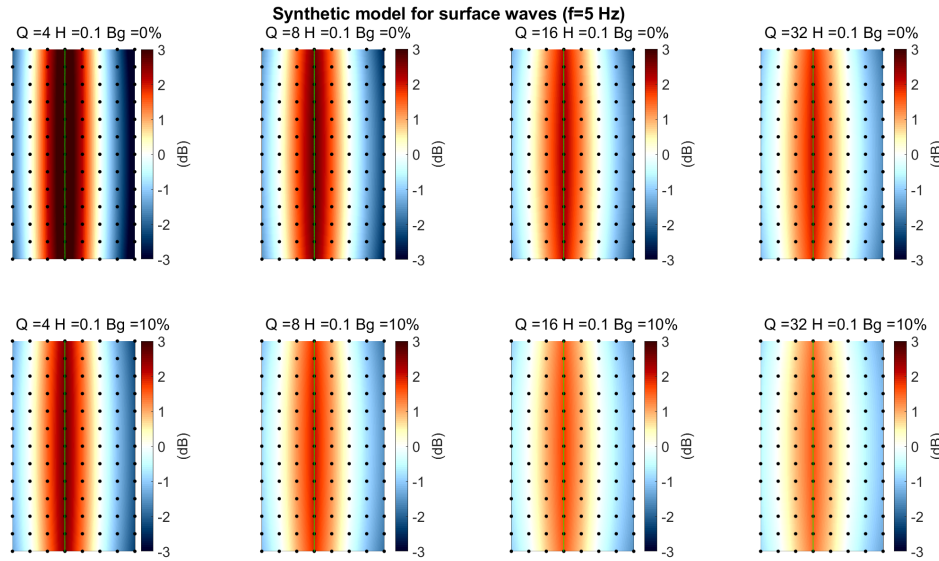
Figure 10.6: Synthetic amplitude anomaly calculated over the 98 sensors for line-sources. Different quality factor Q and background noise (1 or 10 %) are tested for sources located at the surface that generate surface waves with a central frequency of 5 Hz. Color bar shows relative amplitude over the array.

10.4   Discussion

Perspectives

I presented that we observe strong spatial heterogeneity in the amplitude field when the hydraulic efficiency of the subglacial drainage system is low (low hydraulic radius) and that the subglacial water pressure is high (high sliding velocities and hydraulic pressure gradient). On the contrary the median and smooth pattern is observed when the hydraulic efficiency is high (doubling of the hydraulic radius) and the subglacial water pressure lower (lower sliding velocities and hydraulic pressure gradient). This transition in the hydrodynamic is the same as the one shown in Figs. 9.4 and 9.5. I suggest that the amplitude anomalies observed in April 24th, May 3rd, 4th and 5th (Fig. 10.1) are caused by the development of subglacial channels. I suggest that the two areas of high seismic amplitude correspond to the surface signature of subglacial channels. The relatively low but yet pressurized water flow at that time allows to have a spatially limited seismic signature that kept the sources geometry. I also suggest that the zone of seismic amplitude in the right flank (Fig. 10.1) of the glacier is a signature of potentially pressurized water flow that occurs whether on subglacial channels or within the englacial drainage system as this zone is highly crevassed and relatively shallow (c. 100m of ice). At this time, the channelized drainage system is still poorly developed with low values of hydraulic radius and a rapid increase in the water supply is expected to generate a strong contrast on the amplitude field because of the strong dependency of the seismic power to the hydraulic pressure gradient (Nanni *et al.*, 2020). As the water discharge continues to increase, we observe increasing hydraulic radius rises as soon as the hydraulic pressure gradient decreases. At the same time the spatial anomalies in the seismic amplitude get smoother. This is possibly

to be cause by the increasing energy generated by sources downglacier our array that dominate the amplitude field and blur out the whole array. The condition to observed the geometry of the subglacial drainage system with spatial variations in amplitude could thus be that the sources have to be inside the array and that there are no dominant sources close to the array. There is still, however, clear cross-flow changes in the seismic amplitude that support the presence of subglacial waterflow under our array. I suggest that because the drainage system of Glacier d'Argentière is so small (c. 250, half of the glacier width) we cannot retrieve the geometry of the subglacial channels using only amplitude anomalies. However, I suggest that in larger setup and with array covering wider areas such approach could be used to retrieve the position of subglacial channels, as they still generate a strong contrast in the amplitude field.

With the analysis of spatial anomalies in the seismic amplitude I suggest that we can retrieve information on the localization and properties of the subglacial drainage system. This information is complementary to the one yielded from the analysis of the phase component conducted with the matched-field-processing. The preliminary analyzes I have shown here question the significance of spatial changes in ampliude within the first wavelengths from the sources as such observation are yet very uncommon.

10.5 Similarities and discrepancies between phase and amplitude information

The discrepancies between the phase (Fig. 9.4) and amplitude (Fig. 10.1) information suggest that these components show a different sensitivity to the properties of the subglacial drainage system. Here I discuss the potential origin of such discrepancies. The matched-field-processing approach is likely capable to map the dominant sources only, while the amplitude anomaly approach is likely to reflect the spatial extent of all sources. As sources get more active, their intensities are summing up and create patches where spatial variations of single group of sources cannot be resolved anymore. On the contrary as sources get more active, the MFP process would only locate the strongest sources as subglacial turbulent water flow induced noise is not expected to be coherent neither over space nor time. As a result of those different seismic properties, I suggest that the spatial pattern previously described is not incompatible with common subglacial sources but rather indicates a clear evolution of both spatial extent and the intensity of the subglacial turbulent water flow over our study period. From a glaciological point of view, our observations support that the phase of the seismic wave field is sensitive to the development of the channelized and distributed drainage system, while the spatial variations in the amplitude of the seismic wave field is sensitive to the change in pressure conditions within the subglacial drainage system.

Part V

Structural analysis from ground motion amplitude

〜〜〜〜〜〜〜 **Methodological question n°3:**

To which extent ground motion amplitudes can be used for studying glacier features such as crevasses, thickness or ice crystallographic anisotropy?

In the crevasses of the Glacier d'Argentière. © *Benoit Urruty*.

Chapter 11

Using high frequency (> 3 Hz) seismic ground motion amplitude to study glacier structure

This chapter is centred on a work-in-progress study conducted with Philippe Roux, Florent Gimbert and Agnès Helmstetter. I present here preliminary results and this chapter mostly consists in illustrating the potential of using seismic ground motion amplitude to study glacier structure.

In the previous chapter, I presented the spatial investigation of the subglacial drainage with dense seismic observations. I show that both the phase and the amplitude components of the seismic signal can be used to retrieve the spatial configuration and properties of subglacial water flow. In Chapter 8 we used phase analyzes to investigate the medium properties (e.g. wave velocities, structure's inversion from dispersion curves). When working on the amplitude component to investigate source properties in Chapter 10, I found that further analysis on how the medium properties influence the spatial variations in amplitude should be conducted in order to be able to separate site effect from source effect.

The first step to do so is to well characterize the attenuation parameters and especially the ice quality factor that controls the amplitude decay in space. I decided to use the impulsive events located from matched-field-processing (Chapter 8) and investigate how the associated amplitude is affected by the path that takes the seismic wave. I then went a step further thanks to this unique dataset and conducted a **study focused on evaluating up to which extent seismic amplitudes can be used for studying glacier features such as crevasses, thickness or ice crystallographic anisotropy**. Those issues are traditionally addressed by analyzing the phase component of the seismic signal and I find very exciting to see to which extent amplitude analysis can yield complementary information to classical approaches. In addition, with the rise of environmental seismology that often use high-frequency analysis, it becomes more important to understand what controls the variations of seismic amplitudes at high frequency, and our dense array experiment is a good opportunity to do so.

11.1 Introduction

Glaciers host a wide range of seismic sources whose signals occupy high frequency ranges (> 1 Hz; see Podolskiy and Walter (2016); Aster and Winberry (2017) for recent reviews). Glacier seismologists have used those sources to infer glacier processes and properties through analysing both impulsive events and seismic noise sources. Events-based approaches focus on mechanisms related to the movement of glaciers such as crevasses opening (Neave and Savage, 1970), basal sliding (Helmstetter *et al.*, 2015b) or iceberg calving (Köhler *et al.*, 2012a). Noise-based studies of glaciers are relatively recent and the main source of seismic noise is water flow (Bartholomaus *et al.*, 2015a; Preiswerk, 2018; Nanni *et al.*, 2020) and its resonance within conduits (Röösli *et al.*, 2014; Roeoesli *et al.*, 2016). Similarly to in river, turbulent subglacial water flow generates seismic noise through the force it exerts on the conduit's wall (e.g. soft sediment, hard-bed and/or ice) (Gimbert *et al.*, 2014, 2016). Because of the complexity of the medium properties (e.g. sedimentary/soil layers, fractured medium, 3D geometries) it remains however uncertain how high frequency seismic amplitude measured at a seismic station can be interpreted in term of source properties. This is particularly important for estimating the rupture length and slip accommodated by basal stick-slip events (Helmstetter *et al.*, 2015b; Lipovsky and Dunham, 2016; Lipovsky *et al.*, 2019), the ice masses involved in a given calving event (Bartholomaus *et al.*, 2015b) or to invert absolute rather than relative subglacial hydraulic properties (Nanni *et al.*, 2020). Understanding what causes changes in seismic amplitude within a glacier is also important as is gives insights on the medium attenuation properties (e.g. scattering, attenuation or amplification). In this study we investigate how wave propagation within a glacier affects seismic amplitudes with an extensive amplitude-decay analysis of more than 7000 well-located events on an Alpine glacier (Glacier d'Argentière-French Alps, Fig. 1).

Our study is rooted in the RESOLVE-Argentière project (see Chapter 8 for details) that combines multi-physics sensors to refine quantitative interpretation of the process acting within a glacier. With 98-sensors and 40 to 50-m sensors spacing, our dense array covers an area of 400x600 m^2 that allows us to densely sample the seismic wavefield close to the sources and over a large range of distances, which is ideal to study propagation effects. This setup is also ideal to assess the benefits of seismic amplitude analysis compared to phase analysis because anisotropy (Sergeant *et al.*, 2020) and phase velocity analysis (Chapter 8) have been previously conducted there. Our use of impulsive events rather than seismic noise is supported by high frequency ambient noise being often too sparse in glaciated environment because of limiting scattering features (Sergeant *et al.*, 2020) and/or too unstable in time because of multiple superimposed noise sources (Podolskiy and Walter, 2016) (avalanches, water flow, basal tremor). In addition, the use of a high number of well-located impulsive sources allows us to better quantify the wave attenuation parameters (Levy *et al.*, 2015) than with noise-analysis (Kumagai *et al.*, 2013).

11.2 Overview on how medium properties influence seismic amplitudes

In an infinitely homogeneous medium the decay of seismic amplitude with distance is controlled by attenuation due to geometrical spreading, which depends on the wave type (body or surface waves), and anelastic attenuation, which depends on the material intrinsic properties. In naturals environments structures geometry, damage and medium anisotropy can greatly influence high frequency seismic amplitudes, often leading to biased evaluation of source mechanisms and/or location(Walter *et al.*, 2017). Geometrical structures (e.g. layering of rock, soil or ice) can create resonance effects that tend to amplify the seismic signal at given frequencies (Preiswerk and Walter, 2018). Damages of the medium (e.g. cracks, crevasses, fractures) can result in a scattering that tends to attenuate the seismic signal (Caudron *et al.*, 2018; Moreau *et al.*, 2011). Seismic anisotropy due to oriented structures (i.e. cracks, crevasses or preferential orientation of minerals) can lead to azimuthal variations of propagation velocities (Sergeant *et al.*, 2020). Discriminating the seismic sources properties from the effects of internal changes of the medium requires quantifying the seismic amplitude sensitivity to materials elastic properties but also to structure geometry, material anisotropy and damage as well as to wave types. In this study we first invert for the elastic and anelastic attenuation parameter before evaluating the deviation from a homogeneous model to study the structure properties.

11.3 Methods and materials

Source selection and location

We use the impulsive events located in Chapter. 9, which have also been used in Sergeant *et al.* (2020) to investigate ice crystallographic anisotropy with phase analysis. The epicentral coordinates and associated phase velocity of those sources are obtained using a match-field-processing approach that we described in Sect. 9.3 (page 146). This approach is based on the spatial coherence of the phase component of the seismic wavefield. The method consists in matching every 0.5 sec the phase delays of a model-based synthetic wave field with the phase delays observed between the sensors over the array for the vertical component. The MFP outputs, here calculated for the [9-13] Hz frequencies, range from 0 to 1, the closer to 1 the more the modeled phase-delays matches to observations, and therefore the more likely the synthetic source properties (x, y, z, c) represent the true properties. I use this frequency band as it is the one the most suitable to locate the impulsive events linked to crevasses (Chapter 8).

In this study we keep the source location associated with MFP output higher than 0.8 in order to focus on impulsive events whose wavefield is observed throughout the array. We also narrow our selection by keeping only the locations yielding realistic phase velocities ([1200-4000] m.sec-1), the locations close to the array (± 700m from the array centre and within 400 m below glacier surface). For each events we extract the associated 1.5 second vertical-component-waveform that we band-pass filter within [2-70]
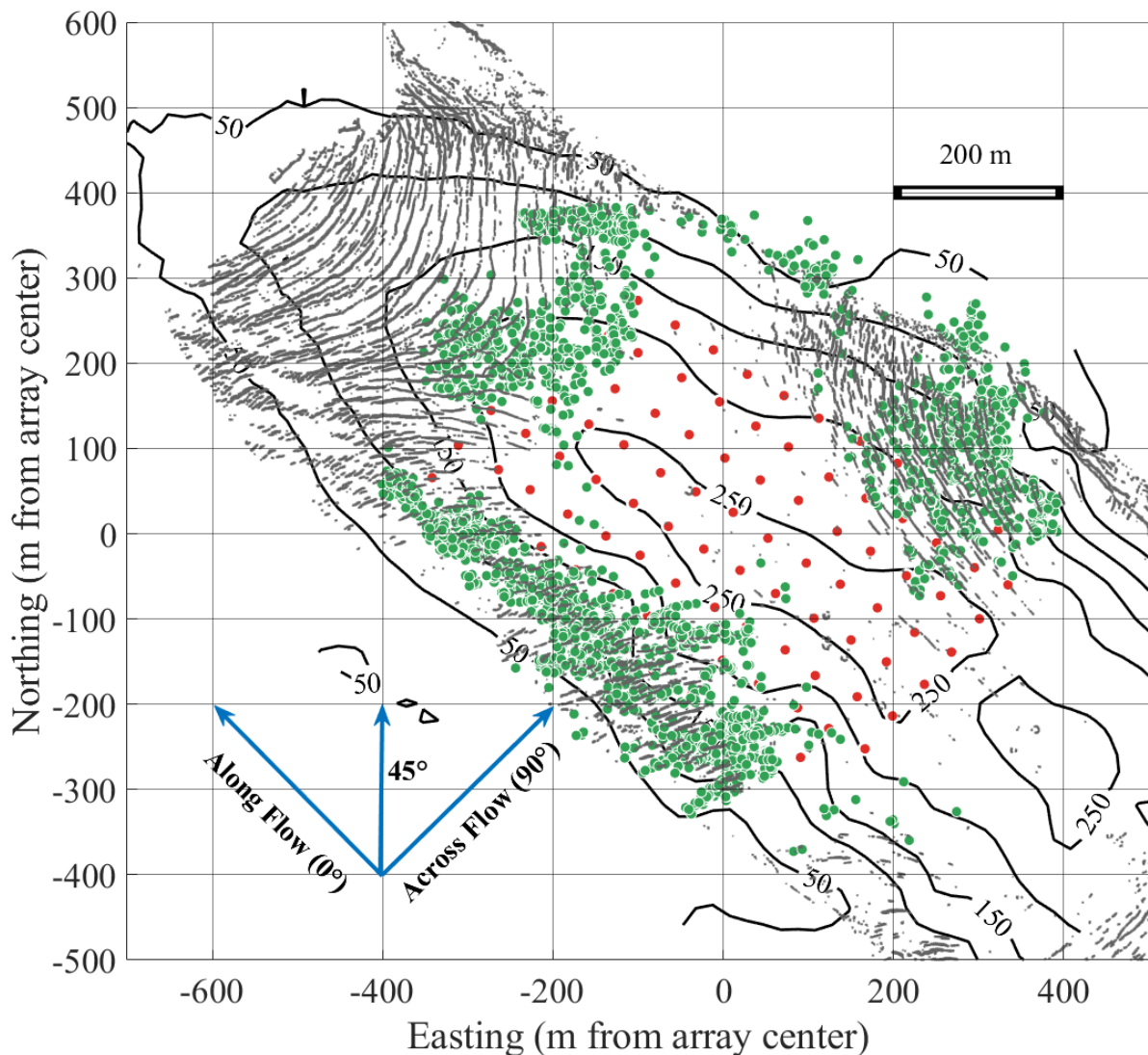
Figure 11.1: Monitoring setup of Glacier d'Argentière and events location. The seismic network (red dots) is composed of 98 seismic stations Fairfield Nodal Z-Land 3C and is located according to positions at the beginning of the survey period (see Part. IV from page 101 for details). Green dots shows seismic event location in range. Contour lines show glacier thickness as obtained from combining radar measurements and surface elevations. Black dots show crevasses whose location is based on altitude variations in the surface digital elevation model. Glacier flows towards northeast and azimuth relative to glacier flow are shown for illustration.

Hz. We show in Fig. 11.1 the spatial distribution of the event we selected. Those events are mainly located on the edge of the seismic array, where crevasses are present. We observe that the crevasses orientation changes in space, with crevasses at c. 90° from glacier flow down glacier while at c. 45° on the left side and down to c. 20° on the right side. We also observe that the selected events are not uniformly distributed around the array because of non-uniform crevasses occurrence as shown with the sources azimuthal distribution around the array center in Fig. 11.2 and the associated number of events "seen" by each nodes depending on the source-to-station ray path azimuth.

We show in Fig.11.3 the average spectral signature of the investigated events. We can see that those events have a spectral signature mainly within the [5-40] Hz frequency
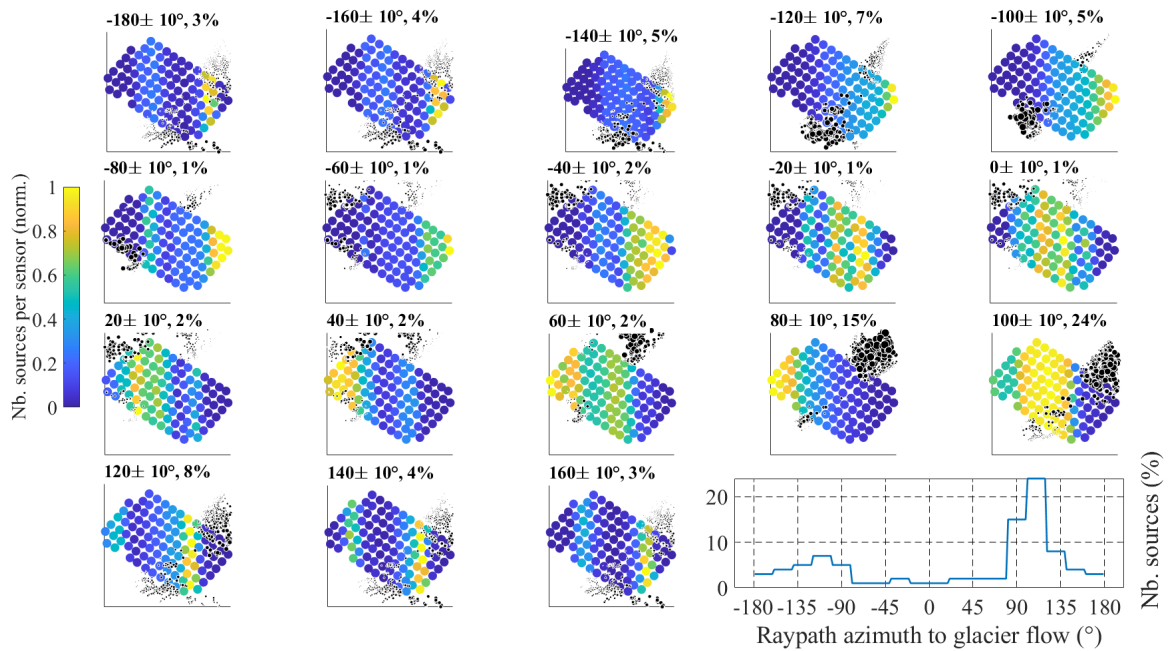
Figure 11.2: Number of events seen by each station for a given sources-to-station ray path azimuth with respect to glacier flow, i.e. azimuth 0° is along glacier flow. Color indicates the relative number of event number of events and each panel represent a 20° azimuth range. Black dots show event location whose size corresponds to how much the illuminate the array. Colorbar is scaled for each azimuth to the number of raypath analyzed within the given azimuth. The relative number of ray path per azimuth is shown in the last panel.

range. This supports our choice to investigate such large range of frequency to analyze the amplitude decay.
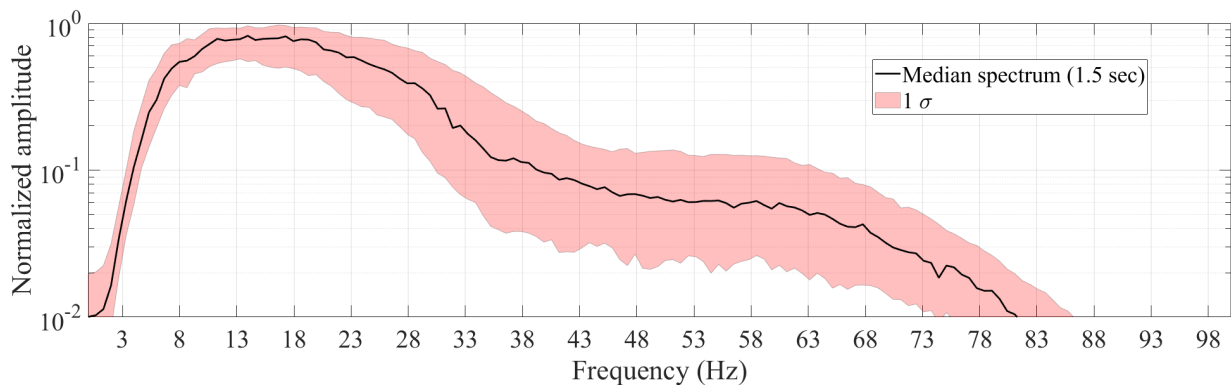
Figure 11.3: Average power spectral density of all events.

We show in Fig. 11.4 the distribution of the signal-to-noise ratio (SNR) of the peak amplitude compared to the 0.25 sec of the lowest amplitude in the 1.5 sec window of each event. We observe that most of the peak-ground-amplitude are one order of magnitude higher than the background noise for low and high frequencies and up to two order of magnitude for mid-frequencies. First, this supports the suitability of the selected events to investigate peak-ground-amplitude, which are well constrained. Second, the lower SNR can be explained at low amplitude by a background noise that
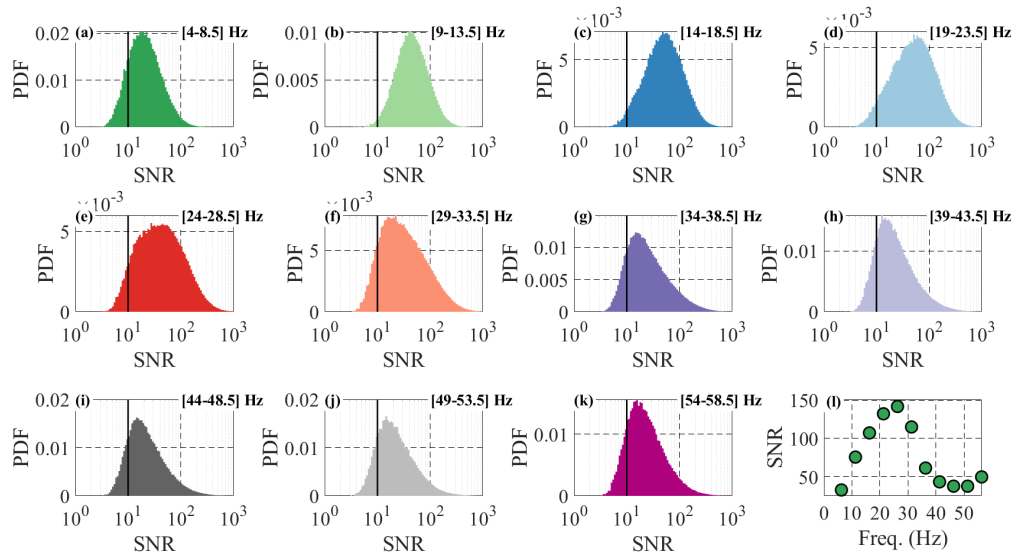
Figure 11.4: (a to k) Distribution of the signal-to-noise ratio (SNR) of the peak amplitude compared to the 0.25 sec of the lowest amplitude in the 1.5 sec window of each event. (l) Median SNR versus frequency.

might be influenced by noise sources (e.g. turbulent water flow) or by signals that have limited low-frequency content. At high frequency this could be related to scattering and attenuation effects that tend to limit the amplitude of the peak-ground-amplitude. In our analyzes we keep only seismic signal associated to $SNR > 10$ (black horizontal lines in Fig. 11.4).

Inversion of attenuation parameters

To investigate the amplitude decay and how it is influenced by frequency, we filter the waveforms with eleven 5 Hz-wide frequency bands from 5 to 55 Hz using a band pass butter-worth filter of second order. For each event and associated 98 waveforms (i.e. one at each sensor), we extract the 98 peak amplitudes using the maximum value of each Hilbert envelope as shown in Fig. 11.5. We discard sensors whose peak amplitude is not greater by at least an order of magnitude than the background noise. For each event we calculate the associated group velocity v_g (shown in Fig. 11.7) by linearly fitting the times of peak amplitude as a function of the source-to-sensor distance. We then normalize the peak amplitudes by the total energy of the signal within -0.25 s of the earliest arrival and +0.25 s of the latest arrival.

We characterize the amplitude decay for each event by inverting the source amplitude A_0, the attenuation parameter α that characterizes attenuation due to geometrical spreading and Q that characterizes attenuation due to anelastic attenuation. Q is the quality factor of the ice, the lower Q the higher the attenuation is. For a given event of amplitude A_0 located at a distance r from a seismic station, the theoretical amplitude decays $A(r)$ follows

$$A(r) = A_0 * r^{-\alpha} * e^{-\beta r} \tag{11.1}$$

with $\alpha = 0.5$ for surface waves and $\alpha = 1$ for body waves and β the anelastic attenuation parameter that depends on the frequency f, the wave group velocity v_g and the quality factor Q such as

$$Q = \frac{\pi f}{2 v_g \beta}. \tag{11.2}$$

We linearize Eq. 11.1 such as:

$$ln(A(r)) = ln(A_0) - \alpha * ln(r) - \beta r \tag{11.3}$$

and fit for each event the predicted amplitude decay and invert for the best attenuation parameters α and β as shown in Fig. 11.5. As Eq. 11.1 holds for far-field attenuation, we only fit events measured at a station that is at more than $\frac{5}{4}\lambda$ from the source. We do not invert for attenuation parameters if less than 20 station can be used to constrain the amplitude decay for a given event. We do not invert for attenuation parameters also if the amplitude decay do not span more than one wavelength and one order of magnitude in the amplitude. After inverting for the attenuation parameters, we compute the distribution of the α parameter and select for each frequency band range the most representative value of α (median value). We discard negative values of alpha and keep only values associated with a fit yielding a R^2 (corrected from the degrees of freedom) larger than 0.25. When selecting the best α we also assure a azimuthal distribution of the sources as shown in Fig. 11.17. We then use this fixed α to invert again for the parameter Q using Eq. 11.3. We then select the most representative value of β in a similar way that we did for alpha, and fit a third time our observations with constant β and α. Doing so we assume that there is an average model that describe the attenuation over our array with no site influence. This allows us then to evaluate the deviation from this averaged model of investigate for potential medium and wave propagation influences on the seismic amplitudes.

Evaluation of amplitude anomalies

For each event e we compare the fit obtained with the averaged attenuation model to the observations. At each sensor n we can therefore evaluate a difference from the observed and the modeled amplitude such as

$$\Delta A(n,e) = \frac{A_{obs}(n,e)}{A_{mod}(n,e)}. \tag{11.4}$$

We then evaluate ΔA in term of changes in α or β only to analyze the potential causes of those variations. In the case of changes in α only we consider that the observed β is equal to the modeled β such as
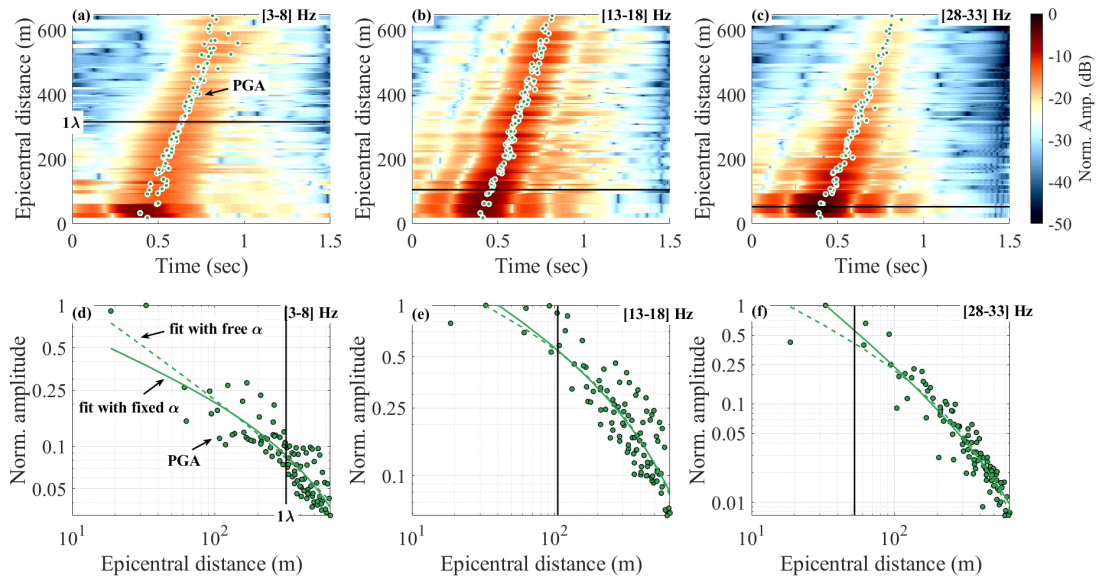
Figure 11.5: Amplitude decay as a function of the epicentral distance for one selected event. (a, b, c) Hilbert envelope of the filtered waveforms recorded at each node for three frequency ranges and picked maximum of the envelope (peak-ground-acceleration; green dots). The epicentral distance equivalent to one wavelength is show with the black horizontal line. (d, e, f) Observed (dots) and fitted peak-ground-acceleration with a free parameter of geometric attenuation α (dashed line) and a fixed one (plain lines). Peak amplitude are from the event shown in the upper panel. The epicentral distance equivalent to $\frac{5}{4}\lambda$ is shown with the black vertical line.

$$\frac{A_{obs}}{A_{mod}} = \frac{r^{-\alpha_{obs}} * e^{-\beta_{obs}r}}{r^{-\alpha_{mod}} * e^{-\beta_{mod}r}}.$$

$$\frac{A_{obs}}{A_{mod}} = \frac{r^{-\alpha_{obs}}}{r^{-\alpha_{mod}}}.$$

$$\frac{A_{obs}}{A_{mod}} = r^{-\alpha_{obs}+\alpha_{mod}}.$$

$$ln\left(\frac{A_{obs}}{A_{mod}}\right)/ln(r) = \alpha_{mod} - \alpha_{obs}. \tag{11.5}$$

In a similar manner and when considering only changes in β

$$\frac{A_{obs}}{A_{mod}} = \frac{r^{-\alpha_{obs}} * e^{-\beta_{obs}r}}{r^{-\alpha_{mod}} * e^{-\beta_{mod}r}}.$$

$$\frac{A_{obs}}{A_{mod}} = \frac{e^{-\beta_{obs}r}}{e^{-\beta_{mod}r}}.$$

$$\frac{A_{obs}}{A_{mod}} = e^{(-\beta_{obs}+\beta_{mod})r}.$$

$$ln\left(\frac{A_{obs}}{A_{mod}}\right)/r = \beta_{mod} - \beta_{obs}. \tag{11.6}$$

11.4   Results

General characteristics of selected events

To characterize the wave type we first evaluate the particle motion associated to each
event. To do so we rotate the north-south and east-west components into radial and
transverse components and evaluate the ratio of the major and minor axes of the el-
lipse that fits the radial versus vertical displacement. We show the distribution of the
major over minor axis ratios of the ellipse that fits the radial VS vertical components as
averaged per event and calculated over all events and the different frequency ranges in
Fig. 11.6. For Rayleigh waves, particle motion are expected to be similar in the vertical
and radial directions leading to ellipticity close to unity while for volume waves (e.g.
P and S waves) the vertical and radial of the particle are different leading to an ellip-
ticity greater than one (Aki and Richards, 2002). We observe that the median ellipticy
(Fig. 11.6 (l)) is closer to 1 at frequencies lower than 20 Hz than for frequencies higher
than 30 Hz for which it is closer to 2 to 2.5. This suggests that Rayleigh waves dom-
inate the seismic signal at low frequencies and that volume waves dominate at high
frequency.
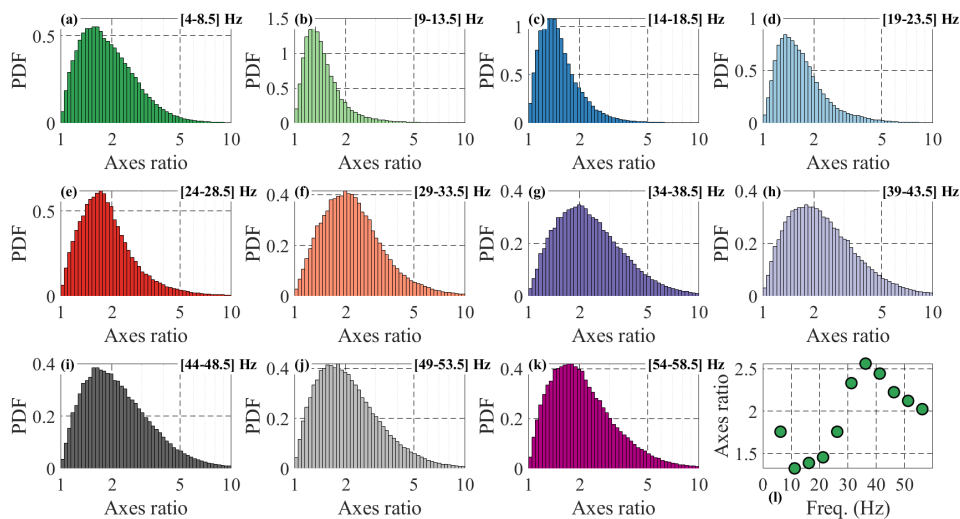
Figure 11.6: (a to k). Distribution of the major over minor axis ratios of the ellipse that fits
the radial VS vertical components as averaged per event and calculated over all events and the
different frequency ranges. (l) Median axes ratio versus frequency.

To complement our wave type characterization we also calculate the group velocity
associated to each event over the different frequency bands (Fig. 11.7). At frequencies
lower than c. 15 Hz we calculate group velocities on the order of 1530 m.sec^{-1}, which
is similar to the velocities inverted by (Sergeant *et al.*, 2020) for Rayleigh waves, i.e.
surface waves. From frequencies around 40 Hz we calculate group velocities on the
order of 1800 m.sec^{-1} which is similar to the values inverted in Sect. 8.3 (page 119)
for S-waves, i.e. volume waves. For frequencies around 50 Hz we calculate group ve-
locities on the order of 2000 to 3000 m.sec^{-1}, which suggest a contribution of both S-
waves (c. 1800 m.sec^{-1}) and P-waves (c. 3600 m.sec^{-1}) (Helmstetter *et al.*, 2015b). This

gradual transition from surface-wave dominated to volume-waves dominated seismic signal corroborates what we observed with the ellipticity in Fig. 11.6 and is in agreement with the general expectation of waves-type splitting with frequency (Aki and Richards, 2002).
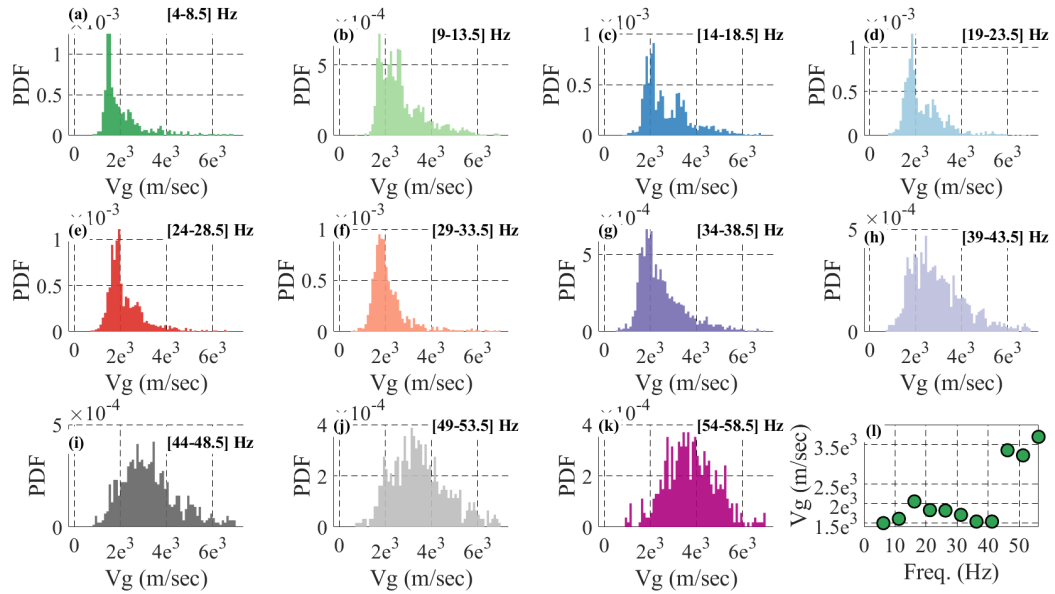
Figure 11.7: (a to k). Distribution of the group velocity V_g calculated for each events and over the different frequency ranges. (l) Median group velocity versus frequency.

Quality of the fit

We show in Fig. 11.8 the distribution of the R^2 (corrected from the degree of freedom) of the fit we applied to invert for the attenuation parameters. This parameter characterizes the quality of the fit, the closer to 1 the more the fit represents the observation. We observe that fixing both α and β (plain distribution) does significantly increase the quality of the fit compared to when we let free α and β. This increase is also due to the fact that when fixing both α and β we use only value of R^2 greater than 0.25 obtained from the fit with free α and β. We also observe that quality of the fit varies with frequency with peak distribution around $R^2 = 0.25$ a low frequencies (< 10 Hz), up to $R^2 = 0.7$ at mid-frequencies (~ 20 Hz) and around $R^2 = 0.25$ at the highest frequencies (> 40 Hz) . This might be caused by the fact that at low frequencies the amplitude decay spans only a few wavelengths (as shown in Fig. 11.5) and is therefore of limited magnitude compared to at high frequencies. The low R^2 values at high frequency might be due to lower signal-to-noise ratio that limits the accuracy of the observations.

Attenuation parameter from individual event's fit

In Fig. 11.5 we show examples of observed amplitude decay and corresponding fit for individual events filtered over the [3-8], [13-18] and [28-33] Hz frequency bands. For
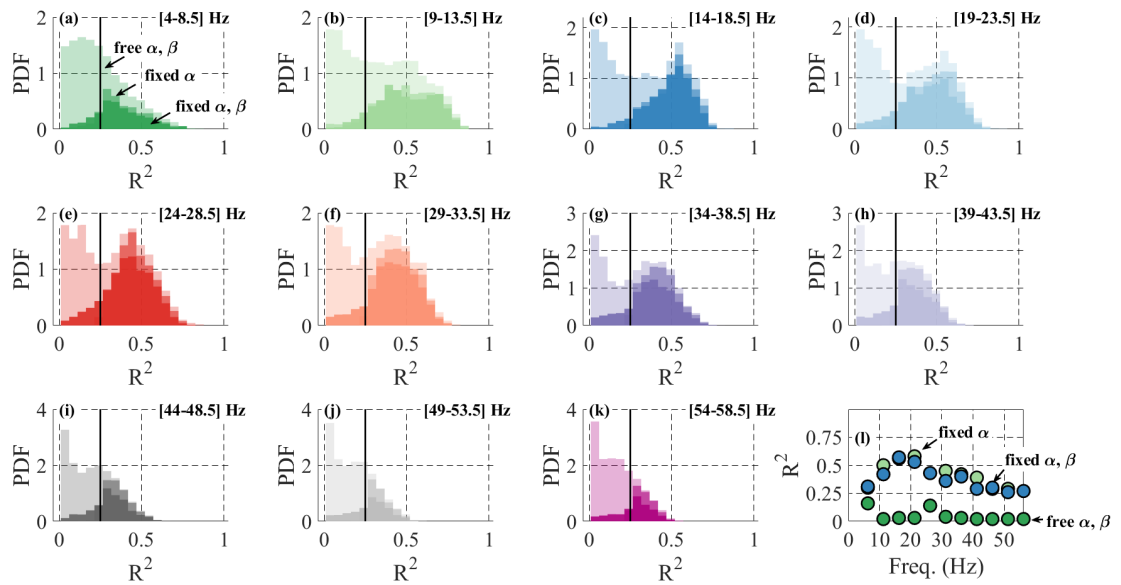
Figure 11.8: (a to k) Distribution of R^2 (corrected from the degree of freedom) of the fit applied to invert for the attenuation parameters. This parameter characterizes the quality of the fit, the closer to 1 the more the fit represents the observation. Shaded distribution show the first fit with free α and β, and plain one with the fixed α and β. Black vertical lines show the value of R^2 under which the associated event is not taken into account when investigating amplitude anomalies. (l) Median R^2 versus frequency. Plain green show the fits obtained with free α and β, shaded green with fixed α and free β and blue one with fixed α and β.

the three frequency bands we observe clear peak amplitudes (Fig. 11.5 (a, b, c)) and clear amplitude decays (Fig. 11.5 (d, e, f)). The amplitude decay is from one order (Fig. 11.5 (d)) to two orders of magnitude (Fig. 11.5 (e, f)) over distance that varies by about one order of magnitude. At low frequency (Fig. 11.5 (d)) the amplitude decay appears to be dominated by the geometric attenuation, as shown by the clear linear amplitude decay in the log-log diagrams. At high frequency (Fig. 11.5 (e, f)), the effect of anelastic attenuation is much more pronounced, with a more pronounced curvature of the amplitude decay compared to low frequencies. Overall, the theoretical prediction seems to well fit our observations.

Geometric attenuation

In Fig. 11.9 we show the distribution of the parameter of geometric attenuation α calculated for each event and over the different frequency ranges. We show in Fig. 11.9 all values of α inverted even when yielding unrealistic physical values (gray shaded). At frequencies lower than 10 Hz the distributions are well spread with median values around $\alpha = 1$. For frequencies between 15 and 30 Hz the distributions are more centered on $\alpha = 0.5$ with limited occurrence of non-realistic values compared to at lower frequency. For frequencies higher than 40 Hz, the distributions are centered around $\alpha = 0.75$, also with limited occurrence of non-realistic values. The spreading of α at frequencies lower than 10 Hz might be related to the fact that at such frequencies the
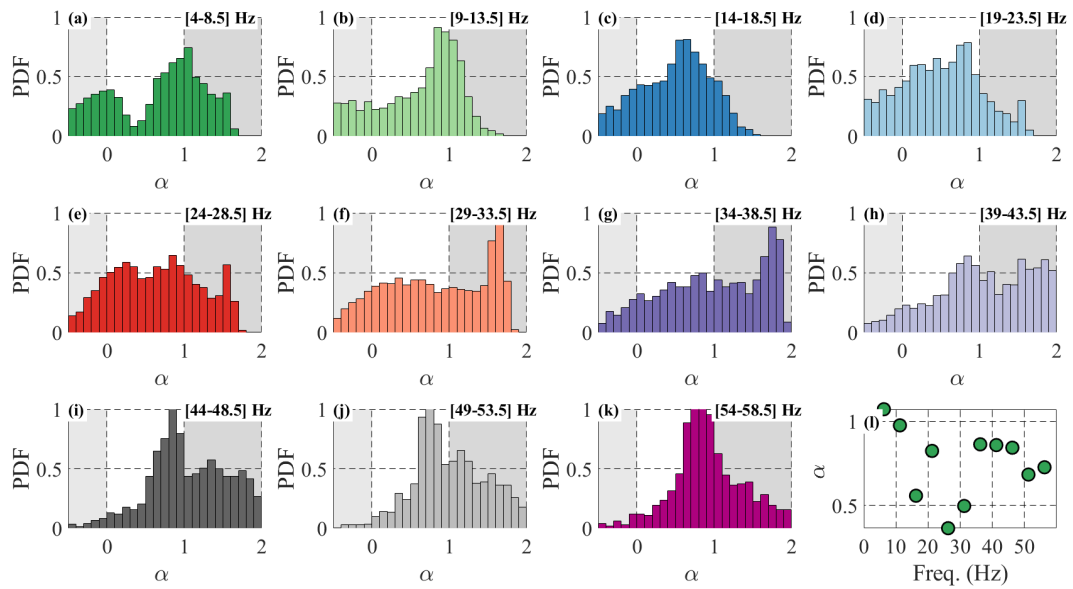
Figure 11.9: (a to k) Distribution of the parameter of geometric attenuation α calculated for each event and over the different frequency ranges. Grey shaded area show unrealistic attenuation parameters. (l) Median inverted α versus frequency. Unrealistic values (grey shaded area above) are not taken into account to calculate the median value.

amplitude decay spans only a few wavelengths, rendering difficult a good fit as shown by lower R^2 than at mid-frequencies (Fig. 11.8). When excluding those low frequencies, the general trend of α versus frequency supports a predominance of surface waves ($\alpha = 0.5$) under c. 30 Hz compared to a a predominance of volume waves ($\alpha \sim 1$) at higher frequencies.

Quality factor

In Fig. 11.10 we show the distribution of the quality factor Q calculated for each event and over the different frequency ranges. The quality factor is calculated for both free (shaded) and fixed (plain) α following Eq. 11.2. First we observe that fixing α tends to reduce the spread of Q distribution and yields higher Q values at frequencies lower than 10 Hz and higher values at frequencies around 40 Hz. When fixing α (Fig. 11.10 (l)) we observe than the median Q ranges from c. $Q = 8$ at low frequency up to $Q = 10$ at high frequency. There is therefore a very limited spectral dependency of Q.

Amplitude anomalies

Overview

We show in Fig. 11.11 the distribution of the amplitude anomalies ΔA calculated at each node, for each event and over the different frequency ranges (see Eq. 11.4). We first observe that the distributions are well represented by a Gaussian shape, which is typically expected because of changes in elastic properties over large seismic array
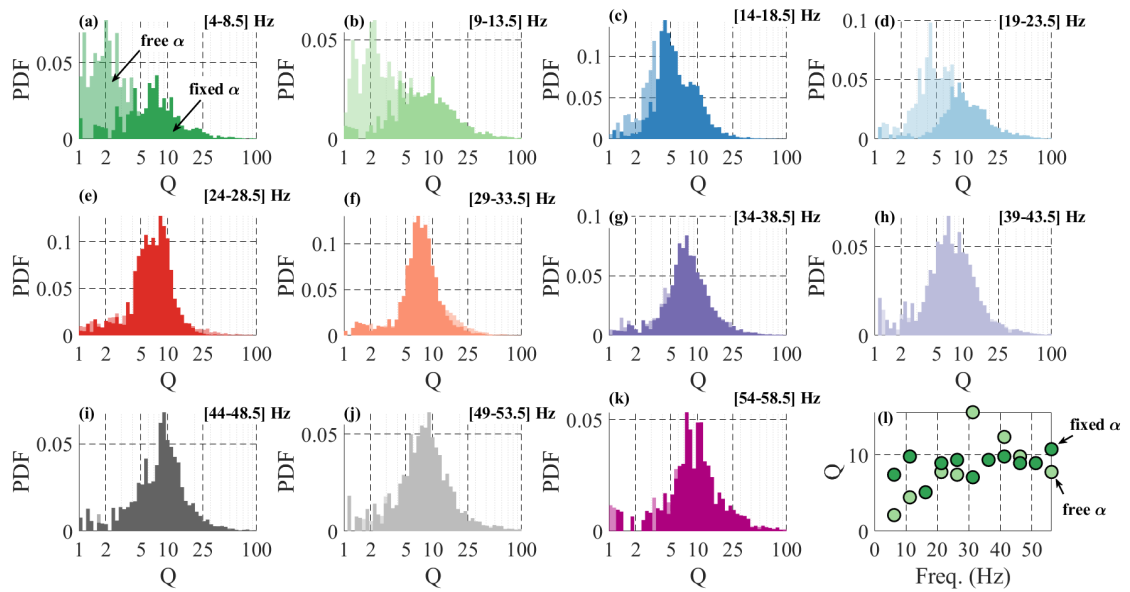
Figure 11.10: (a to k) Distribution of the quality factor Q calculated for each event and over the different frequency ranges (see Eq. 11.2). Shaded distribution show the first fit with free α and β, and plain one with the fixed α and free β. (l) Median quality factor Q versus frequency. Shaded points show values obtained with free α and β, and plain one with the fixed α and free β.

as shown for the USARRAY (Eddy and Ekström, 2014) or the Long-Beach (Lin *et al.*, 2013a) seismological experiments. We observe a much larger spreading of the distributions at high frequency than at low ones. For a PDF of c. $1e^{-4}$ we indeed observe a spread of c. 3 dB around 10 Hz while of c. 10 dB around 50 Hz. The peak of the distribution is however almost independent of the frequency with an average amplitude anomaly near within ± 0.5 dB for all frequencies. For frequencies higher than 40 Hz we observe heavier tails towards positive values (i.e. amplification) than towards negative ones (i.e. attenuation).

Spatial distribution

We show in Fig. 11.12 maps of the median amplitude anomaly measured at each sensor over the whole study period for the different frequency ranges. We observe that the sensor-averaged amplitude anomalies cover a range of ±3 dB with spatial variations that typically varies over c. 200 m at low frequency and over c. 100 m at high frequency with up to 5 dB of amplification. We do not observe clear change in the spatial pattern with frequency expect that the amplitude anomalies are up to + 10 dB at certain nodes at high frequency and only up to + 3 dB at low frequency. Such higher amplification was also highlighted by the distributions shown in Fig. 11.11 but we can observe with the maps that those high amplifications are limited to certain part of the seismic array and not a general amplification. Over all frequencies, we observe indeed that the sensors located on the northwestern and southeastern corner of our array present a pattern of amplitude amplification while sensors located on the northeastern and southwestern corner of our array present a pattern of amplitude attenuation. The
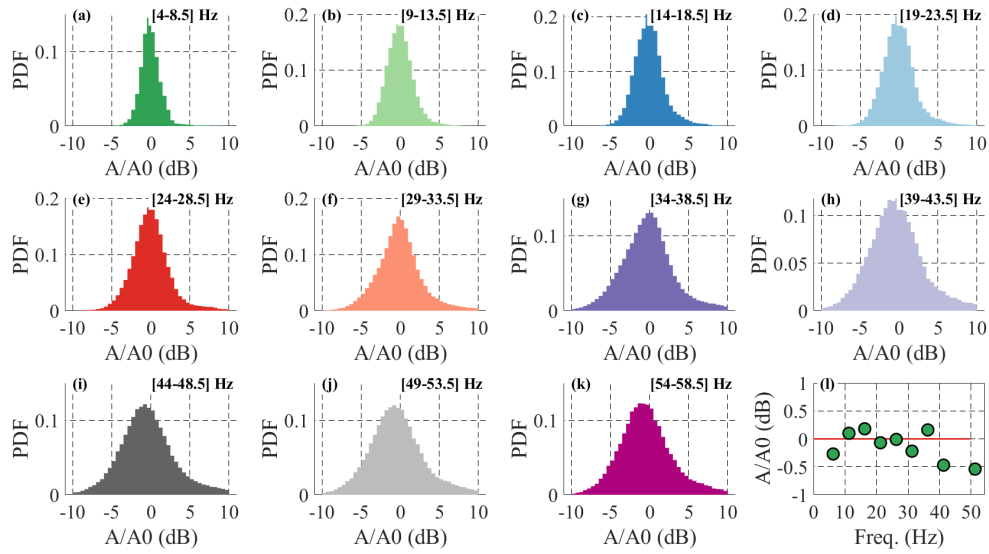
Figure 11.11: (a to k) Distribution of the amplitude anomalies ΔA calculated at each node, for each event and over the different frequency ranges (see Eq. 11.4). (l) Median quality factor amplitude anomaly ΔA versus frequency.

areas of amplification are also the one where crevasses are the most present, but also the one where the azimuths of the source-to-stations ray path form a c. -15° ± 180° angle with the along flow direction (Fig. 11.2).

Azimuthal distribution

We show in Fig. 11.13 the amplitude anomaly versus the source-to-stations ray path azimuth in order to investigate potential influence of the glacier anisotropy on the wave propagation. We observe a general trend for all frequencies, with a tendency of amplification for source-to-station raypath azimuth around -140°, -90° and 45° with respect to the along flow direction. Those peaks are more pronounced at high frequency (>20 Hz), with an amplification that reaches up to 2 dB for the highest frequencies. We also observe trend of attenuation for azimuth of c. 0°C, which correspond to wave traveling in the along flow direction.

We therefore observe a clear azimuthal variation in the seismic amplitude anomalies, which could have different origins that we discus in the following Sect. 11.5
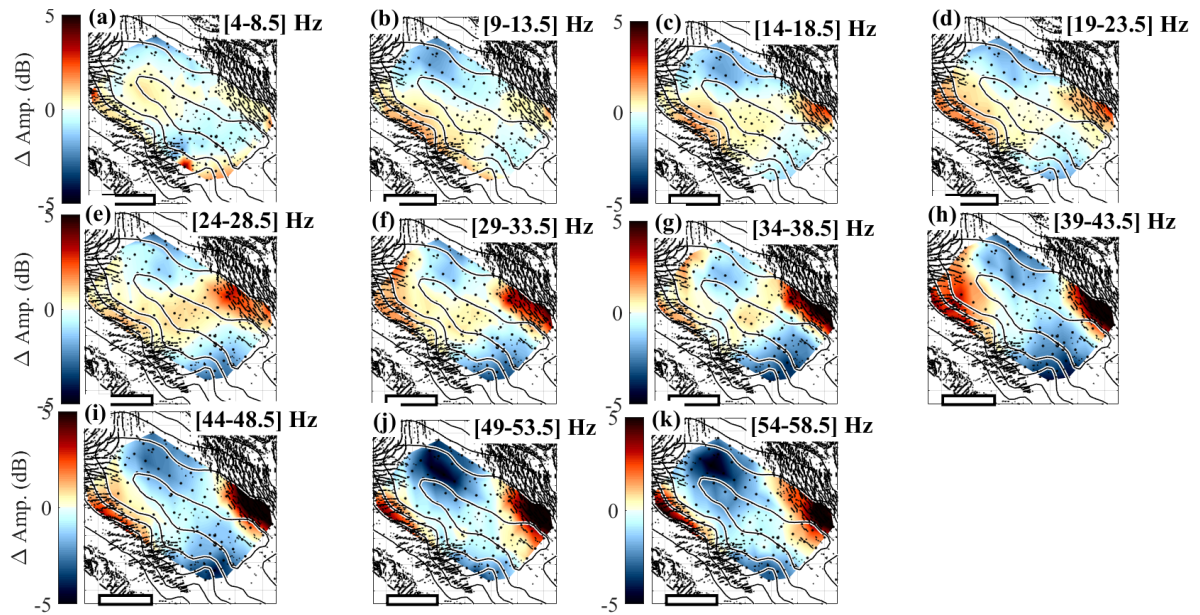
Figure 11.12: (a to k) Spatial distribution of the amplitude anomalies ΔA as averaged per node node and event over the different frequency ranges (see Eq. 11.4). Note that ranges of colorbars stay constant with frequency.

11.5   Discussion and Perspectives

Estimation of Quality factor

In Fig. 11.10 we observe a little dependecy of Q on the frequency. By applying a linear fit to this evolution we calculate a frequency dependent evolution as $Q = 7.15 * (f/f_0)^{0.13}$. Such dependency is similar to the one of $Q = 11.47 * (f/f_0)^{0.15}$ found by Bakker *et al.* (2020) for river sediments and slightly differs to the theory proposed by Tsai *et al.* (2012) that rather proposes a Q independent of frequency. Such low values of Q are quite unexpected for the ice compared to the soft sediment investigated in Bakker *et al.* (2020). Only a few measurements of seismic attenuation have been conducted on glacier (Gusmeroli *et al.*, 2010) but there is a general agreement that Q is significantly influenced by the temperature of the ice. Values of $Q \sim 1000$ at 136 Hz have been estimated by Bentley (1973) for an ice temperature of -28° and values of $Q = 65$ at 120-1000 Hz have been obtained for ice at the melting point. However it is very difficult to obtain a clear range of Q values for the ice and compare our result to previous studies as they often use different methods and evaluate different frequency ranges. Our estimation of Q is similar to the one recently obtained by Gusmeroli *et al.* (2010) of $Q = 5 \sim 8$ derived between 100 and 300 Hz. They conducted their study on a small valley glacier with an average temperature of about -1°C. In Glacier d'Argentière temperature are close to 0°C and our values of $Q \sim 5$ are consistent with those previous studies that show that attenuation increases with rising ice temperature. In addition, most of sources are located at the glacier surface, where the ice might be more damaged and water content up to 18 % (Hantz, 1981), leading to stronger attenuation than for dry and undamaged ice.
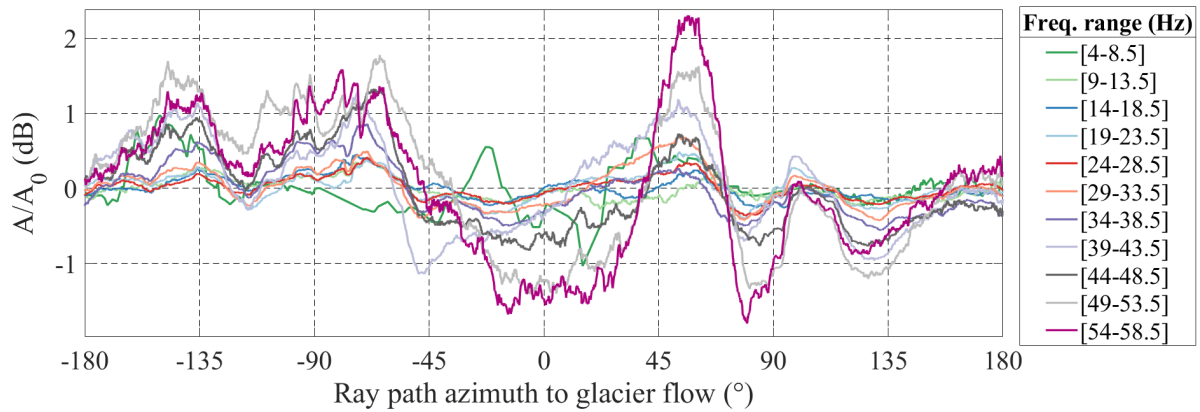
Figure 11.13: (a) Amplitude anomaly ΔA (see Eq. 11.4) calculated at each node, for each event and over the different frequency ranges and averaged per 10° source-to-station ray path azimuth bands.

Origin(s) of the azimuthal variation

The strong influence of the raypath azimuth on the amplitude anomalies could be of diverse origins:

• a crystallographic anisotropy of the ice as the wave traveling at 45 and -135° follow the same cross-flow direction (as in Sergeant *et al.* (2020)).

• the influence of crevasses, because the azimuth of higher amplification are also the one where the stations are the closer to the crevasse fields (Fig. 11.12) and also the one where the wave originates the most from the crevasse field (fig. 11.2).

• an artifact due to our methodology, for instance the uneven sampling of the different azimuths.

In general, the presence of crevasses damage in the medium is expected to cause scattering and amplitude attenuation (Moreau *et al.*, 2017) for wavelengths similar to the crevasses depth (c. [25-50] m) (Vaughan, 1993). Crevasses could also act as a resonance structure for wavelength that are on the order of the spacing between crevasses (c. [10-100] m), in such case the presence of crevasses favours amplification rather than attenuation (Preiswerk, 2018). Here I briefly address the influence of crevasses on these anomalies. To do so I have calculated the density of crevasse occurrence over our array and then calculated for each of the 700 000 source-to-station raypath the relative presence of crevasse along the wave path. To take into account the different sizes of the wavelengths at thus the "width" of the raypath at different azimuth I have averaged the presence of crevasses within $\pm$ $\lambda/2$ around the raypath. I show in Fig. 11.14 the crevasse surface density along raypath as a function of the raypath azimuth, similarly to what I shown in Fig. 11.13.

In Fig. 11.14 I observe that the crevasses presence along raypath is constant through raypath azimuth. For all frequencies, expect the lowest one, the presence of crevasses is more marked for azimuth around -90° and 70°. Those azimuth roughly represent the across-flow direction. On the contrary the crevasse are less present for the azimuths that travel along flow. This difference can be due to both the fact that crevasses are non
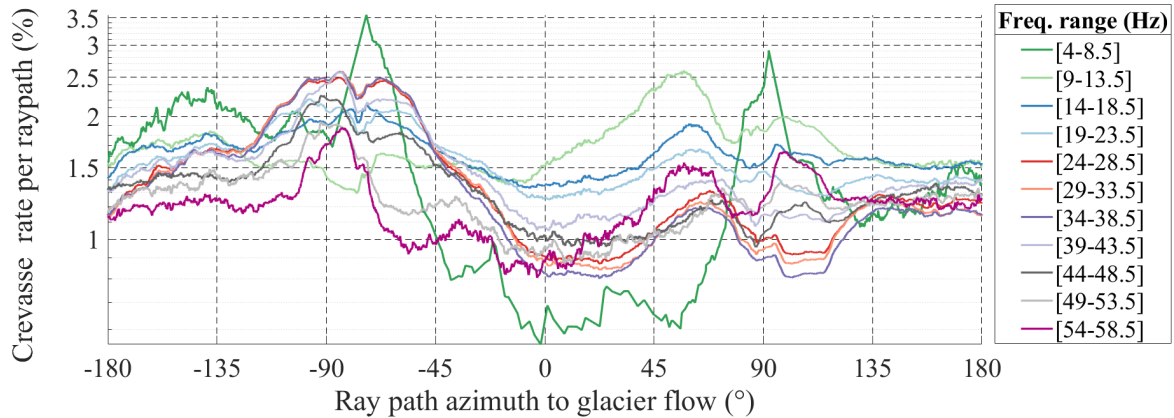
Figure 11.14: (a) Crevasse surface density per ray path as averaged per 10° source-to-station azimuth bands.

evenly distributed around our array, but also because the along flow raypath tends to be longer than the across flow one because of the shape of the array. We cannot explain the azimuthal variations in amplitude only from this azimuthal variation on the presence of crevasses along raypath, but is seems that crevasses play an important role on the amplitude anomalies.
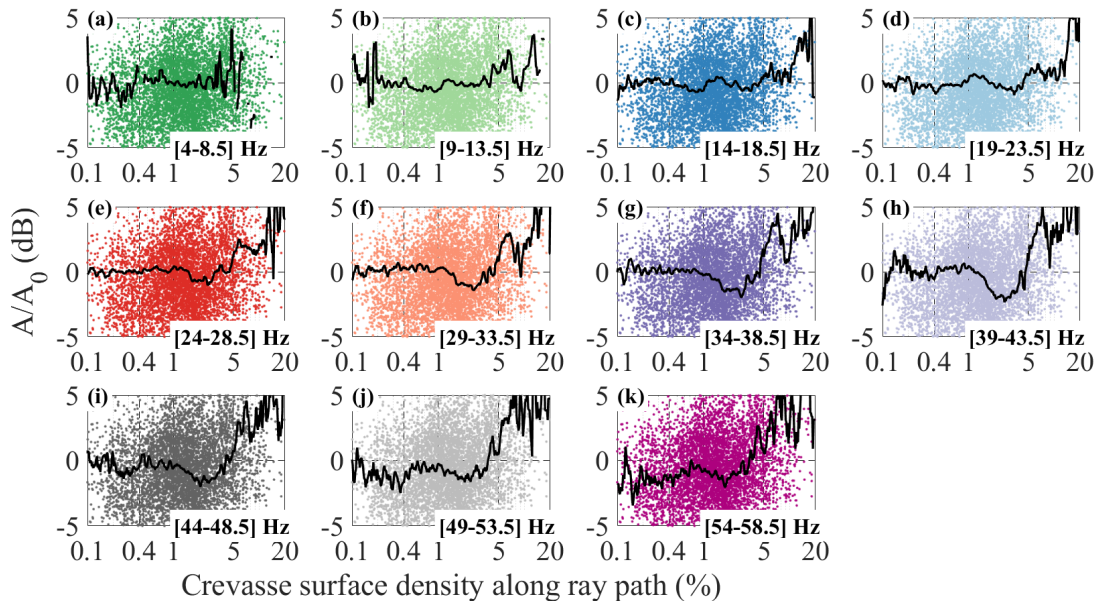
Figure 11.15: (a) Amplitude anomaly ΔA (see Eq. 11.4) evaluated against the crevasse surface density along each ray-path.

In order to go one step further, I have evaluated the amplitude anomaly against the crevasse rate over the array. I show in Fig. 11.15 the distribution for all crevasse rates (0 to 20%) and in Fig. 11.16 for the crevasse rates that are the most representative, i.e. the [1-5] % one that dominate the azimuthal distribution in Fig. 11.14. There is a general trend of amplification (3-5 dB) for higher presence of crevasses (>5%) but there is only a limited number of observations at such high rates. We also observe a trend of no significant amplitude anomaly for crevasse rate lower that c. 0.5 %, followed by a trend of attenuation by c. 1 to 3 dB when the crevasse rate increases up to c. 3 to 4 %.

Such crevasse rates are the one the most observed in our array (Fig. 11.14).

When focusing on the most representative crevasse occurrence (Fig. 11.16), we observe that crevasse presence has a relatively low influence on the amplitude anomalies at frequency lower than 20 Hz. This suggests that at low frequency crevasses occurrence do not strongly influence the seismic amplitude, and therefore that the medium can be considered as poorly damaged even in the presence of crevasses. This absence of clear attenuation because of crevasses is also well observable in Fig. 11.11 where we do not observe a strong deviation from the Gaussian distribution towards negative amplitude anomalies. We suggest that this is because crevasses are mainly present within the first 30 to 50 m from the surface and therefore poorly affect wavelengths that are almost 10 times larger. Such observations are similar to those made by Preiswerk (2018) that show little to none effect of crevasses on the wavefield measured at Alestchgletscher (a glacier of similar shape ratio than Argentière glacier) whereas crevasses led to 2D/3D eigenvibrations in the Eiger-Westflank glacier, a glacier with a more complex geometry and higher shape ratio than Argentière. The little influence of crevasses on the amplitude anomalies at low frequency might implies that subglacial water flow investigation within [3-7] Hz could be conducted on glacier environment without significant influence from the crevasse.

At higher frequencies (> 25 Hz), we first observe a trend of increasing attenuation with
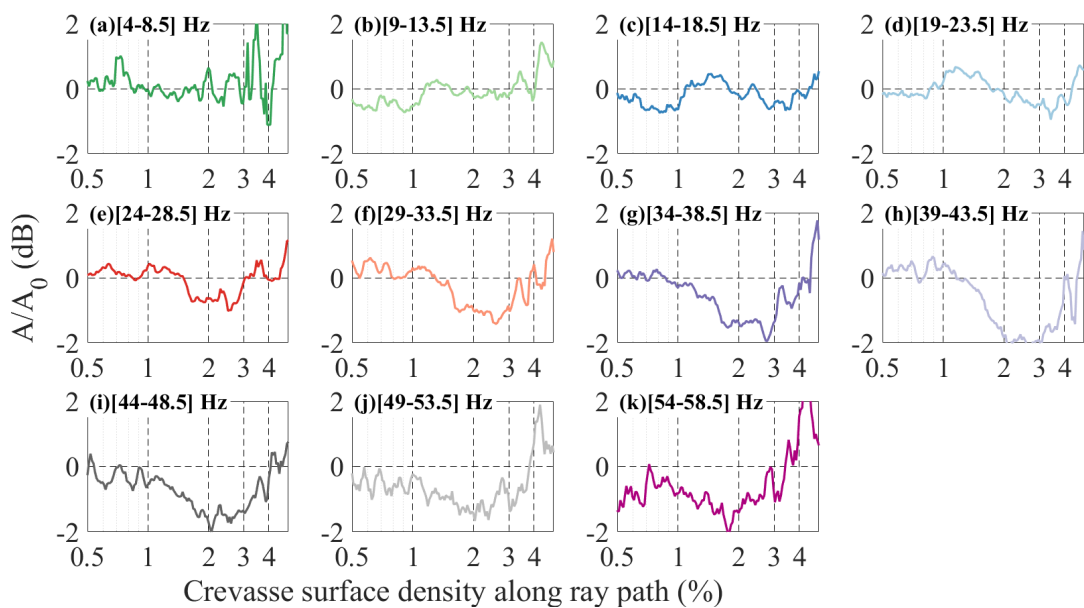
Figure 11.16: Same as in Fig. 11.15 but with a focus on the most representative crevasses density as shown in Fig. 11.14

crevasse presence and then a trend of increasing amplification with crevasse presence. Such complex evolution on the effect of crevasses might implies that other factors play a role on the amplitude anomalies or that the influence of crevasse is not unique. The trend of increasing attenuation, indicates that crevasse occurrence tends to attenuate amplitude at frequencies with wavelengths similar to the crevasses depth. The recent study of Lindner *et al.* (2018) also conducted on an Alpine glacier, shows similar behavior with crevasses that cause anisotropy up to 8%, and preferentially influence

the seismic wavefield at frequency higher than 15 Hz. This suggests that the effect of crevasses on the amplitude field results from both a scattering effect and induced azimuthal anisotropy.

Further study on the influence of the crevasses width and depth should be conducted to better constrain the relation between the frequency-dependent crevasses sensitivity and the crevasse geometry, which would be a precious way to remotely monitor crevasses and calving. Further study should also be conducted on the potential effect of crevasses on amplifying the seismic signal. This study shows that seismic amplitude might be used to investigate the medium properties and investigate changes in structure that are traditionally investigated through phase analysis.

Appendix

Sources distribution

We show in Fig. 11.17 the sources azimuthal distribution with respect to North and the source-to-station ray path azimuthal distribution. As shown in Figure 1, the sources are unevenly spread around the seimsic array because most of the sources are related to crevasses than mostly are little present upglacier of the array and on the upper right flank of the glacier. By selecting only a limited number of sources (flattened distribution) we greatly reduce the potential bias that would come from unevenly sampling the glacier from all direction. When we evaluate the best α and β we use the sources of the flattened histogram. The source-to-sensor azimuth distribution is much more even that the source azimuths because our seismic array cover a large areas and as sources are around the array almost all azimuths are covered by the ray-paths.
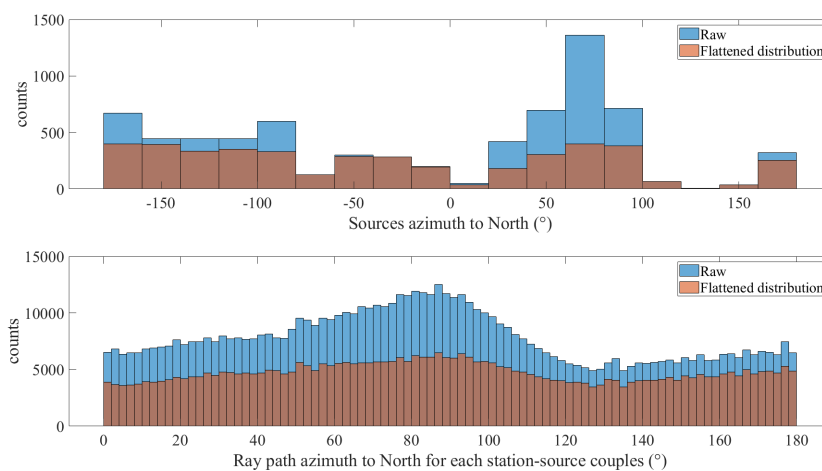
Figure 11.17: (a) Sources azimuthal distribution with respect to North and (b) source-to-station ray path azimuthal distribution. Blue distributions show the original event selection while brown one show the distribution after applying a correcting the number of event per azimuth.

Part VI

Conclusions and Perspectives

Time to pack up and leave the Glacier d'Argentière. © *Adrien Wherlé*.

Summary of the results and perspectives

This PhD work has outcomes in the two research fields of glaciology and seismology. On the hydrology side I provided novel, and previously lacking, observations of the subglacial drainage system. I first inverted the hydraulic pressure gradient and hydraulic radii over two melt-seasons and down to sub-hourly timescales and then retrieved the spatial configuration of subglacial water flow and its day-to-day evolution at the beginning of the melt-season. On the seismology side I have shown that a careful investigation of the seismic power within [3-7] Hz is appropriated to study the hydrodynamics of subglacial water flow at various timescales (from seasonal to hourly) and across a wide range of water discharges (from 0.25 to 10 $m^3.sec^{-1}$). I then proposed a novel methodology to address the previously unsolved challenge of locating distributed sources of seismic noise varying in time. Finally I have shown that spatial spatial variations in seismic amplitude at high frequency (> 1Hz) can be used to investigate medium properties such as the presence of scattering or anisotropic structures. Below, I summarize the responses to the key questions I have addressed.
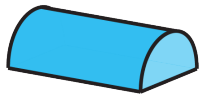
© Peb & Fox

Thematic question n°1:

How do subglacial hydraulic properties evolve over the melt-season and down to sub-diurnal timescales?

In Chapter 5 (page. 55), I inverted relative changes in the average hydraulic radius and hydraulic pressure gradient of the subglacial drainage system in the lower ablation zone of the Glacier d'Argentière and from Spring 2017 to Fall 2018. The method I used was not novel in itself (Gimbert *et al.*, 2016), but it was the first time it was applied over a complete melt-season and through winter. With our multi-year temporal series, I show that both hydraulic radius and hydraulic pressure gradient present at least a 2-fold increase from spring to summer, followed by a comparable decrease towards autumn. I also show that during summertime subglacial channels undergo strong changes in hydraulic pressure gradient because of the high diurnal water-supply variability.

Comparing our analysis with the theoretical predictions of Röthlisberger (1972) I identified seasonal channel dynamics characterized by two distinct regimes and yet unprecendently described on an Alpine glacier (see Fig. 5.10 on page 75). At low discharge I show that channels behave at equilibrium and respond to variations in discharge mainly through changes in hydraulic radius. At high discharge and pronounced diurnal variability I show that channels behave out of equilibrium and undergo strong changes in hydraulic pressure gradient that may help sustain high water pressure in cavities and thus high glacier sliding speed. Those observations are of particular interest as they question the traditional notion of subglacial channels/cavities duality and indicate that channel-like structure can be pressurized all summer-long.

I suggest that during periods of short-term variability in water supply, the subglacial drainage system becomes well-connected but with a limited drainage capacity. At such times, channels may also participate at maintaining high basal water pressure and therefore high sliding speed. Such behavior deserves more investigation as the impact of short-lived water input events (e.g. strong melt episodes or storms) on glacier dynamics is still under-investigated and the occurrence of such events is expected to increase due to climate change (Hynčica and Huth, 2019). I deem important to evaluate up to which extent our observations may be represented by current subglacial hydrology - glacier dynamics models (Fleurian *et al.*, 2018; Gagliardini and Werder, 2018) and which process and parameters are better constrained thanks to seismically-derived hydraulic dynamics.
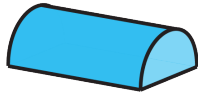
 Thematic question n°2:

What is the spatial configuration of the subglacial drainage system and how does it evolve through time?

In Chapter 9 (page 141) and using the unique observations of the RESOLVE-Argentière project, I retrieved 2D maps of the subglacial drainage system over a c. 500 m^2 area in the lower ablation zone of the glacier d'Argentière and its day-to-day evolution during the first month of the 2018 melt-season. Doing so I could observe when and where the subglacial drainage system is distributed through a connected cavity-system that enhances rapid glacier flow versus when and where it is localized through a channel-system that impedes rapid glacier flow. This is clearly one step forward compared to previous study as this is the first time that a map of the subglacial drainage system is retrieved from observations only.

I found that subglacial water flow is preferentially localized at the minimum of the hydraulic potential gradient forming along-flow water routes. I observed that when water discharge is low (< 2 m^3.sec^{-1}) the drainage system remains distributed with a low efficiency, which results in strong changes in hydraulic pressure in response to water supply. At that time, the presence of distributed water flow detectable with seismic noise suggests that there exist connections between cavities that present channel-like dynamics and control the hydraulic connectivity of the distributed system. Those connections have been theoretically suggested by Kamb (1987) and inferred from basal water pressure by Rada and Schoof (2018) and Andrews *et al.* (2014) but yet not observed with such a spatial resolution and over time.

I also observed that a large part of the bed does not present detectable turbulent water flow seimic sources, which suggests the presence of weakly-connected/hydraulically-isolated cavities as previously documented by Andrews *et al.* (2014); Rada and Schoof (2018). This shows that not only one can determine when and where the transition between a cavity-dominated and a channel-dominated drainage systems occurs, but also determine the hydraulic connectivity across the cavities. Such an approach will allow the glaciological community to study the route that water follows at the glacial bed and its influence on basal traction without the need for laborious and/or expensive instrumentation. Being capable of such observation is particularly important for regions such as Greenland where it is yet unclear under what conditions (e.g., water supply, glacier geometry) meltwater supply to the glacial bed enhances or limits glacier flow.

Methodological question n°1:

How well can we identify the seismic signature of subglacial water flow from other sources?

In Chapter 5 (page. 55) I analyzed two years of passive seismic measurements conducted on the glacier d'Argentière. I show that, in our setup, subglacial-water-flow-induced seismic noise is best expressed within the [3-7] Hz frequency range. I propose a methodology to limit the influence on the seismic power at such frequencies of other sources such as impulsive events (e.g. crevasse opening) and anthropogenic noise. In doing so I maximized the representativeness of the [3-7] Hz averaged seismic power to the continuous subglacial-water-flow-induced seismic noise and allowed us to study the associated hydrodynamic properties from water discharge as low as $0.25\mathrm{m}^3.\mathrm{sec}^{-1}$ and at sub-hourly timescales. This opens the door for monitoring subglacial hydrology dynamics in a variety of setup where it was previously difficult.

In Nanni *et al.* (2020) I suggest that seismic power $P_{[3-7]Hz}$ could be used to invert subglacial water discharge Q following a non-linear scaling on the form of $Q \propto P_{[3-7]Hz}^{11/24}$ during periods of high surface melt and in settings with strong seasonal variability in water input (e.g. Alpine and Greenland glaciers), while an almost linear scaling $Q \propto P_{[3-7]Hz}^{33/31}$ could be used for periods of low water input and in settings with limited water input variability such as in Antarctica. These empirical scalings should be tested on different sites and might allow one to monitor subglacial water discharge with surface seismometers even under hundreds of meters of ice.

Methodological question n°2:

How, and at what resolution, can we locate sources of seismic noise that are distributed in space and varying in time?

In Chapters 8 (page 109) and 9 (page 141), I analyzed one month of seismic measurements acquired on the glacier d'Argentière with a 98-sensors dense seismic array during the RESOLVE-Argentière project. I show that we can locate sources of noise distributed in space and varying in time such as those generated by subglacial water flow. To do so I (i) systematically evaluated the phase coherence each 1-sec long time windows over our seismic array, (ii) applied an efficient gradient-based minimization algorithm that allows for simultaneous multiple source location and (iii) conducted a statistical analysis of the sources location corresponding with local phase coherence. This is a step forward in source location since locating epicentral coordinates of simultaneously active and spatially distributed noise sources remained a major seismological challenge.

I observe that with a spatial sampling of the seismic wavefield at a sub-wavelength scale and in the near-field of targeted sources (i.e. within a couple of wavelengths) we can obtain a spatial resolution down to 1/6 to 1/8 of the investigated wavelength. This is up to four times more resolved than for far-field analysis. Such a novel approach is particularly appropriate to study numerous processes that generate similar spatially spread seismic noise in other environments such as lava flows on volcanoes (Soubestre *et al.*, 2019), tremors in fault zones (Mordret *et al.*, 2019) or sediment transport in rivers (Bakker *et al.*, 2020).

The approach we developed is already of great interest in our community as we have been discussing with A. Booth (U. Leeds) and S. Livingstone (U. Sheffield) about the installation of dense seismic array to investigate subglacial lake drainage in Greenland. I have also discussed with B. Davison (U. St Andrews) about installing dense seismic array in Antarctica to study subglacial hydrology and with the team of L. Zoet (U. Madison) to apply our methodology on a dense seismic array they installed on an Alaskan Glacier. We also plan to apply this approach on a dense seismic array installed on a mountain river (the one of Bakker *et al.* (2020)).

〜〜〜〜〜〜〜〜 **Methodological question n°3:**

To what extent can ground motion amplitudes be used for studying glacier features such as crevasses, thickness or ice anisotropy?

In Chapter 10 and Chapter 11 (page. 169) I analyzed how spatial variations in ground motion amplitudes can be used to study both sources properties and medium characteristics. By investigating the amplitude decay of more than 7000 events recorded on a 98-sensors dense seismic array I have first retrieved the average attenuation parameters of the glacier medium. I show that the ice quality factor can be as low as 5 to 8 for frequencies between 5 and 55 Hz, possibly because of the ice being temperate. I then evaluated how deviations from a uniform amplitude decay model yield information on the structure properties. I show that the amplitude anomalies varies by up to 3 dB with the azimuth of the source-to-station ray-path. Such variations could be related to the presence of crevasses that cause both attenuation and amplification of the ground motion amplitude depending on their orientation with respect to glacier flow and the wavelengths of the seismic waves.

I will conduct further investigations, but these preliminary results show that ground motion amplitude could be used in a complementary way to the traditional phase analysis to study site properties and retrieve source location. Quantifying site effects might allow us to focus on source effects such as crevasses mechanisms (Lindner *et al.*, 2020), stick-slip magnitude (Helmstetter *et al.*, 2015b) or turbulent water flow absolute hydraulic properties (Nanni *et al.*, 2020). Such outcomes are also of particularity interest for the environmental seismology community that, yet, poorly analyses the ground motion amplitude because of the complex interaction with the medium at high-frequency.

13

Sharing my work beyond academia

When I first started University in 2011, I wanted to gain knowledge in natural sciences to be able to become a documentary-filmmaker. I wanted to know more in order to share better. I wanted to walk on the footsteps of Cousteau, Paul-Emile Victor and Jules Verne's characters. One year after the other I continued in academia, throughout my Bachelor, my Master and soon my PhD. During that time, my will share the simple complexity of the Nature's beauty was still present, side to side with my hunger of knowledge. The PhD was for me a good opportunity to combine both. During those three years I tried different ways to share my works beyond academia. I found that as a young scientist my strength not only lies on the knowledge I can share but also on my personal experiences. My personal experiences as a young man trying to understand the world he is living in, trying to understand and share its complexity. I thus focused on communicating on how, as a young glaciologist, I conduct my research, how I do observe glaciers and what could we do, as a community, to share our works full of wonders beyond academia. I deem this to be an important aspect of my PhD. From a personal perspective, the PhD is not only about answering questions but also about sharing those answers and our process of answering, with our community and beyond. The projects I did beyond academia truly contributed to strengthen my capabilities to make connections between the different field of research (seismology-glaciology), take a step back to analyze the wider picture as well as formalize my ideas when discussing with both researcher or a non-academic public. I have selected here some of the works I have conducted that are in close link with my PhD research topic's.

Comics and cryoseismology

First project

In fall 2018 I have been selected for joining the project "Sciences en bulles". This project is led by the French government within the context of the "Fete de la Science", a national event that took place every year during one week and aims at sharing science in schools, universities, public events and more. Every year a book is made for this occasion and addresses a topic of particular interest. This book is then published at
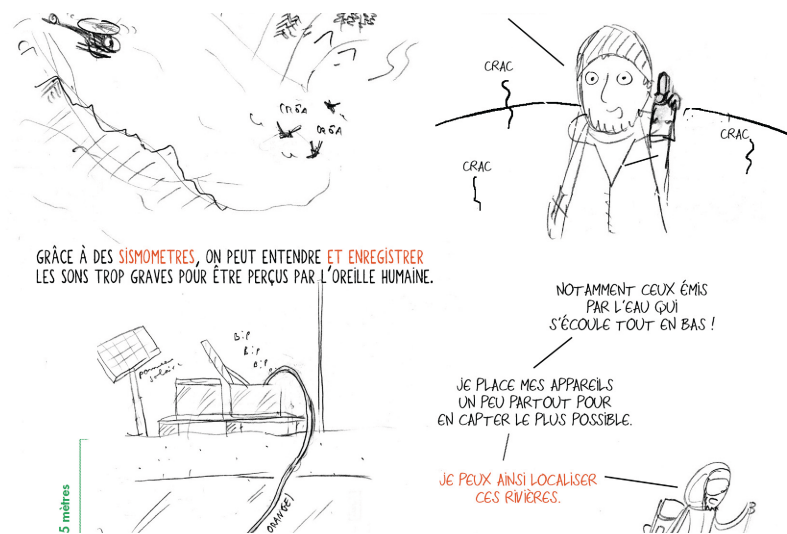
One of the first draft for the comic on my PhD work.

up to 100 000 exemplars and freely distributed across France in library, schools and universities. For the year 2019, they choose for the first time to make a comic book focused on PhD students and their research. 12 PhD students have been selected across France, with research topics spanning from social sciences to plastics in the oceans and the strength of ants. I was one of these 12 PhD student. From December 2018 to October 2019 we had different meetings in Paris, Angoulême, Lyon and Grenoble with comic-makers to make a comic on our research topic. In October and November 2019 I presented in Grenoble, Lyon and Paris the book in a series of conferences in libraries, schools, bars and theaters. This has been the occasion to share our research, to reflect on how to present complex research topics to a wide audience and to collaborate with experts outside of natural sciences. You can find the complete comic here[1].

Presenting our comic-book during the "Fete de la Science" in Paris with *Fred* from the famous TV show "C'est pas Sorcier" that has taught sScience for a generation of young people.

Working on a comic about the movement of glacier.

Second project

In fall 2019, when I was presenting our comic book in Grenoble I met a drawer and we decided to collaborate to make comics about the everyday life of researchers in glaciology. We created short stories that present examples of moments in the life of a scientist and introduce at the same time scientific concepts about glaciology. For instance, we made a four-pages comic on the PhD defence or one on the way glacier develop and react to climate change. We recently made a website to share our work (click here[2]) and we plan to publish those drawings when we reach a sufficient number of stories. I presented this work at the American Geosciences Union 2019 and was awarded the student innovation prize of the Cryosphere section. This prize helped us to pursue our collaboration and for the drawer to participate in a workshop about sharing science through comics. This project is more personal than the previous and allows me to share sciences also by sharing my vision of Science between dreams, adventures and society.
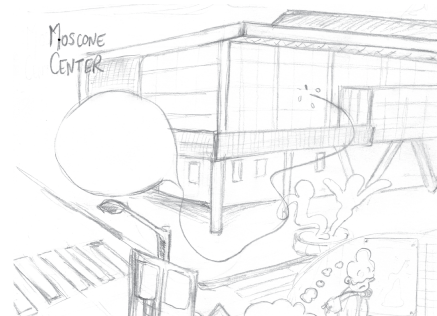
Working on a comic about the American Geophysical Union conference.

---

[1]or here: https://theconversation.com/profiles/ugo-nanni-857074/articles
[2]or here: https://didtinon.wixsite.com/glacebd

Video game and cryoseismology

Our video game on glacier and seismology.

In winter 2019 I participated to the "Grenoble Scientific Game Jam" that put together game developers, designers and PhD students in order to share Science through video games. This event consists in a 48-hour team-work between young game developers and a PhD student with the aim to address its research topic through a video game. This year, 10 PhD students were selected to participate. As for the comic-book, this was a very rich experience interacting with professional outside of natural sciences to create a story and a game all together. After the 48 hours we presented our games to a wide audience of kids, families and professional of video games and our project got awarded the highest prize, the "Golden Pixel". Our success lied into our ability to be able to make a simple game that yet allowed the user to learn something about my research topic. The video game can be downloaded and tested here[3]. Thanks to our success, we presented our project at several occasion, among which the "Fete de la Science" 2019 in Grenoble but also during a very interesting one-day workshop about the "New Ideas in Scientific Mediation", i.e. new ways to communicate science. I continue working with the game designer, which is now doing her master research in between game design and social science in order to analyze how to include sciences in video games.
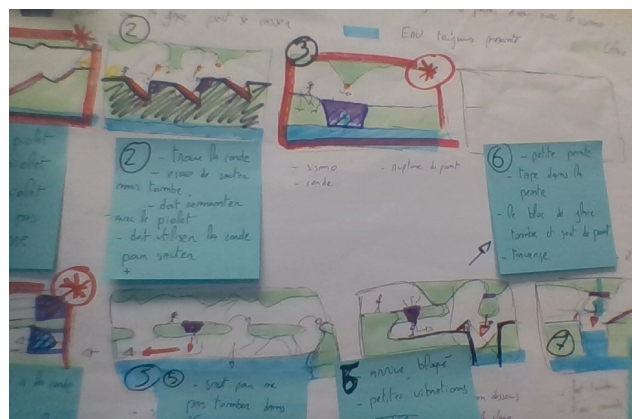
Team work between a glaciologist and game developers.

---

[3]or here: https://cracks.itch.io/the-sound-of-ice

Bibliography

Aki, K. and Richards, P. G.: Quantitative seismology, University Science Books,U.S., 2002.

Alley, R. B., Cuffey, K. M., and Zoet, L. K.: Glacial erosion: Status and outlook, Annals of Glaciology, 60, 1–13, doi: 10.1017/aog.2019.38, 2019.

Allstadt, K. and Malone, S. D.: Swarms of repeating stick-slip icequakes triggered by snow loading at Mount Rainier volcano, Journal of Geophysical Research: Earth Surface, 119, 1180–1203, 2014.

Almendros, J., Ibáñez, J. M., Alguacil, G., and Del Pezzo, E.: Array analysis using circular-wave-front geometry: An application to locate the nearby seismo-volcanic source, Geophysical Journal International, 136, 159–170, doi: 10.1046/j.1365-246X.1999.00699.x, 1999.

Anderson, S. and Radić, V.: Identification of local water resource vulnerability to rapid deglaciation in Alberta, Nature Climate Change, doi: 10.1038/s41558-020-0863-4, 2020.

Anderson, S. P., Longacre, S. A., and Kraal, E. R.: Patterns of water chemistry and discharge in the glacier-fed Kennicott River, Alaska: evidence for subglacial water storage cycles, Chemical Geology, 202, 297–312, 2003.

Andrews, L. C., Catania, G. A., Hoffman, M. J., Gulley, J. D., Lüthi, M. P., Ryser, C., Hawley, R. L., and Neumann, T. A.: Direct observations of evolving subglacial drainage beneath the Greenland Ice Sheet, Nature, 514, 80–83, doi: 10.1038/nature13796, URL http://www.nature.com/doifinder/10.1038/nature13796, 2014.

Anthony, R. E., Aster, R. C., Wiens, D., Nyblade, A., Anandakrishnan, S., Huerta, A., Winberry, J. P., Wilson, T., and Rowe, C.: The seismic noise environment of Antarctica, Seismological Research Letters, 86, 89–100, 2015.

Aso, N., Tsai, V. C., Schoof, C., Flowers, G. E., Whiteford, A., and Rada, C.: Seismologically observed spatiotemporal drainage activity at moulins, Journal of Geophysical Research: Solid Earth, 122, 9095–9108, 2017.

Aster, R. C. and Winberry, J. P.: Glacial Seismology (submitted), Reports on Progress in Physics, 2017.

Bakker, M., Gimbert, F., Geay, T., Misset, C., Zanker, S., and Recking, A.: Field Application and Validation of a Seismic Bedload Transport Model, Journal of Geophysical Research: Earth Surface, 125, 0–3, doi: 10.1029/2019jf005416, 2020.

Banerji, S. K.: Microseisms associated with disturbed weather in the Indian seas, Philosophical Transactions of the Royal Society of London. Series A, Containing Papers of a Mathematical or Physical Character, 229, 287–328, 1930.

Bartholomaus, T. C., Anderson, R. S., and Anderson, S. P.: Response of glacier basal motion to transient water storage, Nature Geoscience, 1, 33–37, doi: 10.1038/ngeo.2007.52, URL http://www.nature.com/doifinder/10.1038/ngeo.2007.52, 2008.

Bartholomaus, T. C., Anderson, R. S., and Anderson, S. P.: Growth and collapse of the distributed subglacial hydrologic system of Kennicott Glacier, Alaska, USA, and its effects

on basal motion, Journal of Glaciology, 57, 985–1002, doi: 10.3189/002214311798843269, 2011.

Bartholomaus, T. C., Amundson, J. M., Walter, J. I., O'Neel, S., West, M. E., and Larsen, C. F.: Subglacial discharge at tidewater glaciers revealed by seismic tremor, Geophysical Research Letters, 42, 6391–6398, doi: 10.1002/2015GL064590, 2015a.

Bartholomaus, T. C., Larsen, C. F., West, M. E., Neel, S. O., Pettit, E. C., and Truffer, M.: Journal of Geophysical Research : Earth Surface Tidal and seasonal variations in calving flux observed with passive seismology, pp. 1–20, doi: 10.1002/2015JF003641.The, 2015b.

Bartholomew, I., Nienow, P., Mair, D., Hubbard, A., King, M. A., and Sole, A.: Seasonal evolution of subglacial drainage and acceleration in a Greenland outlet glacier, Nature Geoscience, 3, 408–411, doi: 10.1038/ngeo863, URL `http://www.nature.com/doifinder/10.1038/ngeo863`, 2010.

Battaglia, J.: Location of long-period events below Kilauea Volcano using seismic amplitudes and accurate relative relocation, Journal of Geophysical Research, 108, doi: 10.1029/2003jb002517, 2003a.

Battaglia, J.: Location of seismic events and eruptive fissures on the Piton de la Fournaise volcano using seismic amplitudes, Journal of Geophysical Research, 108, 1–14, doi: 10.1029/2002jb002193, 2003b.

Bentley, C. R.: Impurities and seismic w a v e attenuation in the West A n t a r c t i c ice sheet, pp. 13–16, 1973.

Booth, A. D., Christoffersen, P., Schoonman, C., Clarke, A., Hubbard, B., Law, R., Doyle, S. H., Chudley, T. R., and Chalari, A.: Distributed Acoustic Sensing (DAS) of Seismic Properties in a Borehole drilled on a Fast-Flowing Greenlandic Outlet Glacier, Geophysical Research Letters, pp. 0–3, doi: 10.1002/ESSOAR.10502609.1, 2020.

Boulton, G. S. and Hindmarsh, R. C. A.: Sediment deformation beneath glaciers: rheology and geological consequences, Journal of Geophysical Research: Solid Earth, 92, 9059–9082, 1987.

Braun, J.: Pecube: A new finite-element code to solve the 3D heat transport equation including the effects of a time-varying, finite amplitude surface topography, Computers and Geosciences, 29, 787–794, doi: 10.1016/S0098-3004(03)00052-9, 2003.

Brondex, J., Gagliardini, O., Gillet-Chaulet, F., and Durand, G.: Sensitivity of grounding line dynamics to the choice of the friction law, Journal of Glaciology, 63, 854–866, doi: 10.1017/jog.2017.51, 2017.

Brun, F., Buri, P., Miles, E. S., Wagnon, P., Steiner, J., Berthier, E., Ragettli, S., Kraaijenbrink, P., Immerzeel, W. W., and Pellicciotti, F.: Quantifying volume loss from ice cliffs on debris-covered glaciers using high-resolution terrestrial and aerial photogrammetry, Journal of Glaciology, 62, 684–695, 2016.

Burtin, A., Bollinger, L., Vergne, J., Cattin, R., Nábělek, J. L., and Na, J. L.: Spectral analysis of seismic noise induced by rivers : A new tool to monitor spatiotemporal changes in stream hydrodynamics, Journal of Geophysical Research: Solid Earth, 113, 1–14, doi: 10.1029/2007JB005034, 2008.

Burtin, A., Vergne, J., Rivera, L., and Dubernet, P.: Location of river-induced seismic signal from noise correlation functions, Geophysical Journal International, 182, 1161–1173, doi: 10.1111/j.1365-246X.2010.04701.x, 2010.

Campillo, M. and Paul, A.: Long-range correlations in the diffuse seismic coda, Science, 299, 547–549, 2003.

Capon, J.: High-resolution frequency-wavenumber spectrum analysis, Proceedings of the IEEE, 57, 1408–1418, 1969.

Caudron, C., White, R. S., Green, R. G., Woods, J., Ágústsdóttir, T., Donaldson, C., Greenfield, T., Rivalta, E., and Brandsdóttir, B.: Journal of Geophysical Research : Solid Earth Seismic Amplitude Ratio Analysis of the 2014 – 2015 Bár ð arbunga-Holuhraun Dike Propagation and Eruption, pp. 264–276, doi: 10.1002/2017JB014660, 2018.

Chandler, D. M., Wadham, J. L., Lis, G. P., Cowton, T., Sole, A., Bartholomew, I., Telling, J., Nienow, P., Bagshaw, E. B., Mair, D., Vinen, S., Hubbard, A., Others, Vinen, S., and Hubbard, A.: Evolution of the subglacial drainage system beneath the Greenland Ice Sheet revealed by tracers, Nature Geoscience, 6, 195–198, doi: 10.1038/ngeo1737, URL http://www.nature.com/doifinder/10.1038/ngeo1737http://dx.doi.org/10.1038/ngeo1737, 2013.

Chmiel, M., Roux, P., and Bardainne, T.: Extraction of phase and group velocities from ambient surface noise in a patch-array configuration, Geophysics, 81, KS231–KS240, doi: 10.1190/GEO2016-0027.1, 2016.

Chmiel, M., Roux, P., and Bardainne, T.: High-sensitivity microseismic monitoring: Automatic detection and localization of subsurface noise sources using matched-field processing and dense patch arrays, Geophysics, 84, KS211–KS223, doi: 10.1190/geo2018-0537.1, 2019.

Church, G., Bauder, A., Grab, M., Rabenstein, L., Singh, S., and Maurer, H.: Detecting and characterising an englacial conduit network within a temperate Swiss glacier using active seismic , ground penetrating radar and borehole analysis, Annals of Glaciology, 60, 1–13, doi: 10.1017/aog.2019.19, 2019.

Colgan, W., Rajaram, H., Anderson, R. S., Steffen, K., Zwally, H. J., Phillips, T., and Abdalati, W.: The annual glaciohydrology cycle in the ablation zone of the Greenland ice sheet: Part 2. Observed and modeled ice flow, Journal of Glaciology, 58, 51–64, doi: 10.3189/2012JoG11J081, 2012.

Collins, D. N.: Quantitative determination of the subglacial hydrology of two Alpine glaciers., Journal of Glaciology, 23, 347–362, doi: 10.1017/S0022143000029956, 1979.

Corciulo, M., Roux, P., Campillo, M., Dubucq, D., and Kuperman, W. A.: Multiscale matched-field processing for noise-source localization in exploration geophysics, Geophysics, 77, 2012.

Cuffey, K. M. and Paterson, W. S. B.: The physics of glaciers, Academic Press, 2010.

Davison, B. J., Sole, A. J., Livingstone, S. J., Cowton, T. R., and Nienow, P. W.: The influence of hydrology on the dynamics of land-terminating sectors of the Greenland ice sheet, Frontiers in Earth Science, 7, doi: 10.3389/feart.2019.00010, 2019.

De Fleurian, B., Gagliardini, O., Zwinger, T., Durand, G., Le Meur, E., Mair, D., and Räback, P.: A double continuum hydrological model for glacier applications, Cryosphere, 8, 137–153, doi: 10.5194/tc-8-137-2014, 2014.

de Fleurian, B., Morlighem, M., Seroussi, H., Rignot, E., van den Broeke, M. R., Kuipers Munneke, P., Mouginot, J., Smeets, P. C. J. P., Tedstone, A. J., Fleurian, B., Morlighem, M., Seroussi, H., Rignot, E., Broeke, M. R., Munneke, P. K., Mouginot, J., Smeets, P. C. J. P., and Tedstone, A. J.: A modeling study of the effect of runoff variability on the effective pressure beneath Russell Glacier, West Greenland, Journal of Geophysical Research F: Earth Surface, 121, 1834–1848, doi: 10.1002/2016JF003842, 2016.

Dehecq, A., Gourmelen, N., Gardner, A. S., Brun, F., Goldberg, D., Nienow, P. W., Berthier, E., Vincent, C., Wagnon, P., and Trouvé, E.: Twenty-first century glacier slowdown driven by, Nature Geoscience, 12, 22, doi: 10.1038/s41561-018-0271-9, URL http://dx.doi.org/10.1038/s41561-018-0271-9, 2019.

Diaz, J., Ruiz, M., Sánchez-Pastor, P. S., Romero, P., Díaz, J., Ruiz, M., Sánchez-Pastor, P. S., and Romero, P.: Urban Seismology: On the origin of earth vibrations within a city, Scientific Reports, 7, 1–11, doi: 10.1038/s41598-017-15499-y, 2017.

Dziewonski, A. M. and Anderson, D. L.: Preliminary reference Earth model, Physics of the earth and planetary interiors, 25, 297–356, 1981.

Eddy, C. L. and Ekström, G.: Local amplification of Rayleigh waves in the continental United States observed on the USArray, Earth and Planetary Science Letters, 402, 50–57, doi: 10.1016/j.epsl.2014.01.013, URL http://dx.doi.org/10.1016/j.epsl.2014.01.013, 2014.

Egholm, D. L., Nielsen, S. B., Pedersen, V. K., and Lesemann, J.-E.: Glacial effects limiting mountain height, Nature, 460, 884–887, doi: 10.1038/nature08263, URL http://www.nature.com/doifinder/10.1038/nature08263, 2009.

Ekström, G., Nettles, M., and Abers, G. A.: Glacial Earthquakes, Science, 302, 622–624, doi: 10.1126/science.1088057, 2003.

Fichtner, A. and Tsai, V.: Theoretical foundations of noise interferometry, Seismic ambient noise, pp. 109–143, 2019.

Fleming, S. W. and Clarke, G. K.: Attenuation of high-frequency interannual streamflow variability by watershed glacial cover, Journal of Hydraulic Engineering, 131, 615–618, 2005.

Fleurian, B. D., Werder, M. A., Beyer, S., Brinkerhoff, D. J., Delaney Ian, Dow, C. F., Downs, J., Gagliardini, O., Hoffman, M. J., Hooke, R. L. B., Seguinot, J., Sommers, A. N., and Others: SHMIP The subglacial hydrology model intercomparison Project, Journal of Glaciology, 64, 1–20, doi: 10.1017/jog.2018.78, URL `https://www.cambridge.org/core/product/identifier/S0022143018000783/type/journal{_}article`, 2018.

Flowers, G. E.: Modelling water flow under glaciers and ice sheets, Proceedings of the Royal Society A: Mathematical, Physical and Engineering Sciences, 471, 20140 907, doi: 10.1098/rspa.2014.0907, 2015.

Flowers, G. E. and Clarke, G. K. C.: A multicomponent coupled model of glacier hydrology 1. Theory and synthetic examples, Journal of Geophysical Research: Solid Earth, 107, ECV–9, doi: https://doi.org/10.1029/2001JB001122, 2002.

Floyd, P.: Learning To Fly, On A Momentary Lapse of Reason [audiotape]. London, UK: EMI, 1987.

Foroutan, M., Marshall, S. J., and Menounos, B.: Automatic mapping and geomorphometry extraction technique for crevasses in geodetic mass-balance calculations at Haig Glacier, Canadian Rockies, Journal of Glaciology, 65, 971–982, 2019.

Fountain, A. G.: Borehole water-level variations and implications for the subglacial hydraulics of South Cascade Glacier, Washington State, USA, Journal of Glaciology, 40, 293–304, 1994.

Frederikse, T., Landerer, F., Caron, L., Adhikari, S., Parkes, D., Humphrey, V. W., Dangendorf, S., Hogarth, P., Zanna, L., Cheng, L., and Wu, Y. H.: The causes of sea-level rise since 1900, Nature, 584, 393–397, doi: 10.1038/s41586-020-2591-3, URL `http://dx.doi.org/10.1038/s41586-020-2591-3`, 2020.

Gagliardini, O. and Werder, M. A.: Influence of increasing surface melt over decadal timescales on land-terminating Greenland-type outlet glaciers, Journal of Glaciology, 64, 700–710, doi: 10.1017/jog.2018.59, 2018.

Gagliardini, O., Cohen, D., Råback, P., and Zwinger, T.: Finite-element modeling of subglacial cavities and related friction law, Journal of Geophysical Research: Earth Surface, 112, 1–11, doi: 10.1029/2006JF000576, 2007.

Gajek, W., Malinowski, M., Schweitzer, J., Majdanski, M., Geissler, H., Chamarczuk, M., and Wuestefeld, A.: Seismological monitoring of Svalbard's cryosphere: current status and knowledge gaps (CRYOSEIS) 5, SESS Report 2019, pp. 136–159, 2019.

Garambois, S., Legchenko, A., Vincent, C., and Thibert, E.: Ground-penetrating radar and surface nuclear magnetic resonance monitoring of an englacial water-filled cavity in the polythermal glacier of Tête RousseGPR monitoring of a polythermal glacier, Geophysics, 81, WA131—-WA146, 2016.

Gibbons, S. J. and Ringdal, F.: The detection of low magnitude seismic events using array-based waveform correlation, Geophysical Journal International, 165, 149–166, 2006.

Gimbert, F. and Tsai, V. C.: Predicting short-period, wind-wave-generated seismic noise in coastal regions, Earth and Planetary Science Letters, 426, 280–292, doi: 10.1016/j.epsl.2015.06.017, URL `http://dx.doi.org/10.1016/j.epsl.2015.06.017`, 2015.

Gimbert, F., Tsai, V. C., and Lamb, M. P.: A physical model for seismic noise generation by turbulent flow in rivers, Journal of Geophysical Research: Earth Surface, 119, 2209–2238, 2014.

Gimbert, F., Tsai, V. C., Amundson, J. M., Bartholomaus, T. C., Jacob, I., and Walter, J. I.: Subseasonal changes observed in subglacial channel pressure, size, and sediment transport, Geophysical Research Letters, 43, 3786–3794, doi: 10.1002/2016GL068337, 2016.

Glen, J. W.: Experiments on the Deformation of Ice, Journal of Glaciology, 2, 111–114, doi: 10.1017/S0022143000034067, URL https://www.cambridge.org/core/product/identifier/S0022143000034067/type/journal{_}article, 1952.

Gradon, C., Moreau, L., Roux, P., and Ben-Zion, Y.: Analysis of surface and seismic sources in dense array data with match field processing and Markov chain Monte Carlo sampling, Geophysical Journal International, 218, 1044–1056, doi: 10.1093/gji/ggz224, 2019.

Gulley, J. D., Benn, D. I., Screaton, E., and Martin, J.: Mechanisms of englacial conduit formation and their implications for subglacial recharge, Quaternary Science Reviews, 28, 1984–1999, doi: 10.1016/j.quascirev.2009.04.002, URL http://dx.doi.org/10.1016/j.quascirev.2009.04.002, 2009.

Gusmeroli, A., Clark, R. A., Murray, T., Booth, A. D., Kulessa, B., and Barrett, B. E.: Instruments and Methods Seismic wave attenuation in the uppermost glacier ice of Storglaci ¨ aren , Sweden, Journal of Geophysical Research, 56, 249–256, doi: 10.3189/002214310791968485, 2010.

Hansen, P. C. and O'Leary, D. P.: The use of the L-curve in the regularization of discrete ill-posed problems, SIAM journal on scientific computing, 14, 1487–1503, 1993.

Hantz, D.: Dynamique et hydrologie du glacier d ' Argenti ' ere (Alpes Didier Hantz, PhD, 1981.

Hantz, D. and Lliboutry, L.: Waterways, ice permeability at depth, and water pressures at Glacier d'Argentiere, French Alps, Journal of glaciology, 29, 227–239, 1983.

Hasselmann, K.: A statistical analysis of the generation of microseisms, Reviews of Geophysics, 1, 177–210, 1963.

Helmstetter, A., Moreau, L., Nicolas, B., Comon, P., and Gay, M.: Intermediate-depth icequakes and harmonic tremor in an Alpine glacier (Glacier d'Argentière, France): Evidence for hydraulic fracturing, Journal of Geophysical Research: Earth Surface, 120, 402–416, doi: 10.1002/2014JF003289, 2015a.

Helmstetter, A., Nicolas, B., Comon, P., and Gay, M.: Basal icequakes recorded beneath an alpine glacier (Glacier d'Argentière, Mont Blanc, France): Evidence for stick-slip motion?, Journal of Geophysical Research: Earth Surface, 120, 379–401, doi: 10.1002/2014JF003288, 2015b.

Herman, F., Copeland, P., Avouac, J. P., Bollinger, L., Maheo, G., Le Fort, P., Rai, S., Foster, D., Pecher, A., Stuwe, K., and Henry, P.: Exhumation, crustal deformation, and thermal structure of the Nepal Himalaya derived from the inversion of thermochronological and thermobarometric data and modeling of the topography, Journal of Geophysical Research: Solid Earth, 115, 1–38, doi: 10.1029/2008JB006126, 2010.

Herman, F., Beyssac, O., Brughelli, M., Lane, S. N., Leprince, S., Adatte, T., Lin, J. Y. Y., Avouac, J.-P., and Cox, S. C.: Erosion by an Alpine glacier, Science, 350, 193–195, doi: 10.1126/science.aab2386, URL http://www.sciencemag.org/cgi/doi/10.1126/science.aab2386, 2015.

Herring, T. A., King, R. W., and McClusky, S. C.: Introduction to GAMIT/GLOBK Introduction to GAMIT/GLOBK, 2010.

Herrmann, R. B.: Computer programs in seismology: An evolving tool for instruction and research, Seismological Research Letters, 84, 1081–1088, 2013.

Hewitt, I. J.: Seasonal changes in ice sheet motion due to melt water lubrication, Earth and Planetary Science Letters, 371-372, 16–25, doi: 10.1016/j.epsl.2013.04.022, URL http://dx.doi.org/10.1016/j.epsl.2013.04.022, 2013.

Hoffman, M. J., Andrews, L. C., Price, S. A. F., Catania, G. A., Neumann, T. A., Lüthi, M. P., Gulley, J., Ryser, C., Hawley, R. L., and Morriss, B.: Greenland subglacial drainage evolution

regulated by weakly connected regions of the bed, Nature Communications, 7, 13 903, doi: 10.1038/ncomms13903, 2016.

Hooke, R. L.: On the role of mechanical energy in maintaining subglacial water conduits at atmospheric pressure, Journal of Glaciology, 30, 180–187, 1984.

Hubbard, B. and Nienow, P.: Alpine subglacial hydrology, Quaternary Science Reviews, 16, 939–955, doi: 10.1016/S0277-3791(97)00031-0, 1997.

Hubbard, B. P., Sharp, M. J., Willis, I., Nielsen, M. K., and Smart, C. C.: Borehole water-level variations and the structure of the subglacial hydrological systelll of Haut Glacier d ' Arolla ,, Journal of Glaciology, 41, 572–583, 1995.

Hynčica, M. and Huth, R.: Long-term changes in precipitation phase in Europe in cold half year, Atmospheric Research, 227, 79–88, 2019.

Iken, A. and Bindschadler, R. A.: Combined measurements of subglacial water pressure and surface velocity of Findelengletscher, Switzerland: conclusions about drainage system and sliding mechanism, Journal of Glaciology, 32, 101–119, doi: 10.1017/S0022143000006936, URL https://www.cambridge.org/core/product/identifier/S0022143000006936/type/journal{_}article, 1986.

Iken, A. L. M. U. T., Truffer, M., and Truffe, M.: The relationship between subglacial water pressure and velocity of Findelengletscher, Switzerland, during its advance and retreat, Journal of Glaciology, 43, 328–338, doi: 10.1017/CBO9781107415324.004, 1997.

Inbal, A., Ampuero, J. P., and Clayton, R. W.: Localized seismic deformation in the upper mantle revealed by dense seismic arrays, Science, 354, 88–92, 2016.

Inza, L. A., Mars, J. I., Métaxian, J. P., O'Brien, G. S., and Macedo, O.: Seismo-volcano source localization with triaxial broad-band seismic array, Geophysical Journal International, 187, 371–384, doi: 10.1111/j.1365-246X.2011.05148.x, 2011.

Irvine-Fynn, T. D. L., Moorman, B. J., Williams, J. L. M., and Walter, F. S. A.: Seasonal changes in ground-penetrating radar signature observed at a polythermal glacier, Bylots Island, Canada, Earth Surface Processes and Landforms, 31, 892–909, doi: 10.1002/esp.1299, 2006.

Jansson, P., Hock, R., and Schneider, T.: The concept of glacier storage: a review, Journal of Hydrology, 282, 116–129, 2003.

Jones, G. A., Kulessa, B., Doyle, S. H., Dow, C. F., and Hubbard, A.: An automated approach to the location of icequakes using seismic waveform amplitudes, Annals of Glaciology, 54, 1–9, doi: 10.3189/2013AoG64A074, 2013.

Joughin, I., Smith, B. E., and Howat, I.: Greenland Ice Mapping Project: Ice flow velocity variation at sub-monthly to decadal timescales, Cryosphere, 12, 2211–2227, doi: 10.5194/tc-12-2211-2018, 2018.

Kamb, B.: Glacier surge mechanism based on linked cavity configuration of the basal water conduit system, Journal of Geophysical Research, 92, 9083, doi: 10.1029/JB092iB09p09083, URL http://doi.wiley.com/10.1029/JB092iB09p09083, 1987.

Kamb, B. and LaChapelle, E.: Direct Observation of the Mechanism of Glacier Sliding over Bedrock, Journal of Glaciology, 5, 159–172, 1964.

King, M. D., Howat, I. M., Candela, S. G., Noh, M. J., Jeong, S., Noël, B. P. Y., van den Broeke, M. R., Wouters, B., and Negrete, A.: Dynamic ice loss from the Greenland Ice Sheet driven by sustained glacier retreat, Communications Earth & Environment, 1, 1–7, doi: 10.1038/s43247-020-0001-2, URL http://dx.doi.org/10.1038/s43247-020-0001-2, 2020.

Köhler, A., Chapuis, A., Nuth, C., Kohler, J., and Weidle, C.: Autonomous detection of calving-related seismicity at Kronebreen, Svalbard, Cryosphere, 6, 393–406, doi: 10.5194/tc-6-393-2012, 2012a.

Köhler, A., Weidle, C., and Maupin, V.: On the effect of topography on surface wave propagation in the ambient noise frequency range, Journal of Seismology, 16, 221–231, doi: 10.1007/s10950-011-9264-5, 2012b.

Kohler, A., Maupin, V., Nuth, C., Van Pelt, W., Köhler, A., Maupin, V., Nuth, C., and Pelt, W. V. A. N.: Characterization of seasonal glacial seismicity from a single-station on-ice record at Holtedahlfonna, Svalbard, Annals of Glaciology, 60, 23–36, doi: 10.1017/aog.2019.15, 2019.

Kohnen, H.: Über die Absorption elastischer longitudinaler Wellen im Eis, Polarforschung, 39, 269–275, 1969.

Kolmogorov, A. N.: The local structure of turbulence in incompressible viscous fluid for very large Reynolds numbers, Cr Acad. Sci. URSS, 30, 301–305, 1941.

Koppes, M., Hallet, B., Rignot, E., Mouginot, J., Wellner, J. S., and Boldt, K.: Observed latitudinal variations in erosion as a function of glacier dynamics, Nature, 526, 100–103, doi: 10.1038/nature15385, URL http://www.nature.com/doifinder/10.1038/nature15385, 2015.

Kraaijenbrink, P. D., Shea, J. M., Pellicciotti, F., Jong, S. M., and Immerzeel, W. W.: Object-based analysis of unmanned aerial vehicle imagery to map and characterise surface features on a debris-covered glacier, Remote Sensing of Environment, 186, 581–595, doi: 10.1016/j.rse.2016.09.013, URL http://dx.doi.org/10.1016/j.rse.2016.09.013, 2016.

Kumagai, H., Palacios, P., Maeda, T., Castillo, D. B., and Nakano, M.: Seismic tracking of lahars using tremor signals, Journal of Volcanology and Geothermal Research, 183, 112–121, doi: 10.1016/j.jvolgeores.2009.03.010, URL http://dx.doi.org/10.1016/j.jvolgeores.2009.03.010, 2009.

Kumagai, H., Lacson, R., Maeda, Y., Figueroa, M. S., Yamashina, T., Ruiz, M., Palacios, P., Ortiz, H., and Yepes, H.: Source amplitudes of volcano-seismic signals determined by the amplitude source location method as a quantitative measure of event size, Journal of Volcanology and Geothermal Research, 257, 57–71, doi: 10.1016/j.jvolgeores.2013.03.002, URL http://dx.doi.org/10.1016/j.jvolgeores.2013.03.002, 2013.

Kuperman, W. A. and Turek, G.: Matched field acoustics, Mechanical Systems and Signal Processing, 11, 141–148, doi: 10.1006/mssp.1996.0066, 1997.

Larose, E., Stehly, L., and Campillo, M.: Imaging the solid Earth with seismic noise, Journal of Physics: Conference Series, 118, doi: 10.1088/1742-6596/118/1/012003, 2008.

Larose, E., Carrière, S., Voisin, C., Bottelin, P., Baillet, L., Guéguen, P., Walter, F., Jongmans, D., Guillier, B., Garambois, S., Gimbert, F., and Massey, C.: Environmental seismology: What can we learn on earth surface processes with ambient noise?, Journal of Applied Geophysics, 116, 62–74, doi: 10.1016/j.jappgeo.2015.02.001, URL http://dx.doi.org/10.1016/j.jappgeo.2015.02.001, 2015.

Legaz, A., Revil, A., Roux, P., Vandemeulebrouck, J., Gouédard, P., Hurst, T., and Bolève, A.: Self-potential and passive seismic monitoring of hydrothermal activity: A case study at Iodine Pool, Waimangu geothermal valley, New Zealand, Journal of Volcanology and Geothermal Research, 179, 11–18, doi: 10.1016/j.jvolgeores.2008.09.015, URL http://dx.doi.org/10.1016/j.jvolgeores.2008.09.015, 2009.

Levy, C., Mangeney, A., Bonilla, F., Hibert, C., Calder, E. S., Smith, P. J., and Al, L. E. T.: Journal of Geophysical Research : Solid Earth Friction weakening in granular flows deduced from seismic records at the Soufrière Hills Volcano , Montserrat, pp. 1–22, doi: 10.1002/2015JB012151.Accurate, 2015.

Li, Z., Peng, Z., Hollis, D., Zhu, L., and McClellan, J.: High-resolution seismic event detection using local similarity for Large-N arrays, Scientific reports, 8, 1646, 2018.

Lin, F.-c., Li, D., Clayton, R. W., and Hollis, D.: High-resolution 3D shallow crustal structure in Long Beach , California : Application of ambient noise tomography on a dense seismic array, 78, 2013a.

Lin, F.-C., Li, D., Clayton, R. W., and Hollis, D.: High-resolution 3D shallow crustal structure in Long Beach, California: Application of ambient noise tomography on a dense seismic arrayNoise tomography with a dense array, Geophysics, 78, Q45—-Q56, 2013b.

Lindner, F., Laske, G., Walter, F., and Doran, A. K.: Crevasse-induced Rayleigh-wave azimuthal

anisotropy on Glacier de la Plaine Morte , Switzerland, Annals of Glaciology, 60, 1–16, doi: 10.1017/aog.2018.25, 2018.

Lindner, F., Walter, F., Laske, G., and Gimbert, F.: Glaciohydraulic seismic tremors on an Alpine glacier, Cryosphere, 14, 287–308, doi: 10.5194/tc-14-287-2020, URL `https://www.the-cryosphere.net/14/287/2020/`, 2020.

Lipovsky, B. P. and Dunham, E. M.: Tremor during ice-stream stick slip, Cryosphere, 10, 385–399, doi: 10.5194/tc-10-385-2016, 2016.

Lipovsky, B. P., Meyer, C. R., Zoet, L. K., McCarthy, C., Hansen, D. D., Rempel, A. W., and Gimbert, F.: Glacier sliding, seismicity and sediment entrainment, Annals of Glaciology, 60, 182–192, doi: 10.1017/aog.2019.24, 2019.

Lliboutry, L.: General Theory of Subglacial Cavitation and Sliding of Temperate Glaciers, Journal of Glaciology, 7, 21–58, doi: 10.1017/S0022143000020396, URL `https://www.cambridge.org/core/product/identifier/S0022143000020396/type/journal{_}article`, 1968.

Lliboutry, L.: Modifications to the theory of intraglacial waterways for the case of subglacial ones., Journal of Glaciology, 29, 216–226, doi: 10.1017/S0022143000008273, 1983.

Lobkis, O. I. and Weaver, R. L.: On the emergence of the Green's function in the correlations of a diffuse field: Journal of the Acoustical Society ofAmerica, 2001.

Lomax, A., Virieux, J., Volant, P., and Berge-Thierry, C.: Probabilistic earthquake location in 3D and layered models, in: Advances in seismic event location, pp. 101–134, Springer, 2000.

Longuet-Higgins, M. S.: A theory of the origin of microseisms, Philosophical Transactions of the Royal Society of London. Series A, Mathematical and Physical Sciences, 243, 1–35, 1950.

Maier, N., Humphrey, N., Harper, J., and Meierbachtol, T.: Sliding dominates slow-flowing margin regions, Greenland Ice Sheet, Science Advances, 5, doi: 10.1126/sciadv.aaw5406, 2019.

Marshall, S., Roads, J. O., and Glatzmaier, G.: Snow hydrology in a general circulation model, Journal of Climate, 7, 1251–1269, 1994.

Meng, H. and Ben-Zion, Y.: Detection of small earthquakes with dense array data: Example from the San Jacinto fault zone, southern California, Geophysical Journal International, 212, 442–457, 2018.

Mikesell, T. D., Wijk, K. V., Haney, M. M., Bradford, J. H., Marshall, H. P., Harper, J. T., Van Wijk, K., Haney, M. M., Bradford, J. H., Marshall, H. P., and Harper, J. T.: Monitoring glacier surface seismicity in time and space using Rayleigh waves, Journal of Geophysical Research: Earth Surface, 117, 1–12, doi: 10.1029/2011JF002259, 2012.

Minchew, B. and Joughin, I.: Toward a universal glacier slip law, Science, 368, 29–30, doi: 10.1126/science.abb3566, 2020.

Moon, T., Joughin, I., Smith, B., Van Den Broeke, M. R., Van De Berg, W. J., Noël, B., Usher, M., Broeke, M. R., Berg, W. J., Noël, B., Usher, M., Van Den Broeke, M. R., Van De Berg, W. J., Noël, B., and Usher, M.: Distinct patterns of seasonal Greenland glacier velocity, Geophysical Research Letters, 41, 7209–7216, doi: 10.1002/2014GL061836, 2014.

Moon, T., Joughin, I., and Smith, B.: Journal of Geophysical Research : Earth Surface, Journal of Geophysical Research: Earth Surface, pp. 1–16, doi: 10.1002/2015JF003494.Received, 2015.

Mordret, A., Landès, M., and Roux, P.: Studying seabed above the Valhall oil field with Ambient Noise Surface Wave Tomography.

Mordret, A., Roux, P., Boué, P., and Ben-Zion, Y.: Shallow three-dimensional structure of the San Jacinto fault zone revealed from ambient noise imaging with a dense seismic array, Geophysical Journal International, 216, 896–905, doi: 10.1093/gji/ggy464, 2019.

Moreau, L., Caleap, M., Velichko, A., and Wilcox, P. D.: Scattering of guided waves by through-thickness cavities with irregular shapes, Wave Motion, 48, 586–602, doi: 10.

1016/j.wavemoti.2011.04.010, URL `http://dx.doi.org/10.1016/j.wavemoti.2011.04.010`, 2011.

Moreau, L., Lachaud, C., Théry, R., Predoi, M. V., Marsan, D., Larose, E., Weiss, J., and Montagnat, M.: Monitoring ice thickness and elastic properties from the measurement of leaky guided waves: A laboratory experiment, The Journal of the Acoustical Society of America, 142, 2873–2880, doi: 10.1121/1.5009933, 2017.

Moustard, F. and Leduc, F.: Nos liens au monde: Penser la complexité, Editions L'Harmattan, 2020.

Murray, T. and Clarke, G. K. C.: Black-box modeling of the subglacial water system, Journal of Geophysical Research: Solid Earth, 100, 10 231–10 245, 1995.

Nanni, U., Gimbert, F., Vincent, C., Gräff, D., Walter, F., Piard, L., and Moreau, L.: Quantification of seasonal and diurnal dynamics of subglacial channels using seismic observations on an Alpine glacier, Cryosphere, 14, 1475–1496, doi: 10.5194/tc-14-1475-2020, 2020.

Neave, K. G. and Savage, J. C.: Icequakes on the Athabasca Glacier, J Geophys Res, 75, 1351–1362, 1970.

Nienow, P. W., Sharp, M., and Willis, I. C.: Velocity–discharge relationships derived from dye tracer experiments in glacial meltwaters: implications for subglacial flow conditions, Hydrological Processes, 10, 1411–1426, 1996.

Nienow, P. W., Hubbard, A. L., Hubbard, B. P., Chandler, D. M., Mair, D. W. F., Sharp, M. J., and Willis, I. C.: Hydrological controls on diurnal ice flow variability in valley glaciers, Journal of Geophysical Research: Earth Surface, 110, 1–11, doi: 10.1029/2003JF000112, 2005.

Nye, J. F.: The Flow of a Glacier in a Channel of Rectangular, Elliptic or Parabolic Cross-Section, Journal of Glaciology, 5, 661–690, doi: 10.1017/S0022143000018670, URL `https://www.cambridge.org/core/product/identifier/S0022143000018670/type/journal{_}article`, 1965.

Ogiso, M. and Yomogida, K.: Estimation of locations and migration of debris flows on Izu-Oshima Island, Japan, on 16 October 2013 by the distribution of high frequency seismic amplitudes, Journal of Volcanology and Geothermal Research, 298, 15–26, doi: 10.1016/j.jvolgeores.2015.03.015, URL `http://dx.doi.org/10.1016/j.jvolgeores.2015.03.015`, 2015.

Palmer, S., Shepherd, A., Nienow, P., and Joughin, I.: Seasonal speedup of the Greenland Ice Sheet linked to routing of surface water, Earth and Planetary Science Letters, 302, 423–428, doi: 10.1016/j.epsl.2010.12.037, URL `http://dx.doi.org/10.1016/j.epsl.2010.12.037`, 2011.

Podolskiy, E. A. and Walter, F.: Cryoseismology, Reviews of Geophysics, 54, 708–758, doi: 10.1002/2016RG000526, 2016.

Podolskiy, E. A., Fujita, K., Sunako, S., and Sato, Y.: Viscoelastic Modeling of Nocturnal Thermal Fracturing in a Himalayan Debris-Covered Glacier, Journal of Geophysical Research: Earth Surface, 124, 1485–1515, doi: 10.1029/2018JF004848, 2019.

Polvi, L. E., Dietze, M., Lotsari, E., Turowski, J. M., and Lind, L.: Seismic monitoring of a subarctic river: seasonal variations in hydraulics, sediment transport and ice dynamics, Journal of Geophysical Research: Earth Surface, pp. 1–22, doi: 10.1029/2019jf005333, 2020.

Preiswerk, L. E.: MONITORING AND STRUCTURAL STUDIES WITH, PhD, 2018.

Preiswerk, L. E. and Walter, F.: High-Frequency (>2 Hz) Ambient Seismic Noise on High-Melt Glaciers: Green's Function Estimation and Source Characterization, Journal of Geophysical Research: Earth Surface, 123, 1667–1681, doi: 10.1029/2017JF004498, 2018.

Preiswerk, L. E., Michel, C., Walter, F., and Fäh, D.: Effects of geometry on the seismic wavefield of Alpine glaciers, Annals of Glaciology, 60, 1–13, doi: 10.1017/aog.2018.27, 2018.

Pyrak-nolte, L. J., Mullenbach, B. L., Li, X., Nolte, D. D., and Grader, A. S.: synthetic sediments using seismic wave transmission Sample, Geophysical Research Letters, 26, 127–130, 1999.

Rada, C. and Schoof, C.: Channelized , distributed , and disconnected : subglacial drainage under a valley glacier in the Yukon, Cryosphere, 12, 2609–2636, 2018.

Richards, K. S., Sharp, M. J., Arnold, N. S., Gurnell, A. M., Clark, M. M. J., Tranter, M. M., Nienow, P. W., Brown, G. H., Willis, I. C., and Lawson, W.: An integrated approach to modelling hydrology and water quality in glacierised catchments, Hydrological Processes, 10, 479–508, doi: 10.1002/(SICI)1099-1085(199604)10:4<479::AID-HYP406>3.0.CO;2-D, 1996.

Ritz, C., Edwards, T. L., Durand, G., Payne, A. J., Peyaud, V., and Hindmarsh, R. C. A.: Potential sea-level rise from Antarctic ice-sheet instability constrained by observations, Nature, 528, 115–118, doi: 10.1038/nature16147, URL http://www.nature.com/doifinder/10.1038/nature16147, 2015.

Roeoesli, C., Helmstetter, A., Walter, F., and Kissling, E.: Meltwater influences on deep stick-slip icequakes near the base of the Greenland Ice Sheet, Journal of Geophysical Research F: Earth Surface, 121, 223–240, doi: 10.1002/2015JF003601, URL http://doi.wiley.com/10.1002/2015JF003601, 2016.

Röösli, C., Walter, F., Husen, S., Andrews, L. C., Lüthi, M. P., Catania, G. A., and Kissling, E.: Sustained seismic tremors and icequakes detected in the ablation zone of the Greenland ice sheet, Journal of Glaciology, 60, 563–575, doi: 10.3189/2014joG13j210, 2014.

Rost, S. and Thomas, C.: Array seismology: Methods and applications, Reviews of Geophysics, 40, 2–1–2–27, doi: 10.1029/2000RG000100, 2002.

Roth, D. L., Brodsky, E. E., Finnegan, N. J., Rickenmann, D., Turowski, J. M., and Badoux, A.: Bed load sediment transport inferred from seismic signals near a river, Journal of Geophysical Research: Earth Surface, 121, 725–747, 2016.

Röthlisberger, H.: Water Pressure in Intra- and Subglacial Channels, Journal of Glaciology, 11, 177–203, doi: 10.3189/S0022143000022188, URL https://www.cambridge.org/core/product/identifier/S0022143000022188/type/journal{_}article, 1972.

Roux, P. F., Walter, F., Riesen, P., Sugiyama, S., and Funk, M.: Observation of surface seismic activity changes of an Alpine glacier during a glacier-dammed lake outburst, Journal of Geophysical Research: Earth Surface, 115, 1–13, doi: 10.1029/2009JF001535, 2010.

Roux, P.-F. F., Marsan, D., Métaxian, J.-P. P., O'Brien, G., and Moreau, L.: Micro-seismic activity within a serac zone in an alpine glacier (glacier d ' Argentière , France), Journal of Glaciology, 8, 157–168, 2008.

Scherler, D., Bookhagen, B., and Strecker, M. R.: Hillslope-glacier coupling: The interplay of topography and glacial dynamics in High Asia, Journal of Geophysical Research: Earth Surface, 116, 1–21, doi: 10.1029/2010JF001751, 2011.

Schmandt, B., Aster, R. C., Scherler, D., Tsai, V. C., and Karlstrom, K.: Multiple fluvial processes detected by riverside seismic and infrasound monitoring of a controlled flood in the Grand Canyon, Geophysical Research Letters, 40, 4858–4863, 2013.

Schoof, C.: Ice-sheet acceleration driven by melt supply variability, Nature, 468, 803–806, doi: 10.1038/nature09618, URL http://www.nature.com/doifinder/10.1038/nature09618, 2010.

Schwanghart, W. and Scherler, D.: Short Communication: TopoToolbox 2 - MATLAB-based software for topographic analysis and modeling in Earth surface sciences, Earth Surface Dynamics, 2, 1–7, doi: 10.5194/esurf-2-1-2014, 2014.

Sergeant, A., Chmiel, M., Lindner, F., Walter, F., Roux, P., Chaput, J., Gimbert, F., and Mordret, A.: On the Green's function emergence from interferometry of seismic wave fields generated in high-melt glaciers: Implications for passive imaging and monitoring, Cryosphere, 14, 1139–1171, doi: 10.5194/tc-14-1139-2020, 2020.

Sergienko, O. V., Macayeal, D. R., and Bindschadler, R. A.: Stick-slip behavior of ice streams: Modeling investigations, Annals of Glaciology, 50, 87–94, doi: 10.3189/172756409789624274, 2009.

Shapiro, N. M., Ritzwoller, M. H., and Bensen, G. D.: Surce location of the 26 sec microseism from cross-correlations of ambient seismic noise, Geophysical Research Letters, 33, 1–5, doi: 10.1029/2006GL027010, 2006.

Shreve, R. L.: Movement of Water in Glaciers, Journal of Glaciology, 11, 205–214, doi: 10.3189/s002214300002219x, 1972.

Smith, L. C., Chu, V. W., Yang, K., Gleason, C. J., Pitcher, L. H., Rennermalm, A. K., Legleiter, C. J., Behar, A. E., Overstreet, B. T., Moustafa, S. E., Others, Tedesco, M., Forster, R. R., LeWinter, A. L., Finnegan, D. C., Sheng, Y., and Balog, J.: Efficient meltwater drainage through supraglacial streams and rivers on the southwest Greenland ice sheet, Proceedings of the National Academy of Sciences, 112, 1001–1006, doi: 10.1073/pnas.1413024112, URL http://www.pnas.org/lookup/doi/10.1073/pnas.1413024112, 2015.

Sole, A., Nienow, P., Bartholomew, I., Mair, D., Cowton, T., Tedstone, A., and King, M. A.: Winter motion mediates dynamic response of the Greenland Ice Sheet to warmer summers, Geophysical Research Letters, 40, 3940–3944, doi: 10.1002/grl.50764, 2013.

Soubestre, J., Seydoux, L., Shapiro, N. M., de Rosny, J., Droznin, D. V., Droznina, S. Y., Senyukov, S. L., and Gordeev, E. I.: Depth Migration of Seismovolcanic Tremor Sources Below the Klyuchevskoy Volcanic Group (Kamchatka) Determined From a Network-Based Analysis, Geophysical Research Letters, 46, 8018–8030, doi: 10.1029/2019GL083465, 2019.

Stehly, L., Campillo, M., and Shapiro, N. M.: A study of the seismic noise from its long-range correlation properties, Journal of Geophysical Research: Solid Earth, 111, 2006.

Stein, S. and Wysession, M.: An introduction to seismology, earthquakes, and earth structure, John Wiley & Sons, 2009.

Stolt, R. H.: Migration by Fourier transform, Geophysics, 43, 23–48, 1978.

Strickler, A.: Contributions to the Question of a Velocity Formula and Roughness Data for Streams, Channels and Closed Pipelines, Lab. of Hydraul. and Water Resour, URL https://authors.library.caltech.edu/29103/1/T-10{_}{_}1981.pdfhttps://resolver.caltech.edu/CaltechAUTHORS:20120202-142837599, 1981.

Tedstone, A. J., Nienow, P. W., Sole, A. J., Mair, D. W. F., Cowton, T. R., Bartholomew, I. D., and King, M. A.: Greenland ice sheet motion insensitive to exceptional meltwater forcing, Proceedings of the National Academy of Sciences, 110, 19 719–19 724, doi: 10.1073/pnas.1315843110, URL http://www.pnas.org/cgi/doi/10.1073/pnas.1315843110, 2013.

Tedstone, A. J., Nienow, P. W., Gourmelen, N., Dehecq, A., Goldberg, D., and Hanna, E.: Decadal slowdown of a land-terminating sector of the Greenland Ice Sheet despite warming, Nature, 526, 692–695, doi: 10.1038/nature15722, URL http://www.nature.com/doifinder/10.1038/nature15722, 2015.

Tranter, M., Brown, G. H., Hodson, A. J., and Gurnell, A. M.: Hydrochemistry as an indicator of subglacial drainage system structure: a comparison of Alpine and Sub-Polar environments, Hydrological Processes, 10, 541–556, doi: 10.1002/(SICI)1099-1085(199604)10:4<541::AID-HYP391>3.3.CO;2-0, 1996.

Tsai, V. C., Rice, J. R., and Fahnestock, M.: Possible mechanisms for glacial earthquakes, Journal of Geophysical Research: Earth Surface, 113, 1–17, doi: 10.1029/2007JF000944, 2008.

Tsai, V. C., Minchew, B., Lamb, M. P., and Ampuero, J.-P.: A physical model for seismic noise generation from sediment transport in rivers, Geophysical Research Letters, 39, doi: https://doi.org/10.1029/2011GL050255, 2012.

Vallis, G.: Climate and the Ocean Circulation, Monthly Weather Review, 97, 806–827, doi: 10.1175/1520-0493(1969)097<0806:CATOC>2.3.CO;2, 1969.

Vandemeulebrouck, J., Roux, P., and Cros, E.: The plumbing of Old Faithful Geyser revealed by hydrothermal tremor, Geophysical Research Letters, 40, 1989–1993, doi: 10.1002/grl.50422, 2013.

Vaughan, D. G.: Relating the occurrence of crevasses to surface strain rates, Journal of Glaciology, 39, 255–266, doi: 10.1017/S0022143000015926, 1993.

Venkatesh, S. R., Polak, D. R., and Narayanan, S.: Beamforming algorithm for distributed source localization and its application to jet noise, AIAA Journal, 41, 1238–1246, doi: 10.2514/2.2092, 2003.

Vincent, C. and Moreau, L.: Sliding velocity fluctuations and subglacial hydrology over the last two decades on Argentière glacier, Mont Blanc area, Journal of Glaciology, 62, 805–815, doi: 10.1017/jog.2016.35, 2016.

Vincent, C., Soruco, A., Six, D., Le Meur, E., and Meur, E. L.: Glacier thickening and decay analysis from 50 years of glaciological observations performed on Glacier d'Argentière, Mont Blanc area, France, Annals of Glaciology, 50, 73–79, doi: 10.3189/172756409787769500, 2009.

Vivian, R. and Bocquet, G.: Subglacial cavitation phenomena under the {G}lacier d'{A}rgenti{è}re, Journal of Glaciology, 12, 439–451, 1973.

Vore, M. E., Bartholomaus, T. C., Winberry, J. P., Walter, J. I., and Amundson, J. M.: Seismic Tremor Reveals Spatial Organization and Temporal Changes of Subglacial Water System, Journal of Geophysical Research: Earth Surface, 124, 427–446, doi: 10.1029/2018JF004819, 2019.

Walder, B. J. S.: Hydraulics of sub glacial cavities, 2017.

Walder, J. S. and Fowler, A.: Channelized subglacial drainage over a deformable bed, Journal of Glaciology, 40, 3–15, doi: 10.1017/S0022143000003750, 1994.

Walter, F., Roux, P.-F. F. P., Roeoesli, C., Lecointre, A., Kilb, D., and Roux, P.-F. F. P.: Using glacier seismicity for phase velocity measurements and Green's function retrieval, Geophysical Journal International, 201, 1722–1737, doi: 10.1093/gji/ggv069, 2015.

Walter, F., Burtin, A., McArdell, B. W., Hovius, N., Weder, B., and Turowski, J. M.: Testing seismic amplitude source location for fast debris-flow detection at Illgraben, Switzerland, Natural Hazards and Earth System Sciences, 17, 939–955, doi: 10.5194/nhess-17-939-2017, 2017.

Walter, F., Gräff, D., Lindner, F., Paitz, P., Köpfli, M., Chmiel, M., and Fichtner, A.: Distributed acoustic sensing of microseismic sources and wave propagation in glaciated terrain, Nature Communications, 11, doi: 10.1038/s41467-020-15824-6, 2020.

Wathelet, M., Chatelain, J.-L., Cornou, C., Giulio, G. D., Guillier, B., Ohrnberger, M., and Savvaidis, A.: Geopsy: A User-Friendly Open-Source Tool Set for Ambient Vibration Processing, Seismological Research Letters, 91, 1878–1889, 2020.

Weaver, C. S. and Malone, S. D.: Seismic evidence for discrete glacier motion at the rock-ice interface., Journal of Glaciology, 23, 171–184, doi: 10.1017/S0022143000029816, 1979.

Weertman, J.: On the sliding of glaciers, Journal of Glaciology, 3, 33–38, 1957.

Welch, P.: The use of fast Fourier transform for the estimation of power spectra: a method based on time averaging over short, modified periodograms, IEEE Transactions on audio and electroacoustics, 15, 70–73, 1967.

Werder, M. A., Hewitt, I. J., Schoof, C. G., and Flowers, G. E.: Modeling channelized and distributed subglacial drainage in two dimensions, Journal of Geophysical Research: Earth Surface, 118, 2140–2158, doi: 10.1002/jgrf.20146, 2013.

Willis, I. C.: Intra-annual variations in glacier motion: a review, Progress in Physical Geography, 19, 61–106, doi: 10.1177/030913339501900104, URL http://journals.sagepub.com/doi/10.1177/030913339501900104, 1995.

Winberry, J. P., Anandakrishnan, S., Alley, R. B., Bindschadler, R. A., and King, M. A.: Basal mechanics of ice streams: Insights from the stick-slip motion of Whillans Ice Stream, West Antarctica, Journal of Geophysical Research: Earth Surface, 114, 1–11, doi: 10.1029/2008JF001035, 2009.

Winberry, J. P., Anandakrishnan, S., Wiens, D. A., and Alley, R. B.: Nucleation and seismic tremor associated with the glacial earthquakes of Whillans Ice Stream, Antarctica, Geophysical Research Letters, 40, 312–315, doi: 10.1002/grl.50130, 2013.

Winberry, J. P., Anandakrishnan, S., Alley, R. B., Wiens, D. A., and Pratt, M. J.: Tidal pacing, skipped slips and the slowdown of Whillans Ice Stream, Antarctica, Journal of Glaciology, 60, 795–807, doi: 10.3189/2014JoG14J038, 2014.

Zhan, Z.: Seismic Noise Interferometry Reveals Transverse Drainage Configuration Beneath the Surging Bering Glacier, Geophysical Research Letters, 46, 4747–4756, doi: 10.1029/ 2019GL082411, 2019.

Zoet, L. K., Carpenter, B., Scuderi, M., Alley, R. B., Anandakrishnan, S., Marone, C., and Jackson, M.: The effects of entrained debris on the basal sliding stability of a glacier, Journal of Geophysical Research: Earth Surface, 118, 656–666, doi: 10.1002/jgrf.20052, 2013.

Zwally, H. J., Abdalati, W., Herring, T., Larson, K., Saba, J., and Steffen, K.: Surface melt-induced acceleration of Greenland ice-sheet flow, Science, 297, 218–222, 2002.